LANCASTER UNIVERSITY
DEPARTMENT OF PHYSICS
LANCASTER UK

THERMOELECTRIC PROPERTIES OF ULTRA-THIN FILM FORMED BY MOLECULAR SELF ASSEMBLY AND LANGMUIR-BLODGETT DEPOSITION

ANGELO LAMANTIA

Thesis submitted for the degree of doctor of philosophy

September 23, 2020

Declaration

This thesis is my original work and has not been submitted, in whole or in part, for a degree at this or any other university. Nor does it contain, to the best of my knowledge and belief, any material published or written by another person, except as acknowledged in the text.

Abstract

In the era of nanotechnology and nanosciences, the scalability and miniaturisation of the electronics component in a single chip to obtain superior devices is crucial. This aim creates new challenges for the scientific community in order to develop the materials of the future and understand their behaviour at the nanoscale. Indeed, new phenomena require specific matching tools that, in turn, open new investigation prospects. Among the branches of nanoscience, molecular electronics and, in particular thermoelectricity of molecular-based structures or devices, have gained a discrete interest especially in the past decade, not only for the basic physical knowledge of the phenomena but also for the perspective of technological developments, making molecules and molecular assembly a particular and interesting substitute to the conventional semiconductors.

Whereas conventional techniques to investigate the thermoelectric properties of molecular assembly are usually not efficient or designed to study these "soft" materials, Conductive Atomic Force Microscopy (CAFM) offers high sensitivity to the nanoscale electric and thermoelectric properties and a spatial resolution of few nm. In addition, AFM-based techniques provide outstanding control of the normal force applied by the nanometric probe on the molecules, preserving their conformation and properties. This thesis aims to find a suitable, non-destructive and reproducible way to measure the thermoelectric effect in molecular self-assembly and molecular thin-films created by Langmuir-Blodgett deposition based on CAFM.

The developments of CAFM in intermitting contact mode by combining it with Peak-force AFM (PF-AFM) allows the measurements of the electrical properties and the thermoelectric signature of the molecular films preserving the molecular conformation, thanks to the soft contact ensured by the intermitting contact. Also, by combining those two AFM modes, it was possible acquiring electric and nanomechanical properties simultaneously, which has never been reported before.

The developed technique was employed to measure the thermoelectric properties of different families of molecules. The measurement system was initially tested with some

well known alkyl thiolate molecules. More complex structures were also analysed to find the dependency of the thermal power on the thickness of the molecular film and the eventual chemical structure itself. Interestingly, results were found to be quite sensitive to the growth condition of the molecular samples too, revealing outstanding thermal power values for the thicker films growth by LB technique.

The research presented in this thesis has then a two-fold impact. On the one hand, the measurement setup development, which represents the major challenge, was answered by developing and studying an intermitting contact technique based on CAFM and PF-AFM, opening a new route for further investigations. On the other hand, new insights from the properties studied during the measurements were obtained on the molecular film quality and uniformity dependence. In addition, the information gained from the doping of metallo-porphyrin molecules opens a new way to tailor the thermal power of molecular assembly *ex-situ*.

Contents

List of Figures

List of Tables

Aim and Motivation

In the year 1965, Intel co-founder Gordon E. Moore published his famous empiric prediction in Electronics Magazine known as Moore's law [1]. This law states that the processing power of computers will double every 18 months. Surprisingly, the empiric Moore's law fitted very well the increases of the number of transistors in microprocessors for almost half-century after being proposed.
Germanium (Ge) and Silicon (Si) were employed for nearly 30 years as fundamental building block for transistors and memories until the silicon-based industry is facing a "silicon wall". Indeed, as the silicon components' size was further scaled, it resulted in more difficulty to obtain uniform doping levels of the material due to the complex bulk behaviours. Thus, it appears challenging to make more densely packed silicon transistors, respecting Moore's law.

The idea to replace inorganic semiconductor with molecules is an idea that Richard P. Feynman already had in his famous talk "There's Plenty of Room at the Bottom" at the annual American meeting Physical Society at the California Institute of Technology [2]. He proposed an important concept during the speech, which is making manipulations under the molecular or even atomic level.
Thus, since the beginning of molecular electronics, the field has been driven by the dream of incorporating molecular units as functional components in electronic devices. When in the '70s, the first single molecule diode was proposed [3], the main advantage of using molecular devices laid in their small size compared to the transistors of that time, mostly made from gallium arsenide (GaAs) or silicon carbide (SiC) with channel lengths of several microns [4]. The use of nanometer-sized molecules, therefore, sounded very appealing for electronic purposes. Consequently, besides the rectifier, applications such as a molecular processor [5], interconnects [6], logic gates [7], memory devices [8] and shift registers [9] were proposed.
Molecules in addition, can provide additional functionalities compared to conventional

semiconductors. Using synthetic chemistry, scientist can realise an almost endless choice of molecular structures and compositions. With the proper knowledge in principle, it is possible to design single molecules that can perform a variety of tasks that would be unthinkable in solid-state devices or would require a very high degree of complexity. The opportunity to make molecules with specialized functions (highly conductive or photo/chemical/bias switchable), pushes molecular electronics a step further towards real application and mass production.

Whilst the field of molecular electronics has long focused on the isolation and characterisation of single molecules for the study of fundamental electrical and thermal transport properties, it has been increasingly evident that, for practical applications, these tailored molecules need to be incorporated into a scalable ultra thin-film architecture on surfaces and at interfaces. Such architecture requirements are highly anisotropic and may range over many orders of magnitude from long-range lateral order of meters to controlled vertical thickness of nanometers which still ensure the enhancing of the physical properties due to the confinements of the charge carriers. In the past decades, many strategies have been explored to achieve such control. Among these techniques, molecular self-assembly, Langmuir-Blodgett deposition and Thermal sublimation in ultra-high vacuum (UHV) demonstrated proper control of the morphology and arrangements of a molecular layer onto metallic and carbon-based substrates.
However, if the realisation of molecular thin film has been well established, standard methodologies to characterise the electric and thermal transport and the thermoelectric properties of these ultra-thin molecular layers still present challenges in obtaining stable and reproducible results. Indeed, characterising the thermoelectric effect in molecular layers is an area of great and growing interest in fundamental knowledge and applications. Since the discovery of this effect in molecules by *P.Reddy et Al* in 2007, a lot of attention has grown for molecular thermoelectric materials, believed as one of the potential solutions for crucial energy problems like the problem of waste heat recovery or the heat dissipation problem in microelectronic devices and server farms.
One possible approach to this problem can be found in scanning probe microscopy techniques (SPM), which results in a powerful method to characterise molecular thin film properties at the nanoscale. SPM enables simultaneously different material properties to be obtained, controlling the normal force applied and thus, controlling the contacted molecules with the nanometric probe.

Molecular junctions formed using scanning probe techniques and using Conductive atomic force microscopy (CAFM) constitute an excellent model system to study the processes occurring at the organic-inorganic interface at a fundamental level as well as the intrinsic electric properties of the organic monolayer. Quite recently, the possibility of measuring the thermopower to give further insight into the transport process has been demonstrated and is currently used by just a few groups, even with some difficulties, in order to provide a standardised methodology for the thermoelectric characterisation of a molecular monolayer.

The aim of this thesis is to design, characterise and develop a modified CAFM to measure the thermoelectric properties of molecules. First, an optimised monolayer deposition method was studied, exploring different technique and substrates. Then the molecular layer properties were studied by mean SPM technique. A non-invasive and destructive way to characterise the studied molecules' thermoelectric properties was developed combining a well established non-contact AFM technique with CAFM. This method allows the preservation of the molecular layer during the thermoelectric measurements, increasing the Pt-coated electric probe's lifetime due to the suppression of the friction at the interface between the probe and the sample surface.

Part I

Background

Chapter 1

Quantum electronic transport in molecules

1.1 Classic transport

In a macroscopic conductor, the electric transport is described by Ohm's law, in which the conductance G (inverse of the resistance), is proportional to its cross-section (A) area and proportional to the inverse of its length (L):

$$G = \sigma \frac{A}{L} \tag{1.1}$$

where σ is the intrinsic conductivity of the material. This simple relationship has been shown to be valid for a very wide class of materials, from thin film of conductors and semiconductors and also for molecular films, within a threshold dimension. However, this classic point of view breaks down when the conductor's size approaches the carriers' De-Broglie wavelength. At this scales, the transport of the carriers turns from diffusive $L > l$ to ballistic $L < l$, where l is the free main path of the electrons in the material and, in this regime, Ohm's law is not enough to describe the transport as is based on the conduction scattering.

1.2 Quantum electric transport: Landauer's formula

The scattering approach is the most popular theoretical formalism to describe the coherent transport in nanoscale material between macroscopic metallic electrodes. This configuration is known as nanojunction. The transport and the diffusion of the carrier inside the media are regulated by the chemical potential μ of the electrodes and

the energy level of the nanodimensional material. The electrodes represent the electron reservoirs with a defined chemical potential and with a dependence of their temperature T.

From the quantum theories, the scattering approach's idea is to connect the transmission and reflection probabilities through the sample with the electronic transport.

As shown in figure 1.1, we can consider the typical transport experiment where the system to be examined is the nanodimensional sample (nanojunction with dimensions at the nanoscale), connected to the macroscopic contacts by two leads.

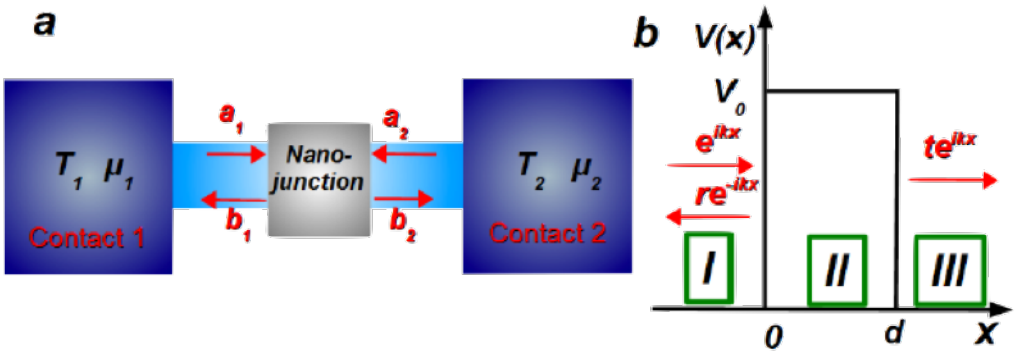

Figure 1.1: Transport through a nanojunction. (a) Nanojunction connected to two large contacts through two leads. (b) Rectangular potential barrier of height and width.

Let us first consider the nanojunction as the one dimensional rectangular potential barrier shown in Figure 1.1b. The electrons coming from the leads are scattered from this potential. If we consider an incoming electron as a plane wave, e^{ikx}, which will be partially reflected by the barrier re^{-ikx} ,where r represents the amplitutde of the incident wave, and partially transmitted, te^{ikx}, then the probability that one electron reachs the second electrode will be given by the square modulus of the transmitted wave amplitude, $|t|^2 = T(k)$ [10]. In this picture we can express the electrical current density J for a given k state as:

$$J_k = \frac{\hbar}{2m^*}\left[\psi^*\frac{d\psi}{dx} - \psi\frac{d\psi^*}{dx}\right] = \frac{e}{d}v(k)T(k) \tag{1.2}$$

where $v(k) = \dfrac{\hbar k}{m^*}$ is the group velocity of the electrons in the state k, d the length of the nanodimensional material, and $T(k)$ the probability that an electron travels from one electrode to the other.

For the system we examine, many electrons are participating in the transport so we have to consider a sum over all the states k and take into account the Pauli principle

by introducing a factor $f_1(k)[1 - f_2(k)]$, where $f_{1,2}$ are the Fermi distributions in the reservoirs 1 and 2. This factor will ensure that the initial occupied states of reservoir 1 and the empty states of reservoir 2 are contributing to the current flow from 1 to 2 which will be given by:

$$J_{1,2} = \sum_k \frac{e}{d} v(k) T(k) \left[f_1(k) \left(1 - f_2(k)\right)\right] \tag{1.3}$$

Converting the sum over K values into an integral over all the energy per k value and introducing the density of the states per k value :

$$J_{1\to 2} = \frac{e}{h} \int_{-\infty}^{+\infty} T(E) \left[f_1(E) \left(1 - f_2(E)\right)\right] dE \tag{1.4}$$

And in the same way, for the electron flowing from the second to the first electrode:

$$J_{2\to 1} = \frac{e}{h} \int_{-\infty}^{+\infty} T(E) \left[f_2(E) \left(1 - f_1(E)\right)\right] dE \tag{1.5}$$

So the total current I results as the net difference between $J_{1\to 2}$ and $J_{2\to 1}$:

$$I = J_{1\to 2} - J_{2\to 1} = \frac{2e}{h} \int_{-\infty}^{+\infty} T(E) \left[f_1(E) - f_2(E)\right] dE \tag{1.6}$$

Equation 1.6 is the Landauer formula and describes the strict relationship between the electric transport and the transmission function $T(E)$. Factor 2 is added to take into account the spin degeneracy of the electrons. In the case where the temperature of the system approaches to zero, the two Fermi distributions $f_{1,2}$ are step functions with values 1 below their chemical potential $\mu_1 = E_f + \frac{eV}{2}$ and $\mu_2 = E_f - \frac{eV}{2}$, and zero otherwise. Then, at the limit of $T \to 0$ and low bias voltage, the current is given by $I = GV$, where the conductance G is:

$$G = \frac{2e^2}{h} T(E_f) \tag{1.7}$$

For a two-level system, in a perfectly conductive channel, it is easy to observe that there is a maximum in the conductance G_0, representing a fundamental constant related to the electron charge and the Planck's constant h:

$$G_0 = \frac{2e^2}{h} = 7.74810^5 \mathrm{S} \tag{1.8}$$

The value G_0 is known as *conductance quantum* and is often used as a reference value for the electric conductance of nanodimensional systems. The beauty of this is that it clearly

shows the electrical conductance at the nanoscale, in a ballistic regime, is quantised and is mainly shown as a 1D channel as reported in fig 1.2

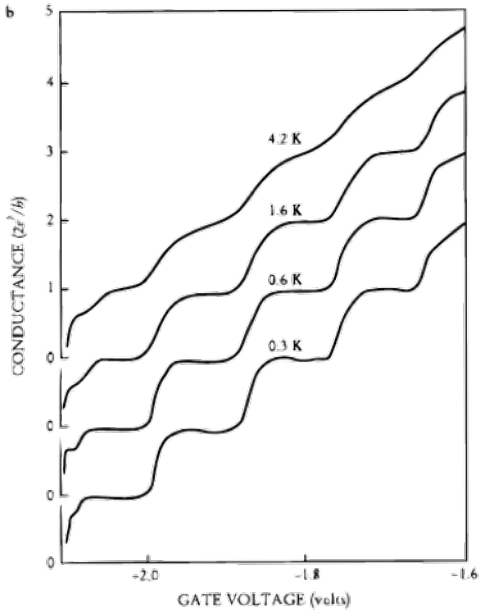

Figure 1.2: Conductance quantisation of a quantum point contact in units of $\frac{2e^2}{h}$ at different T in a GaAs/AlGaAs channel. As the gate voltage become more negative the constriction is shrunk, removing charges from the chanel and eventually totally emptied at $-2.1V_g$. The successive 1D sub-bands become occupied as V_g increase, each contributing with $1G_0$ [11].

Generalisation of Landauer formula

The Landauer formula can also be generalised for one-dimensional multiple channel transport; assuming that the electron's motion can be separated in transverse (perpendicular to the transport direction) and longitudinal (parallel to the transport direction). In the longitudinal direction the system is characterised by a continuous wavevector k_l and an energy $E_l = \frac{\hbar^2 k^2}{2m^*}$. On the other hand, the transverse motion results quantised and so described by a discrete index n and the transverse energies $E_{1,2;n}$. These states are called quantum channels. This system's total energy is $E = E_l + E_{1,2;n}$, and since E_l is positive, for a given total energy,E, there will only be a finite number of channels possible.

Considering fig. 1.1, let's consider a multiple channel picture in which $a_{1,2\ldots j;n}$, and $b_{1,2\ldots k;n}$ are operators which describe the incoming electrons impinging on the sample and the outgoing respectively per each channel. These electrons are related by the scattering matrix $\hat{S}$:

$$\begin{pmatrix} b_{1,1} \\ b_{2,1} \\ \vdots \\ b_{k,n} \end{pmatrix} = \hat{S} \begin{pmatrix} a_{1,1} \\ a_{2,1} \\ \vdots \\ a_{j,n} \end{pmatrix} \tag{1.9}$$

where:

$$\hat{S} = \begin{pmatrix} r & t^{'} \\ t & r^{'} \end{pmatrix} \tag{1.10}$$

In eq.1.10, r and $r^{'}$ are reflection amplitudes and t and t' are the transmission amplitudes associated with this potential [11].

The Landauer formula can be generalised to multiple transverse energies, by introducing the matrix $tt^{\dagger}$ which can be extracted with simple matrix algebra from the scattering matrix 1.10. This matrix's eigenvalues will be the transmission coefficients of the multiple channel system $T_n(E)$, with values 0 and 1. The corresponding wavefunctions are the eigenchannels or conduction channels, and n is the index for the electrons' transverse quantised motion. With this consideration, we can write the current as:

$$I(E_f, V, T) = \frac{2e}{h} \sum_n \int_{-\infty}^{+\infty} T_n(E) \left[f_1(E) - f_2(E) \right] dE \tag{1.11}$$

and the conductance:

$$G = \frac{2e^2}{h} \sum_n T_n(E_f) \tag{1.12}$$

which represents the generalisation of the Landauer formula for a multiple channel electrical conductance [10].

1.3 Quantum transport in molecular junctions

The idea to use molecular bridges to contact spaced electrodes was first proopsed in 1974 and is at the basis of molecular electronics [12–14]. Understanding the charge transport properties in a single molecule is an essential need in molecular electronics. As will be presented elsewhere in this work, single-molecular junctions earlier and SAMs and molecular ultra-thin film more recently have been largely used to gain more insight into

the electronic structure of the molecules.

Transport in single molecular junctions (MJs) is dictated by the laws of quantum mechanics and can be described as a particular case of the Landauer Formula presented in Sec. 1.2, where a molecule is connected to macroscopic electrodes as shown in fig 1.3.

The small size of the molecule causes spatial confinement of the charge carriers (either electrons or holes) on the molecule, leading to a discrete set of energy levels with various spacings. In addition to this effect, the spatial confinements lead to an extra charging energy due to the Coulomb interactions between the electrons.

The charge carriers on the molecule are only allowed to populate discrete energy states, of which the shape is determined by the potential landscape formed by the nuclei of the atoms forming the molecule. These states are called molecular orbitals and electrons fill these orbitals starting from the ones with the lowest available energy before filling higher ones with up to two electrons per level, following the *Pauli exclusion principle*.

The highest occupied molecular orbital is known as HOMO, in analogy with the semiconductors valence band. The Fermi energy E_f of the molecular junction lies between the HOMO and the lowest unoccupied molecular orbital (LUMO) of the molecule, which is the analogous of Conduction band in semiconductor. The energy difference between the HOMO and LUMO is called the HOMO-LUMO gap, and can be experimentally determined from UV/vis spectroscopy.

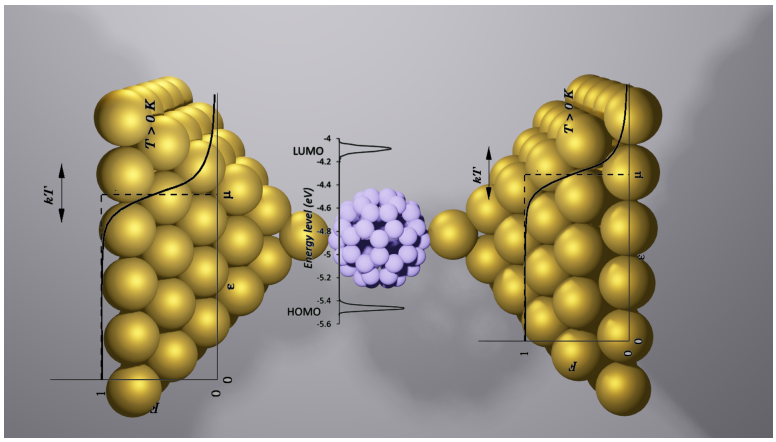

Figure 1.3: 3D representation of a molecular junction where, in this case, a fullerene molecule is trapped between two Au electrodes at different temperature T and with their respective Fermi distribution. The molecular frontier orbitals HOMO and LUMO for the C_{60} molecule are also reported.

In figure 1.3, the electrons orbitals of a molecule can be imagined as the energy levels in a semiconductor connected with two metallic electrodes.

When describing charge transport through a molecule one also has to take into account

the fact that the number of electrons on the molecule changes. When a molecule is brought in the vicinity of the electrodes (Source and Drain), the presence of the metallic surface has several important consequences. First, the electrodes act as reservoirs for charge carriers with chemical potential μ which, at $T = 0$ K is equivalent to the Fermi Energy E_f. For $T > 0$ K, the energy distribution of the electrons in the electrodes is smeared out by thermal broadening and given by the Fermi-Dirac distribution function:

$$f(E) = \frac{1}{1 + exp(\frac{\varepsilon - \mu}{k_B T})} \tag{1.13}$$

where ε is the electron energy, k_B the Boltzmann constant, μ the chemical potential of reservoir and T the temperature. At the equilibrium, the electrodes have same chemical potential μ and no current flows in the junction.
Applying a symmetrical bias voltage V_b, the chemical potential of the electrodes will shift according to:

$$\mu_s = \varepsilon_f + {}^{eV_b}/_2 \tag{1.14}$$

$$\mu_d = \varepsilon_f - {}^{eV_b}/_2 \tag{1.15}$$

with $\mu_{s/d}$ the chemical potential of source and drain respectively. This results in occupied states in the source, and empty states in the drain. For convenience, the energy range between the chemical potential of the source and the drain electrode is called the bias window, and when no molecular level is present in the bias window, transport is blocked, as the electrons do not have the necessary energy to occupy/empty an orbital (Fig. 1.4). Increasing the bias voltage across the junction increases the bias window, and as soon as the chemical potential of one of the electrodes is aligned with the molecular level (see Fig. 1.4), the blockade is lifted and current flows.

The transport mechanism through a molecule consists of tunnelling and can be described with the scattering approach and in terms of a transmission function.
In addition, the molecular orbitals are broadened depending on the metal-molecule coupling strength and temperature; many molecular orbitals can participate in the transport.
A simplified transport model can be built considering single-level resonant tunnelling, where the electrons participating in the transport will be the ones closer to the Fermi energy of the metal electrodes. In this case, the electric transport's main parameters

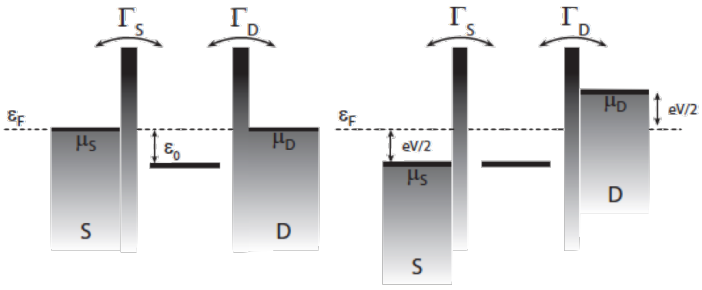

Figure 1.4: Single-level model, in which transport is described by the level alignment ε_0 and the electronic coupling Γ. In equilibrium , no net current can flow as forwar and reverse currents cancel out. Upon application of a bias, the chemical potential of the leads are different and current flows once the level is inside the bias window.

depend on the position of the frontier orbitals of the molecule $\varepsilon_0(V)$ with respect to the Fermi energy of the electrodes and the scattering rates $\Gamma_{l,r}$ describing the coupling to the metal electrodes. Therefore, using the Landauer formula 1.6, it is possible to gain vital information about a molecular junction's electric transport characteristics. The only differences with the previous case discussed in Sec.1.2 are that the transmission function $T(E)$ needs to be adjusted to take into account the strict dependence from the voltage and the coupling strength of the electrodes, and is given by the Breit-Wigner formula:

$$T(E,V) = \frac{4\Gamma_l\Gamma_r}{[E-\varepsilon_0(V)]^2 + [\Gamma_l - \Gamma_r]^2} \tag{1.16}$$

so the conductance G:

$$G = \frac{2e^2}{h}T(E,V) = \frac{2e^2}{h}\frac{4\Gamma_l\Gamma_r}{[E-\varepsilon_0(V)]^2 + [\Gamma_l - \Gamma_r]^2} \tag{1.17}$$

Which represents the generalisation of the Landauer formula for a molecular junction.

Chapter 2

Thermoelectric effect

2.1 Thermoelectric effect

In many metals and semiconductors the coupling between the electrical and thermal current, gives rise to thermoelectric phenomena [15]. This phenomena is caused by the unbalancing of charge between two side of the material due a difference of temperature in a non-equilibrium state. This difference establishes an electric field across the material until the thermal equilibrium is reached. There are two thermoelectric effects that appear in thermoelectric materials and devices: the Seebeck effect and Peltier effect.

2.1.1 Thermal conductivity and thermal current

The Seebeck effect is the direct conversion of a temperature difference to electricity. When a metallic bar is subjected to a voltage, V, or a temperature difference ΔT an electric current will be generated. Indeed, in a conductor the current is not just driven by an applied electric field E but an additional small contribution to the total current density is given by the temperature gradient established along a material (Fourier's Law) [16]:

$$\bar{j_q} = -\kappa \nabla T \tag{2.1}$$

where $\bar{j_q}$ is the current associated with the motion of the electron due to the temperature gradient and κ represents the "resistance" of the material to the heat and is known as thermal conductivity. The negative sign of $\bar{j_q}$ indicates the current always flows in the opposite direction to the temperature gradient. Introducing the collision time τ as the time between consecutive electron scattering and $\varepsilon(T)$ the thermal energy of the electrons at equilibrium temperature T in the Drude scattering model, then an

electron arriving at position x from the high temperature side (red side in fig 2.1) will have its last collision at $x - v\tau$, where v is the velocity of the electron. These electrons will carry an energy of $\varepsilon(T[x - v\tau])$.

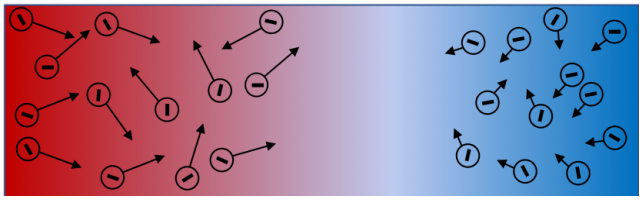

Figure 2.1: Illustration of electrons' density and motion in a material under a temperature gradient

The opposite situation will apply to the electrons coming from the cold part, where the electrons will carry less energy, $\varepsilon(T[x + v\tau])$. Adding these two contributions, the total thermal current density can be demonstrated to be:

$$j_q = nv^2\tau\frac{d\varepsilon}{dT}\left(-\frac{dT}{dx}\right) \tag{2.2}$$

where n represents the electrons' density in the material and is defined as the number of electrons N per unit volume V, $n = N/V$. To extend this model to the 3D case, the thermal mean square electron velocity v_{th}^2 along all the directions needs to be considered to take into account the average speed of the electrons. In addition, considering $nd\varepsilon/dT = N/Vd\varepsilon/dT = c_v$, the electronic specific heat, one obtains:

$$\mathbf{j_q} = \frac{1}{3}v_{th}^2\tau c_v(-\nabla T) \tag{2.3}$$

equivalent to eq.2.1 with the proportional constant κ:

$$\kappa = \frac{1}{3}v_{th}^2\tau c_v \tag{2.4}$$

known as thermal conductivity.

In a more rigorous approach known as Sommerfeld theory of electrons, the electronic speed considered in eq.2.3 needs to be adjusted to take into account the electron distribution and the density of the available states around the Fermi energy ε_f. Substituting v_{th}^2 in 2.4 with the electrons velocity at the Fermi energy $v_f^2 = 2\varepsilon/m^*$ and dividing for the electrical conductivity:

$$\frac{\kappa}{\sigma} = \frac{\pi^2}{3}\left(\frac{k_b}{e}\right)^2 T \tag{2.5}$$

which represents the Wiedemann-Franz law that correlates the electrical conductivity σ with the thermal conductivity κ and is crucial for the design of thermoelectric materials.

2.1.2 The Seebeck Effect

As discussed in the previous section, electrons in a material where a temperature gradient is established are more energetic at the hot end and, a diffusion of electrons from the hot end to the cold end will eventually occur (as in fig. 2.1). Positive carriers will then accumulate in the hot region due to the electrons migration towards the cold region, and, *viceversa*, an accumulation of negative charge will appear in the cold region. This separation of the carriers produces an electric field opposed to the temperature gradient, generating a voltage difference between the two ends of the material. The existence of such a field is known as Seebeck effect, or Thermoelectric effect, and the magnitude of the voltage difference ($\mathbf{E_{th}} = -S\nabla T$) will depend on the temperature gradient:

$$\mathbf{E_{th}} = -S\nabla T \tag{2.6}$$

where the coefficient S is known as Seebeck coefficient and is often used to characterise thermoelectric materials.

However, thermoelectricity is a competitive and non-equilibrium process and, if the temperature gradient is not maintained, low energy electrons from the cold end will start diffusing in the opposite direction suppressing the established electric field.

Considering both the electric and the thermal contribution to the total current density, it is possible to write:

$$\mathbf{J_{tot}} = \sigma(-\nabla V + \mathbf{E_{th}}) \tag{2.7}$$

Substituting eq.2.6 in eq.2.7 and considering a stationary state, in which $\mathbf{J_{tot}} = 0$ everywhere, is possible obtain a formal expression for the Seebeck coefficient S:

$$S = -\frac{\nabla V}{\nabla T} \tag{2.8}$$

That for small variations of temperature T can be written as:

$$S = -\frac{\Delta V}{\Delta T} \tag{2.9}$$

where ΔT is the temperature difference at the two ends of the material, and ΔV is the thermovoltage arising from the difference of temperature. The voltage gradient in the material is directed against the temperature gradient. For metals, both electrons and holes contribute to the thermoelectric voltage, and, as a consequence, they almost cancel each other out, giving a very low Seebeck value. Semiconductors instead, due to their carriers duplicity, can give high values of S, with a $S < 0$ for n-type semiconductors and $S > 0$ for p-type. Thus, the sign of the thermopower is a clear consequence of the carrier type which dominates the transport in the material.

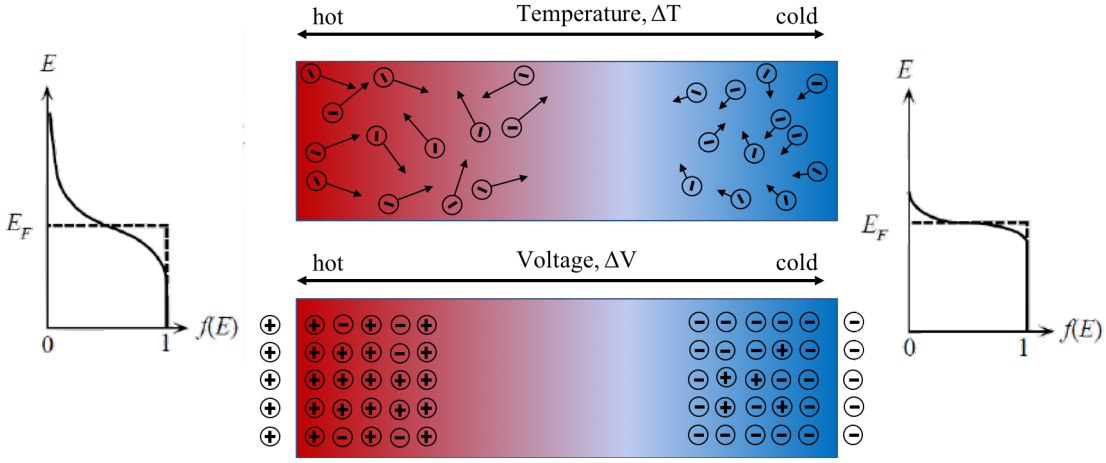

Figure 2.2: Fermi-Dirac distributions of electrons at the hot side (left) and cold side(right) of the thermoelectric material. Cartoon in the middle schematise the carries dynamic, which leads an equilibrium state in which a net electric field is generated.

The dynamics of electrons in metals and semiconductors to a first approximation can be described with the free electron model (Drude-Sommerfeld), considering the motion of the electrons without taking into account the scattering by lattice vibrations (phonons), impurities or crystal defects during diffusion. This simplified model gives a very good approximation of the Seebeck coefficient of many metals.

According to the free electrons model, for a metal where the electrons follow the Fermi-Dirac distribution $f(E) = \dfrac{1}{1 + exp(\frac{E-E_f}{k_b T})}$ and the 3D density of the states $g(E) = \dfrac{m_e}{\pi^2 \hbar^3}\sqrt{2 m_e E} = \dfrac{3}{2}\dfrac{n}{E_f}\sqrt{\dfrac{E}{E_f}}$, it can be demonstrated that the average energy per electron at the limit of $T \to 0$ is [17]:

$$E_{av}(T) \approx \frac{3}{5} E_{f0}\left[1 - \frac{5\pi^2}{12}\left(\frac{k_b T}{E_{f0}}\right)^2\right] \tag{2.10}$$

where E_{f0} is the Fermi energy at $T = 0$.

According to the Fermi-Dirac distribution in fig. 2.2, at the hot side, the electrons will have higher energy than in the cold. This will cause the diffusion of these energetic electrons to the cold side, generating a localised electric field, and for a small temperature difference ΔT, a voltage difference will be created. Therefore, at the equilibrium, the variation of the average energy 2.10, $\Delta E_{av}(T)$ needs to be balanced by the generated electric field $-q\Delta V = e\Delta V$:

$$\Delta E_{av}(T) = \frac{\partial E}{\partial T}\Delta T = \frac{\pi^2 k_b^2 T}{2E_{f0}} = e\Delta V \tag{2.11}$$

From this equation, we can obtain the value of the thermalpower S as fuction of T and the Fermi energy E_f:

$$S = -\frac{\Delta V}{\Delta T} = -\frac{\pi^2 k_b^2}{2eE_{f0}}T \tag{2.12}$$

However, equation 2.12 does not take into account any scattering with phonons, impurities or interfaces and the correct formulation will be treated in section 2.2.
Table 2.1 and fig 2.3 report the Seebeck coefficient S values for some common metals calculated with eq. 2.12:

Material	**S at 20**K [μV K^{-1}]	**S at 300**K [μV K^{-1}]
Au	1.79	1.94
Al	-1.6	-1.8
Cu	1.7	1.84
Pt	4.45	-5.28

Table 2.1: Seebeck values in μV K^{-1} for common metals at 20K and room temperature calculated with the free electron model. Values from [18].

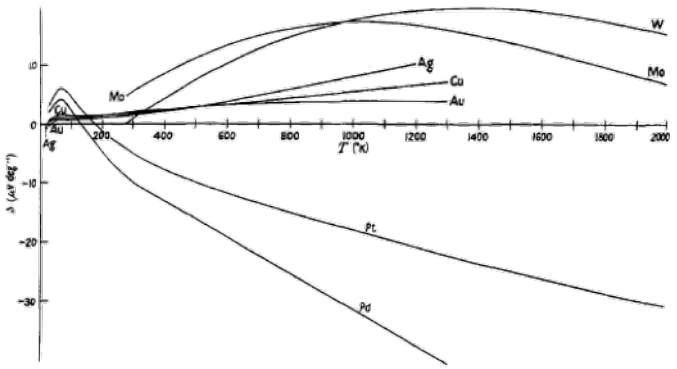

Figure 2.3: Seebeck coefficients for different metals at different temperatures obtained with the free electron model. Image from [18].

2.1.3 Thermalpower generation and figure of merit ZT

As described in Sec.2.1.2, semiconductor materials are, due to their carrier dualism, particularly suitable for thermoelectric power generation. The different signs in the conduction, depending whether *p-type* or *n-type*, give rise to a positive or a negative Seebeck.

A simple model for a power generator can be built with a positive (p-type) and a negative (n-type) branch as shown in figure 2.4.

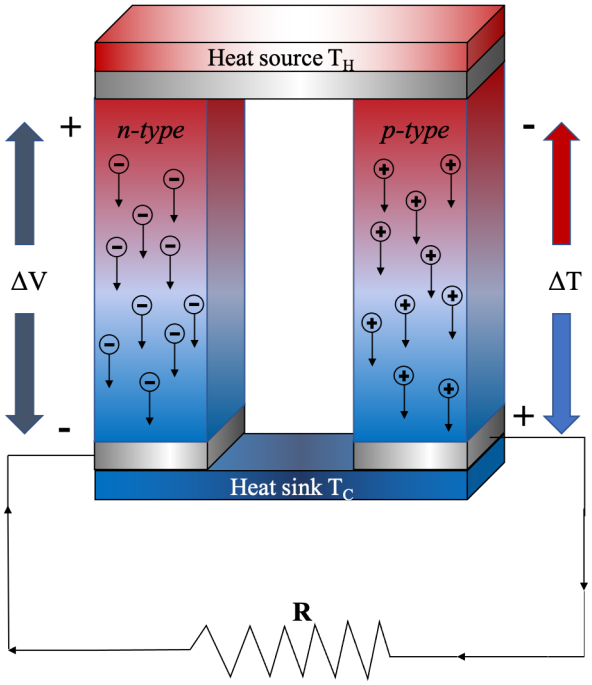

Figure 2.4: *n-type* and *p-type* semiconductors used as a thermoelectric generator. The two semiconductor legs are electrically connected in series (grey bars) and in contact with a heat source and sink. R represent a load connected in the circuit, and the generated current direction I is showed by the arrows. Carrier motion due to the temperature difference is also shown.

A resistive load is placed between the other two ends and, as shown, the two branches are electrically connected in series and thermally connected in parallel. Due to the thermoelectric effect, the supply of heat and the temperature gradient along the legs, will causes an electrical current to flow around the circuit as shown by the arrows.

The variation of electric field due to the thermal gradient $\Delta E_{th} = (S_p - S_n)(T_H - T_C)$ will produces a voltage difference ΔV that produce a current flowing in the circuit:

$$I = \frac{(S_p - S_n)(T_H - T_C)}{R_p + R_n + R} \tag{2.13}$$

where S_p, S_n are the Seebeck values of two legs and T_H and T_C are the temperature of

the heat source and the cold sink, while R_n and R_p are respectively the the resistance of the two legs and R is the load resistor.

The power W dissipated in the load resistor R is given by:

$$W = I^2 R = \left[\frac{(S_p - S_n)(T_H - T_C)}{R_p + R_n + R}\right]^2 R \tag{2.14}$$

However, the thermoelectric effect is a competitive process, and this means that if the temperature gradient needs to be maintained in order to guarantee the generation of the potential difference, this last itself, due to a process known as Peltier cooling, will slightly suppress the thermal gradient reducing then the magnitude ΔT. For this reason, balancing in the heat flow need to be established in order to determine the total efficiency of such a system.

The heat source is then used to balance the Peltier effect associated with the flow of current. The rate of cooling can be expressed in terms of the Seebeck coefficient as $\dot{Q}_{Peltier} = (S_p - S_n)/T_H$. From the other side, the heat flow is given by
$\dot{Q}_h = (\kappa_p + \kappa_n)(T_H - T_C)$, where $\kappa n, p$ are the thermal conductivity of the two legs. So the total heat current flowing in the legs will be:

$$\dot{Q}_{tot} = \frac{(S_p - S_n)}{T_H} + (\kappa_n + \kappa_p)(T_H - T_C) \tag{2.15}$$

The thermodynamic efficiency is $\eta/\dot{Q}_{tot}$. The maximum efficiency can be obtained by maximising W with respect to R. In this case η is maximum when the ratio of the load resistance, R, to the internal resistance $R_p + R_n$, is:

$$\frac{R}{R_p + R_n} = \sqrt{1 + ZT} \tag{2.16}$$

where T is the average temperature $(T_H - T_C)/2$ and Z is a parameter known as figure of merit and expressed by:

$$Z = \frac{S^2 G}{\kappa} \tag{2.17}$$

where $\kappa = \kappa_p + \kappa_n$ is the thermal conductivity of the branches thermally connected in parallel, $S = S_p - S_n$ is the thermal power of the material, and G represents the electrical conductance. The figure of merit Z has the dimension of a temperature but, usually, it is expressed as a dimensionless parameter ZT, at a specific temperature T.

Therefore, the efficiency η can be written as a function of ZT:

$$\eta = \frac{(T_H - T_C)}{T_H} \frac{\sqrt{1+ZT}-1}{\sqrt{1+ZT}+T_C/T_H} \tag{2.18}$$

is easy to observe in eq 2.18 that the efficiency η increase when Z increases. From eq. 2.17, it is clear that in order to increase Z the contribution of the heat flow $\dot{Q}_h = (\kappa_n + \kappa_p)(T_H - T_C)$ which depends on the electrical resistance and thermal conductance of the material, need to be minimised [19, 20]. Equation 2.17 implies that an efficient thermoelectric device should maximise the electrical conductance (then minimising its internal resistance) and minimise the thermal conductance simultaneously so that temperature gradient will be maintained in the device. Finally, the S should be maximised to ensure that coupling between thermal and electrical current is as large as possible [19][21].

More generally, the figure of merit Z for a specific temperature is expressed as:

$$ZT = \frac{S^2 G}{\kappa} T \tag{2.19}$$

where G is the electrical conductance of the material, S is the absolute thermopower of the material, and κ is given by the sum of two contributes: the electronic contribution κ_e to the thermal conductivity and a bigger contribution from the lattice phonons κ_{Ph}. So:

$$\kappa = \kappa_e + \kappa_{Ph} \tag{2.20}$$

Unfortunately, increasing the figure of merit for a certain material by increasing the electrical conductance or decreasing the thermal conductance is not straightforward; since the Wiedemann-Franz law obtained in eq. 2.5 is still valid, which indicates that the ratio of the electronic contribution to the thermal conductance κ_e and the electrical conductance G is proportional to the temperature. This represents one of the main limitation for thermoelectric materials and devices since it is impossible to increase the electrical or thermal conductivity independently. The Wiedemann-Franz can also be written as:

$$\frac{\kappa_e}{\sigma} = LT \tag{2.21}$$

where L is the Lorentz number and is equal to $L = 2.44 \times 10^{-8} \mathrm{W\Omega K^{-2}}$. Even though these values come out from a very simple model explained in the previous sections, its

value is surprisingly close to the experimental values. From the relation 2.21, it is easy to notice that any increase of the electrical conductance will increase the thermal conductance. So in terms of efficiency, the electronic contribution that appears in the figure of merit ZT cannot be reduced unless the electrical conductance is reduced. Thus, strategies to reduce as much as is possible the value of the phonon contribution κ_{Ph} must be adopted. So, to increase the figure of merit in a thermoelectric material, the Seebeck coefficient S has to be maximised and the phonon thermal conductivity κ_{Ph} minimised. For practical applications, a $ZT > 1$ (at least) is needed. Ideally, a material with $ZT \geq 3$ would represent the solution for many heating/cooling issues at the nano- and macro-scale, achieving highly efficient solid state devices without any carbon footprint. The best performing thermoelectric materials realised until today consist in Quantum dots Superlattices (QDSL) nanostructures based on PbSeTe/PbTe have $ZT \approx 3$ at 500K and ≈ 1.6 at 300K, while commercial thermoelectric devices with ZT between 1 and 2 are quite often made by Bi_2Te_3 alloys [22, 23]. Others strategies based on nanocomposites based on PbSe or Si nanowires exhibited ZT of 1.5 and 0.9 respectively [24, 25]. Although a high ZT has been reported in nanostructured materials such as superlattices, quantum dots, and nanowires, many of these materials are not practical for large-scale commercial use because they are fabricated by atomic layer deposition processes such as molecular beam epitaxy, making them slow and expensive to fabricate and restricting the amount of material that can be produced. [19, 26].

2.2 Thermoelectricity at the nanoscale and its extention to molecular junctions

2.2.1 Thermoelectricity at the nanoscale

With their large surface/volume ratio and superior electrical conductance, nano-structured materials are one of the most adopted solutions in order to maximise the figure of merit of thermoelectric materials. Indeed, it has been largely demonstrated that nanostructured samples suppress the phononic transport thanks to multiple scattering, which occurs at the surfaces and interfaces. Nanocomposites and SiGe superlattices have shown that they are able to achieve a thermal conductivity lower than that of their bulk counterparts [27, 28]. Since phonons in a material have a spectrum of wavelengths, and phonons with different wavelengths contribute different amounts to the total thermal conductivity, introducing the alloyed phase or nanostructures causes short wavelength phonons to be strongly scattered by impurity atoms, while mid- to long-wavelength phonons are less affected resulting in a reduced thermal conductivity [29]
The thermopower at the nanoscale can be described using the same Landauer formalism for the electronic transport treated in Section 1.2. Usually, when a difference of temperature is applied to the two sides of a macroscopic material, a continuous and linear thermal gradient is established (2.5.b). Instead, in a nano-dimensional constriction between two electrodes, the shape of the thermal gradient is a sharp drop of the temperature in the proximity of the nanoconstriction. In this case, the electrons will be more energetic due to the sharp thermal gradient as shown in fig. 2.5.d and start to flow through the nanometric junction on the cold side of the material [30].

As with macroscopic materials, the charge carriers will start to be accumulated on one side of the junction, leaving a positive charge on the hot side. When equilibrium is established, an electric field will be created and, consequentially, a voltage difference. Since the thermoelectric effect at the nanoscale is just a characteristic transport property, it is possible to correlate S and $T(E)$ of the carriers across the nanojuntion. Considering eq.1.6 and set to zero in the case of "open-circuit" and expanding the difference of the lead's distribution functions in reference to the lead 1, we can write:

$$0 = \frac{2e}{h}\int_{-\infty}^{+\infty} T(E)\left[\left(\frac{\partial f}{\partial \mu}\Big|_{\mu=\mu_1}\right)_{T_1}\Delta\mu_{1-2} + \left(\frac{\partial f}{\partial T}\Big|_{T=T_1}\right)_{\mu_1}\Delta T_{1-2}\right]dE \qquad (2.22)$$

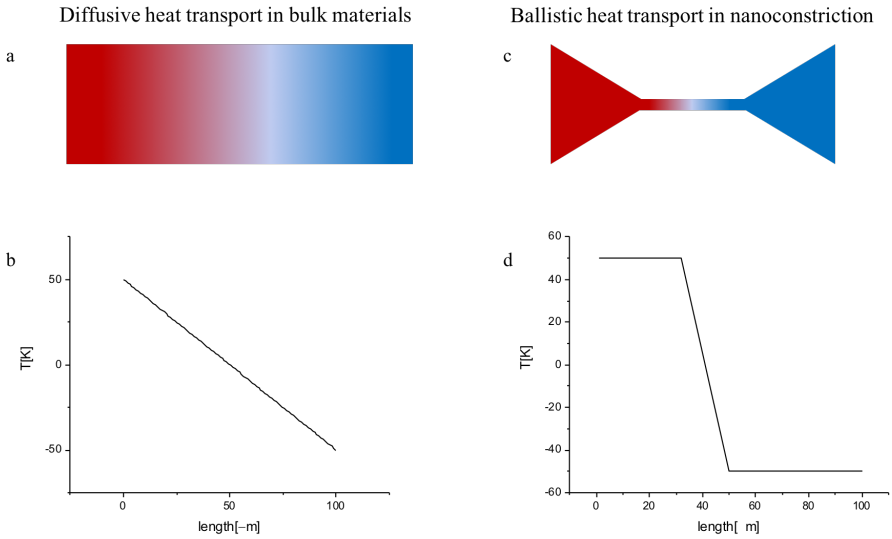

Figure 2.5: Comparison between heat transport in bulk material and in nanoconstriction. In the case of bulk material (a) the heat transport is diffusive, with a low gradient of temperature along the material (b); In nanojunction or constriction (c) the heat transport is ballistic and with a sharp drop of temperature in the proximity of the bottleneck (d) .

Considering $\partial f/\partial \mu = -\partial f/\partial E \approx \delta(E-\mu)$ and the derivative with respect to the temperature can be approximated as $\partial f/\partial T = -\dfrac{E-\mu}{T}\dfrac{\partial f}{\partial E}$, equation 2.22 becomes:

$$\frac{\Delta\mu_{1-2}}{\Delta T_{1-2}} = \frac{1}{T(E)|_{\mu=\mu_1}} \int_{-\infty}^{+\infty} T(E)\frac{E-\mu}{T_1}\frac{\partial f_1}{\partial E}dE \tag{2.23}$$

The change in the chemical potential will create a diffusive flow of charge $\Delta\mu_{1-2} = -q\Delta V_{1-2}$. Expanding the transmission function $T(E)$ in Taylor series and, using the Sommerfeld expansion, we obtain[16]:

$$S = -\frac{\Delta V}{\Delta T} = -\frac{\pi k_b^2 T}{3e}\frac{\partial[lnT(E)]}{\partial E}\Big|_{E=\mu} \tag{2.24}$$

This equation, known as Mott formula, represents the generalisation of eq. 2.12 obtained for metals with a free electron model and neglecting the eventual scattering process. In this case, the equation 2.24 correlates the S to the energy-dependent transmission function and to the chemical potential of the two electrodes. This formula is valid for small variation of temperatures and away from transition resonances so that the variation of the transmission function can be considered small [31] and demonstrates that S is enhanced by increasing the slope of $lnT(E)$ near $E = E_f$

To better understand how transport resonances affect the thermoelectric phenomena, we can assume, supposing a linear-response regime, that the electrical current I and heat current $\dot{Q}$ flowing through a device are related to the voltage difference ΔV and

temperature difference ΔT by [32–34]:

$$\begin{pmatrix} I \\ \\ \dot{Q} \end{pmatrix} = \frac{1}{h} \begin{pmatrix} e^2 L_0 & \frac{e}{T} L_0 \\ \\ eL_1 & \frac{1}{T} L_1 \end{pmatrix} \begin{pmatrix} \Delta V \\ \\ \Delta T \end{pmatrix} \tag{2.25}$$

The coefficients L_n, supposing a phase-coherent transport, are given by the sum of the two spin contributions on the transport $L_n = L_n^{\uparrow} + L_n^{\downarrow}$, with $n = 0, 1, 2$, and where L_n^{σ} is:

$$L_n^{\sigma} = \int_{-\infty}^{\infty} dE (E - E_f)^n T^{\sigma}(E) \left(-\frac{\partial f}{\partial E} \right) \tag{2.26}$$

Here, $T^{\sigma}(E)$ is the transmission function for electrons passing through the nanojunction with energy E and spin $\sigma = [\uparrow, \downarrow]$ from an electrode to another[35]. Equation 2.25 can be rewritten using measurable thermoelectric parameters[34]:

$$\begin{pmatrix} \Delta V \\ \\ \dot{Q} \end{pmatrix} = \frac{1}{h} \begin{pmatrix} 1/G & S \\ \\ \Pi & \kappa \end{pmatrix} \begin{pmatrix} I \\ \\ \Delta T \end{pmatrix} \tag{2.27}$$

where:

$$G = \frac{e^2}{h} \tag{2.28}$$

$$S = -\Delta V / \Delta T = \frac{1}{eT} \frac{L_1}{L_0} \tag{2.29}$$

$$\Pi = \frac{1}{e} \frac{L_1}{L_2} \tag{2.30}$$

$$\kappa = \frac{1}{hT} \left(L_2 - \frac{L_1^2}{L_0} \right) \tag{2.31}$$

From this expression, the figure of merit at the reference temperature T will be expressed by:

$$ZT = \frac{L_1^2}{(L_0 L_2) - L_1^2} \tag{2.32}$$

At the nanoscale, in the linear regime and at room temperature, the contribution to the thermal conductivity from the lattice, and thus the phonons, is however negligible so the thermal conductivity can be considered totally dominated by the electrons

$\kappa = \kappa_e$[36].

This fact underlines the strong correlation between electrical and thermal transport, which is even more evident at the nanoscale, making any increase in thermal power difficult.

2.2.2 Thermoelectricity in molecular junctions

As an alternative to conventional inorganic thermoelectric materials, organic materials are being investigated and are beginning to show promising values of both ZT and S. However, a fundamental understanding at the molecular level is needed to increase these parameters to values beyond currently attainable limits of $ZT \approx 10^{-4}$.

In this case, the big advantage of using molecules consist in their low thermal conductivity that ensures the temperature difference remains constant during the time. In addition, their relatively small size ensures a ballistic electronic transport along the junction, allowing the formalism developed in the previous section for the thermoelectricity in nanostructured materials to be used.

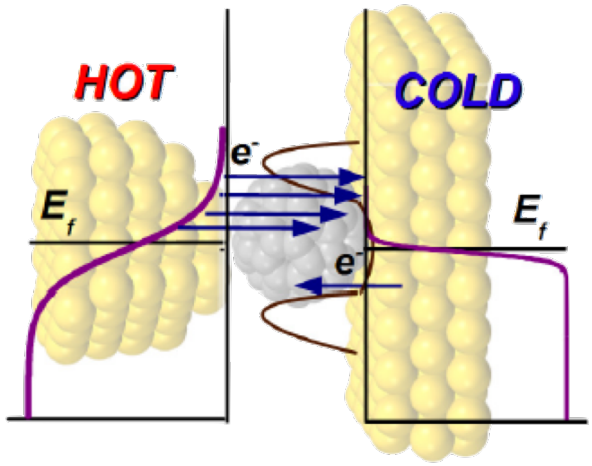

Figure 2.6: Molecular junction showing some of the electrons from the hot side of the junction having higher energy than the Fermi energy E_f, can tunnel to the cold side through the empty energy levels of the molecular bridge. In the cold side, the electrons able to tunnell in the hot side will be much less, considering that the molecular levels are all filled up to E_f. Image from [37].

Considering fig. 2.6, the electrons from the hot side have, on average, more energy than the Fermi energy E_f, compared to the cold side electrons, which have, in general, energies below the Fermi energy. This energy difference in the chemical potentials $\Delta\mu$ ensures a tunnel of the electrons flow from one lead to the other through the energy

levels of the molecule. Although there will also be a flow of electrons from the cold to the hot side, this is less likely since the molecular energy level below the Fermi energy will be filled.

The thermoelectric effect in molecular junction can provide new insights into the electron transport of this system and allows us to give an estimation of the location of the Fermi energy relative to the frontier molecular orbitals.

Indeed, in an analogous way to the hot point probe measurements generally used to establish the p or n character of inorganic semiconductors, the thermovoltage arising from the difference of temperature across the molecular junction yields vital information regarding the location of the Fermi energy [38, 39].

As described in Sec.1.3, when a low voltage is applied to the junction, the transport mechanism through a molecule is tunneling and can be described with the scattering approach and in terms of a transmission function. If we consider E_{HOMO} and E_{LUMO} as the energies relative to the frontier orbitals of a particular molecule, it is possible to describe the system in an analogous way to that developed in Sec.1.3 but, considering this time a two level system in which both levels contribute to the transport. In this model, the transmission function can be assumed as two Lorenzian peaks centered at E_{HOMO} and E_{LUMO} respectively [38].

$$T(E) = \frac{\Gamma_1\Gamma_2}{\Gamma^2 + (E - E_{HOMO})^2} + \frac{\Gamma_1\Gamma_2}{\Gamma^2 + (E - E_{LUMO})^2} \tag{2.33}$$

Where $\Gamma_{1,2}$ are the broadenings due to the contacts with the leads 1 and 2 and,
$\Gamma = \dfrac{(\Gamma_1 + \Gamma_2)}{2}$.

Assuming the Fermi energy is in the middle of the HOMO-LUMO gap and far from the energy levels, in the weak coupling limit $|E_f - E_{H,L}| >> |\Gamma_1 + \Gamma_2|$, we can expand in Taylor series equation 2.24 in the middle point of the HOMO-LUMO gap where $E = (E_H + E_L)/2$, and obtain:

$$S = -\frac{8\pi^2 k_b^2 T}{e} \frac{1}{(E_H - E_L)^2} \left(E_f - \frac{E_H + E_L}{2} \right) \tag{2.34}$$

This equation shows that the Seebeck coefficient in a molecular junction, to the first order of approximation, is clearly independent from the coupling with the electrodes. This only applies in the particular case when the Fermi energy E_f lies in the midpoint of the HOMO-LUMO bandgap and depends only on the relative alignments of the energy levels. In contrast the electrical conductance depends strongly from the coupling

strength with the electrodes [40]. From this model, we can observe that for a certain value of the transmission function between the frontier orbitals energy levels, there will be two values of E_f satisfying the 2.33, making the determination of the Fermi energy impossible. In contrast, it is possible to determine the position of E_f relative to the centre of the HOMO-LUMO gap from the sign of the Seebeck coefficient given by 2.34.

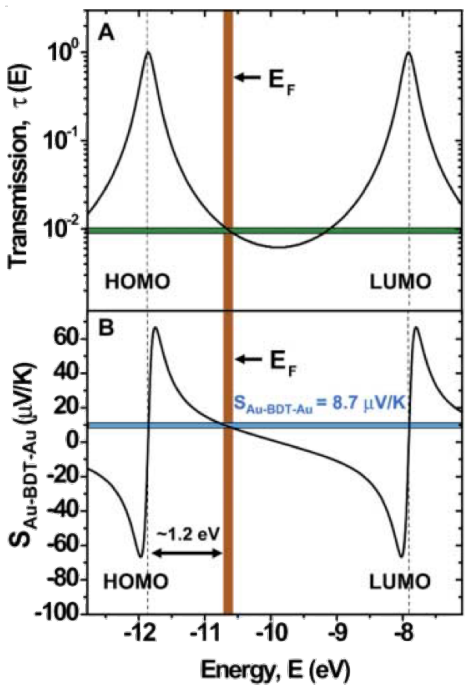

Figure 2.7: Comparison between transmission function $T(E)$ of equation 2.33 and the Seebeck coefficient S which is proportional to the derivative of $lnT(E)$, calculated for benzenedithiol between Au electrodes. Figure from [41].

This result is quite clear in fig. 2.7, which shows the transmission function $T(E)$ relative to the position of the Fermi energy. The electrical conductance will be related to the magnitude of $T(E)$ calculated at the Fermi energy. As it is possible to observe from fig. 2.7, the thermal power S is identified by the derivative of $lnT(E)$ calculated at the Fermi energy E_f, and results positive $S > 0$ for HOMO dominated molecules and, negative $S < 0$, for LUMO dominated molecules [40, 41].

Chapter 3

Experimental instrument

3.1 Deposition of molecular ultra-thin film

In the field of nanoscience, one of the distinguishable and unique characteristics of nanostructured materials is their high surface/volume ratio, resulting in a high percentage of the material's atoms at the surface. The scaling along with one or more dimensions of the material makes possible, in some cases, structures where all the atoms are interfacial like in quantum dots or 2D materials, consisting in groups of few atoms or, in the second case, in a single atomic "sheet" of atoms.

This clearly means that atoms or molecules at the surface of such nanostructures experience a different environment than those in bulk, leading to different free energy, mobility, charge recombination, and electronic states [42, 43]. Therefore, a nanostructure's physical properties have a significant dependence on its surface and on the interaction of the interface with the surrounding environment.

In particular, metals and metal oxide nanostructures possess strongly reactive surfaces, with the tendency to easily absorb organic materials since the adsorbates lower the free surface energy of the interface between the metallic surface and the external environment [42]. The adsorbates significantly modify the stability of the nanostructure and its physical properties [44], acting as electrostatic barriers for the charge carriers, reducing further contamination from other organic compounds and thus decreasing the surface reactivity and changing the wettability of the surface [45].

The nanostructure concept as an object in which one of its physical dimension is comparable to the De-Broglie wavelength of the material's electrons can be extended to small molecules or groups of few molecules in-between two metallic electrodes. In fact, a single molecule in a junction can be imagined as a quantum dot system connected with two

leads. To realise reliable nano junctions based on molecules, it is necessary to find a feasible and easy way to realise controlled size and scalable molecular and organic layers onto electrodes and well-defined device architectures to study their properties and characteristics.

3.1.1 Self-assembled Monolayers

Self-assembled monolayer or SAM maybe the most simple, flexible and versatile methodology to functionalise metal, semiconductor and oxide surfaces through the adsorption of a molecular film and thus tailor their physical interfacial properties.
SAMs have been largely employed to study nanoscience because are easy to prepare not requiring UHV environment or additional equipment for their formation. Furthermore, they tend to form well organised structures with large lateral range and are crucial components in order to stabilise and functionalise the surfaces they grow on.
SAMs are formed by the adsorption of molecules from solution or gas phase in a regular structure on the surface. Quite often, the component molecules organise spontaneously in crystalline or semi-crystalline structures, forming a strong physical or chemical bond between the atoms at the interface.

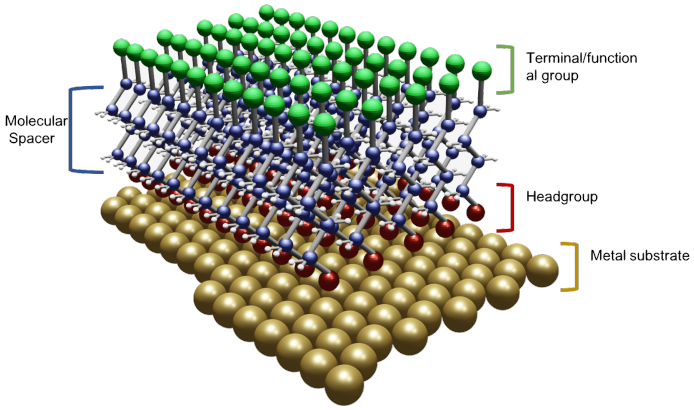

Figure 3.1: Schematic 3D cartoon of SAM of alkythiolate molecules on gold surface. The characteristics of the SAM are highlighted. The green atoms representing a terminal group will determine the surface properties, while the headgroup atoms (red spheres) stabilise the existing surface and modify the electronic properties. The body of the SAM is represented in this particular case from alkane molecules acting as a spacer and provide the thickness of the SAM and the electronic properties.

As shown in fig 3.1, the molecules that form a SAM consist of a chemical functional "headgroup", with a particular affinity for binding with the substrate's atoms. The affinity of the headgroup dictates the eventual displacement of other adventitious or-

ganic compounds adsorbed on the surface. At the other end of the SAM, a particular terminal group will determine the modified surface physical properties of the substrate due to the molecular layer's presence. Much of the early literature on molecular SAMs focused on alkanethiols and similar molecules, producing an extensive knowledge of how molecules grow on different metallic substrates and the effects of the molecular length, solvent and substrates [46–49]. Furthermore, there has been significant research on other molecular SAMs such as non-thiol terminated like metallo-phorphyrins and phthalocyanine [50, 51], pyridine [52], oligo(phenylene-ethynylene)s (OPEs) [53] and also fullerene [54]. Depending on the particular affinity of the headgroup with the surface of metals, this can lead to a well-defined molecular surface with a wide variety of chemical functionalities of the interface exposed to air [49, 55].

The thickness of a molecular SAM is usually 0.5-3 nm, depending on the SAM's components' molecular structure. In addition, the molecular components also determine the particular angle formed between the atoms at the surface of the metallic substrate and the headgroup of the molecule [56].

SAMs form on the surface of the substrates by spontaneous chemical adsorption from either gas or liquid phase. The assembly in solution is probably the most convenient for most of the subsequential applications of SAMs. Otherwise, for some spectroscopy techniques, the preparation under UHV results more suitable for some applications like the electric transport characterisation, where a long-range of crystalline order is required [46].

The surface on which the SAM is grown represents a crucial point in the molecular layer's growth. Substrates can range from simple planar thin film (metallic films on glass, silicon or mica) or more complex nanostructured substrates including nanojuntion [57] , nanorods [58, 59], trenches [60, 61] and nanoholes [62]. However, the most common substrates use for a wide class of studies consist of planar metallic film (Au,Ag,Pt) or highly orientated substrates like HOPG, mica and graphene. The choice of a particular substrate is dependent on the particular application of the SAM.

Among the many substrates used for SAM growth, gold is the most widely used and studied substrate for two different reasons. Firstly, Au is a relatively inert material, with a low oxidation rate, not reacting with O_2 and other atmospheric agents, making it practical to manipulate outside UHV environments [63]. Secondly, Au is relatively easy to deposit and etch as thin films or colloids [64–66]. Au has a high affinity with a wide

range of chemical headgroups due to its partially filled electronic 6s orbital [67]. For example, thiol groups act as displacer for adventitious materials from the Au surface. In addition, the use of Au is compatible with a range of spectroscopic and analytical techniques such as Quartz Cyrstal Microbalance (QCM) [68, 69], ellipsometry [70, 71], electrical transport measurements [72].

Other metallic substrates offer similar characteristics, although SAMs grown on these materials have generally been less studied. Silver (Ag) has been studied for a long time as an alternative to gold, but its higher oxidisation rate and toxicity to cells has made it less attractive in its regards, despite the ability to grow high-quality SAMs, with a smaller tilt angle than Au [48, 73]. Copper (Cu) like Silver, produces high quality SAMs but is even more sensitive to O_2 than Ag [48].

An excellent alternative to gold has been found in Palladium Pd which, for some applications, results in superior SAM formation thanks to its useful properties. Indeed, Palladium crystal grains are in general 2-3 times smaller than those in gold, giving smoother surfaces and low defect density [74–76]. Palladium, rather than gold, results compatible with the existing complementary metal-oxide-semiconductor (CMOS) technology [77], and has good catalytic properties and biocompatible with a low oxidation rate at room temperature [78].

Protocols for preparing SAMs The most used protocol in order to form SAMs on metallic surfaces consists of the immersion of a clean substrate in a fresh dilute solution ($\sim$ 1-10mM) of the designated molecules for a specific range of time, from minute to several hours, depending from the particular dynamics of the molecules, usually at room temperature. In a range of milli- to a few seconds, a dense coverage of adsorbed molecules is obtained onto the surface of the substrate but, a slower dynamics process and reorganisation process requires longer time to maximise the order and the density of the obtained layer and, at the same time, minimise the defects [49, 56]. However, the adsorption and organisation process's kinetics is strictly dependent on several factors like the choice of solvent, the time, the temperature, and the solution's concentration.

Solvent The role of the solvents used affect the kinetics and/or the mechanism of assembly of the molecules on the substrates [79]. The actual mechanism of how the SAMs growth is affected by the solvent is not totally understood, however it is clear that the presence of the solvent in the substrate-molecule system introduces additional parameters which complicate the dynamic equilibrium leading the adsorptions of the

molecule and complicating the thermodynamics of the assembly. Indeed, the solvent-substrate and solvent-molecules interactions need to be taken into account in order to have a clear picture of the role of different solvents [80, 81].
Ethanol based solution are the most widely used for alkanethiol chains, leading to a well established methodology of assembling from a solution phase [82, 83]. Other solvents such as hydrocarbon solvents have been shown to reduce the adsorption time, but generally produce however poorer quality films due to the strong solvent-molecule interactio [84].

Temperature The temperature of the SAMs formation has a significant influence on the growth dynamics. It has been reported that temperatures above 25°C can improve the quality of alkanethiols film and the growth kinetics, reducing defects in the final film [85, 86]. High temperature also increases the rate of desorption of physisorbed solvent molecules on the surface and, due to the higher energy, the molecules can cross the activation barrier facilitating eventual rearrangements of the SAM than at room temperature.

Time and Concentration In the growth of a SAM, the immersion time and the relative concentration of the solution play a fundamental role in the molecular layer's quality formed on the substrate. These parameters are proportionally inverse and, quite intuitively, a more dilute solution will require longer immersion time and depend on the dimension of the molecule [87, 88]. It has been reported that SAMs immersed for longer times (e.g. a week) but with low concentration than a µM, will not present the same physical characteristics as those grow from a more concentrated solution for a shorter time [88]. This process is mainly due to the slower molecular dynamics, and it could vary depending on the stability of the particular molecules over the time or accumulation of impurities and contaminants either in the solution or on the surface of the substrate.
From the other side, different studies reported that the properties of the molecular layer would not vary significantly for SAMs grown in $\sim$ mM concentrated solution for 12-18h. In addition, the formation and organisation of a SAM continues to evolve even after a week of immersion time [89, 90]. This implies an increase of the surface coverage with the immersion time and the consequential reduction of defects like pins and holes, forming well-defined structures suitable for electron transport studies.

3.1.2 Langmuir-Blodgett deposition and Electro-spray ionisation

The organisation of amphiphilic molecules into unsoluble molecular films onto water surface was widely studied over the last two century since, for the first time, Benjamin Franklin observed the spreading of oil droplets onto a water surface [91]. Years later, with the contribution of Rayleigh and Pockels, Irving Langmuir developed the Langmuir (or better known as Langmuir-Blodgett) trough, which represents one of the most useful methods to study and control the organisation of amphiphilic and water-insoluble molecules onto films [92–94]. Amphiphilic molecules are molecules with both hydrophobic and hydrophilic moieties or hydrophobic moieties only. These molecules have been shown to align on the water surface predictably, and Irvin Langmuir, in 1917, was the first to study systematically the formation of monolayers of amphiphilic molecules aligned at the air-water interface [95]. Together with Katherine Blodgett, they carried out multilayer depositions onto solid substrates [96, 97] using the so-called Langmuir-Blodgett (LB) deposition.

LB deposition is a powerful, scalable and versatile technique used to deposit a molecular thin film or even monolayer onto a solid substrate. In addition, as will be shown below, the LB technique enables precise control of the thickness of the desired molecular layer, allowing multiple depositions of the same molecules or even different molecules [98–100]. This characteristic, together with its relatively simple working principle (no UHV required), makes this technique very desirable in molecular electronics and nanoelectronics.

Molecules at gas-liquid interface To minimise their free energy, some organic molecules will migrate at the interface between a gaseous and a liquid phase [101]. The resulting floating film is called a monomolecular layer or, more commonly, monolayer. The formation of the monolayer is a direct consequence of thermodynamics. Molecules in liquid can be considered as being in a bulk phase, where a number of molecules surround each molecule. Depending on the nature of the attractive and repulsive forces acting on the molecules, some of them will migrate towards the surface, where they will be surrounded by fewer molecules than in its bulk phase [102, 103]. Therefore, considering the interface in a dynamic equilibrium state, there will be as many molecules diffusing from surface to bulk per unit time as leaving the bulk towards the surface. This diffusion is shown in fig. 3.2, where it is easy to observe the different intermolecular forces environment felt from the molecules in bulk and at the interface liquid-air.

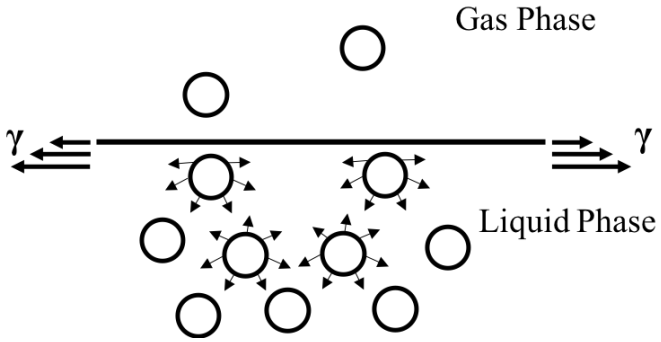

Figure 3.2: Forces experienced (black arrows) from the molecules (black circles) at the interface between liquid and gas phases.

When the intermolecular actractive and repulsive forces in the liquid phase are equal to the activation energy of a molecule to escape from the bulk to the surface, then the state of equilibrium will be reached. The force acting on the molecules on the surface is known as surface tension γ [104].
At thermodynamic equilibrium, the surface tension of a planar surface can be shown to be related to the free energy (G) and the area of the surface A as

$$\gamma_f = \left(\frac{\partial G}{\partial A}\right)_{T,P} \tag{3.1}$$

For a pure liquid in a thermodynamic equilibrium, γ can be express as the excess of Helmholtz free energy F^S per unit of area

$$\gamma_0 = \frac{F^S}{A} \tag{3.2}$$

The presence of the molecular film at the liquid-gas interface will then affect the surface tension. Typically in experimental studies of molecular alignment at the gas-liquid interface, the variation of surface tension is defined as the difference between the surface tension of the pure liquid γ_0, which remains almost constant during the compression of the film, and the surface tension of the molecular film at the surface γ.

$$\Pi = \gamma_0 - \gamma_f \tag{3.3}$$

The parameter Π has the dimension of $\mathrm{mN\,m^{-1}}$ and represents a key parameter for monitoring the evolution of molecular thin films on liquid surfaces and on water air interfaces.

Phases of a monolayer at the water-air interface When a layer of insoluble or amphiphilic molecules at the water air interface is compressed, it will go through a series of 2 dimensional phases transitions analogous to the well known bulk phases. The evolution of the film under compression is one of the critical points of the LB deposition as will be discussed in the following paragraphs.

During the compression of the LB barriers, the molecules will experience higher intermolecular forces and smaller available area, producing a variation of the surface tension γ of the molecular floating film. Therefore the surface pressure change Π can be used to monitor the evolution of the molecular film as a function of area occupied in an equivalent two-dimensional version of the pressure vs volume isotherm [101].

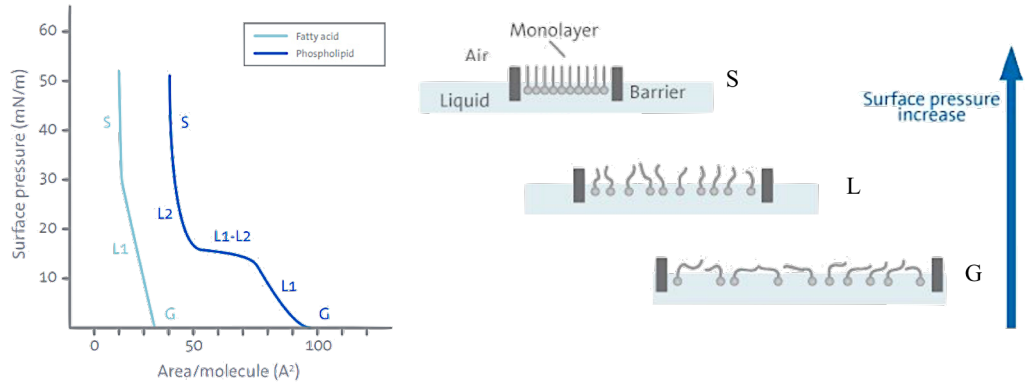

Figure 3.3: Surface pressure vs area per molecules isotherm for fatty acid and phospholipid molecule. At large trough area, the monolayers exist in the gaseous state (G) and can, on compression, undergo a phase transition to the liquid-expanded state (L1). Upon further compression, the L1 phase undergoes a transition to the liquid condensed state (L2), and at even higher densities, the monolayer finally reaches the solid state (S). The different phases of the molecule are illustrated on the right side by the letter G, L, S for gas, liquid and solid phases. Image from [105].

Figure 3.3 shows the isotherm for amphiphilic organic molecules, representing the variation of the surface pressure for a film of molecules as a function of the available area occupied by a molecule and defined as the available area A divided by the number of molecules at the water-air interface.

$$a = \frac{AM}{CN_AV} = \frac{A}{cN_AV} \tag{3.4}$$

where M is the molecular weight, N_A the Avogadro number, C and V the concentration of the solution and its volume respectively.

Referring to fig.3.3, when the molecules are far apart from each other, they can be

considered as being in a "gas" phase since each molecule will experiences negligible intermolecular forces due to the distance between them [106]. As the available surface A is compressed, some of the molecules will start to interact weekly. At this stage, the molecules are in a so-called liquid or "liquid expanded" phase. In this phase, the molecules' orientation is totally random [107, 108]. But, when A is further reduced, a "solid" phase is reached where even progressive compression of the available area will not substantially change the film arrangement. In this phase, the molecules are closely packed and well orientated, with eventual hydrophobic chains pointing out the water surface. In addition, as is easy to observe from fig.3.3, the area per molecule, in the solid phase, does not change substantially and should match the cross-sectional area of the molecules [103, 109].
Investigating the isotherm of a given molecule plays a crucial role in LB film deposition as it is possible to predict the final thickness of the floating film, multilayer formation and even the viscosity of the film [103, 110].
Compressing films in a solid phase will ultimately lead to the collapse of the film on itself leading to a drop in the surface pressure.

Deposition of Langmuir-Blodgett film In a typical Langmuir-Blodgett deposition, the molecules are spread in a hydrophobic trough filled with a liquid media called the subphase, usually water. Once the molecules touch the subphase's surface, they will move randomly all around the available water surface. During the compression, made possible by two mobile hydrophilic barriers, the molecules will pass through different phases, as described above, and form an insoluble monolayer on the water surface [99, 111]. This layer can then be transferred onto different substrates by different techniques.
The variation of Π is measured by a Wilhelmy Plate, based on the surface pressure of water at the equilibrium and before spreading the molecules.
Figure 3.4 illustrates a typical setup for a LB deposition.

Before transfer to the solid substrate, the hydrophobic LB trough (labelled (1) in fig3.4) is filled with ultra-pure water ($\rho = 18\text{M}\Omega$). A precise volume of molecules with a known concentration of molecules is then applied to the water's surface by a microsyringe. The designated molecules are often dissolved in solvents that will evaporate from the water's surface in the trough. The molecules settle into different phases during the compression of the two hydrophilic barriers, indicate by 2 in fig.3.3 forming a packed monolayer on the water surface. The barriers' material is chosen so that the water meniscus is above

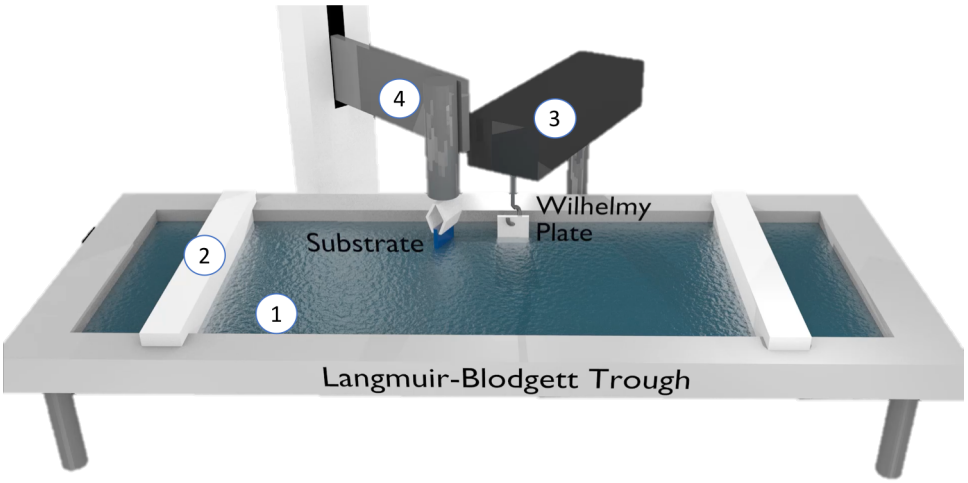

Figure 3.4: Scheme of Langmuir-Blodgett trough.(1): The hydrophobic LB trough. (2): Hydrophilic barriers used to compress the layer floating on the water subphase. (3): Wilhelmy plate and plate holder used to record the surface pressure,Π, of the floating layer. (4): the dipping mechanism.

the base of each barrier, and at the same time, the trough material also allows a high meniscus at the front and rear edges between the barriers. Steady motion without disturbing the surface layer is achieved because the added surface material always stays between the barriers whilst the water is able to flow beneath them.

As shown in fig.3.3 (3), the surface tension is measured with a cm of a clean leaf of platinum or, more commonly, a rectangle of filter paper slightly immersed on the water surface known as Wilhelmy plate. The plate is dipped into the water anywhere in the region between the barriers and the capillary force on the plate due to the water is then measured and is used to determine the surface pressure [111]. A dipping mechanism labelled (4) is then used to dip a solid substrate on the subphase and "collect" the floating molecular film.

The deposited substance forms a dispersed layer on the surface of the water, while the water under the layer is not constrained. As the two barriers move towards each other, the insoluble floating molecular film on the surface is compressed, and as the compression increases, the surface area and the mean area occupied per molecule will decrease. Computer-generated surface pressure/area isotherms are characteristic of a given molecule and subphase and can also reveal the film's thickness formed on the surface. The isotherms change with temperature, so maintaining the surrounding temperature is also important [112].

The reliable multiple deposition of several layers is also possible using the LB method by multiple vertical passages of the substrate [43].

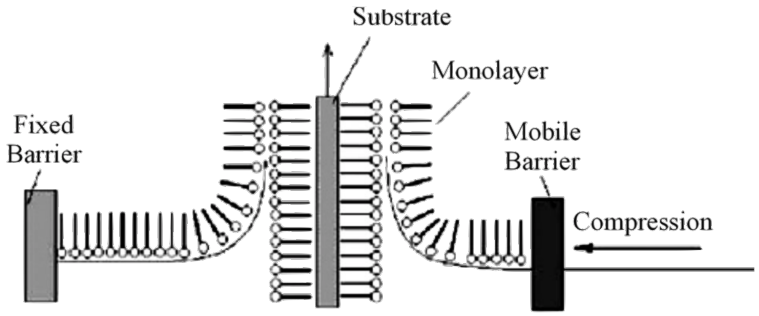

Figure 3.5: Vertical transferring of LB floating molecular film onto substrate by lifting of the substrate through the layer on the subphase

LB deposition was first developed for the deposition of amphiphilic molecules, but the method is used to deposit other material types too. For non-amphiphilic molecules, the surface tension of the water is often enough to ensure they remain on the surface.
The layering of thin films in this precise way is advantageous over the use of purely bulk materials since the possibility to grow epitaxial layer and ensuring a better bonding with the substrate [113, 114]. Successive layers could also consist of differing molecules as shown in figure 3.6 and 3.7 and depending on the nature of the substrate. Indeed, depending from the molecules and the particular substrate three main type of multiple deposition can be observed called *Y*,*X* and *Z*. The *Y* deposition showed in fig.3.6 is the most common situation in which, after the first passage through the layer and its deposition, the substrate is moved in and out from the subphase several time, building structures similar to the one showed in fig. 3.6.

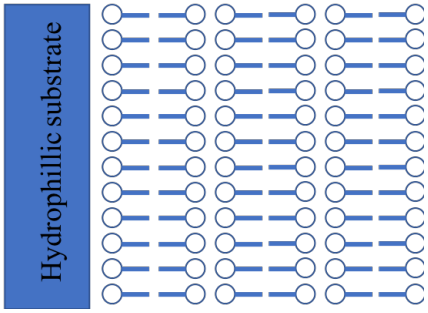

Figure 3.6: Example of *Y* deposition of LB multilayer deposited on hydrophilic substrate.

The *X* and *Z* deposition are particular cases, strictly dependent on the substrate in use and where the multiple depositions will occur either upwards or downwards motion through the floating film as shown in fig. 3.7.

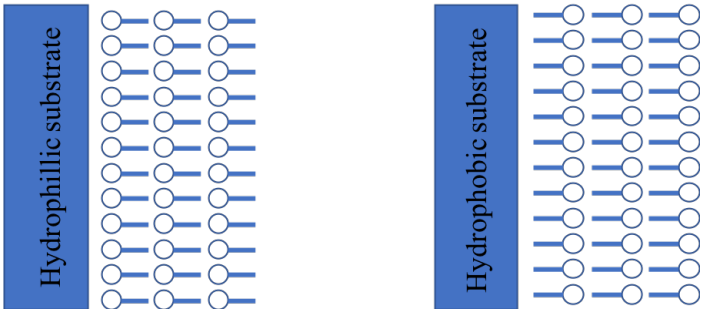

Figure 3.7: Structure for Z and X LB deposition for hydrophobic and hyrdophilic substrates.

However, when the monolayers are too rigid or do not form a closed-packed structure, an alternative transferring method called Langmuir-Schafer (LS), consisting of a "horizontal lifting" of the floating molecular film, is used for transfer the film onto a substrate. This method consists of lifting the monolayer by touching it with a horizontal, hydrophobic substrate as shown in fig. 3.8 [43].

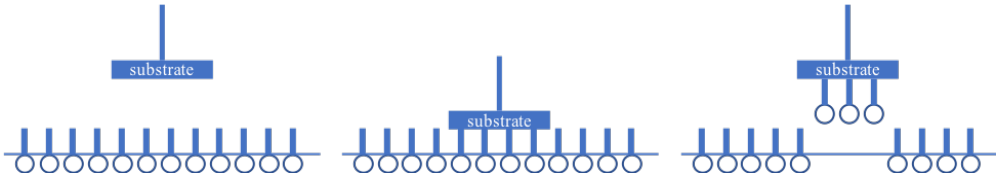

Figure 3.8: The horizontal transfering Langmuir-Schaefer (LS) for depositing floating molecular layer onto a hydrophobic substrate

LS technique is mainly used to transferring monolayers on substrates, but in principle, multiple layers can be achieved in some instances, forming a X-type multilayer [115].

3.2 SPM

To overcome the optical diffraction limit, Binning and Rohrer [116] in 1982 invented the Scanning Tunneling Microscope (STM) and were awarded the 1986 Physics Nobel prize for the invention. In the same year, Binning, Quate and Gerber [117] developed, based on a complementary process the Atomic Force Microscope (AFM). The STM relies on electron tunnelling between a tip and a surface where the tunnelling current is kept constant by varying the tip-sample distance [118]. The main requirement for STM is, therefore, that the sample surface is conducting. Compared to STM, the main advantage of AFM is to remove this necessity as instead of tunnelling current, interatomic forces are kept constant by a feedback loop system [117].

Since these early inventions, many scanning probe microscopy (SPM) techniques have been developed. Each technique is able to probe, with nanoscale resolution, a particular property of a system, such as electrostatic forces, magnetic forces, thermal conductance, elasticity, etc. The basic principle of each SPM technique depends on the particular feedback mechanism it uses [119]. Contact mode AFM for instance, relies on interatomic forces to keep the tip-sample forces constant. The tip-sample interaction forces as a function of separation distance are shown in fig. 3.9. When the tip-sample distance becomes very small, the interaction forces and capillary forces overcome the spring resistance of the cantilever and it snaps-into contact. When the probe pulls out, the attraction forces are generally bigger and therefore a higher separation is needed to break contact. The particular short-long range force is known as Van der Waals interaction and will be discussed in detail below.

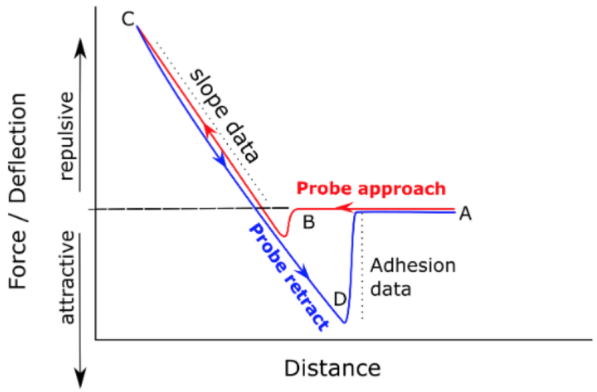

Figure 3.9: Probe-sample interaction forces as the probe is approached (red) and retracted (blue) from the sample. When the tip is in contact with the sample, it obeys Hooke's law.

During scanning, an ultrasharp cantilever (or tip) is brought into contact with the surface of the sample and the probe-sample distance varies to keep the force constant *via* a feedback loop on the displacement. Any change in the sample's surface will causes the probe to deflect and is observed through the deflection of a laser beam on the back of the cantilever itself. This deflection is monitored throughout the scanning process. If it changes slightly, the feedback mechanisms will increase or decrease the tip-sample distance to maintain the same deflection signal using a piezoscanner. Figure 3.10 shows a schematic AFM system with all its components.

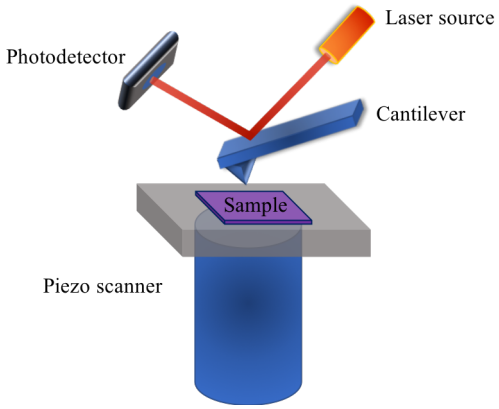

Figure 3.10: Illustration of AFM System. The sample and tip are brought into contact *via* a piezoelectric scanner mounted underneath the sample allow nanometric control of the displacement and the force applied to remain constant during the scanning operations. A laser-photodetector system is used to monitor the normal and lateral deflection of the cantilever which acts to reconstruct the 3D images of the sample surface.

3.2.1 AFM working principle

AFM measurements rely on the short-ranged forces such as Van der Waals (VdW) as well as long-ranged ones such as electrostatic and magnetic forces between the sample surface and tip which cause the cantilever to deflect [119]. This deflection is detected by an optical lever detection system first developed in 1988 by Meyer and Amer [120], consisting of a laser beam shone on the back side of the cantilever, its angular deflection is detected by a quadrant photodiode as shown in figure 3.11. Such a system allows the detection of both normal and lateral deflection of the cantilever. This information is then converted into a set of XYZ point which is converted into line scans to digitally recreate the topography of the sample being investigated.

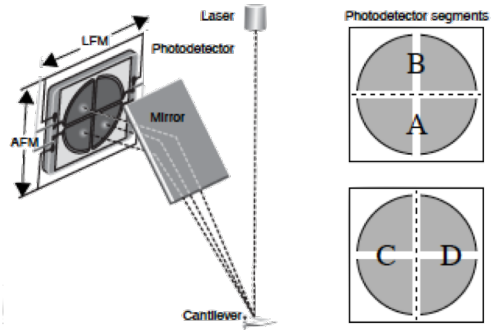

Figure 3.11: Laser deflection photodetector system

Interaction forces The force between sample and probe (F_{st}) is given by the derivative of the potential between the tip and the sample $F_{ts} = \partial V_{ts}/\partial z$ counterbalanced by the deflection of the cantilever which obeys Hooke's law $F_t = -k\Delta z$ with associated natural frequency $f_0 = \frac{1}{2\pi}\sqrt{\frac{k}{m}}$, where k and m are the spring constant and the mass of the AFM tip respectively.

The most common mode of operation in static AFM consists of keeping the force F_{ts} constant while adjusting the displacement Δz. The forces acting between tip and surface are a combination of long-range VdW and electrostatic forces and short-range repulsive chemical forces. As The tip/surface distance increases, long-range forces such as electrostatic forces tend to dominate the interaction. However, because the tip is kept at a very short distance range from the sample during the scanning operation, the VdW forces tend to vary much more slowly compared with the short-range interactions. For static AFM, the Lennard-Jones potential with a well depth ϵ and zero-potential distance σ, provide a good approximation for the short-range interactions[121, 122].

$$U_{L-J}(z) = \epsilon\left[\left(\frac{\sigma}{z}\right)^{12} - 2\left(\frac{\sigma}{z}\right)^{6}\right] \tag{3.5}$$

When the tip approaches the surface, Coulomb and VdW forces dominate, as the tip/surface separation increases the long-range forces and electrostatics characterise the interaction between tip and surface. However, within the typical operating range of a few nanometers from the surface it is the VdW interactions mostly affect the interaction with the AFM probe. The interaction forces vs the tip-surface displacement is shown in figure 3.12.

The shape of the red curve in fig 3.12 suggests the interatomic distance between the tip and surface changes slightly in the repulsive regime, where the cantilever needs to deflect or bend in order to balance force variation.

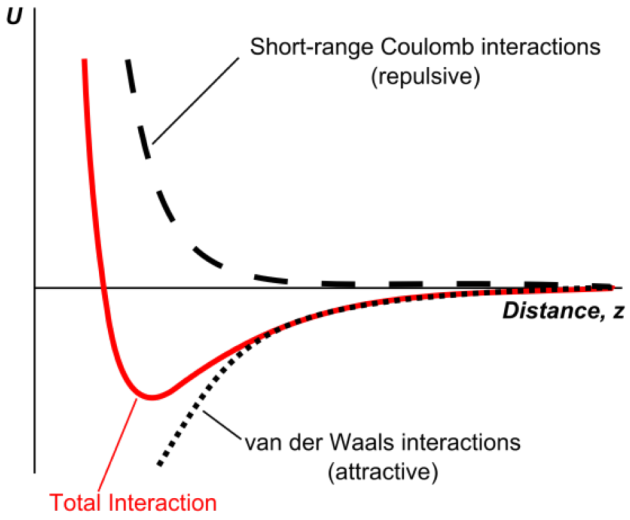

Figure 3.12: Representation of the interaction forces acting on the AFM cantilever during the approach to the surface.

In ambient conditions, short-range VdW forces usually co-exist with long-range forces in the region where the probe is very close to the surface. Capillary forces, for instance, represents a good example of these long-range interactions caused by the surface energy of a thin layer of condensed water and moisture between the sample and the tip. The capillarity tends to wet the cantilever's tip since water-cantilever contact is energetically advantageous to minimise the surface energy. This interaction causes the reshaping of the water layer, producing a meniscus between the water surface and the tip surface. This meniscus deeply affects the cantilever's pulling out motion from the surface, leading to the hysteresis effect shown in fig 3.9 (blue curve) as a consequence of the extra energy needed to withdraw the tip "trapped" in the meniscus, causing further deflection of the cantilever.

Feedback loop and scanning mode As explain at the beginning of the section, AFM principle relies on the presence of a feedback loop system in order to control the motion of the cantilever over the sample under investigation as well as obtaining information about the physical properties of samples.
In most AFM operation modes, the feedback loop is provided by the normal deflection of the cantilever deflection, which is monitored and adjusted in order to maintain a constant force between probe and sample. This is possible by changing the cantilever height by feeding back the deflection error signal. This is the "static" or "contact mode" of AFM in which the cantilever is kept in a repulsive regime to avoid the tip snap from the surface [122].

Beyond static techniques, dynamic detection methods which obtain information relative to the elastic properties of the samples are commonly used to image soft samples such as biological specimens where contact mode would be impractical or destructive to the sample [123, 124]. The cantilever is oscillated over the sample by a piezotransducer and its parameters like amplitude, frequency or phase can then be monitored in order to obtain information regarding the sample's properties. The free oscillation of the cantilever at its resonant frequency is perturbed upon exposure to a force gradient, causing a frequency shift and a corresponding change in amplitude. The cantilever's resonant frequency depends on the dimensions and materials the cantilever is made from, and is determined by sweeping the frequency in a neighbourhood of the resonant frequency [124]. So dynamic modes can either be operated at some distance from the surface (non-contact mode) or in intermittent contact where the tip continuously tap on the surface, also called Peak-Force AFM mode (PF-AFM), as will be described in the next sections.

3.2.2 Conductive probe AFM CAFM

Conducting probe AFM (CAFM) is a secondary imaging mode derived from contact mode that characterises electrical conductivity variations across medium to low conducting and semiconducting materials. It is used to measure and map current in the range of few pA to some mA while simultaneously collecting topographic information with high spatial resolution (typically 10-20 nm) depending from the radius of the probe used [125, 126].

The operation of the CAFM is similar to STM, in which a bias voltage is applied between tip and sample and the tunnelling current between the two is measured. The main difference between the two modes is the type of probe used. STM uses a sharpened metallic wire/tip separated from the surface by some nm, while CAFM uses a conductive cantilever made of Platinum, Gold or even graphene in direct contact with the surface of the sample under investigation.

In CAFM, as shown in figure 3.13, during imaging, while a conductive cantilever scans the sample surface in contact to produce a topography map, the electric current between the cantilever and the sample is measured simultaneously.

Furthermore, during the scanning operation with CAFM it is possible to select a specific bias voltage to apply during the imaging, to test the electrical conductivity of the

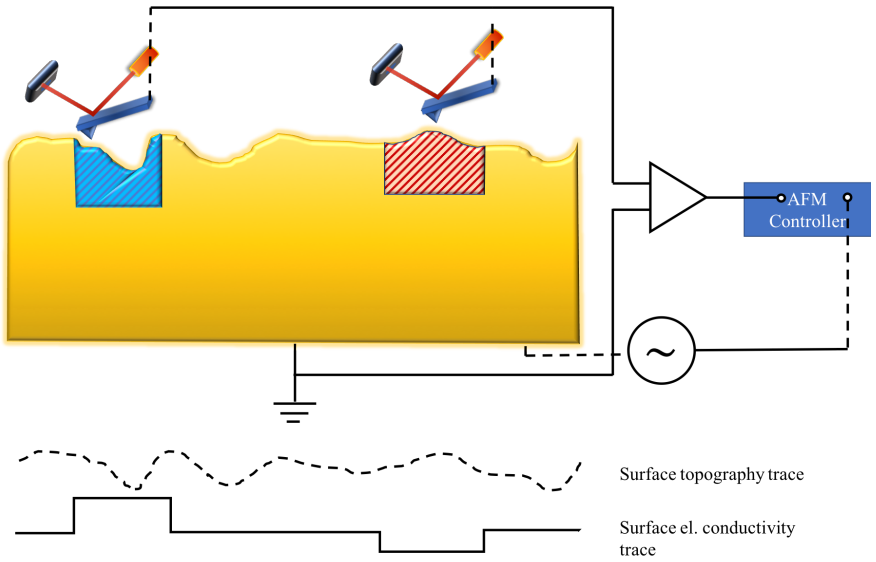

Figure 3.13: Schematic diagram showing the working principle of conductive probe AFM (CAFM). A constant DC bias voltage is applied between the sample and the probe during the traces of the electrically conductive probe along the sample surface. The current relative to the different regions of the surface is then collected by the probe using an I-V converter together with the topography information. The blue and red areas represent regions with high and low electrical conductance, respectively.

different components of the surface as well as the type of electric conduction. Fig. 3.14 shows an example where it is possible observe a non linear behaviour in the electric transport in an organic-2D MoS_2 single layer (SL) junction when the bias voltage turns from positive to negative.

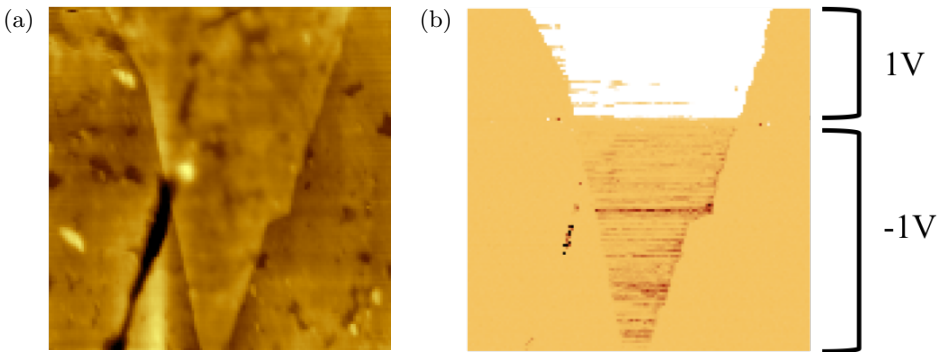

Figure 3.14: (a) CAFM topography map of a single layer MoS_2 on top of a molecular SAM of OPE-3 grown on template stripped Au;(b) Simultaneous current map of the sample acquired switching the DC bias voltage from 1V to -1V (Dashed line). It is easy to observe how, during the switch of the bias sign, the sample shows a rectification behaviour, with low current associated with negative bias and exponential current when a positive bias is applied.

For molecular electronics, CAFM is a powerful tool largely used for the characterisation of the electrical conductance of an assembly of molecules ($\approx 50 - 200$), with nanometric resolution. Unlike STM, CAFM has no tunneling gap between tip and surface so it is

possible to control the pressure applied on the junctions, and hence the area and number of molecular junctions [127–129].

As discussed in the next part of this thesis, one of the most powerful features of CAFM is the ability to do electrical spectroscopy point measurements utilising the precise area control. These "Point measurements" fix the probe in a single point and a triangular wave is applied between the sample and the probe; the response of the sample is collected and then can be manipulated to obtain vital information about the electric transport of the samples, its conductance and also the relative alignment of the Fermi level E_f with respect to the frontier orbitals HOMO-LUMO in a molecular junction.

3.2.3 AFM for nanomechanical properties

As described in Sec.3.2.1, dynamical AFM mode or intermitting contact AFM are often used as a tool in order to characterise the elastic or related mechanical properties of the samples and imaging "soft" samples like organic assembly [130], polymers [131, 132] and biological samples [133] due to their friction-less unique characteristic which avoids damaging of sample. The most common intermitting AFM mode is known as "Tapping mode AFM" [132]. In tapping mode AFM the cantilever is excited with a frequency close to the resonant frequency of the cantilever 75kHz $\rightarrow$ 300kHz [124], and the feedback loop is derived from the amplitude of the cantilever oscillation, which is kept constant during imaging the surface [134]. Together with the topography, Tapping mode AFM provides qualitative nanomechanical information through the changes of phase oscillations which is strictly correlated with the different elastic properties of the surface components.

Another technique, also based on the intermittent contact of the cantilever on the surface is known as PeakForce AFM-QNM [135, 136] and has been recently developed and commercialised by Bruker. This technique results well optimised to map soft samples [137, 138], biological samples [139] with simultaneous acquisition of very precise nanomechanical maps. This AFM dynamic mode suits organic and biological materials since the accurate control of the tip-sample interaction forces, required to preserve the original conformation of the samples [140, 141].

In the auto-optimised PeakForce Tapping-Mode scans, the cantilever is oscillated at high frequencies (0.5 $\rightarrow$ 4kHz), far from its resonant frequency (Figure 3.15). During the imaging process, the feedback loop will maintain a constant force (usually in the range of pN-nN) in the interaction between the probe and the surface per each tap of the surface. A representative force curve is shown in fig.3.15b. These force interaction

plots are acquired per each pixel during the scanning operation and processed in realtime to give additional AFM channels, displaying information such as the elastic properties of the surface derived from the force curves.

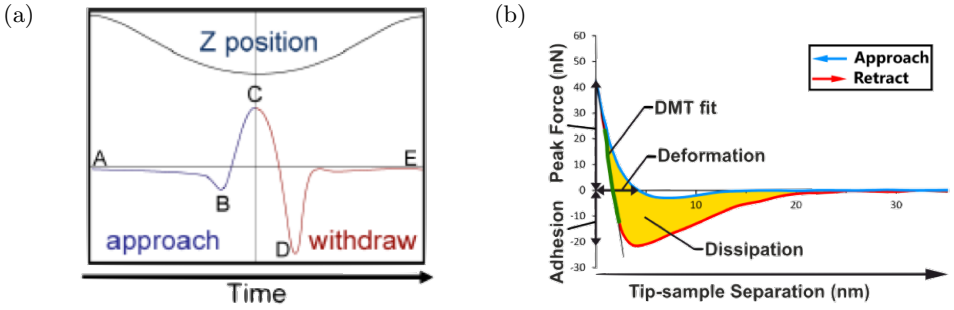

Figure 3.15: (a)Peak force QNM force curve vs. time recorded per each pixel; (b) Force vs. sample-probe separation. Highlighted the PF-QNM additional information processed point by point and used for nanomechanical information. Images from Bruker and [142]

The Young's modulus and the other elastic properties are determined by fitting the force curve in fig.3.15b with a particular model developed by Derjaguin, Muller and Toropov (DMT) [143] and based on the Hertzian modelling of the tip [144] and taking in account the adhesion forces between the tip and the surface [145].

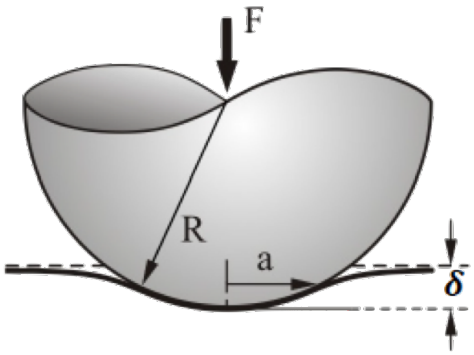

Figure 3.16: Schematic Hertzian model for the tip-sample interaction during the contact. Figure from Bruker

In this model the tip is approximated as a sphere with a half angle much smaller than the tip radius itself as shown in fig.3.16; Young's modulus and forces are given by:

$$E = \frac{\text{Tensile stress}}{\text{Strain}} = \frac{\epsilon}{\sigma} = \frac{FL_0}{A_0 \Delta L_0} \tag{3.6}$$

$$F^{2/3} = \left(\frac{4}{3}\frac{E}{(1-\nu^2)}\sqrt{R}\right)^{2/3}\delta \tag{3.7}$$

Where in equation 3.6 E is the Young's modulus (Modulus of elasticity), F is the force exerted on the object under tension, A_0 is the area where is force is applied and ΔL and L_0 is respectively the length change of the object and the original length of the object. The force F in equation 3.7 depends on the indentation δ of the tip into the surface as shown in figure 3.16, the indenter radius and half angle R and a, the Young's modulus E and Poisson's ratio ν (tipically 0.2-0.5).

Included in the model is the adhesion force $F = F_{tip} - F_{adh}$ and, according to the DMT model, the reduced Young's modulus E^* is:

$$E^* = \left[\frac{1-\nu_t^2}{E_t} - \frac{1-\nu_s^2}{E_s}\right]^{-1} \tag{3.8}$$

where ν_t and ν_s are the Poisson's ratio of tip and the sample while E_t and E_s represent the Young's modulus of tip and sample. Since three of the four mentioned parameters are known, and E_s is automatically obtained from the interaction force curves, through this simple model it is possible to obtain the reduced Young's modulus of the sample under investigation. Therefore, along with the topography, the DMT modulus correlated with the Young's modulus, as well as adhesion, deformation and dissipation properties are recorded.

3.2.4 Scanning thermal microscopy SThM

Scanning thermal microscopy (SThM) is a contact mode technique which provides, together with topography information, nanometrical thermal map, thermophysical and thermal transport information [146, 147].

As shown in figure 3.17, in SThM a sharp probe with a radius of $20 - 50$ nm is brought into contact with the sample surface at a selected deflection setpoint and to act as both temperature sensor and, *via* an external source, heater.

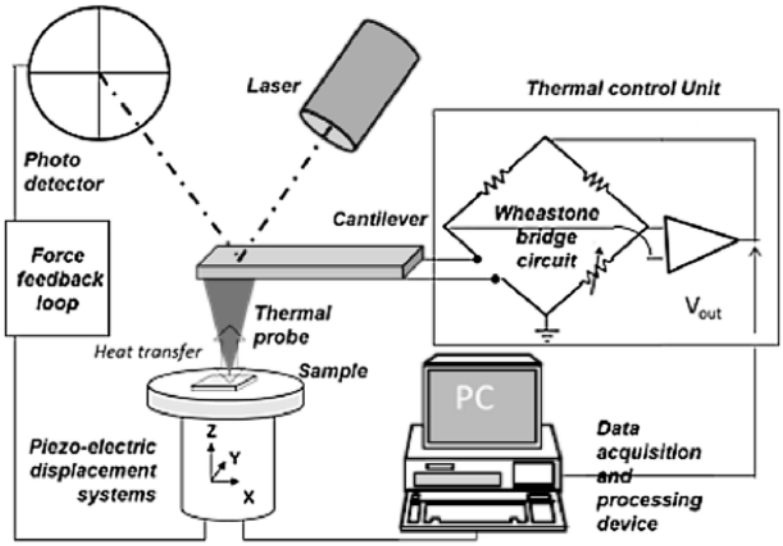

Figure 3.17: Standard SThM configuration and components using the AFM force feedback loop for positioning and a thermal control unit, usually composed of a Wheatstone bridge, for measuring the thermal probe electrical resistance variation. Image from [148].

The most common SThM probes are resistive probes, heated by the Joule effect[146, 149–151], and rely on a similar principle of the electrical resistance dependence from the temperature:

$$R_p(T) = R_{p0}(1 + \alpha(T - T_0)) \tag{3.9}$$

where R_{p0} is the electrical resistance of the probe at a reference temperature T_0 and α is the temperature coefficient of the electrical resistance. Therefore, the resistive element can serve as just a sensor in passive mode for thermometry or as a heater/sensor for thermal transport properties measurements.

In an ideal circuit, the resistive probe is part of a resistor bridge, e.g. a Wheatstone bridge (see figure 3.18) which allows the detection of very small resistance variations.

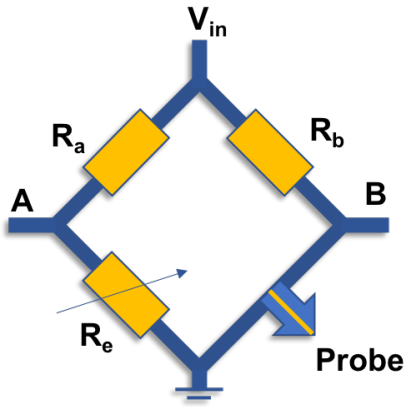

Figure 3.18: Typical Wheatstone bridge for a SThM probe. R_a and R_b are fixed resistors and R_e is variable to balance the probe resistance. The bridge is biased by V_{in} and the bridge output is given by the difference of the two terminals A and B.

The bridge can be balanced when low power is applied to the probe. Both DC and AC operations can be used though AC setup is tipically more sensitive, have lower drift and smaller uncertainties [152]. Once the bridge is balanced and the voltage is applied, any variation in the thermal resistance of the probe due to the contact with the sample surface will be detected by the lock-in amplifier and sent to the AFM controller external input.

SThM can be a powerful tool to investigate heat transfer in nanostructures, molecular structures and complex structures, as long as the surface is smooth enough to avoid dominance of topography-related artefacts [153]. Thermal transport in molecules [57, 154, 155] or even 2D materials [156–158] have been investigated.

Depending on the formalism and setup used, the output of an SThM experiment can give precious information on the thermal resistance or conductance between the heater/sensor and the sample heat sink as will be shown in the next part of this thesis.

Chapter 4

Research background

Widely recognise to have started in 1974 with the seminal paper by Aviram & Ratner, molecular electronics has become a broad interdisciplinary research topic that aims to understand, construct and implement nanoscale circuits based on molecules [12–14]. A key step to achieving this is understanding the quantum transport of electrons through single molecules, SAMs and molecular ultra-thin film.
More recently, the discovery of the thermoelectric phenomena in molecular junctions by *Reddy et al.* in 2007 has opened the possibilities to studying and deeply understanding quantum phenomena in the thermal and thermoelectric transport. Recent reports of the quantum interfecence effects observed at room temperature has opened up new routes to design and optimisation of molecular system [41, 159].

While single molecular junctions provide an interesting fundamental approach to this topic, they typically give values for conductance that could vary with several orders of magnitude depending on the measuring conditions [160]. Devices based on an array of molecules are usually easier to fabricate and could potentially be more reliable for both thermalpower measurements and electric transport studies, even though they sometimes present non-trivial issues related with the identification of the number of molecules in the junction or electrical shorts across the film [161–163].
Recently, molecular thin film and single molecular junctions have been broadly employed as test beds for molecular electronic studies. Conductive scanning probe microscopies such as STM and CAFM, brake junctions measurements, cross bar and micro devices have been employed for many of the set tests to explore the electric transport and the thermoelectric properties of molecular ensembles [164–168].

4.1 Electric transport in molecules

The charge transport through a molecular wire is usually determined by two factors, the intrinsic electrical properties of the wire itself and those of the wire-electrode interface [169–171]. A range of transport phenomenas have been reported for molecular junctions, either in single-molecule measurements or molecular thin films, exhibiting negative differential resistance [13, 172], rectifying characteristics [173], conductance quantisation [174] and switching [175–177].

Early steps towards single-molecule electric measurements were made in 1995 when a current flowing in a single molecule of fullerene C_{60} on Au(110) was measured by *Joachim et al.* using a scanning tunneling microscope breaking junction (STM-BJ) [178]. However, in this work, no current-voltage characteristics were obtained and information about the density of states of the molecule was also limited.
In 1997, the current though a single benzene 1,4-dithiol molecule at room temperature was measured using a mechanically controllable break-junction(MCB) [14]. Thiol (SH-) end groups were used to form a stable metal-molecule-metal junction with gold electrodes. In addition, steps in the current-voltage characteristics were observed as a result of the discreteness of the molecular levels, thereby revealing the quantum nature of the junction.

The quantum nature of the electric transport in single molecular junctions was also observed in 4,4-bipyridine and N-alkanedithiols single molecule contacted by STM-BJ by *Xu et al.* in 2003 [179]. Conductance histograms revealed well-defined peaks at integer multiples of a fundamental conductance value, used then to characterise the conductance of the single molecule. In particular, the researcher observed an increase in the conductance of N-Alkanedithiols molecular junctions with the numbers of carbon bond, exhibiting the characteristic of a tunnel barrier, and attenuation factor β of about 1.0 ± 0.1 per carbon atom in good agreement with similar works with low bias dependency [180].
Among all the measured junctions, 4,4-bipyridine resulted in the most conductive molecular junction, with $1.3 \pm 0,1$. MΩ due to its partial π-aromatic system caused by the effect of the delocalised lone pair electrons of the nitrogen group in the aromatic ring.
In 2000, one of the first single molecule transistors was realised using an electromigration technique to sandwich a C_{60} molecule between two gold electrodes [181]. A third

gate electrode was used to manipulate the current flowing from the source to the drain electrode *via* the electrostatic effect of the gate. Although the device showed transistor behaviour, its performances were significantly inferior to that of semiconducting transistors due to the weak intermolecular electronic coupling, which results in a typically much lower electron or hole mobility than observed in inorganic semiconductors. Furthermore, the dielectric constant of organic semiconductors is much lower (typically 3-5) than that of inorganic semiconductors (10-15) [182].

The characterisation of the electric transport in molecule assemblies is not an easy task since multiple conditions such as temperature, environment and friction and adhesion properties of SAMs have to be respected in order to maintain the molecular structure conformation, stability and reproducibility of the measurement conditions [49, 183–185]. Charge transport in molecular thin films is still fundamentally based on electric transport between two electrodes; in the last 20 years, different ways to measure this property have been explored, e.g. directly putting molecules inside a nano-gap [13, 62, 186], by applying a top electrode to self-assembled monolayers [187, 188], using scanning probe techniques [41, 189], crossbar and magnetic nanoparticle [188] and EGaIn liquid metal electrodes [168, 190].

So far, alkythiols have been the most studied molecular thin film [56, 191–194]. Due to their very large HOMO-LUMO gap of ~ 8 electronvolt [195] which, whilst meaning they are very poor electrical conductors, makes alkythiols very useful for comparisons, modelling, theoretical studies and experiments [179, 180, 195–198]. Early works on the dependency of G on the length of alkanethiol and alkanedithiol SAMs were performed by *Frisbie et al.* using CAFM [165, 199].
They observed current-voltage behaviour which exhibited exponential attenuation of the current with molecular length, finding a β decay parameter of 1.1 per carbon atoms (0.88Å^{-1}) independent of the bias applied and in good agreement with other similar works carried out by STM break junctions (STM-BJ) and nanometric devices [200, 201] and with singlemolecule measurements [179]. In all cases G of the alkanethiol chain was found to drop exponentially with the numbers of carbon bonds from few nS for short chain to several pS for C10 and C12, with an attenuation factor β in between 1.1 and 1.4. Furthermore, negligible variances were observed in the conduction behaviour with the increase of the bias voltage confirming no-changes in the conduction mechanism.

Frisbie et al. in 2000 showed the robustness of this system employing a CAFM in order to measure the conductance of the SAMs with a precise control of the loading force of the AFM metallic coated tip on the SAM [202]. Interestingly, they found small changes in the conductance of longer chains with small increments of the applied force.

The variation in the conductance due to the deformation of the SAM is a pretty common problem in the field [128, 203, 204] not only when SPM techniques are used to characterise the molecular layer but also in more sophisticated configurations. In particular, *Lio et Al.* using a high resolution AFM observed a transition from the thiol overlayer to the Au(111) substrate periodicity at a critical contact pressure of 2.3 GPa [203]. This transition is related with the SAMs' change of conformation due the higher forces applied by the SPM probe which displaces the molecules from their original position [205]. The increase in the loading force on the SAM surface led to slight changes in the electrical conductance below a threshold force of $\sim$ 70 nN. Below this limit, G increased linearly with the loading force, following the exponential power law of the Hertzian Model, which describes the probe-surface indentation [128]. For alkanethiols were found that a 1 nN variation in applied load resulted in a 3% change in the junction contact area, and thus in small change of G. But, when the forces overcome the critical value, a jump in the conductance was measured as results of the SAM's deformation and the consequent formation of probe-substrate contact.
For this reason, the control of the mechanical deformation of the SAM during the characterisation of the electric transport is crucial.

4.1.1 Transport regimes in SAMs

Introducing a delocalised π-π system into the molecular thin film has been reported as an effective way to decrease the HOMO-LUMO gap and to enhance the charge transport through the molecule [12, 206, 207]. The poly-phenylene chain is one of the simplest π-π conjugated wires, however, the freely rotating sigma bond between neighboring phenyl rings results in a range of allowed molecular conformations [208]. Conversely, oligo(phenylene-vinylene)s (OPVs) and Oligo-(phenylene ethynylene)s (OPEs) have been shown to exhibit long range electron transfer, low HOMO-LUMO gap, rigid structure and high synthetic flexibility [209–211].
Further studies have reported that the conductance of OPE/OPV wires can be modified

by adding a side-chain, which leads to a transition from the classic resonant tunnelling to hopping [212]. In 2009, *Choi et al.* reported a dependence in the electrical resistance with molecular length of OPIs-N (Oligo-phenylenemine) based SAMs measured by CAFM [166]. Compared to alkanethiols studies [165, 180] and other molecule length-dependence conductance [213], they found a net change in the transport mechanism in the SAMs evidenced by the shrinking of the HOMO-LUMO bandgap in the I-V traces after 4 nm of film thickness and, from the change in the attenuation factor β, underlying a transition from non-resonant tunneling to hopping [160, 214, 215].

For shorter chain molecules (OPI 4) below 4 nm a linear regime at low bias voltage, as an indication of tunneling behaviour across the junction, is observed and following the Simmons model, the tunnel barrier can be imagined as trapezoidal such that [166, 216],

$$I \propto V \exp\left(-\frac{2d\sqrt{2m_e\phi}}{\hbar}\right) \tag{4.1}$$

where d is the barrier width, m_e is the electron effective mass and ϕ is the barrier height which represents the difference between E_f and the LUMO of the molecule. As the applied bias voltage V is higher than ϕ/e, the trend of the transport mechanism changes due to the strong electric field and, in this case, the shape of the tunnel barrier can be imagined as a triangular barrier [217]. This transport regime is known as Fowler-Nordheim (F-N) tunneling and is described by the relation [195]:

$$ln\left(\frac{I}{V^2}\right) \propto \frac{-4d\sqrt{2m_e\phi^3}}{3\hbar q}\left(\frac{1}{V}\right) \tag{4.2}$$

where q is the electron charge. In addition, from studies in alkanethiols SAMs, this particular tunnel regime results independent from the temperature [195].

Similar relationships have been obtained from different groups using conjugated wires molecules as components for molecular film [167, 218]., showing different regimes depending on the bias voltage applied. on the junction. Furthermore, depending on the length of the molecules, different regimes could be observed. For thicker films, the main transport mechanism at low-bias regime was described by two different Ohmic hopping conduction regions, before the transport became totally dominated by the electric field at high-bias regimes (III' region) and thus described by F-N tunnel regime.

Compared with single molecular junctions or few molecule junctions, SAMs have often demonstrated better stabilities and reproducibilities, showing great potential for

application in molecular devices. In fact, in addition to the covalent bond formed between the headgroup of the molecule and the atoms of the metallic substrate, the intermolecular Van der Waals forces between the backbone of the molecules make SAMs more stable to mechanical deformation and establishing their growth angle relative to the substrate's surface [219–221].

4.1.2 Electrodes engineering

One of the key challenges in molecular electronics is the nature of top contact electrode in vertical junctions [222, 223]. For SPM characterisation, the electrode is formed by the probe, which is usually Au or Pt coated and brought into contact with the molecular thin film surface with a controlled normal force. For devices and other measurement setups, top electrodes are fabricated by direct evaporation of metals, which may damage the SAM and cause short circuits [224, 225]. To solve these problems, several non-destructive methods have been explored in the last two decades. *Loo et al.* first introduced transfer printing to fabricate soft top contact electrodes in Au/1,8-octanedithiol/GaAs junctions making contact between an elastomeric poly(dimethylsiloxane) (PDMS) stamp coated Au film and SAM-modified GaAs [226].
Moreover, using liquid metals, such as Hg [227] and eutectic gallium indium (EGaIn) [168, 228], results in an efficient methodology in order to create "non-invasive" top contacts. Indeed, the liquid metal contact is relatively stable, forming a large contact area to the junction and can effectively prevent problems such as mechanical damage and metal atom penetration [168].

In 2006, *Akkerman et al.* showed that a conductive polymer could be effective as a protection layer for the thermally evaporated top electrode [187]. This was because of the appearance of electrical shorts in SAMs when the top electrodes were thermally evaporated. Since then, large scale molecular thin film measurement have been processed with a high percentage of yield on flexible substrates [229].
High stability of the I-V traces was found in dodecane dithiol SAMs with contact diameters of 40 and 80 µm.

The idea of using graphene (Gr) as soft top-contact electrodes in SAMs and molecular thin film systems has also been tested and has attracted a lot of focus since its recent

discovery in 2004 [230]. Its high conductivity and high transparency, make graphene very appealing as a buffer layer for soft top-contacts. In 2011, *Wang et al.* reported a high device yield and good operational stability in a microwell device using multi-layered CVD graphene as a top contact electrode forming a Au/alkylthiol (and OPE 3) SAMs/Gr/Au sandwich structure [231]. This work showed that graphene could be a good alternative to PEDOT:PSS as a interlayer between SAMs and top electrodes, playing the role of conductive interconnects between junctions in series and acting as an interlayer to protect the molecular film from invasive metal contacts [161].

A similar structure was achieved later by *Li et al.* and *Seo et al.* developing a similar device using reduced graphene oxide (rGO) and graphene oxide (GO) films as top electrode [232, 234]. Reduced graphene oxide (rGO) films as top electrodes showed advantages compared to CDV graphene, suitable for large-area fabrication and easier to transfer without polymer support. In addition, rGO demonstrated to be an optimum top electrode for sub-Kelvin electric transport measurements [233].

A recent strategy to integrate graphene in molecular electronic application has been focused on modifying the probe in AFM measurements of SAMs and molecular thin films. in 2012, *Wen et al.* and *Lanza et al.* have both reported progress on using graphene as a coating layer for conductive AFM probe, with a significant decrease in measurement variance observed for the graphene coated AFM tips compared with the commercial Pt or Au probes [235, 236].

4.2 Thermoelectricity in molecular junction

In the last 15 years, several groups have experimentally quantified the thermoelectric properties of molecular junctions (MJs). So far, measuring the thermal voltage V_{Th} and thermoelectric properties in molecular junctions is a non−trivial task and different techniques have been developed from different groups, such as MJs in two−terminal configurations, a technique that enables the measurement of the thermal voltage output from junctions, trapping the molecules between a hot and a cold electrode (usually STM-BJ, CAFM or MC-BJ) [41, 179, 189, 237].
More recently, three-terminal techniques that enable tuning of the thermoelectric properties of MJs have been refined by different groups, employing electromigration of Au or electroburning Gr electrodes so to create a nanometric gap and using a bottom electrode as gate electrodes to tune the transport through the junction [238–240].
It has been shown that the thermoelectric properties of MJs can depend on the length of the molecule (or alternatively the thickness of the molecular film), end groups, molecular structures and conformation, electrode materials, and temperature, each property of which will be discussed in detail below.

The first step towards thermoelectricity in molecular junctions was made by *Reddy et al.* in 2007 [41]. In this milestone work, an STM−BJ technique previously developed by *Xu & Tao* [179] was employed to measure the thermopower of molecular junctions of benzenedithiol, dibenzenedithiol, tribenzenedithiol trapped between a STM Au tip and a bottom Au electrode.
In this work, the author observed for the first time that the Seebeck coefficient of aromatic molecular junction can increase with the length of the molecules, with an expected linear dependency on the average temperature of the junction and a positive value to the Seebeck coefficient, indicating, as mentioned in section 2.2.2, a HOMO dominated transport mechanism for the junction. However, no conductance was recorded for the junctions due to the necessity to switch the connection of the current and voltage amplifier at a different time in order to measure the thermal voltage of the junction.

Improvement of the *Reddy* characterisation setup were reported by *Widawsky et al.* in 2012 [189]. In this study, a mechanically controlled STM−BJ technique was successful used for the simultaneous measurement of the electrical conductance and thermopower of single MJs measuring both the zero-bias thermocurrent and the electrical conductance

under a small applied bias. *Widawsky et al.* characterised several amine–Au linked and pyridine–Au linked MJs, observing a positive Seebeck coefficient for amine–Au linked junctions and a negative Seebeck coefficient for pyridine–Au linked MJs, as an indication of the different transport mechanism for amine–Au MJs and pyridine–Au MJs.

An STM break junction approach was also used to prove the Landauer formalism. *Kim et al.* [240] conducted a study on the dependence of the thermopower in a Au-BDT-Au STM junction at a range of temperatures (100K-300K). The Seebeck value for the junction was found to be linearly dependent on the temperature as expected from the theory. In contrast, they found no temperature dependency from the electrical conductance G of the junction across the range of temperatures applied between the two electrodes.
In 2010, *Tan et al.* [237] used a CAFM setup to measure the thermal voltage of molecular films. An Au-coated AFM probe kept at room temperature, was placed in contact with a heated Au substrate covered with a monolayer of 1"-terphenyl 1-4-thiol (TPT) molecules, keeping the cantilever deflection at a constant value using the feedback control. A Seebeck coefficient of the film of $16.9 \pm 1.4 \mu V\,K^{-1}$ was measured when a $\Delta T = 12K$ was applied between the cantilever and the substrate.

Further investigation of the usage of the thermopower measurement in order to infer information about the transport mode has been reported previously [241]. In this work, the thermal power of a series of single molecular junctions was measured using a STM-BJ and fitting the thermovoltage vs the substrate temperature. The results were in good agreement with the ones found by *Widasky et al.* [189], confirming that thermopower provides useful information about the molecular energy level alignment, helping to understand the charge transport mechanism. In addition, they found a strict dependency of the thermal power with the transition voltage of the single molecules, which results consistent with the prediction of the tunneling-based theory within the framework of the Landauer formula.

With a similar setup *Evangeli et al.* measured simultaneously the thermo power and the electrical conductance of a single and two stacked C_{60} junction [37]. They found that the thermopower of the C_{60} dimer is almost twice that of a single C_{60} junction, giving a relatively high Seebeck coefficient of $\approx 33 \mu V\,K^{-1}$ (fig.4.1).

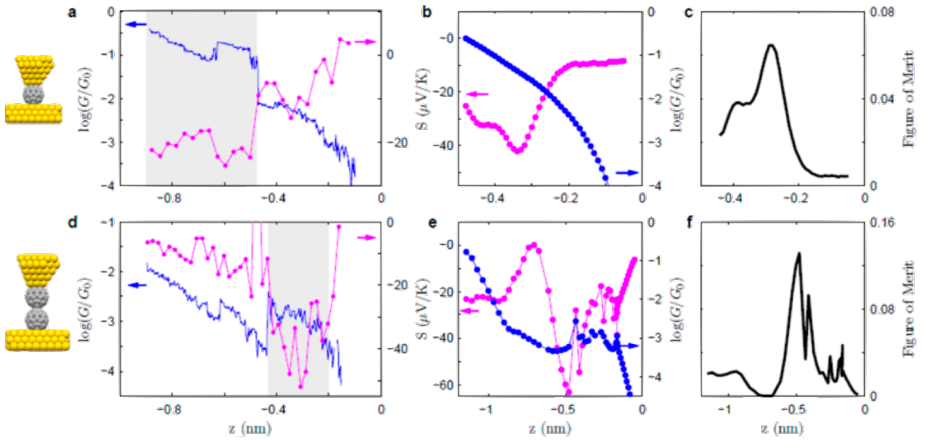

Figure 4.1: (a) Conductance at 100 mV and thermal power, simultaneously acquired at $\Delta T =$ 25K. The grey area shows the z tip−sample displacement where the Au−C_{60}−Au junction is created; (b) Theoretical values conductance and thermal power as function of the distance for a single C_{60}; (c) Calculated figure of merit ZT for a single C_{60}; (d) Conductance at 100 mV and thermal power measured during the formation of the C_{60} dimer (grey area) at $\Delta T = 12$K; (e) Theoretical values for conductance and thermal power as function of distance for the dimer; (f) Calculated figure of merit ZT for the dimer. Images from [37].

The computational calculations performed in this work suggested that the thermopower and ZT increased with the number of C_{60} units in the molecular chain due to the intermolecular coupling between identical molecules, suggesting that it may be possible to improve thermoelectric properties by manipulating C_{60} junctions. In fact, this strategy differs from the various intramolecular approaches to tuning S, which include varying the chemical composition [242], increasing the single-molecule lengths within a family of molecules [243] and systematically varying the conformation of molecules [244]. Their calculations revealed that both the conductance and thermopower was weakly dependent on the orientation of the molecule but sensitive to the intermolecular coupling and the positions of the frontier orbitals relative to the Fermi level, all of which fluctuate as the electrode separation was increased.

The linear dependence of the thermal power from the length of the molecules (e.g. carbon bonds or phenyl rings) has been largely studied theoretically and experimentally. In this direction, *Pauly et al.* [245] in 2008 reported a theoretical study in which a linear increase of the thermal power and an exponential decrease in the conductance by increasing the aromatic group in dithiolated oligophenylenes (OPE) were observed when a difference of temeperature between the two electrodes was applied. *Malen et al.* reported a linear decrease in Au-alkanedithiols-Au junctions [246]. The opposite trend found in alkanedithiols was explained to be caused by gold–sulphur metal contacts gap states that reside between the HOMO and LUMO of the alkanedithiols, as reported

already in literature by different works [247–249]. In contrast to alkanedithiols, for Au–phenylenediamine–Au and Au–phenylenedithiol–Au aromatic junctions, the thermal power was found to increase linearly with the numbers of aromatic rings[41, 243, 246]. Similar results were found for trimethylstannylmethyl terminated polyphenyls with 1 to 4 phenyl rings [250]. Furthermore, a very little length dependence was observed for the thermopower of trimethylstannyl-terminated alkanes junctions with N= 6, 8, and 10, similar to the trend reported for alky-chain junctions [248, 251].

The effect of the length was also studied in SAMs of aromatic molecules with different numbers of aromatic rings and terminal groups [252]. Using a modified CAFM setup and computational analysis a positive Seebeck coefficient exhibiting a linear increase with the thickness of the film was reported. In addition, the effect of the different anchor groups of the SAMs on the thermopower was deeply studied, evidencing a strict relationship between the the thermoelectric properties of the junction and the terminal group of the molecules. In contrast with the values obtained for thiol-terminated SAMs, (-CN) cyanide-terminated SAMs showed negative Seebeck values. With computational studies, the authors demonstrated that this change was to be attributed to transport being dominated by the LUMO based channel in the isocyanide junction, showing the possibility of tuning the thermoelectric properties of molecular junctions via contact chemistry and molecular structure.

The importance and influence of the endgroup of the bridging molecules on the charge transport, the coupling with the electrodes and the thermoelectric properties has been reported in literature [253–255]. Thiol- and dithiol-terminated molecules together with amine-terminated molecules has been the most studied endgroup so far [170]. Seebeck values of thiol-terminated aromatic molecular junctions displayed a positive thermalpower [35, 246] whereas measurements on isocyanide-terminated SAMs showed an opposite trend, exhibiting a negative Seebeck [252]. In 2013 *Balachndran et al.* realised a fundamental theoretical study on the effect of the endgroups on the thermopower of molecular wires. They investigated isocyanide, nitrile, amine, thiol and carboxylic endgroups which interface a triphenyl molecule to the Au electrode. They found a downward shift of the Fermi energy towards the HOMO level for amine-, nitrile- and isocyanide-terminated due to the charge transfer out of the molecule upon coupling with the top electrodes. In contrast thiol- and hydroxyl- terminated molecules present a Fermi level

closer to the LUMO level due to the charge transfer from the electrodes to the molecule. C_{60} terminated MJ has also been studied from *Bilan et al.*. In their theoretical study they compared amine-terminated molecules with thiol-terminated and Fullerene C_{60} anchored molecules (C_{60} Dummbells)[257]. The thermopower of C_{60} terminated phenyl MJs was found to be negative and strongly dependent on the contact geometry. Compared to the results with those obtained with thiol and amine endgroups the conductance of $C_{60}-$terminated molecules is rather sensitive to the binding geometry. Moreover, the conductance of the molecules is typically suppressed by the presence of C_{60}, making the junctions more sensitive to the functionalisation of the molecular core with appropriate side groups.

The chemical structure of the molecular bridge can be tuned to minimise the phonon transport, enhance the electrical conductance through electron-withdrawing/donating sides groups and therefore enhance the thermoelectric properties of the junction. *Baheti et al.* probed the thermoelectricity of BDT with different electron-withdrawing/donating groups and different endgroups using a STM-BJ technique [242]. Studying the role of the substituent they suggested that the presence of electron$-$withdrawing groups like fluorine and chlorine shift the energy levels of the BDT MJ downwards, while the presence of methyl electron-donating groups shifted the molecular levels upwards, leading to an increase of the thermopower. .
Since BDT is HOMO dominated, the shift of the energetic levels up (or down) with respect to the frontier orbitals caused by the presence of the electron-withdrawing/donating groups, will shift the transmission function towards (or against) the Fermi level E_f. This means moving to a higher or smaller slope of the alignment of the transmission function and thus the possibility to tailor the thermopower of molecular junctions with chemical "dopants".

The influence of chemical doping on the conductance and thermoelectric properties has been largely studied in metallo-phthalocyanine and porphyrins [34, 258, 259]. *Xing et al.* measured the Seebeck coefficient and the power factor of a thin film of Copper-Phthalocyanine (CuPc) doped with hexacyano-trimethylene-cyclopropane (CN6-CP), which is a strong electron acceptor. The molecular films were thermally evaporated with different doping ratios and different film geometry. Under optimised conditions, they reported a conductivity of 0.76 $\mathrm{S\,cm^{-1}}$ and a Seebeck coefficient of 130 $\mathrm{mV\,K^{-1}}$,

giving a power factor of 1.3 $\mathrm{mW\,m^{-1}\,K^{-2}}$. The possibility of tuning the thermoelectric properties by chemical doping was studied by *Al-Galiby et al.* in which they studied the effect of chlorine molecules attached on the metallic core of metalloporphyrins. Through computational methods, they showed how it is possible to tailor the Seebeck coefficient of metalloporphyrins molecular junctions due to the oxidation/reduction of the metallic core of the molecule [34].

The role of the chemical and molecular conformations on the electric and thermoelectric properties was investigated in different studies [260–262]. *Lee et al.* in 2015 studied the thermoelectic properties of fullerene-based molecules C_{82} with encapsulated metallic atoms ($Gd@C_{82}$, $Ce@C_{82}$) using a STM-BJ [263]. For the three fullerene derivatives a negative thermopower was found. The values of electrical conductance were found to be the same for all three molecules, however the thermopower showed an increase when metal atoms were encapsulated in the fullerene cages. In particular, the power factor σS^2 obtained for $Gd@C_{82}$ junctions was the highest value obtained for a single-molecule device, with $-31.6\mu\mathrm{V\,K^{-1}}$, compared with $22.7\mu\mathrm{V\,K^{-1}}$ for C_{82}. Through computational analysis, they conclude that although the encapsulated metal atom does not actively contribute to the transport, the enhancement of the thermoelectric properties for the two junctions is due to the substantial changes in the electronic and geometrical structure of the fullerene molecule induced by the encapsulated metal atom.
This mechanical deformation of the molecular structure in a junction is another approach for optimising the thermoelectric properties of a junction. This effect, for example, was tested in aromatic molecules, demonstrating how the angle between the different phenyl rings could vary the conductance up to 30 times [261].
Rincon-Garcia et al. studied the thermoelectric proeprties of an endohedral fullerene $Sc_3N@C_{80}$ contacted with a STM [264]. In their work they reported that the magnitude and the sign of the Seebeck coefficient depends strongly on the orientation of the molecule and on the deformation of the fullerene cage. In further computational analysis they discovered the presence of a sharp resonance close to the Fermi energy E_f due to the Sc_3N molecule, revealing the possibility of "bi-thermoelectric" materials, exhibiting both negative and positive thermal power for Sc_3N.

4.2.1 Influence of electrode material

Electrode engineering is essential for the optimisation of the thermoelectric properties of molecular wires. Although Au is surely the prototypical material for electrodes in molecular junctions, thanks to its easy fabrication in thin films form and because it does not go under oxidation at the typical measurement temperature, the possibility to use other metals instead has been studied [31, 245, 265–267]. The actual advantage in using one metal as an electrode rather than others lies in the opportunity to shift the energy levels of the molecular junctions, trying to bring the Fermi energy E_f closer to the molecular orbitals that dominate the charge transport as possible [268, 269]. Investigation of the top electrode material (Pt, Au, Ag) has been studied in fullerene molecules (C_{60}, PCBM, and C_{70}) in a STM-BJ [270]. The authors proved that the Seebeck coefficient of MJs could be tuned by varying one or both the electrodes. In particular, for Fullerene C_{60} they found that the thermal power was suppressed when Pt was used instead of Au ($S_{Au-Pt} = -8.9 \pm 2.2$ µV K^{-1}) compared with $S_{Au-Au} = -14.5 \pm 1.2$ µV K^{-1} ; in contrast the Seebeck was found doubled when Au was replaced with Ag with a value of -29.6 ± 3.4 µV K^{-1}.

Lee et al. in 2014 studied the effect of Ni and Au in BDT and C_{60} using an STM-BJ [271]. Thermoelectric measurement in fullerene showed a negative thermopower for both the two metallic electrodes, while interestingly, BDT MJs exhibited positive thermal power when the BDT was contacted by Au and negative thermal power with Ni electrodes. This effect was studied through computational analysis, revealing that the switch of the Seebeck's sign arises from the spin-split generated in the energy levels when BDT couples with Ni electrodes.
The role of top electrode was also studied in CAFM junctions of 3, 4, 9, 10-perylene tetracarboxylic dianhydride (PTCDA) thin film, investigating different metallic coated AFM tips [272].

4.2.2 Three-terminal devices

As seen, to improve the thermoelectric properties in MJs, a key strategy is to engineer the transmission function of the junction such that the slope and magnitude of the transmission function at E_f are maximised. Most thermoelectric measurements of MJs have relied on two-terminal measurements, which give limited control of the junc-

tion's electronic structure. For this reason three-terminal devices, capable of tuning the electronic structure in molecular junctions, have also been studied [238, 258, 273–278]. Three-terminal devices are often created by electromigration, electroburning, mechanically controlled BJ or e-beam lithography of the electrode (usually Au/Pt) as described in the previous section. The nanometric sized broken portions of the electrode create two terminals (source S and drain D), while a Si back gate serves as a gate electrode. The molecules are deposited into the nanoscale gap by exposing the electrodes to molecules in a solution.
Thermoelectric measurements on three-terminal devices compared to electric transport measurements on gated devices is a relatively new area. The biggest challenge and probably the main studied topic, in this case, consists of optimising the geometry and the characteristics of the electrodes and establishing a temperature gradient between the two electrodes (S and D) separated by a nanogap [239, 279, 280].

Kim et al. created novel three-terminal devices based on electric-burned junction (EBJ) and integrated an electric heater into one electrode (S or D) [240]. Using this strategy suggested by the finite-element analysis, the researchers established a temperature difference due to the heat's dissipation in one of the two electrodes across the MJs and electrostatically gating their electronic structure. With such a device, the thermal power of Au–biphenyldithiol (BPDT)–Au and Au–C_{60}–Au junctions was probed, revealing that the local back gate can widely tune and improve the thermoelectric properties, effectively moving the dominant transport orbital closer to E_F. For both Au–BPDT–Au and Au–C_{60}–Au junctions, the thermoelectric properties were found to be tunable when a gate voltage was applied, and interestingly they showed how the C_{60} thermal power can be tuned over a large range from -10 to $-50\mu V\,K^{-1}$. This work demonstrated for the first time the feasibility of improving thermoelectric properties by tuning the electronic structure of MJs.

Such a level of control of the electronic structure was obtained in 2006 by *Gehring et al.* They studied the thermoelectric properties of C_{60} employing an electroburned graphene nanogap with a Au microheater underneath one of the electrode [57]. In their work, the researcher found several advantages in using graphene electrodes over conventional Au electrodes, observing a reduced screening of the gate electric field and allowing better control of the alignment of the dominant transport orbitals by hundreds

mV. They found that the power factor $S^2\sigma$ of Gr-C_{60}-Gr could be tuned over several order of magnitude. This study gave one of the first deep sights in the coupling of the molecule with the electrodes as well as the temperature distribution across the junction, highlighting the importance of level alignment and coupling with the electrodes to obtain an optimised thermoelectric conversion in three-terminal molecular devices.

4.3 Quantum interference effect in molecular electronics

Recently the idea of exploiting room-temperature quantum interference effect (QI) at the single-molecule level to enhance molecular conductance and thermoelectric properties has been discussed and investigated both theoretically [34, 244, 281–284] and experimentally [242, 270, 285–292].Thermal power is an intrinsic property of the molecule, and in principle, it should be possible to design molecules with built-in QI functionality and demonstrate that fundamental manifestations of QI can be manipulated and exploited in many-molecule ultra-thin films.

To give a brief overview of the QI effect in molecular junction, the electron wave character must be taken into account when we describe the process of coherent transport across a molecular junction, represented by the transmission function $T(E)$. For instance, the conductance properties of mesoscopic ring structures at low temperatures are dominated by quantum interference. Depending on how the partial waves through the branches of the ring add up destructively (constructively), a suppression (enhancement) of the conductance can be observed [290].

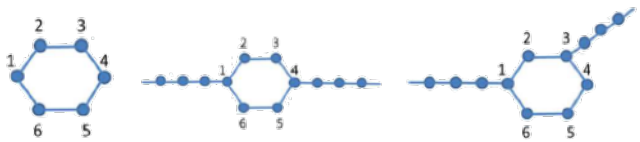

.

Figure 4.2: Example of different electron path in a phenyl ring with 6 π electrons with one electron per orbital and imaginary 1-dimensional lead attached in $i = 1$ (fixed) and the second lead to a different atom in $j = 4$ (*para* or $j = 3$ (*meta*). Depending on the second electrodes' position, the electrons waves will interfere with each other constructively or destructively in analogy to a Mach-Zehnder interferometer.

For conjugated molecular junctions, as shown in fig.4.2, a similar effect is also expected [293–295]. Interference in a molecule has to be described in terms of electron propagation via paths of orbitals, differing not only in space but also in energy. Referring to the phenyl ring in fig.4.2, it is easy to understand that, depending on the position of the lead anchor group on the atom of the ring, the path of the electrons (in a wave picture) from a lead to another can interfere constructively or destructively, depending on their position in the molecule. Since the properties of molecular orbitals can also be manipulated by chemical design, electrostatic gate and mechanical gate, quantum interference could provide great control over the conductance of molecular devices at the

wave function level [283].
Experimental proof of the enhancement of Seebeck by room-temperature QI in single molecular junction and molecular assembly was obtained only recently [296, 297].
As seen, it has been largely demonstrated experimentally that at a molecular scale, thermal power can be controlled by varying the chemical composition [34, 242], tuning the position of intra-molecular energy levels relative to the work function of metallic electrodes [270], systematically increasing the single-molecule lengths and varying the binding groups within a family of molecules [245, 250], by tuning the interaction between two neighbouring molecules [37], and by controlling the transport properties with an electrostatic [155] or electrochemical gate [32]. These experiments yielded room-temperature values of S ranging from ca. 1 to 50 $\mu V\,K^{-1}$.

One of the first, very comprehensive proof of QI effect was given by *Miao et al.* [297]. Their work demonstrates the possibility of varying the thermal power by modifying the molecular configuration of OPE3 molecules. Specifically, they investigated the conductance and Seebeck values for OPE3 when switches between *para-* and *meta-* connections of both thiol anchor groups to gold electrodes.
Using a STM-BJ and a CAFM they distinguished two different values of thermopower for *para*-OPE3 and *meta*-OPE3, which *Ab-initio* calculations attributed to quantum interference effect due to the different shapes of the transmission function of the two molecules. The sharp feature in the transmission function of *meta*-OPE3 gives rise to a larger S of $20.9 \pm 1.54\ \mu V\,K^{-1}$ compared with $10.8 \pm 9.5\ \mu V\,K^{-1}$.

In another recent work, *Wang et al.* demonstrate that the signature of constructive QI can be translated into SAM-on-gold molecular films [296]. Employing a CAFM technique, the researcher showed that the conductance of vertical molecular junctions formed from 4 anthracene-based molecules with different connectivities varied by a factor of about ≈ 15, in agreement with computational analysis of the different junctions. In addition, they demonstrated an improvement of the Seebeck coefficient of 50%, combining the role of QI with appropriate anchor group as shown in fig.4.3.

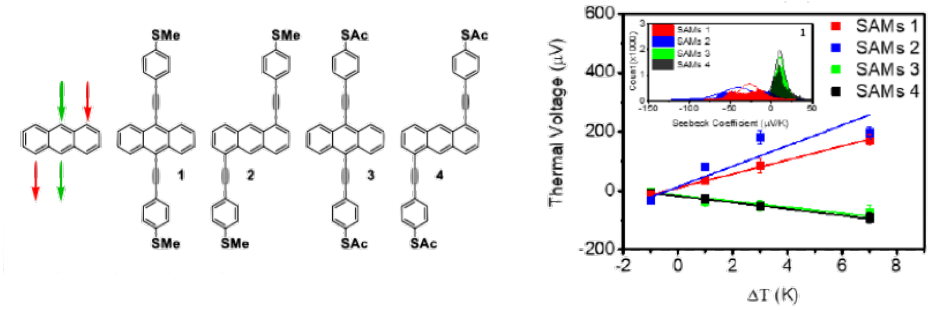

Figure 4.3: Thermal voltage average values vs. ΔT ($T_s - T_p$) for the set of anthracene-based molecules 1-4(shown on the left) with different anchor groups. Images from [296].

Part II

Experimental results

Chapter 5

Materials and Methods

This chapter will discuss the realisation of ultra-thin molecular layers through Langmuir-Blodgett deposition and self-assembly in solution. In particular, the study of C_{60} Langmuir-Blodgett films due to C_{60}'s importance in the field of molecular-scale thermoelectricity [32, 37, 270]. To confirm the presence of transferred molecular layers on the surface of different substrates, optical spectroscopies and scanning probe techniques were employed.

As discussed in Section 3.2, the use of scanning probe techniques in molecular electronics has largely been explored, resulting in a powerful tool to characterise electric and thermal transport as well as thermoelectric properties. However, the development of non-destructive techniques based on conductive probe AFM (CAFM) is needed to measure and quantify thermal power and electrical conductance of the molecular thin film without damaging the sample surface.

One of the main aims of this work was developing an AFM based conductance and thermopower mapping technique based on the intermittent contact of the probe and sample, thereby reducing the damage to the molecular thin film, which typically occurs during scanning. As will be shown, one of the significant advances of this technique is the simultaneous acquisition of electric or thermoelectric signal and the nanomechanical properties of the probe-samples interaction. In addition, the development, realisation, and deployment of graphene coated AFM probes for thermoelectric measurements represent a breakthrough in the field. Indeed, in analogy with the most recent 2 and 3 terminal graphene based devices [57, 161, 235, 236], the possibility to employ graphene coated probes opens new opportunity to extend the knowledge of the electrode's material influence on the thermoelectric properties of molecular thin films (Chapter 4).

Classically, the assembly of molecules into well-defined nanoscale structures or molecularly well-ordered thin-films can be carried out by several different techniques, including self-assembly, casting and spin-coating, and layer by layer procedures.

5.1 Langmuir-blodgett ultra-thin film of C_{60} and Zn-TPP

In the context of this thesis, the study of molecular systems such as fullerenes and Zn-TPP ultra-thin films made by LB are presented for thermoelectric applications. The choice of these molecules is mainly due to their electrons orbital characteristic, tunable electronics properties and semiconductor behaviour.
As already mentioned, LB deposition was initially developed to prepare monomolecular layers of amphiphilic molecules (Sec.3.1.2). However, the insolubility of some molecules in water, such as C_{60} or Zn-TPP, due to their strong hydrophobic character, still allows the preparation of LB films at the air-water interface. It has also been shown that other, roughly spherical hydrophobic molecules can be compressed to rigid films using the LB method [298].
All results presented were obtained using a *Biolin scientific* model KSV NIMA 2003 trough, with a maximum area of 841 cm^2 and minimum area of 29 cm^2, when the hydrophilic barriers are totally closed. The trough has hydrophobic edges, and when in use, the trough was slightly overfilled with ultra-pure deionised water (18.2 $M\Omega\,cm^{-1}$ at 25°C using Millipore Direct-Q 3 UV system) so that the two hydrophilic barriers could constrict the molecules on the water surface. The speed of the barriers was variable from 0.5 to 270 mm/ min, and thus the rate of compression of the film could be automatically regulated by the control software allowing proper control on the molecular film growth dynamic.

During compression of the molecular film floating on the water, the surface pressure was monitored using a Wilhelmy plate, measuring the difference in surface tension between the pure water subphase and the film surface. In particular, a paper (Whatman Grade 1 filter paper) Wilhelmy plate (2×1 cm) was saturated with water for 30 minutes and hung through the water surface. The plate and water surface were necessarily aligned to be perpendicular, as shown in fig.5.1. The surface pressure (Π) evolution during the compression as a function of the available area per molecule for stearic acid is shown as an example in fig.5.2, indicating molecular layer density and its particular

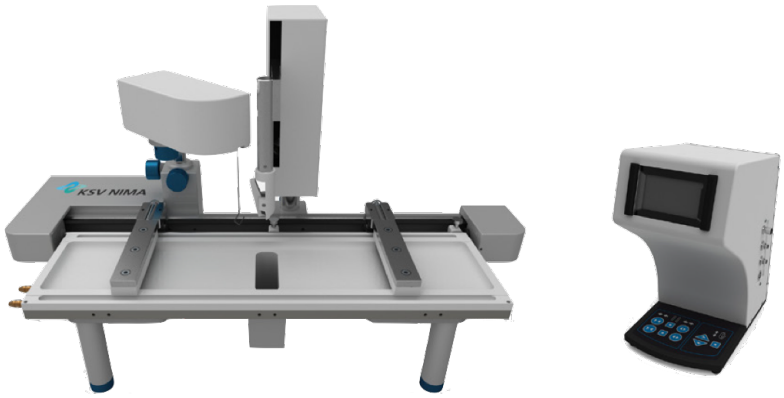

Figure 5.1: KSV NIMA LB 2003 large trough employed for the molecular layer formation and deposition. On the right the LB core controller is shown. Image from [105].

phase (discussed in Section 3.1.2).

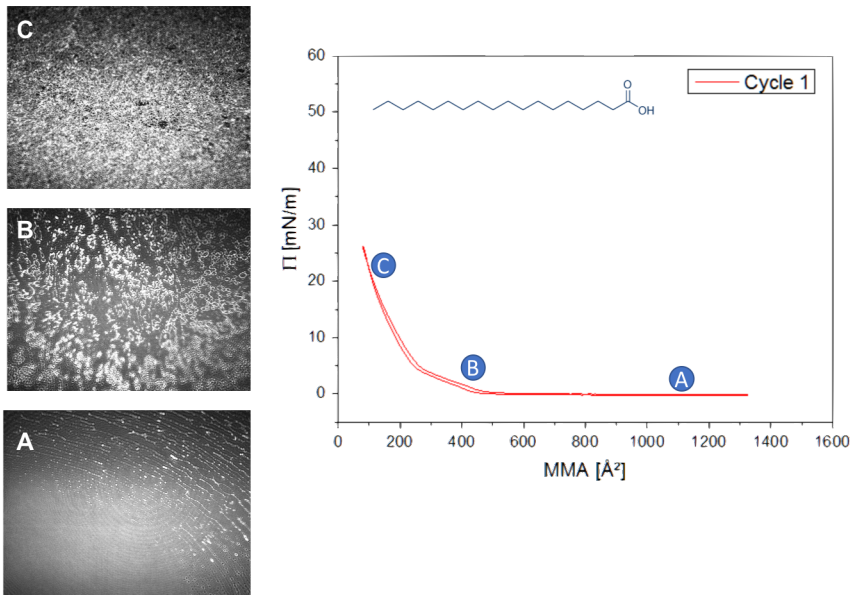

Figure 5.2: Example of LB isotherm for 200µL of stearic acid solution in one cycle of compression-expansion of the LB barrier. The isotherm shows different phase transition points which are highlighted by the blue circles. In support of the LB isotherm, the Brewster angle microscopies at the phase-transition point are also reported here.

From fig.5.2 it is possible to observe 3 phases transition in the LB isotherm, indicated with A (gas phase), B (liquid phase) and C (solid-like phase), and underlying the evolution of the different packing of the floating molecules during the compression of the barriers.

Complementary to surface pressure monitoring, and as shows in fig.5.2, the layer formation in LB was observed in real-time with Brewster angle microscopy (BAM) supplied by KSV NIMA, which used a laser light source and a microscope to image the water

surface. Both the microscope and the polarised light source were aimed at the water surface, with the light oriented at the water Brewster's angle ($\sim 53°$ for the air-water interface) so that there were no reflections when it shone on a pure water surface [299–301]. When the microscope and light source were incident on a region with a molecular cluster, reflections did occur. The pixel resolution of the BAM was 5.6 µm, meaning that several thousand agglomerated molecules represent each captured pixel. As such, the BAM could not identify individual molecules but was used to study and optimise the density of large areas of the surface and characterise phase transition points in a Langmuir-Blodgett isotherm giving valuable information on the formation dynamics of the monolayer.

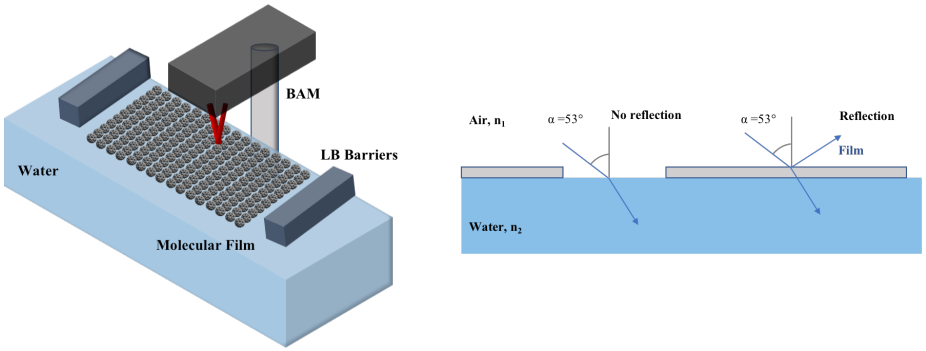

Figure 5.3: Scheme of the BAM used to monitor the molecular film floating on the subphase of LB trough. On the right the working principle of Brewster angle microscopy is shown for air-water interface.

In the early phase of this work molecules in solutions were dispersed onto the water subphase with conventional microlitre syringe spreading which in the best case scenario, spreads relatively large, millimetre diameter droplets [302]. These are large enough to create considerable surface undulations, leading to the loss of molecules inside the subphase [303, 304].

Each time a drop of solution was added, waves spread radially from the point where the drops touched the water surface. Through the BAM it was possible to observe the molecular clusters on the surface moving violently from side to side, colliding with other clusters. To overcome this issue and minimise the loss of molecules into the subphase, a deep study of the effect of different spreading methodology was performed.

In addition to the conventional syringe spreading, automatic dropler (KSV NIMA standard micro dropler) and electrospray ionisation (ESI) were tested and compared in order

to establish the best method for the molecular layer formation.

5.1.1 ESI spreading and Langmuir-Blodgett deposition

Electrospray ionisation spreading of a solution is an electric field driven technique. In this work, a homemade ESI system was realised, employing a high DC voltage generator (0.1 to 5 kV) to supply the large potential difference between the end of the syringe tip and a copper plate placed under the water subphase (figure 5.4). The potential formed an aerosol from the solution with a micron scale droplet size which was many orders of magnitude smaller than using conventional syringe spreading [305, 306].

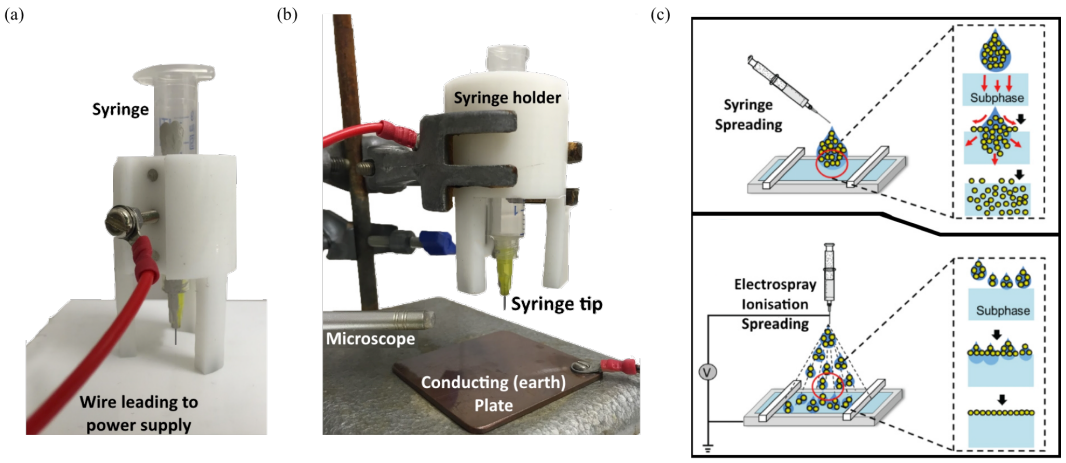

Figure 5.4: (a) ESI syringe and holder; (b) Homemade ESI setup with syringe and holder in a clamp. A digital USB endoscope was positioned at the very end of the syringe needle to monitor the solution aerosol. The copper plate was connected with the ground and placed under the water subphase during spreading and film formation; (c) Solution and subphase mixing during conventional syringe spreading; (d) Representation of ESI-spread droplets, showing the minimises mixing due to surface waving. (c, d) modified from [302].

During these experiments, for all but a few initial test isotherms, ESI spreading was the only way that the solution was spread on the water surface. The homemade ESI system setup consists of a plastic syringe (HSW 5ml Norm-Ject) secured in a plastic holder. The yellow syringe tip needles shown in figure 5.4.a and 5.4.b were 32 Gauge Precision tips manufactured by Adhesive Dispensing Ltd. Silver electrodag conductive coating was applied to the syringe all along its length, joining it electrically to the needle. This was required to connect the needle to the power supply using a screw fixed inside the plastic holder and acting as a locker for the plastic holder's syringe.

During experiments, a 5×5 cm^2 copper plate was grounded and placed under the water subphase avoiding any contact with the barrier.

The needle thickness was chosen carefully to avoid large droplet formation during the application of the electric field and so that the solution would only spread when a consid-

erable potential ($\sim$ 1 to 5 kV) was applied between the end of the needle and grounding plate.

The nature of the solvent, polar or non-polar, is central to whether the electrospray ionisation will occur or not.

Toluene, one of the most widely used solvents in molecular electronics, for example, is a weakly polar solvent, making it unsuitable for ESI spreading in its pure form due to its low coefficient of spreading ($6.8\text{mN}\,\text{m}^{-1}$) [43]. In contrast, water, ethanol and other highly polar solvents enable a high ESI rate at relatively low voltages. The magnitude and sign of the spreading coefficient determine the outcome of a droplet on the water surface. Positive coefficients usually mean spontaneous spreading, not dewetting when the drops get in contact with the water. In contrast, dewetting occurs for solvents with a negative spreading coefficient and inducing the solution to form droplets on the water surface and increases the probability of aggregation.

Some literature strategies suggested that the mixing of solvents in the solution (e.g. ethanol or methanol) could increase the spreading coefficient and, more importantly, make the solution more suitable for ESI than a single solvent solution.

For example, in this work, the addition of a small amount of methanol or ethanol in a ratio of 1:5 to the existing solutions in toluene resulted in spread repeatability, without flow variation over a long time ($\approx$ 1 hour). These efforts were moderately successful, ensuring a reproducible protocol for the spread rate of the solution on the subphase of an LB trough, as shown in the following figure.

During the experiments, the spread rate was controlled by a combination of the needle dimensions and polarity of the solution. Once both these parameters were optimised and fixed, the main factor which regulated the flow rate was the applied potential from the power supply, as shown in figure 5.5. As is possible to observe in the figure, a greater potential led to an increased flow rate. Furthermore, during the spreading of the solution, several different spray regimes were observed based on the DC voltage applied, e.g. fig.5.5. A potential of between 2.5 and 3 kV was typically applied, leading to a steady, single-jet spray which spread into a finer cone after some distance (fig.5.4.a). At higher potentials, the spray was much less stable, oscillating between the larger cone modes.

A UV light was used to highlight the solution's aerosol when it was particularly difficult to see on the microscope.

Spreading a solution of 0.5 ml, within the range (c) and (d) shown in figure 5.5, took

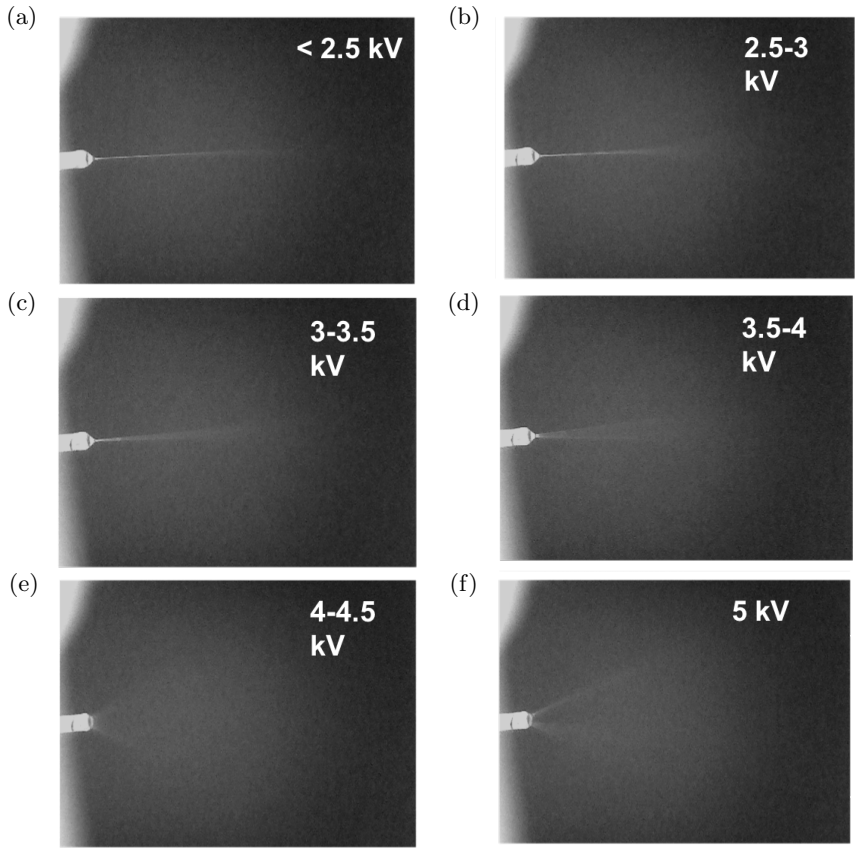

Figure 5.5: Electrospray ionisation (ESI) spray regimes for ethanol based stearic acid solution observed using a USB endoscope as a function of the different DC voltages applied between the needle and the copper plate. The needle is left-centre on each image. Single-jet mode (a-b), spreading cone (c-d) and multi-jet spray (e-f).

approximately 30 minutes. Similar trends for spray rates were observed in other studies [302] but with no specific efforts to determine spray rate.

Once optimised, ESI became the primary choice for solution spreading for the LB film formation. As shown in the next chapter, the reduced drop size due to ESI limited the likelihood of C_{60} molecules being lost to the aqueous subphase. Furthermore, repeatable spreading conditions and vastly lower surface ripples made ESI a preferable choice for C_{60} LB film spreading compared to conventional syringe spreading methods. In particular, it is possible to observe from fig.5.6 the differences among the three principle spreading methods (micro-syringe, automatic dropler and ESI). The different shapes of the resultant LB isotherms, reflecting the different agglomeration dynamics of the molecules during the compression due to different initial state created from the different spreading techniques.

Figure 5.6 displays a surface pressure-mean molecular area (MMA) isotherm of C_{60} solution for the three different spreading methods, showing a substantial difference between the conventional micro syringe spreading and the other two methods.

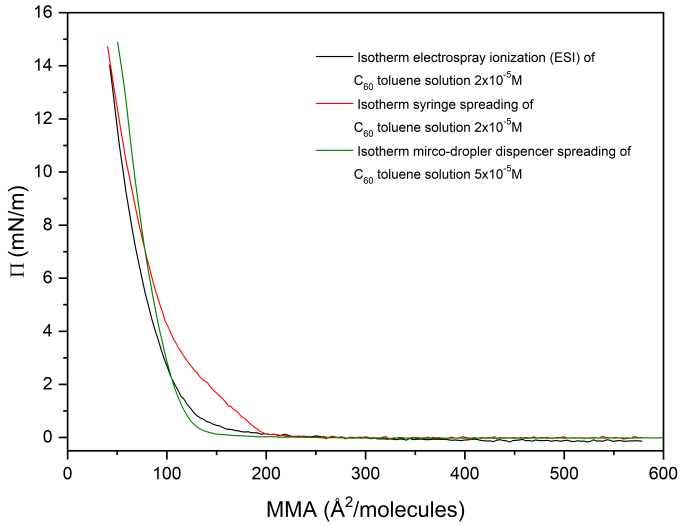

Figure 5.6: Comparison among three isotherm for a C_{60} solution in toluene obtained with the different spreading methods.

It is easy to note that conventional syringe presents a longer liquid phase during the compression and higher limiting area per molecule, extrapolated from the solid-like phase at $\Pi = 0$, compared to ESI or automatic micro-dropler. The reason for this particular difference in the liquid-like phase can be explained considering the reduced aggregation of molecules during the gas phase, which can be interpreted as a smaller liquid-like phase during the compression of the molecules, as shown in fig.5.6.

5.2 Template Stripped Gold (Au) preparation

SAMs and LB films reported here were grown on ultra-flat Au substrates prepared by modifying the template stripped (TS) protocol of *Whitesides and Pinkhassik* [307, 308]. In this work, a Si wafer (5 inches diameter) was cleaned in an ultra-sonication bath with acetone, methanol and isopropanol in series and processed with oxygen plasma for 5 minutes.

Once cleaned, a layer of 200 nm of evaporated Au (99.8%) was thermally grown onto the Si wafer surface. Subsequently, another carrier substrate (usually Si) was cut by a diamond tip scrubber in rectangles of 0.5×1 cm and glued onto the evaporated Au layer with Epotek 353nd epoxy adhesive to form Si/Glue/Au/Si sandwich structure. After 40 minutes curing at 150 °C, the ultra-flat TS gold was obtained by eliminating the bottom Si as displayed in fig.5.7.

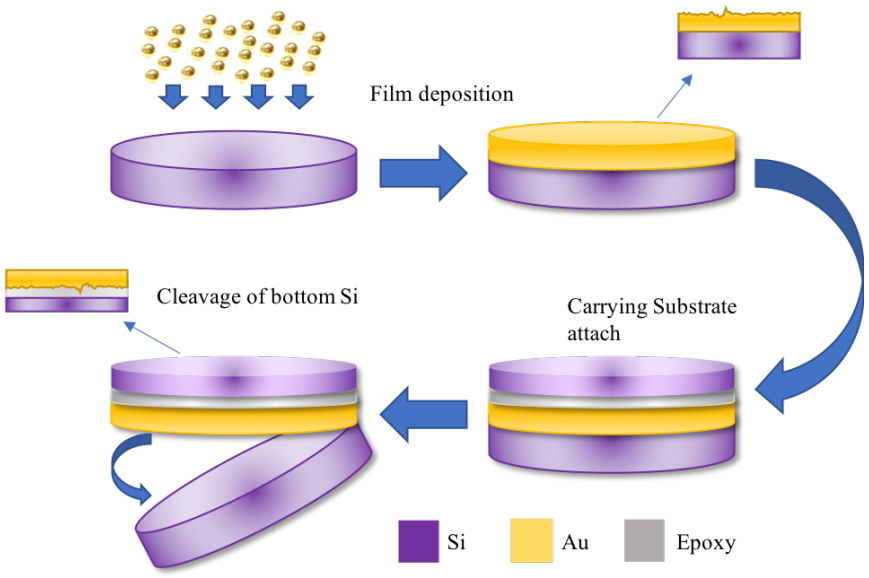

Figure 5.7: Au Template-stripping method for fabrication of atomically smooth gold surfaces. The two small insert represent the surface roughness of the Au film as-dept and after the mechanical cleavage of the bottom substrate.

The prepared Au was then scanned by AFM in 3-5 random spots as a quality test. Figure 5.8 shows one example of roughness and quality test for a set of prepared TS Au in a single terrace.

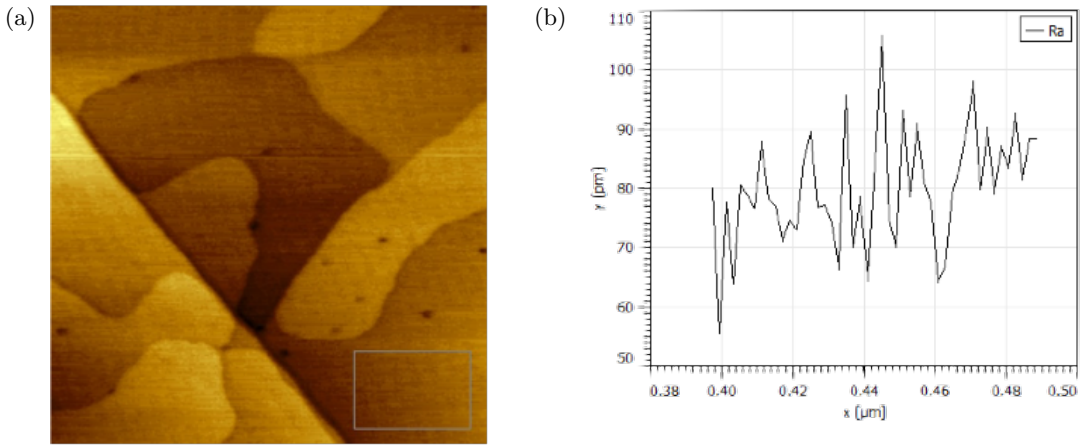

Figure 5.8: (a) Topography of ultra-flat Au obtained by template stripped method (scan area 500nm^2; (b) Average roughness calculated in the bottom right Au terrace of (a).

As is possible to observe in fig.5.8b, the average roughness of the Au terrace highlighted in fig.5.8a was calculated to be between 60 and 80 pm, and was never observed to be above 0.1 nm.

5.3 Quartz Crystal Microbalance (QCM) for SAMs characterisation

Quartz crystal microbalance (QCM) (a high sensitive mass measuring technique) was employed to monitor the quality of the SAMs.

In this work, the SAMs growth was monitored by a QCM system from OpenQCM Q-1, equipped with frequency and dissipation monitoring, with a gold electrode (5mm diameter, 10 MHz resonance frequency). The frequency of the crystal was measured before and after SAM growth.

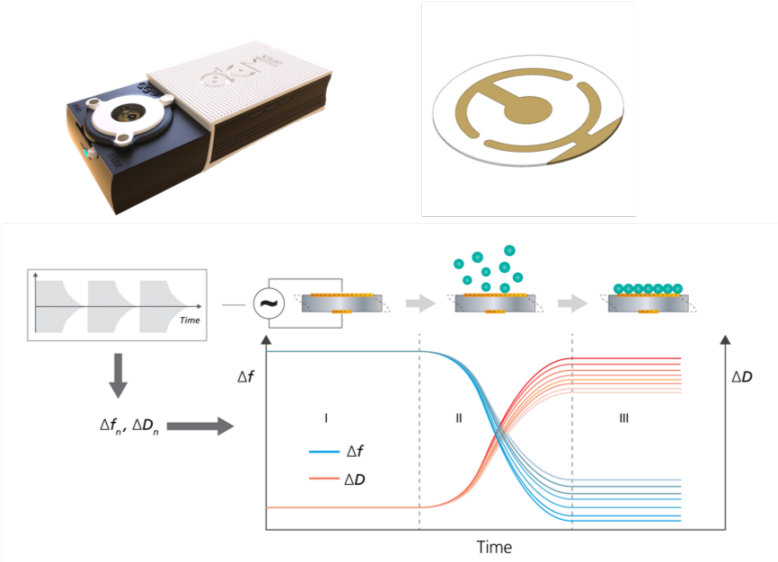

Figure 5.9: Picture of the QCM system from OpenQCM Q-1 used in this work to monitor the molecular SAMs growth. On the bottom, the working principle of QCM is illustrated. Images from [309].

The difference between these two frequencies, as illustrated in fig. 5.9, was proportional to the mass (or the area) of the molecules grown on the Au electrode of the Crystal through the Sauerbrey equation [310]:

$$A_{mol} = \frac{A_{el} \cdot MW}{(k \cdot \Delta f \cdot A_{cry} \cdot N_A)} \tag{5.1}$$

where A_{el} is the real electrode area, A_{cry} the area of the crystal, MW the molecular weight, N_A the Avogadro number, Δf is the frequency shift recorded before and after the growth of the film, and k is given by the equation:

$$k = \frac{\sqrt{\mu\rho}}{2f_0^2} \tag{5.2}$$

In equation 5.2, μ represents the shear modulus of quartz, ρ the quartz density and f_0 is the natural resonance frequency of the QCM crystal before the SAM growth. So using eq.5.1 was possible to obtain the coverage area of the molecular film from the frequency shift recorded.

New QCM crystals (5mm diameter, f_0= 10 MHz) were cleaned with acetone, methanol and isopropanol in series and cleaned with oxygen plasma. The crystal was then incubated in a vacuum oven at 50°C for solvent evaporation. The resonance frequency of the cleaned QCM was measured, and the relative occupancy area was calculated using the equations above.

This technique was employed for all the SAM samples to estimate the growth process's success (different for each molecular species) and prior to the electric and thermoelectric characterisation.

5.4 SPM setup and developing

A Bruker MultiMode 8^{TM} scanning probe microscope fitted to Nanoscope V controller unit was employed for SPM topography characterisation of the molecular ultra-thin film as well as their electrical and thermal transport and the thermoelectric properties. This system is based on a stationary tip that is held firmly by a cantilever holder. During the scan process, samples are moved beneath the tip using a piezo-actuator scanner tube. A "J-Vertical" scanner tube (AS-130V) was used for this work, allowing up to 125 × 125 µm scan range and 5 µm of vertical range. As displayed in figure 5.10b, the scanner tube movements in X, Y and Z directions are controlled by applying AC voltage on the piezoelectric cylinder.

Samples were fixed to a metal disc by carbon tape or electrodag and then magnetically attached to the top of the scanner tube. Figure 5.10 shows the actual system employed for the characterisation.

Following fig. 5.10a, the system can be divided in three major building blocks: the SPM head, the scanner tube and the base unit.

- The head, which is mounted on a stage allowing control of the X and Y position, containing the laser source ($\lambda = 670$ nm), the photodetector, an adjustable mirror and a set of knobs for a fine focus the laser beam in the centre of the detector (figure 5.10b);

- The scanner tube, which allows the motion in the Z direction through a motorised

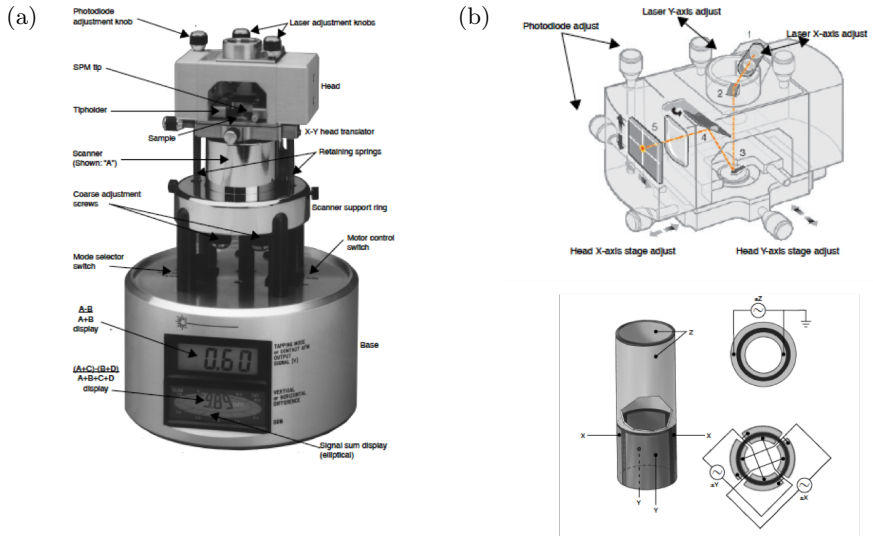

Figure 5.10: (a) Picture of the used SPM AFM Multimode 8™in its three main compartments: the AFM column including the head, the scanner tube and the base; (b) AFM head components: 670 nm laser source (1), mirror (2), cantilever (3), tilt mirror (4) and photodetector (5). The piezo-actuator scanner tube is shown at the bottom of (b). Image adapted from [134].

screw;

- The base unit, housing the microscope electronics and signal displays. A mode selector switch located on the top of the base unit allows switching between different SPM modes.

5.4.1 Contact Mode AFM

Contact mode is a quasi-static AFM operating mode where the probe is in direct contact between the tip apex and the sample surface, and the force acting between tip and sample is counterbalanced by the elastic force generated by the cantilever deflection.
In the context of this work, it was found that contact mode AFM did not give the best results for scanning topography of molecular ultra-thin film due to the high friction generated from the lateral deflection of the cantilever during the scanning operations. However, contact mode AFM was employed in this thesis for "nano-scratching". This process consists in the creation of a window with a defined area on the surface of the sample, sweeping away the molecules with the application of high set forces ($F = 15 - 40$ nN) using a soft probe Multi-75-G Budget Sensor, with a spring constant of $k \approx 3\ \mathrm{N\,m^{-1}}$ and resonant frequency of 75 kHz.
After scratching, the topography of the sample was again characterised using a less invasive intermittent contact AFM like Peak-Force mode. Nano-scratching was also conducted on a bare Au substrate under the same conditions to ensure no Au has scratched

away in the force range used. The height difference measured through the line profiles of the AFM images between the scratched and un-scratched parts then indicates the thickness of SAMs as shown in fig.5.11.

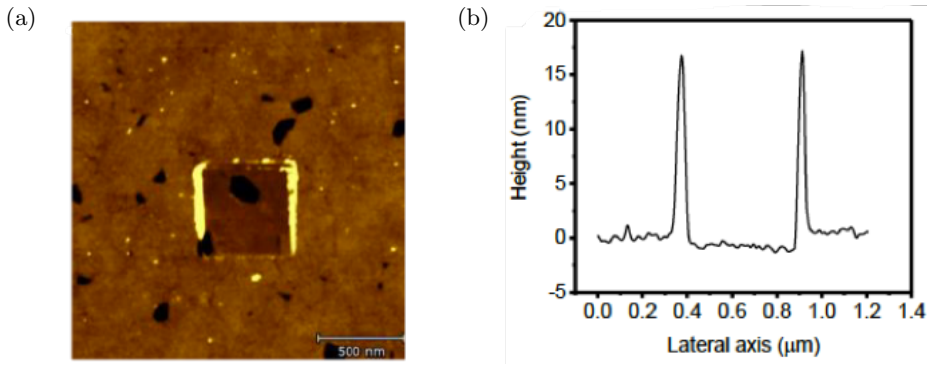

Figure 5.11: Nano-scratching example in a SAM of dodecanethiol (C12S). The opened window at the centre of the scan was obtained applying strong normal forces in a scan area of 500 nm^2, at high scan rate 2 Hz.

It is easy to observe from figure 5.11 that from this informal use of the AFM it is possible to not only confirm the presence of the molecular layer, and thus the eventual success of the growth process, but also obtain information on the uniformity, quality of the film and especially its thickness, as highlighted in the profile plot of the scratched window on the C12S SAMs (fig.5.11b). Nanoscratching was performed for all the molecular samples before performing electric, thermal and thermoelectric measurements.

Also, prior to the actual measurements, the numbers of molecules contacted by the AFM probe needed to be taken into account in order to compare the obtained results with literature values for single molecular junctions. For this reason, the numbers of junctions formed between the AFM probe and sample was estimated from the tip-sample contact radius, using the Hertzian approximation [143]:

$$r = \left(F \times R \times \frac{1}{Y}\right)^{\frac{1}{3}} \tag{5.3}$$

where r is the contact radius, F the applied force from the probe, R the radius of the probe and $\frac{1}{Y}$ is given by:

$$\frac{1}{Y} = \frac{3}{4} \times \left(\frac{1-\nu_1^2}{E_1} + \frac{1-\nu_2^2}{E_2}\right) \tag{5.4}$$

In this equation, $\nu_{1,2}$ are the Poisson ratio of the materials, E_1 and E_2 are the Young's Modulus for the probe ($\sim 10^{11}$Pa) and the molecular layer.

From equation 5.3 it was then possible to estimate the numbers of molecules simply by dividing the calculated contact area by the cross-sectional area of the molecules under investigation.

5.4.2 Conductive probe AFM CAFM

The conductive probe AFM (CAFM) employed for the electric and thermoelectric characterisation of the molecular ultra-thin film is a modified contact mode AFM. The bottom gold substrate of the molecular ultra-thin film was used as the source, and a soft Pt/Cr coated probe Multi75E from Budget Sensors with a spring constant of $k \approx 3$ $\mathrm{N\,m^{-1}}$ and resonant frequency of 75kHz was used as a drain.

During the scanning of the sample and the point measurements, the force between probe and molecule was controlled and kept at 2nN. At this force, the probe was able to penetrate through the water layer on the sample surface but not so strong as to damage or destroy the molecular thin film.

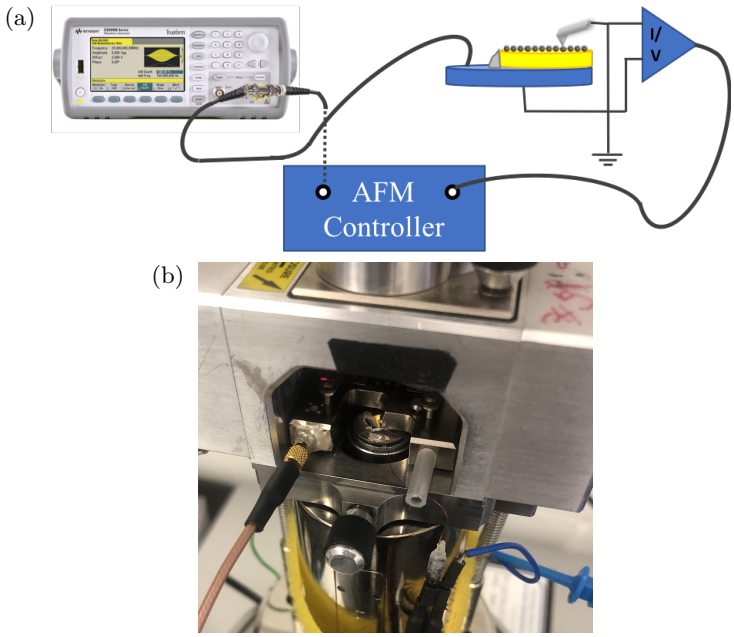

Figure 5.12: (a) Scheme of the employed CAFM system used to map the relative electrical conductance and study the electric transport of the molecular films. DC/AC voltage was supplied to the sample through a waveform generator. The current generated travels from the probe to an I/V converter and is then fed to the AFM controller's input channels; (b) picture of the modified AFM probe holder employed for the electrical measurements of molecular ultra-thin film. An electrical connection was made by drilling a little hole in the front of the probe holder and connecting it with its internal integrated electronics.

As shown in the scheme in fig.5.12a, the samples were fixed with electrodag onto a homemade electric stage consisting of a thin conductive wire welded onto a magnetic

disc with a connector at its end. An Agilent 33500B waveform generator supplied the voltage on the sample, and the current flowing from the sample to the probe, housed in a modified cantilever holder (fig.5.12b), was converted into voltage by a low noise I/V converter FEMTO DLPCA-200 with variable sensitivity from 10^3 to 10^{11} V/A. The converted electric signal from the drain and the input bias voltage were then fed into the AFM controller inputs to produce new channels representing the map of the samples' relative electrical conductance.

Operating in this way, it was then possible to acquire real-time topography and correlated current channel of the scanned areas.

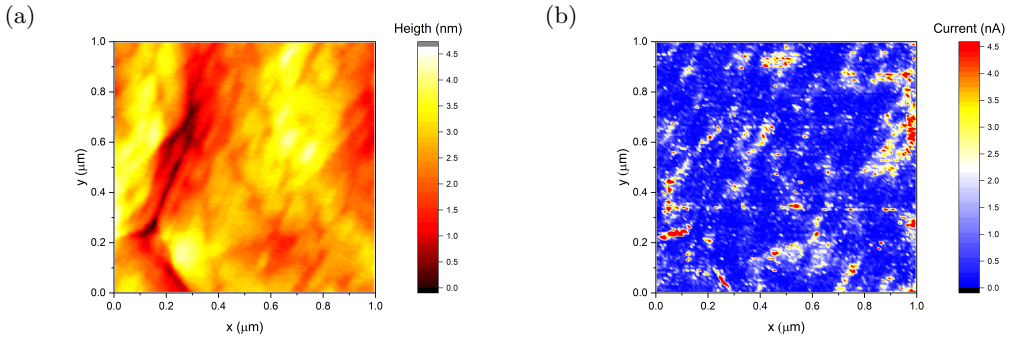

Figure 5.13: Example of electric map of a LB thin film of fullerene C_{60} acquired with CAFM with the simultaneous acquisition of topography (a) and current (b) maps.

The scan area of the two channels shown in figure 5.13 was acquired at constant bias voltage V_{DC}=1 V at a constant force of 2nN. The current maps showed a good resolution of the different areas of the scanned surface, which allowed the qualitative estimation of the relative electrical conductance of the particular features of the sample surface. However, this will not provide any further quantitative information on the electrical conductance value or on the electric transport.

For this reason, in addition to the mapping mode, CAFM was also used for the so-called "point measurements" to acquire I-V traces of the samples and obtain more information on the electric transport.

In this *modus operandi*, once the contact was established, the probe was fixed in a single point (0 nm^2) and a triangular shape AC bias voltage was supplied between the source and drain by the voltage generator (Agilent 33500B). The source to drain current was then acquired by a current pre-amplifier FEMTO DLPCA-200. The two output channel are displayed in fig.5.14.

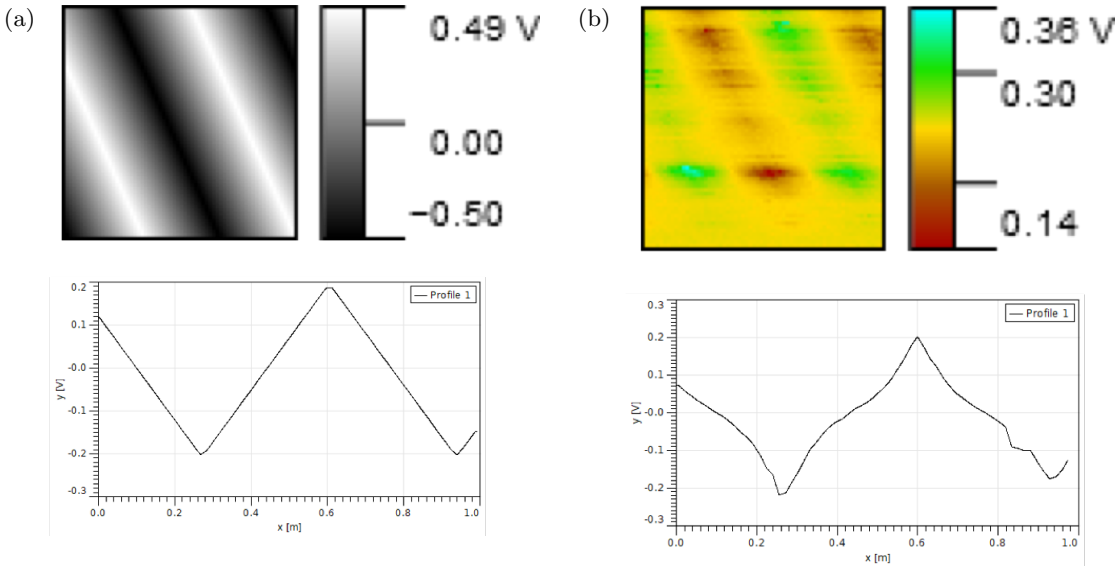

Figure 5.14: (a) Source voltage channel in single point AFM measurements with the relative AC bias voltage profile; (b) Pt probe drain current channel and current profile for CuTTP SAM on TS Au.

The obtained 2D "maps" from the single point measurements and relative to the input bias voltage and the current are shown in fig.5.14. However, since the probe is fixed in a single point without any motion, the maps need to be interpreted from a different perspective.

The easiest way to do this is to imagine the scan process as a continuous acquisition of I-V curves as a triangular wave of a certain amplitude sweeps forward and reverse. In a more rigorous way, each scan line in the maps represent a single sweep of triangular wave at a frequency $f = 2$Hz and its relative current (bottom fig.5.14a and 5.14b). With this methodology, it is then possible to acquire multiple I-V traces of the molecular film, ensuring statistical significance.In this work all the I-V traces and the electrical transport characterisation were performed using the technique described above.

5.4.3 Scanning Thermal Microscopy SThM setup

The SThM system was built on a Bruker Multimode head and Nanoscope III controller, as shown in fig.5.15. As explained in Chapter 3, the technique is based on contact mode AFM where a resistive AFM probe is self-heated and map the relative differences in the samples' thermal conductance.

The main setup consisted of:

- A Peltier plate below the sample to control the sample temperature;

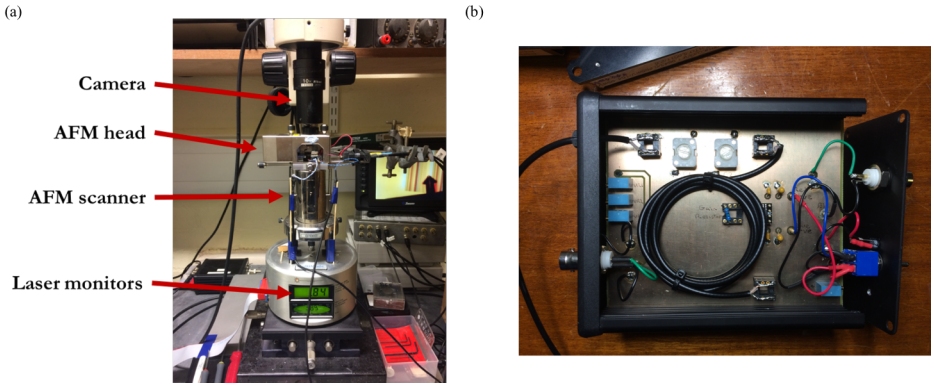

Figure 5.15: (a) Photo of the Bruker Multimode IIIa used for SThM measurements. The red arrows indicate the single section of the microscope; (b) Homemade Maxwell bridge used to monitor the variation of the thermal resistance of the self-heated probe.

- A temperature sensor reading this Peltier plate temperature (Pt resistor or thermistor) glued on the plate;
- A modified probe holder housing the resistive probe;
- A Maxwell bridge used to amplify and monitor the resistance variations of the probe during the scanning operations 5.15.b.

The Pd resistive probes used for this technique were manufactured by Kelvin Nanotechnology (KNT-1an).

The methodology employed for the probe heating was based on a combination of AC+DC bias. Here, the thermal probe represented one part of a balanced Maxwell electric bridge, with a 4 V_{AC} signal at 91 kHz frequency, provided by a precision wavefunction generator (Keithley instruments 3390), and used for resistance variations measurements which are then detected via a lock-in amplifier (Stanford research SR-830). The DC offset provides probe Joule self-heating, noting that a sudden rise of current can burn out the very delicate thermal probe.

The probe's electrical resistance was recorded as a function of applied voltage and temperature. In this case, the bias voltage loaded on the probe could be considered fixed since the actual changes in the thermal resistance of the probe were tiny, as experienced during the measurements.

When balancing the Maxwell bridge, a small AC voltage of $0.1V_{pp}$ was initially applied on the probe to minimise the self-heating. During scanning operations, a $4V_{pp}$ was then applied to the probe, ensuring a high signal, combined with the DC offset (usually $2-3V_{DC}$ for the KNT-1an resistive probes).

Once the contact with the sample was established, the SThM channel represents an

electric signal (Voltage, V) which is strictly correlated with the resistance of the probe. Intuitively, looking at figure 5.16, the different contrast in the SThM maps is due to the relative difference in the thermal conductance of the different sample area but, with proper calibration, it is also possible to convert the SThM voltage maps into temperature maps.

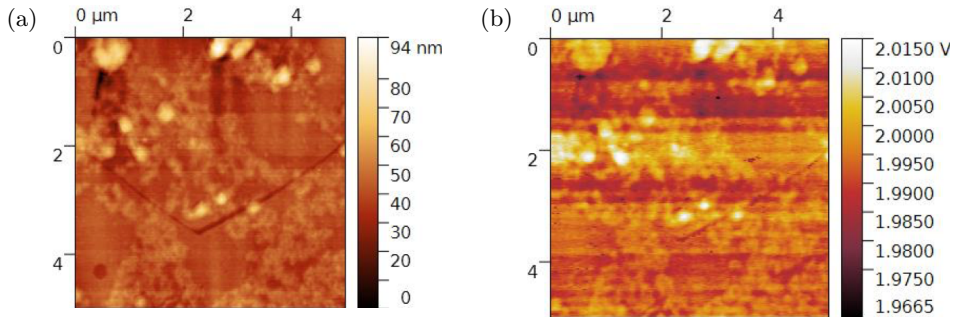

Figure 5.16: SThM scan of LB film of H2-TPP.(a) Topography and (b) thermal channel, here expressed in V before be converted in variation of thermal resistance of the AFM thermal probe.

For quantitative thermal transport analysis of the molecular ultra-thin film, the electrical SThM signal in V, which is proportional to the resistance of the self-heated probe, was recorded as the probe engaged and retracted from the sample surface in a fixed point.

As described in Section 3.2.4, the SThM signal is directly proportional to the heater's excess temperature with respect to the ambient temperature. When the probe approached the surface and solid-solid contact was established, a sharp drop of voltage was observed as a direct consequence of the increase of the heat transport through the R_x channel of fig. 5.18, the thermal resistance at the interface between the probe and the surface of the sample. During the retraction, the adhesion forces required an increased negative force to snap from the contact. Hence the approach and retract curves do not follow the same path, creating hysteresis. In the air, adhesion forces are higher mainly due to the liquid meniscus [311], and the increased hysteresis in the air could be clearly observed during approach and retracting of the probe during the force spectroscopy.

The voltage was recorded immediately prior to probe-sample contact V_{nc} then again in contact V_c as shown in fig.5.17. From these two voltages, it was then possible extract the SThM response dV/V where $dV/V = \frac{V_{nc}-V_c}{V_{nc}}$.

Once dV/V was collected for multiple points per sample, the values were converted into thermal resistance/conductace, using a model developed by *Spiece et al.* [311] based on the heat conduction through different channel (probe, heater, air, interface) as

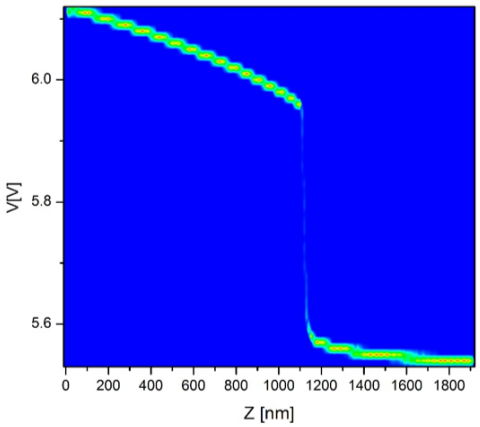

Figure 5.17: Example of SThM force spectroscopy point measurement

displayed in fig.5.18. The heat produced from the heater Q at the position l is exchanged through the 3 channels shown in figure 5.18: Q_B through the cantilever resistance R_B, Q_{air} through the surrounding air resistance R_{air}, and Q_S through the air gap resistance R_p and through the contact resistance R_x [312]. Compared to the simple model used to describe the dependency of the thermal resistance on the temperature and the thermal conductance of the samples (Eq.3.9), the thermal resistance in this thesis was obtained using the multiparametric equation based on the above modellisation of the heat transfer, keeping in account also the probe dimension, the heat capacity of each component of the thermal resistances network and the air contribution.

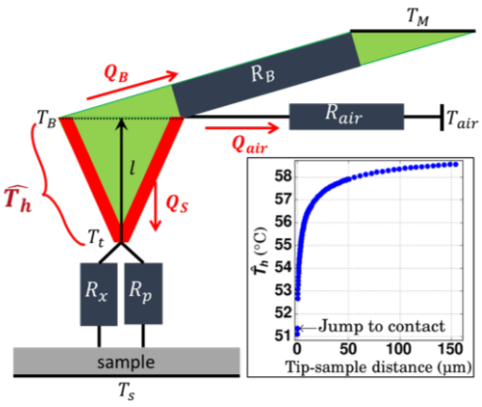

Figure 5.18: Scheme of the active components' thermal resistance with the heater. In the insert is shown the measured probe temperature as a function of tip-sample surface distance. Image from [312].

5.4.4 Thermoelectric force microscopy ThEFM

A large portion of this work was spent developing a reliable and reproducible methodology to measure the thermal power of molecular thin films and characterise their thermoelectric properties. Because of the necessity to measure the thermal voltage with nanometric resolution, CAFM was chosen as the base technique to develop our system. Among the other techniques, CAFM has been largely used as a tool for thermoelectric characterisation of similar samples and ensures precise control of the applied normal force with a resolution of few tens of nm, enabling the simultaneous measurement of clusters of $10 \sim 10^3$ molecules. However, CAFM measures the current flowing between the source (Au substrate) and the drain (CAFM probe) when a bias voltage is applied in the formed vertical junction. Here, however, what was needed was the thermal voltage, stimulated by the Seebeck effect. Principle differences to CAFM are: the inclusion of a heater to establish a temperature difference across the molecular junction and a voltage pre-amplifier instead of the current pre-amplifier, usually employed in electric transport characterisation.

The heater module shown in figure 5.19 was made starting from a Peltier heater (9×9mm, 2.9 W and manufactured by RS Components Ltd) where a copper plate was fixed with epoxy thermal adhesive on the heated surface. The purpose of this layer was to contact the Peltier heater with the common ground of the microscope. A layer of mica was sandwiched between the copper foil in contact with the Peltier device surface, and a thin copper plate used to contact the molecular thin film electrically. The mica, in this case, acted as an electrical insulator and ensured a good transmission of the heat. The samples were then fixed on the heater module with electrodag and, with the help of a multimeter the electric contact was checked.

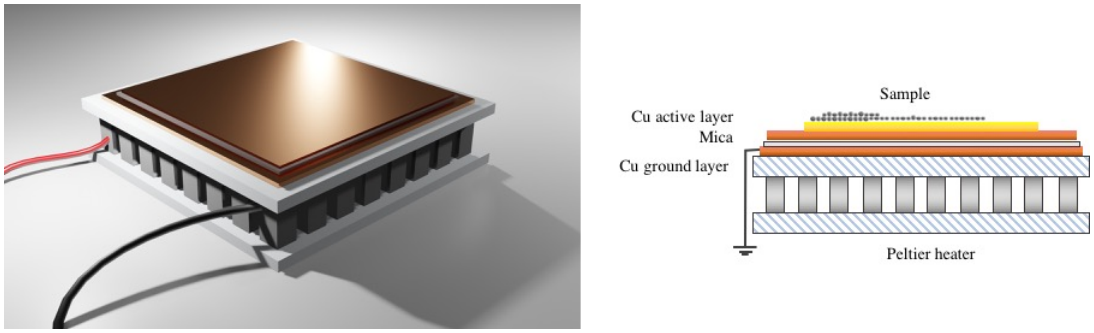

Figure 5.19: 3D representation of the heater module used for the thermoelectric measurements. On the side view picture, the different sections of the device are shown.

The Peltier device was driven by DC voltage using a wavefunction generator (Agilent 33500B) amplified using a 10X voltage amplifier. After calibration of the temperature on the applied voltage on the heater, 4 different voltage setpoint were selected: -20V, 0V, 6V, 16V, which corresponded to $T = 18, 22, 25, 30$°C respectively on the top surface. The temperature of the sample during measurement was calibrated by a Cu-Ni thermocouple on the bare gold before the molecule deposition, and the temperature of the probe was calibrated using the SThM KNT probe (KNT-SThM-1an, Windsor Scientific), which has a similar radius of curvature ($\sim$ 50 nm) as the conductive probe, but has a 45 nm thick palladium thermistor at the end of the probe for temperature sensing.

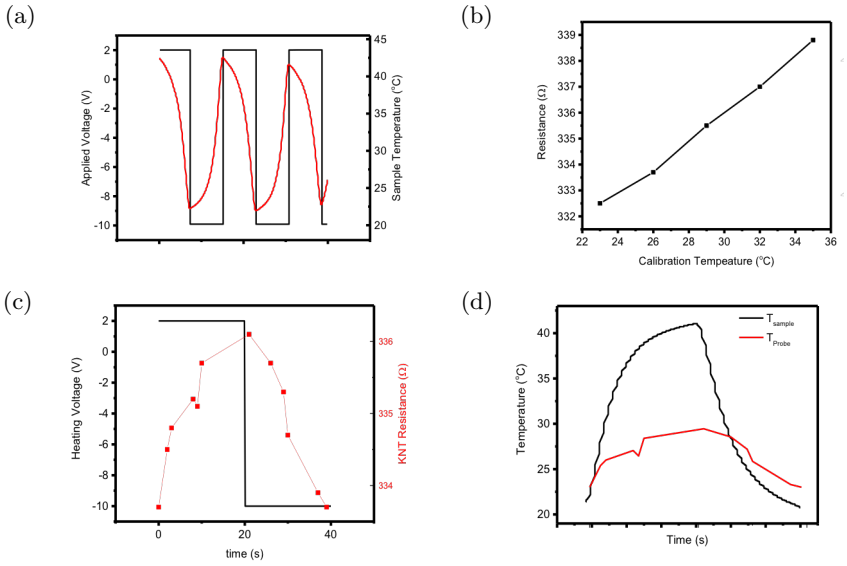

Figure 5.20: (a)Temperature of a bare TS Au surface as a function of the voltage applied to the heater module during different cycles of heating/cooling; (b) Temperature dependency of KNT-1an probe resistance calculated during the calibration process; (c) Variation of thermal resistance of KNT probe used to monitor the temperature of the probe during the junction formation vs heating device voltage. (d) probe temperature vs sample temperature at 1 cycle of heating/cooling.

The voltage difference between sample and probe due to the thermoelectric effect was collected using a high-impedance differential pre-amplifier (SR 550, Stanford Research Systems) at zero bias. The thermoelectric signal was then fed into a low-pass filter (SR 650 Stanford Research Systems) in order to cut off the 50 Hz electric noise, and the filtered signal was acquired by the Nanoscope controller in real-time. Fig.5.21 shows the electric scheme of the setup.

During common scan operations, the thermal voltage was extracted using the *0 current mode*, where V_{th} is directly measured and the Seebeck coefficient of the junction will be given by $S_j = S_{Au} - {}^{\Delta V_{th}}/_{\Delta T}$. A thermally and electrically conductive probe

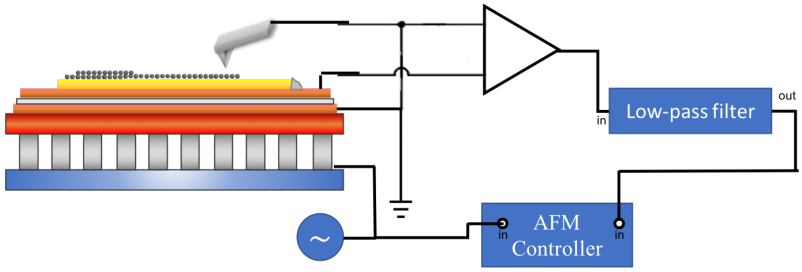

Figure 5.21: Electric diagram of the ThEFM. Probe, sample and heater are connected to the same ground and the thermovoltage is fed into a voltage amplifier and then into the AFM controller.

(Pt coated probe, 50 nm curvature radius) isolated from probe holder was used both as the top electrode and thermal sink during the measurements. The probe was engaged applying a force set point of 2 nN for all the measurements.

In fig.5.22 are shown the two typical ThAFM channel acquired in real-time during the scan. As for the CAFM measurements, the scans were performed in *single point spectroscopy*, in which the probe was fixed in a single point, and the four selected temperatures difference ΔT in the junction were established by applying DC voltage to the heater device (figure 5.22a). On the other channel, the filtered and amplified thermal voltage signal was acquired per each correspondent temperature, as displayed in fig.5.22b.

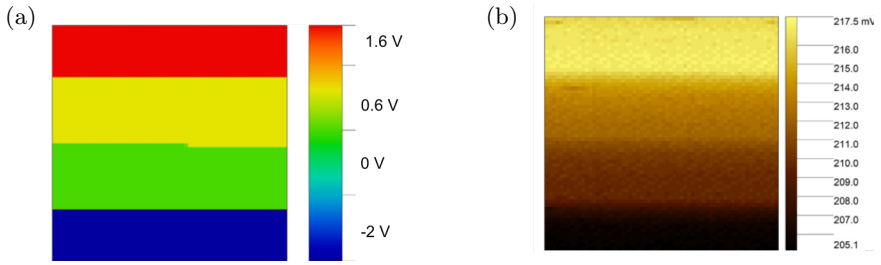

Figure 5.22: ThEFM channels recorded during the sweeping of the temperature difference ΔT : (a) Voltage applied to the Peltier heater. The different voltages -2V, 0V, 0.6V, 1.6V corresponded to $\Delta T = -2, 2, 5, 7$°C; (b) Differential thermal voltage at 0 current V_{th}. The different bands correspond to the four different ΔT.

After multiple acquisitions in different point per sample, the XYZ data from the AFM images were then extracted, and Z values of the thermoelectric channels were converted into a matrix and used for the analysis.

5.4.5 PF-CAFM

As seen in the previous section, CAFM represents a powerful tool to characterise the electric and thermoelectric properties of molecular assembly. However, the high lateral forces in contact mode AFM, in which CAFM is based, usually results in damage to the fragile molecular layers. Indeed, what was noticed during the early stage measurements and testing of the ThEFM, was the rapid degradation of the electric signal due to wearing away of the Pt coating on the electric probe apex and, at the same time, damage to the molecular layer itself after several scans (as shown in figure 5.23). This was attributed to the strong friction and lateral forces always present when contact mode AFM is used.

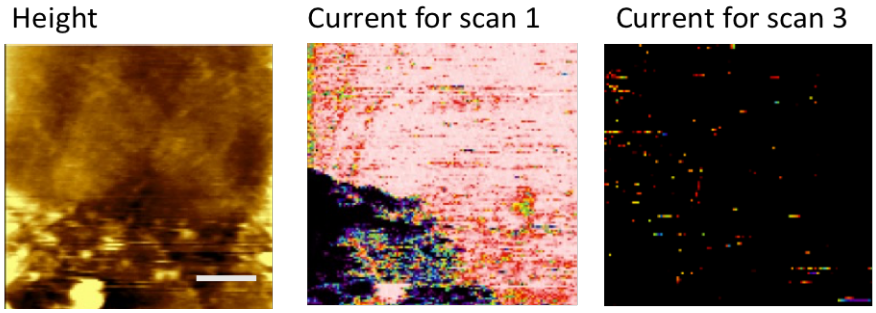

Figure 5.23: Example of CAFM contact mode mapping drawback. The current intensity drops significantly after several scan cycles due to the vanishing of the Pt coating layer of the electric AFM probe caused by the strong lateral forces presents during the scan operations. Scale bar 200 nm.

To overcome these damaging interactions, a less invasive AFM mode is required. Among the different intermittent contact AFM modes, two primary modes were considered: Tapping Mode AFM and Peak Force (PF) AFM. However, Tapping mode AFM was discarded because its high-frequency oscillations (300 kHz) are not comparable with the thermoelectric time scales, too fast to establish a reliable electrical and TE contact with the molecular assembly.

PF mode, as already shown in Section 3.2.3, is a high speed (0.5 – 4 kHz), small distance (20-150 nm) force spectroscopy based on the rapid collection of point by point force curves. The peak interaction force of each force curve is used as the imaging feedback signal; this enables pN-levels of probe-sample interaction measured directly by the deflection of the cantilever. In this way, thanks to the low normal force and effective elimination of lateral forces during scanning make the PF-AFM mode especially suitable for our aim. In addition, PF-AFM mode typically offers better spatial resolution than contact mode for mapping soft materials due to the inherently smaller contact area between probe and sample at low forces and allows the simultaneous acquisition of the

nanomechanical properties of the sample.

The first challenge was synchronising the current signal coming from the cantilever with the PF tapping driving frequency. In this case, the PF z motion was fed into a homemade signal access box that allowed the output of different signals from the Bruker multimode VIII to be accessed and the possibility to fed different input signals back to the microscope itself. The output signal extracted were used as sync to the lock-in amplifier (Stanford research SR-830) for the CAFM current signal. The drain current from the probe was the input of the lock-in, and the output was the CAFM signal synchronised with the cantilever's motion. The electric scheme of the developed setup is shown in fig.5.24.

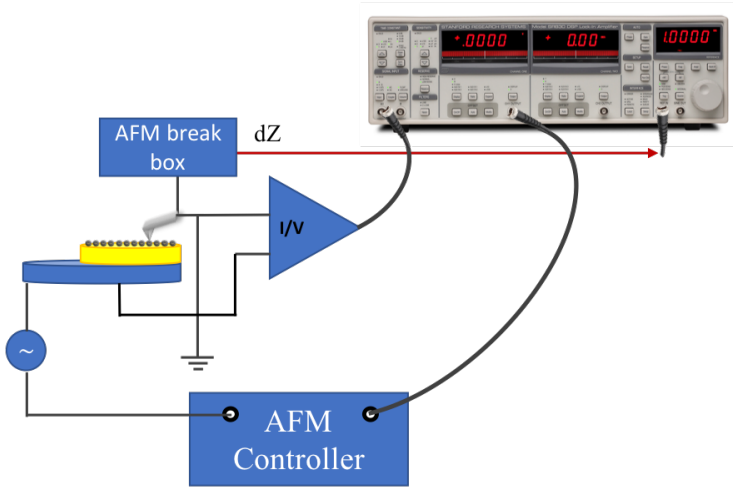

Figure 5.24: Scheme of PF-AFM combined with CAFM.

In an analogous way to the contact mode CAFM, and as displayed in the figure above, both applied bias voltage and current output from the lock-in were fed in the AFM controller for real-time acquisition. To validate the methodology and confirm the working principle, the CAFM electric signal and the deflection error of the cantilever were checked using an oscilloscope in order to monitor the synchronisation of the two signals (figure 5.25).

As is possible observe in fig.5.25, thanks to the sync of the CAFM signal with the z motion of the cantilever, the current will only appear during the contact between tip and sample and not elsewhere.

The PF-CAFM approach was employed in the present work for all the electric maps of the molecular ultra-thin film. At the same time, the conventional contact mode CAFM was still used for all the electric transport characterisation of the samples through the

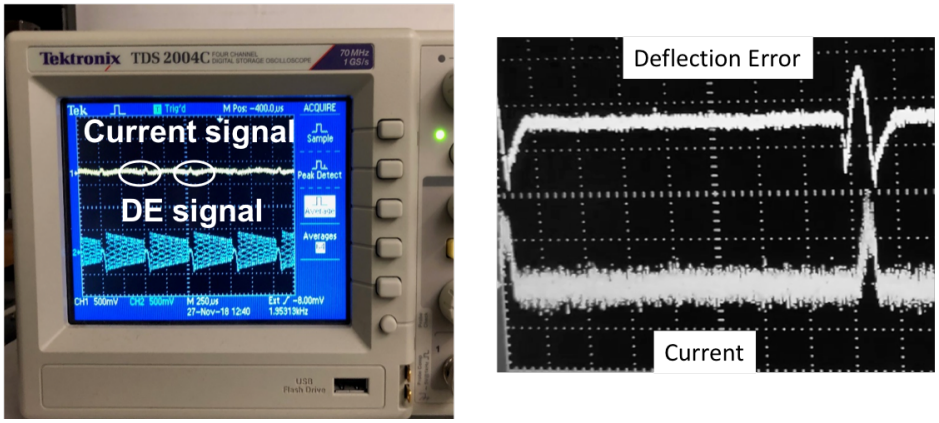

Figure 5.25: Picture of the oscilloscope display, showing the effective working principle of the realised set-up. The right figure shows a detail of a single cycle of approaching/retracting the AFM tip's deflection error in PF mode vs measured current of BPT SAMs, where the current only appears when the contact tip-surface is established.

point measurements.Indeed, while PF-CAFM provides multiple advantages in terms of mapping the electric and nanomechanical properties of the samples, this technique does not allow a precise control of the normal forces but just the peak interaction force, as can be seen in figure 5.25 (right side) showing a dynamical force range during the time interval in which probe and sample are in contact.

This issue is particularly problematic for the determination of the number of molecules contacted by the probe during the interaction, as determined by eq.5.3. Figure 5.26 shows an example of current mapping using PF-CAFM and contact mode CAFM for a SAM of biphenylthiol (BPT).

This example is quite crucial since it is possible to observe one of the biggest advantages of using PF-CAFM, which consists of the simultaneous acquisition of multiphysics properties (here the electrical and nanomechanical properties of the molecular layers 5.26.b and 5.26.c). Here, the nanomechanical properties are represented by the PF-AFM adhesion channel, which provides more important information (probe-molecule interaction, presence of solvent) than the topography alone.

Both the electrical conductance maps in fig.5.26.b and 5.26.e, obtained with the two methods, shows different features with the same resolution; however, as expected, the IV heat maps of BPT from contact mode and peak force mode shown in fig.5.26.f, show that the current intensity obtained from contact mode CAFM was typically 5 times higher than the one obtained using the peak force mode due to the oscillation of the sample-probe interaction time. For this reason, conventional mode CAFM was employed for the characterisation of the electric transport in the molecular junction while the elec-

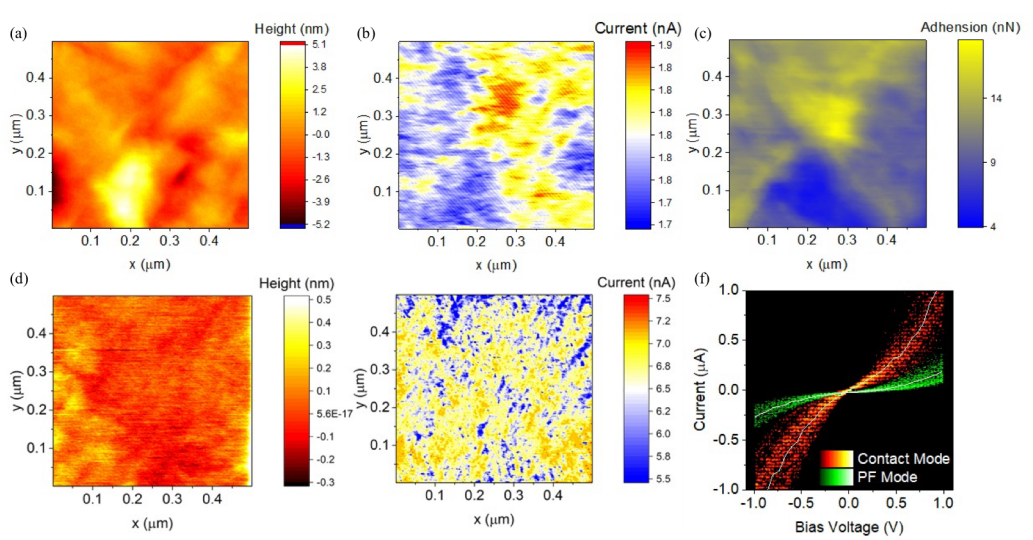

Figure 5.26: (a-c) Topography (a), current (b) and adhesion map (c) of BPT SAMs on Au substrate by peak force mode CAFM; (d, e) Topography and current map of BPT SAMs acquired using contact mode CAFM; (f) I-V traces of BPT SAM obtained from contact and peak force mode.

tric mapping of the samples was performed with PF-CAFM.

5.4.6 PF-ThEFM

As the same strongly damaging effect arising from the lateral forces between probe and samples will also be present during the thermoelectric measurements, the PF-CAFM setup was further tested for its efficiency in performing thermal power measurements of the molecular thin film samples. In fact, as can be seen in fig.5.27, during the CAFM scanning for thermal power measurements, the thermal voltage signal rapidly degraded in analogy with the current measurements described in the previous section.

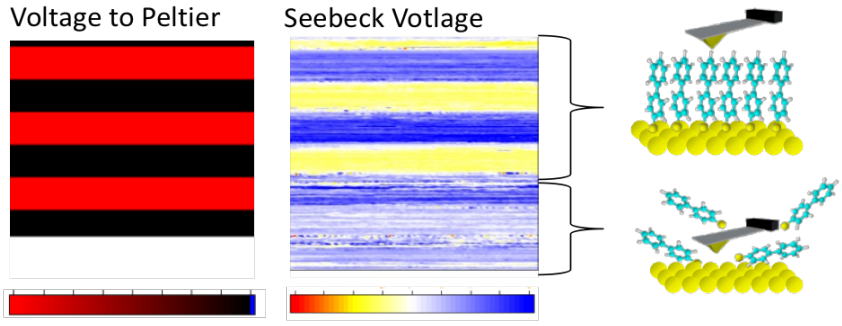

Figure 5.27: Degradation of the thermoelectric signal channel after different cycles of heating/cooling of the heater device. On the right side a cartoon representing the effect of the lateral forces on the molecular layer is shown.

Here the main challenge for measuring the thermal voltage in peak force "0 current"

mode was mainly due to the timescales' incompatibility; in this case, the rate of voltage change was much slower than the peak force frequency. This difference makes triggering the signal difficult with a lock-in amplifier. Therefore, *non-0 current* mode was used in where the thermal current I_{th}, flowing in the molecular junction due to the Seebeck effect, is monitored instead of the thermal voltage V_{th}.

Since, as has been shown, the current only appears in the time window the probe-sample contact is formed, therefore the frequency of the current signal directly corresponds to the peak-force frequency (Figure 5.25).

A Pt coated probe was also used in this case as the top electrode, and the sample temperature was controlled by the heater device described above. A triangular wave with a frequency of 2Hz and 2mV$_{pp}$ was applied constantly between tip and sample in order to stimulate an electric current. A current pre-amplifier (SR 556, SRS) was used to amplify the small current signal between sample and tip and then fed into the lock-in amplifier (SR830, SRS). Also, in this case, the Z motion signal of the piezo in the microscope was used as the reference signal for the lock-in amplifier and the modulated current at different temperatures was returned to the microscope controller for the collection, as shown in fig.5.28.

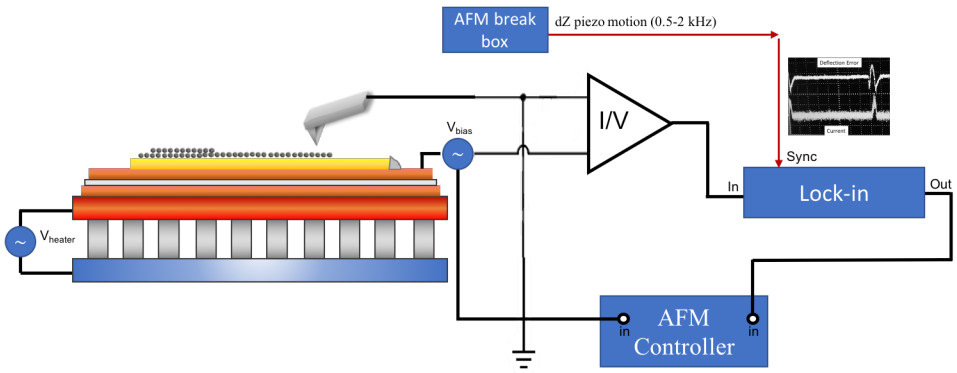

Figure 5.28: Scheme of the PF-CAFM setup for thermoelectric characterisation. The z motion of the cantilever was extracted using a homemade signal access box and used as a reference signal for the lock-in amplifier. The syncronised thermalvoltage was then fed as input into the AFM controller.

In this particular mode of measurements, the thermal power S was calculate from the excess of the total current flowing in the junction due the additional thermal current arising from the thermoelectric effect when a difference of temperature was applied between sample and probe. Following the formalism used for Eq.2.7, the thermal power

was derived starting from the measured thermal current:

$$I_{th} = I_{el} - GS\Delta T \tag{5.5}$$

$$\frac{I_{th}}{I_{el}} = 1 - \frac{GS\Delta T}{I_{el}} \tag{5.6}$$

where G is the electrical conductance of the molecular layer, ΔT is the difference of temperature and S the Seebeck coefficient. The current I_{el} represents the current flowing in the junction due the small triangular AC bias applied.

$$I_{el} = GV_{bias} \tag{5.7}$$

Combining Eq.5.6 with 5.7,

$$\frac{I_{th}}{I_{el}} = 1 - \frac{S\Delta T}{V_{bias}} \tag{5.8}$$

$$S = \frac{\left(1 - \frac{I_{th}}{I_{el}}\right) * V_{bias}}{\Delta T} \tag{5.9}$$

In this way, S is derived only from known parameters since when $\Delta T = 0$, I_{el} is the measured current; the thermal current I_{th} is measured when $\Delta T \neq 0$. G is the conductance of the molecules, and V_{bias} the bias voltage between sample and probe.
Figure 5.29 shows an example of I_{el} and I_{th} for a SAM of Octanethiols (OT) acquired at $\Delta T = 0$K and 14 K using PF-CAFM.

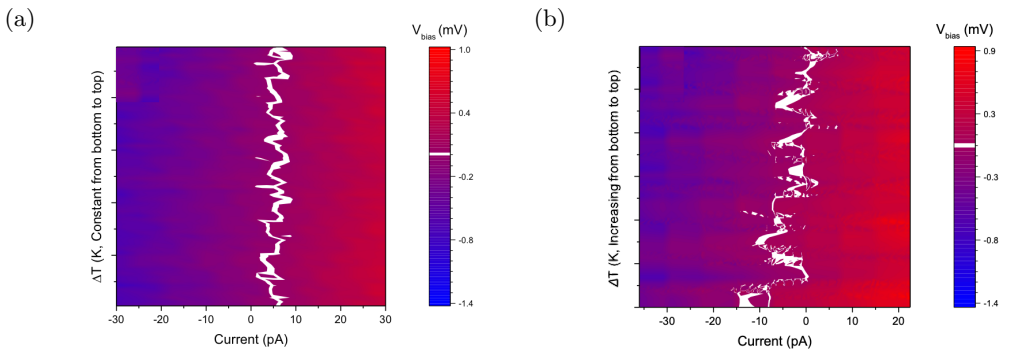

Figure 5.29: Plot of voltage vs current at constant (a) and increasing (b) temperature in PF-CAFM for Octanethiols SAM. The white line represents the thermal current at 0 bias.

In fig.5.29a it is possible to observe no significant changes in the fluctuation of the current measured without applying voltage on the heater device. But when the tem-

perature started to increase (from bottom to top in fig.5.29b), a shift in the current at zero bias can be observed due to the "extra" thermal current I_{th}. A typical Seebeck mapping in PF *non-0 current* mode is shown in fig.5.30 for a OtT SAM grown on TS Au.

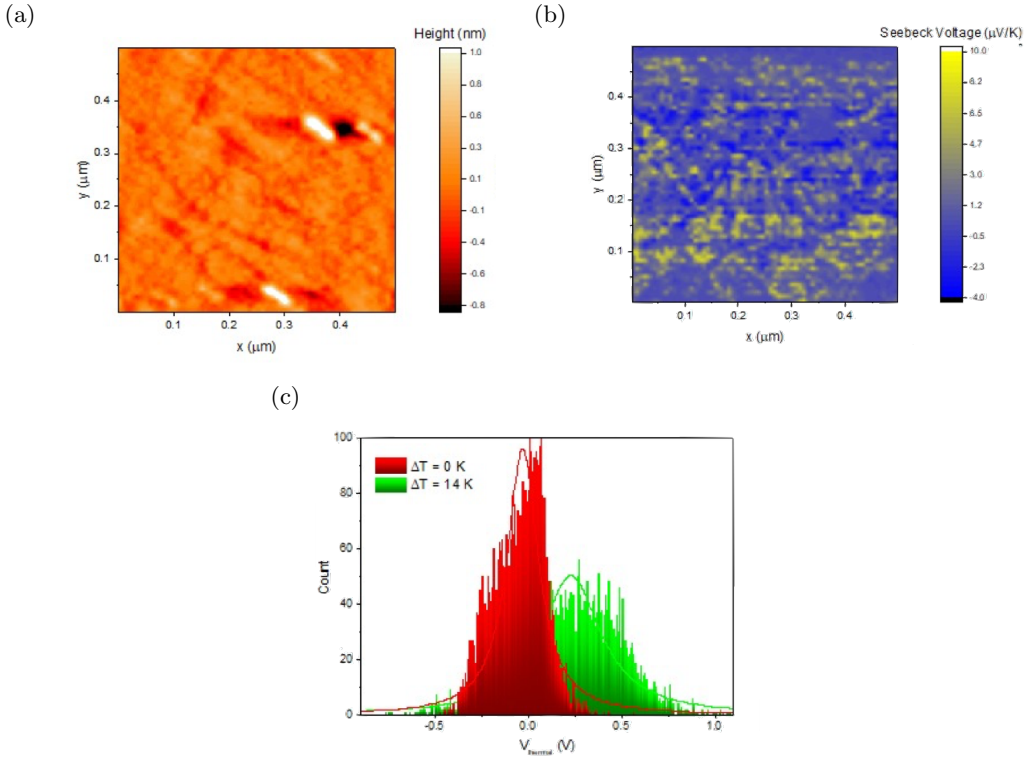

Figure 5.30: Mapping of Seebeck voltage of OT SAM (500 nm^2 using PF-CAFM. (a) Topography of OT SAMs measured in PF mode; (b) Overlapped Seebeck map of (a) derived from two current maps at 1 mV bias, $\Delta T = 0$ K and 14 K; (c) statistical distribution of Seebeck voltage in the two overlapped Seebeck maps.

Figure 5.30b shows the superposition of two thermoelectric maps for the Octanethiol SAM for two different temperature differences. It is easy to observe how the contrast in the map changes suddenly when a difference of temperature $\Delta T = 14$K was established, as further reported in fig.5.30c and giving further proof of the reliability of the measurement setup. The Seebeck maps were obtained starting from two current maps of an OT sample at the same area (500 × 500) nm, at two different temperatures ($\Delta T = 0$K and 14 K), applying a triangular bias voltage of ±1mV. The data was then transferred in matrix form and processed with the equation 5.9 in order to convert the single-pixel XYZ data onto thermal power or S. The Seebeck map was thus obtained by collecting the change of these two matrices (in percentage).

The methodology described was used as a proof of concept for a new alternative to

characterise the thermoelectric properties of SAMs and molecular thin film. The results and the comparison of the electric transport and the thermoelectric characterisation measured by both conventional CAFM and PF-CAFM of alkanethiols and π molecule containing phenyl rings SAMs will be shown in the next chapter.

5.4.7 Graphene coated probe for CAFM measurements

As seen in the literature review chapter, one of the biggest challenges of integrating self-assembled molecules in device fabrication was the short circuit from filament formation during the top electrode evaporation, and the most efficient way to solve this problem recently was using graphene as the interlayer junction for the electronic devices [161, 231]. A graphene coated probe for SPM measurements would provide an efficient test-bed to understand the role of graphene electrodes in molecular junctions.
The graphene coating process has been explored and developed by different techniques, from direct CVD grown of graphene on the probe [236, 313–315] to wet transfer of graphene on the probe [235] or even by dipping the probe into liquid phase reduced graphene oxide solution [316]. However, all these solutions create significant problems linked to the coating yield, resolution, undesired effect from the polymer residues during the transfer process, and complicated procedure, which limits the application of these coating processes.
Here Langmuir-Blodgett film deposition was used for the coating of the probe with graphene.

Graphene flakes dispersion in dimethylformamide (DMF) (Sigma-Aldrich, 0.2 mg/ml, 1-3 layers) were evenly dispensed by a microsyringe ($\sim$ 15 µL per droplet) onto the LB trough filled with DI water sub-phase. Optimum conditions were found for 200 µL of solution compressed at 5 mm/min formed a densely packed graphene film floating on water surface with a layer thickness in the range of 3 - 6 nm.
Figure 5.31 shows the LB isotherm curve obtained for the graphene solution dispersed on the LB trough using the parameter listed above. The dipping surface pressure was in the range of 8 - 10 mN/m, when the solid-like phase was established equivalent to a "close-packed" film of 2D flakes of non-uniform lateral dimensions. Furthermore, the BAM images reported in fig.5.31, shows the evolution of the graphene LB layer density during the different phases, corresponding to the highlighted points in the LB isotherm.

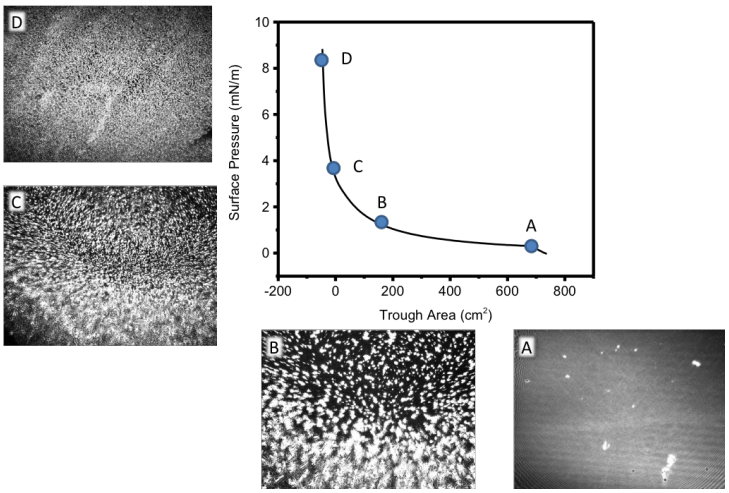

Figure 5.31: 200 µL graphene dispersion LB isotherm on water surface with corresponded Brewster angle microscope (BAM) images acquired at different points during the compression cycle. (A) Gas-like phase; (B-C) liquid extended phase; (D) solid like phase.

A series of Pt/Cr coated AFM probe (Multi-75E, Bruker) was fixed on a silicon wafer with carbon tape and dipped in the compressed film using the Langmuir-Schaefer (LS) technique. The coated probe was then placed in a vacuum oven (10^{-2} mBar, 80 °C) overnight to aid solvent evaporation.

Figure 5.32 shows the scanning electron microscopy images of the Gr coated electric probes after the process in the vacuum oven.

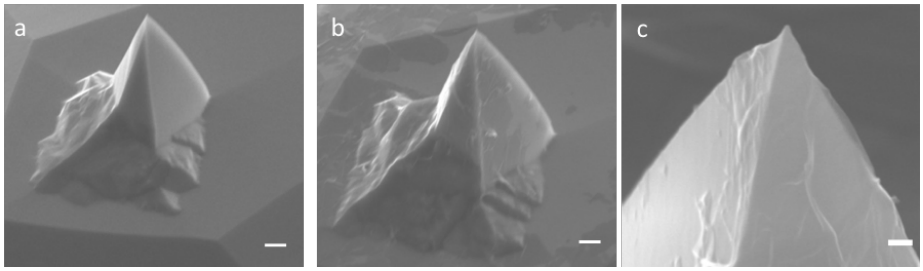

Figure 5.32: SEM images of: (a) conductive AFM probe (scale bar 1 µm); (b) conductive AFM probe coated with LB graphene film (scale bar 1 µm); (c) particular of (b) (scale bar 100 nm).

The probes' electrical lifetime and stability over several measuring cycles were initially tested with CAFM electric measurements. Probes were tested and studied by collecting a series of I-V curves of a SAM of BPT by a Pt/Cr coated probe with and without the graphene coating as shown in fig.5.33, where the red I-V traces were measured using a brand new probe and the green curves were measured by the same probe but after 3 cycles of imaging (500 nm x 500 nm, 1 Hz scan rate and 5 nN force).

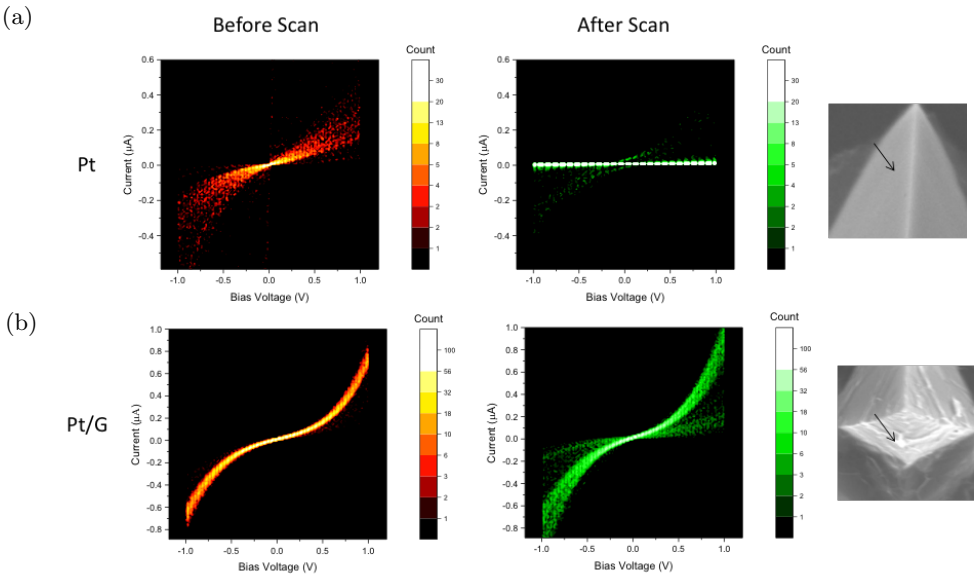

Figure 5.33: I-V statistics counter maps for BPT measured by a Pt probe and a graphene coated Pt probe (Pt/Gr) before and after 3 cycles of image scanning ($500x500$ nm, 5 nN in contact mode), and the corresponding SEM image of the probe after scanning

From the I-V traces obtained using Pt coated probes, it is evident that after few measurements, the acquired current density relative to the molecular junction of BPT significantly dropped, caused by the wearing of the metal from the probe during the scanning process, as observed in SEM, where the black arrow highlights the place where the metal coating was vanished. In contrast, from figure 5.33b, no significant current drop after image scanning for the graphene coated probe is observed. The SEM image in the insert in fig.5.33b further suggest that graphene remained on the top of the probe after the scanning operation, protecting the probe from metal wear (black arrow region).

One biggest concern when using graphene coated probes is the possibility of decreased topography resolution due to the additional graphene layer. In this work, we imaged an OPE2 coated gold surface to test the resolution of a series of measurements as shown in figure 5.34.

Surprising, a good resolution for both topography and electric maps up to 500 nm × 500 nm was obtained.

For the image with 300 nm x 300 nm scan size, the image started to be slightly undefined, even though 300 nm scanning size, in our experience, was also the detection limit of a Multi-75 E probe without graphene coating. In any case, even at this scan size, a high current resolution has been obtained, confirming, for our satisfaction, that the image resolution was not sacrificed due to the additional LB graphene layer.

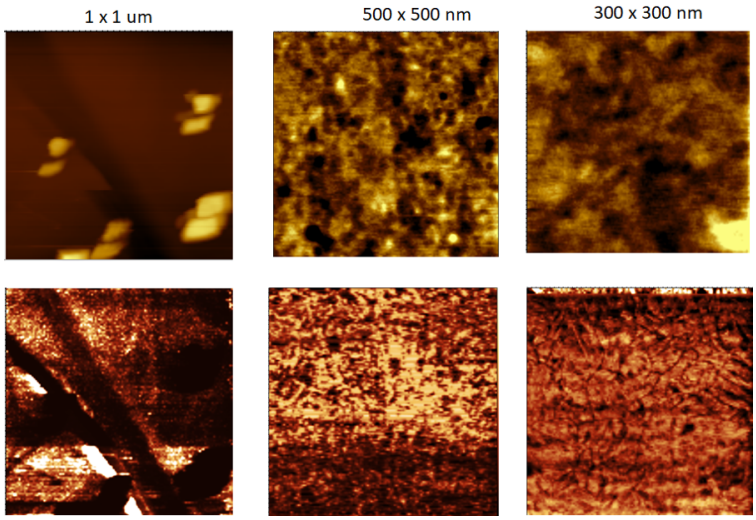

Figure 5.34: Series of CAFM scan fot resolution test of graphene coated probe. Topography (top) and current maps (bottom line) of OPE2 SAMs on Au substrate acquired by contact mode CAFM using graphene coated probe. Scanning size is 1 µm^2, 500 nm^2 and 300nm^2.

Chapter 6

Experimental Results

This chapter presents all the experimental results related to the electric transport and thermoelectric characterisation of molecular ultra-thin films. The first part is mainly focused on the characterisation of simple and well known molecular SAM systems like n-alkylthiols (C[n]S) and Biphenylthiol (BPT) in order to test the different equipment reliability, reproducibility and stability of measurements. The other sections will treat the characterisation of the electric and thermoelectric properties of some particular molecular systems such as Fullerene C_{60} and Zinc thetraphenyl porphyrin (ZnTPP). The results for different preparation techniques were compared, with attention to the enhancements of thermal power, adopting strategies already largely used in the literature.

First studies were made on the electric transport and thermoelectric characterisation n alkanethiols and BPT SAMs, investigating different AFM technique as well as different AFM probes in order to establish the validity of the measurements.

Sample quality and thicknesses were checked using Quartz Crystal Microbalance (QCM) and by nanoscratch method (see Sec.5.4.1). The electric characterisation was performed by acquiring I-V traces from the different samples by mean CAFM, following the methodology described in Sec.5.4.2. The multiple I-V traces (usually 1000-5000 I-V curves per sample) were used to determine the different electric transport characteristics of the SAMs and ultra-thin films.

6.1 Alkythiols and BPT SAMs

Three different saturated wires with increasing lengths formed from n-Alkyl-thiolate (C6S, C8S, C12S) and a conjugated wire formed from Biphenylthiol (BPT) were chosen for the SAMs formation and the comparison of the electric properties. The SAMs of n-alkylthiols were prepared by dispersing the molecules in ethanol (99.9%), forming a 100 µM concentrated solution. The obtained solutions were deoxygenated for 10 min using nitrogen bubbling.
BPT SAMs were formed by dissolving BPT molecules in toluene (99.9% HPLC level), forming a 10 µM solution and deoxygenated for 10 minutes by nitrogen bubbling.
The TS-Au was immersed into the solutions straight after the deoxygenation and incubated for 24 hours in a nitrogen atmosphere.
After SAMs growth, the samples were rinsed five times with fresh ethanol (for BPT, samples were rinsed initially with toluene followed by ethanol washing) to eliminate any physisorbed molecules or residuals. The samples were then dried with nitrogen for a minute and incubated in a vacuum oven (10^{-2} mbar) overnight at 35 °C to evaporate any solvent residual on the samples.

The four SAMs' growth was monitored using a QCM, with a gold electrode (2.5 mm diameter, $\sim$ 10 kHz), whose frequency was measured before and after SAM growth. The QCM electrode was cleaned following the procedure described in Sec.5.3 and the occupation area per molecule was estimated using eq. 5.1. Figure 6.1 shows the measured frequencies for the QCM resonator system before and after the SAMs growth onto the QCM electrode for the 4 studied SAMs.
Assuming 100% surface coverage, the frequency shift $\Delta f = f_0 - f_{SAM}$ measured before and after the molecules growth was 43.2, 45.4, 73.3 and 61.5 Hz for C6S, C8S, C12S and BPT SAMs respectively, corresponding to an occupation area per single molecule on the Au substrate of 22.9, 24.1, 20.7 and 22.6 Å^2, which is comparable with literature values obtained by reductive desorption [317] and theoretical calculations [318].

As expected, the occupation area of C12S was smaller than C6S and C8S due to the long tail of the molecules, which increases the inter-molecule hydrophobic interaction and enhances the packing density of the SAM [55, 56]. However, the lower occupation area of BPT compared with C8S (similar length) was not expected as phenyl rings should occupy a larger space than an alkyl-unit. This effect was attributed to the more closely

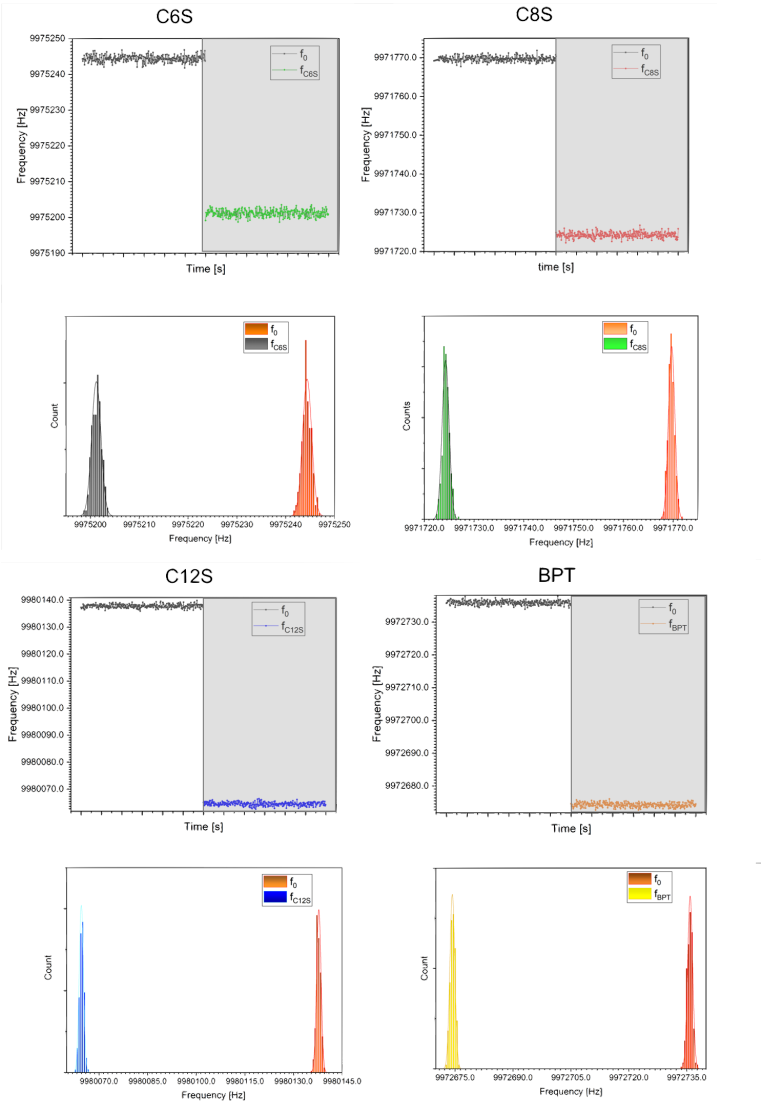

Figure 6.1: QCM frequencies measured for 5 min and frequency distributions before and after (shaded area) SAMs growth of the 4 molecules Hexanethiol C6S, Octanethiol C8S, Dodecanethiol C12S and Biphenylthiol BPT onto the QCM Au electrode.

packed structure of BPT arising from the π-π interaction between the phenyl rings [319]. SAM quality was characterised by AFM measurements of the average roughness of the sample. For C6S, C8S and C12S SAMs, the average roughness of the samples measured by AFM was < 70 pm, which is inside the range of the measurement fluctuation of the AFM instrument, which means the SAMs were arranged in a highly uniform manner. For BPT SAMs, the measured average roughness was ~ 1.5 Å^2. This higher value recorder for BPT compared with the n-alkylthiolates might be due to the higher conformational degree of freedom of BPT SAMs due to intermolecular interactions.

SAM heights were measured by nano-scratching scanning a small area of a SAM repeatedly in contact mode at high force load (30 nN), followed by a larger area scan at low normal force (2 nN). For all samples, the SAM thicknesses were in the expected range

	f_0 (Hz)	f_{SAM} (Hz)	Δf (Hz)	Δm (ng m^{-2})	Occ. area/mol (Å^2)
C6S	9975244.3	9975201.1	43.2	$1.14 \cdot 10^6$	22.9
C8S	9971769.7	9971724.3	45.4	1.2	24.1
C12S	9980137.8	9980064.5	73.3	1.63	20.7
BPT	9972735.8	9972674.3	61.5	1.37	22.6

Table 6.1: QCM frequencies, derivated mass and occupation area per molecule for the four molecules used for the SAMs growth.

corresponding to the molecular lengths (0.7 to 1.5 nm), indicating that the molecules were "standing up" on the sample surface with tilting angles of about 20° to 75° in good agreement with the measured QCM values of the occupational area per molecule. In all cases, the sample's averaged roughness was smaller than 15% of the SAM thickness, with low pin-holes (> 10 nm) density or physisorbed clusters on top of the SAMs.

6.1.1 I-Vs characteristics and electric transport characterisation

The electric characteristics of the 4 SAMs were investigated by CAFM using both Pt and Graphene coated AFM probes. In addition, in order to compare the results obtained with different methods, the electric properties of the SAMs were also characterised employing the PF-CAFM setup introduced in Section 5.4.5.

Firstly, AFM topography maps were acquired to check film quality and select an area on the SAM surface for investigation. Once the area was picked up, the I-V traces were obtained using CAFM in "single point spectroscopy", fixing the CAFM conductive Pt probe in the selected area, sweeping the bias voltage and collect the current flowing through the junctions.

The junction's current signal was collected by applying a triangular wave bias voltage from -1 to 1 V between the AFM probe and the sample and using a current amplifier with selectable sensitivity. The triangular bias voltage had a frequency of 2 Hz, ensuring two I-V traces per AFM scan line. In this way, by increasing the number of scan lines, it was possible to increase the numbers of I-V traces collected per second and thus increasing the statistics on the collected data.

The I-V curves were acquired in 5 different spots on the SAMs surface and, per each point, 5 cycles of single-point measurements were performed so, keeping the number of scan lines between 128 and 256 lines/second, this ensured an acquisition of 6000 to 13000 I-V traces per each sample.

In fig.6.2 the I-V trace histograms for the 3 sets of n-alkylthiols (C6S, C8S and C12S)

collected with CAFM using a Pt probe (20 nm radius, 75 kHz res. freq.) with fixed normal force applied of 2 nN are shown, including the average current extrapolated from the histograms.

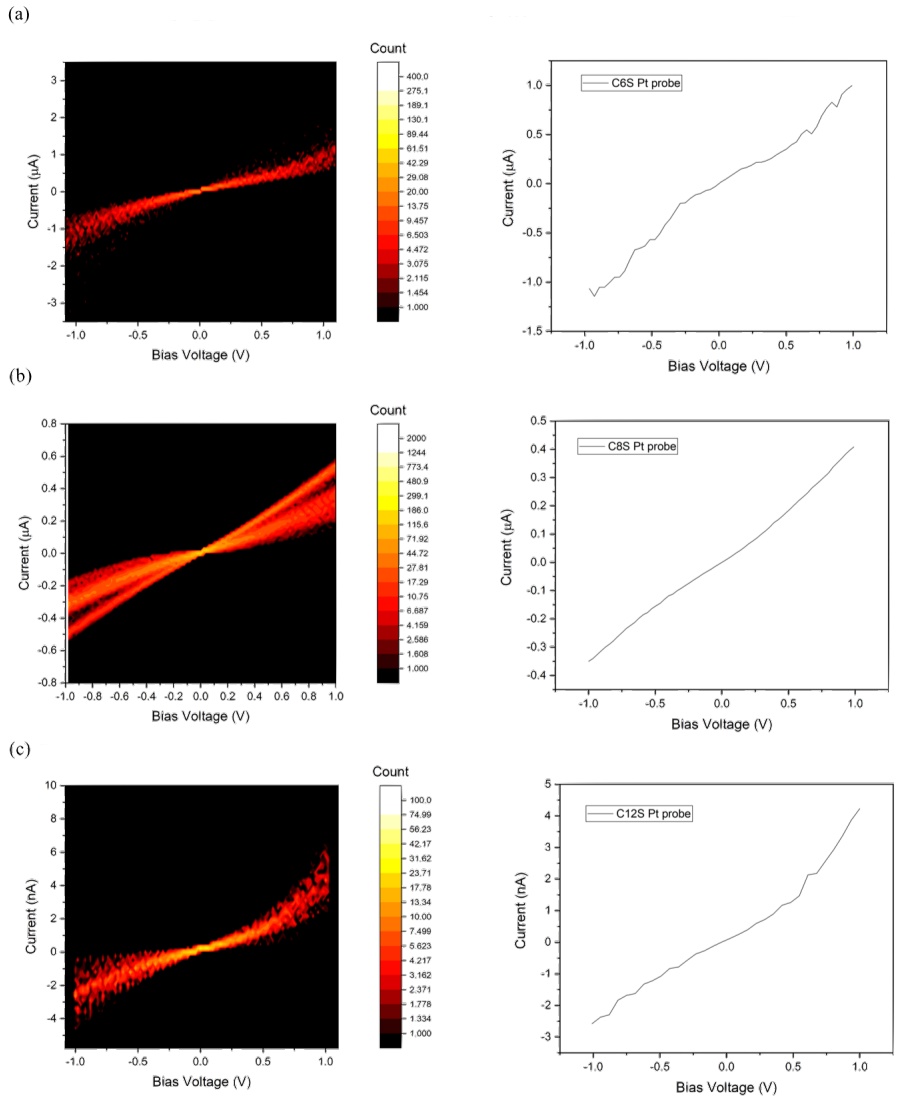

Figure 6.2: I-V traces histograms constructed from 6000 consecutive acquisition in different points of the (a) hexanethiol (C6S), (b) octanethiol (C8S) and (c) dodecanethiol (C12S). The I(V) average curve obtained from the I-V 2D counter maps are shown per each alkanethiol based SAM.

The I-V histograms show linear responses for the shorter alkyl thiolate SAMs, evolving in a typical semiconductor I-V shape for C12S and a decrease in the films' conductivity with the increasing length of the alkyl-chains.

The evolution of the I-V characteristics is to attribute either to the decrease in the HOMO-LUMO bandgap due to the addition of CH_2 units, and to the quality of SAMs, which is not only dependent on the thiol-Au coupling but also depends on the inter-

molecular interaction between the tails (VdW or hydrophobic forces). In fact, even for the same HOMO-LUMO gap, the strength of these interactions determines the geometry of molecules stand on the surface (tilt angle, uniformity etc.) and the coupling with the electrodes Γ, which broadens or sharpens the transmission curve. This is clearer to observe in the differential conductance $^{dI}/_{dV}$ histograms and suggests a tunnelling transport of the electrons through the junctions [320].

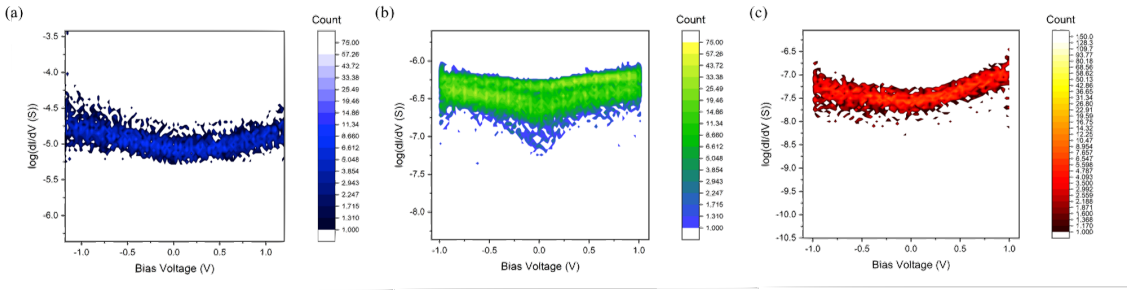

Figure 6.3: Conductance histograms for the 3 alkythiol SAMs: (a) C6S; (b) C8S and (c) C12S, calculated from the I-V traces acquired with CAFM single point measurements.

The values of the electrical conductance found for the three alkanethiol SAMs by the $^{dI}/_{dV}$ histograms in fig.6.3 was $(1.02\pm0.37)\cdot10^{-5}$S, $(3.34\pm0.52)\cdot10^{-7}$S, $(2.63\pm0.36)\cdot10^{-8}$S respectively for C6S, C8S and C12S SAMs. The uncertainties on the conductance values were calculated by the standard deviation of the distribution of G at near 0 bias.
The current attenuation factor β for alkylthiol SAMs was calculated from the equation:

$$G = G_0 e^{-\beta d} \tag{6.1}$$

Fitting the natural logarithm of the electrical conductance against the film thickness the β decay factor was found to be 9.1 ± 1.2 nm^{-1} as shown in fig.6.4, in good agreement with the typical values found in literature [179, 236, 321].

It is easy to observe that the data show a linear dependency with the thickness of the SAMs when the natural logarithm of the conductance is plotted against the molecular length, suggesting an exponential decay of the conductance and confirming the hypothesis of coherent tunneling transport of the electrons across the SAM junctions.
Following the same procedure for the (n)-alkyl thiols SAMs, the electric transport for Biphenyl thiol SAM was studied by contact mode CAFM. In fig.6.5 are shown the I-V traces histogram measured directly with the CAFM point measurement with the average I-V curve obtained from the traces.

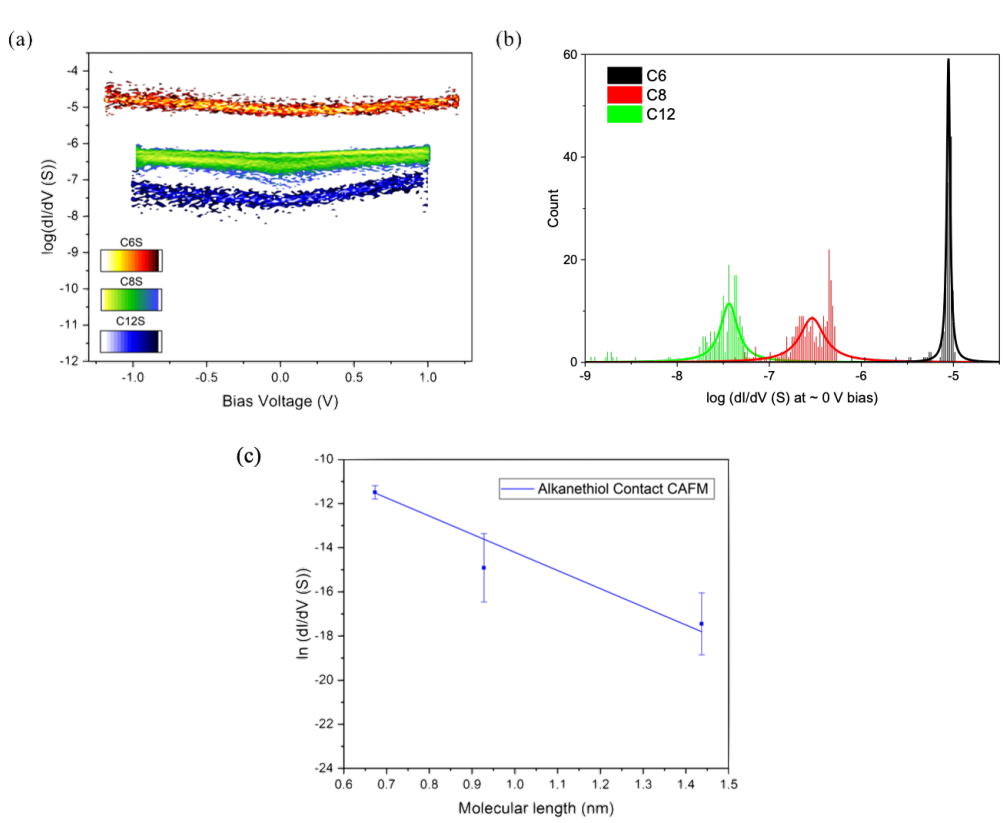

Figure 6.4: (a) Comparison of electrical conductance G calculated from the CAFM measurements; (b) Statistical histograms of measured conductance of C6, C8 and C12 thiol at near 0 bias; (c) Plot of tunnelling decay β coefficient of alkyl thiolate SAMs measured by contact mode CAFM point with Pt coated AFM probe.

I-V shows a semiconducting behaviour for the electric transport with a typical S shape of the current response. The total electrical conductance measured at zero bias voltage for BPT SAM was $(5.42 \pm 2.31) \cdot 10^{-7}$S, which results similar to the conductance measured of C8S SAMs.

As expected, the conductance measured for the four films produces higher conductances than the measured single molecules equivalents in literature because of the collective effect of the series of molecular junctions contacted with the AFM conductive probe during the measurements. Indeed, as introduced in the previous Chapter, the CAFM probe (radius $\sim$ 20nm) is big enough to contact 100-500 molecules at the same time, giving the enhancement of the electric current flowing in the junction. The amount of junctions between probe and sample were estimated from the tip-sample contact radius, via Equations 5.3 and 5.4, assuming E_1 and E_2 the Young's Modulus for probe ($\sim$ 100 GPa) and SAMs ($\sim 0.5-1$ GPa for alkyl thiolates, 9 GPa for BPT) [320, 322, 323]. The

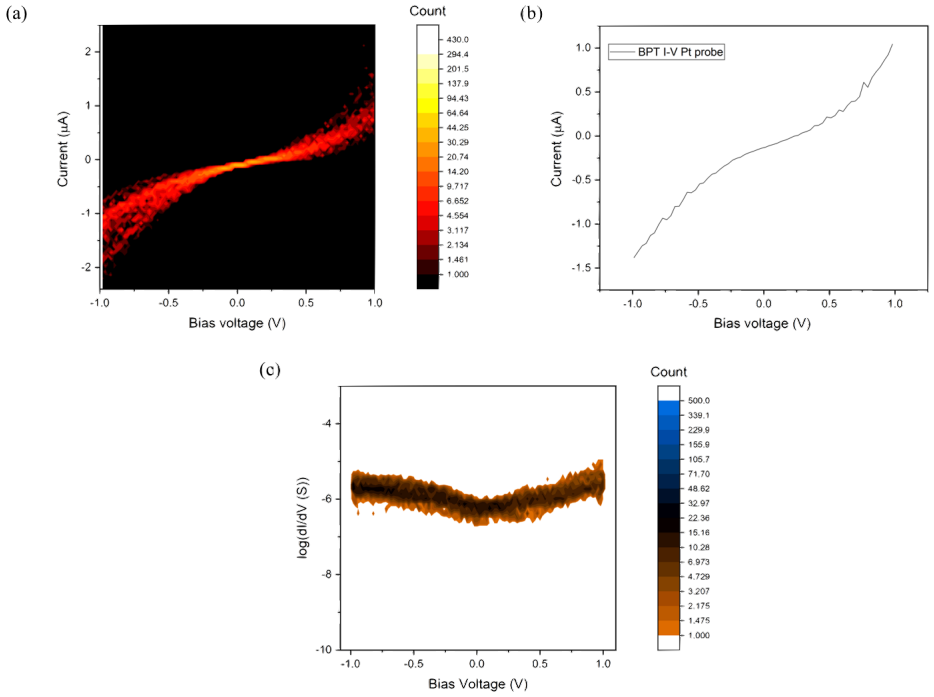

Figure 6.5: (a) I-V counter map histogram of BPT SAM measured by CAFM using Pt coated probe; (b) average I-V curve calculated from the multiple traces acquired; (c) electrical conductance histogram.

molecular area of BPT was assumed to be 25 $\mathring{A}^2$,while for alkyl thiolate was assumed to be 18 $\mathring{A}^2$.

In this way, the single molecular conductance G of BPT, C6S, C8S and C12S was calculated to be $(3.1\pm0.6)\cdot10^{-8}$S, $(1.6\pm0.1)\cdot10^{-8}$S, $(7.4\pm2.8)\cdot10^{-10}$S, and $(1.7\pm0.4)\cdot10^{-12}$S correspondingly.

It is worth noting that BPT molecules, which have a similar length to C8S, exhibit a molecular conductance one order magnitude higher than C8S, which is not evident in the measurement of the SAMs conductances. Since the two molecules have the same length, the differences in the single molecular conductance G can be attributed to the smaller HOMO-LUMO gap of BPT molecules and to the effect of the phenyl rings of the conjugated wire on the electrical conductance G, which enhances the electric transport in the junction.

6.1.2 Effect of CAFM probe material

In order to explore the influence of the top electrode material on the electric and thermoelectric properties of the SAMs, the I-V characteristics were measured by using a Gr coated CAFM probe, following the procedure described in Section 5.4.7. In figure 6.6 the I-V traces measured by CAFM for the 3 series of alkanethiol SAMs contacted by the CAFM Gr coated probe are presented together with the histograms of the conductance histograms.

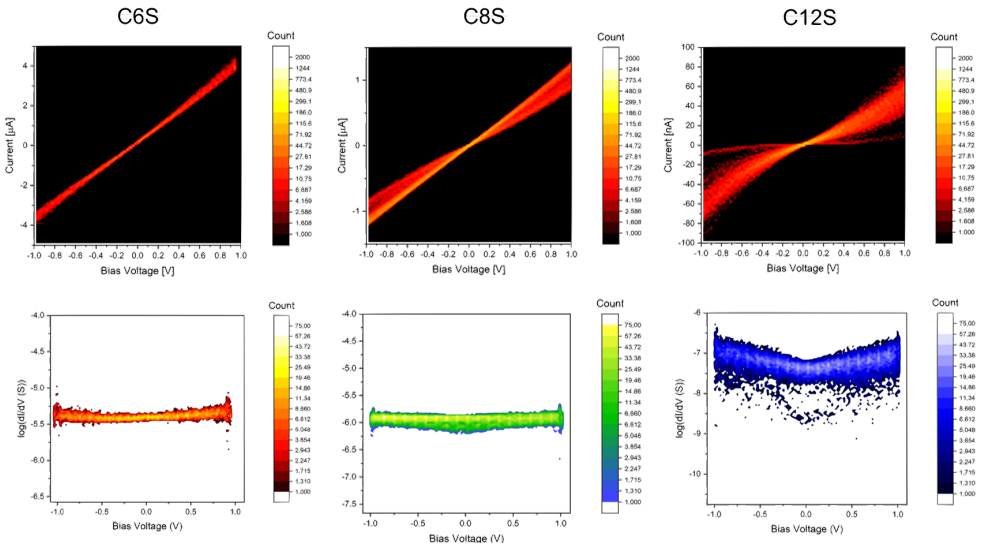

Figure 6.6: I-V traces histograms (top) for the 3 alkyl thiolate SAMs acquired with contact mode CAFM employing a Graphene coated probe. The bottom line shows the electrical conductance counter maps obtained from the I-Vs.

Electric transport measured across the molecular junctions by Gr coated probes shown the same trend observed using Pt coated CAFM probe, characterised by an exponential drop on the current intensity (fig.6.7).

In analogy with the data obtained for Pt CAFM probe, we observe a linear dependency of the natural logarithm of the electrical conductance G with increasing SAMs thickness, highlighting the coherent tunnel transport across the SAMs [165, 199]. The decay factor β was found to be 8.8 ± 2.2 nm^{-1}, which results very close to the value found employing Pt coated CAFM probes.

The values of electrical conductance measured in the 3 alkyl thiolate SAMs were respectively $(6.52 \pm 0.14) \cdot 10^{-6}$S, $(1.04 \pm 0.21) \cdot 10^{-6}$S, $(3.31 \pm 0.53) \cdot 10^{-8}$S for C6S, C8S and C12S, still in good agreement with the data obtained with Pt probes in Sec.6.1.1.

The electrical properties of biphenyl thiol SAM was also studied using Graphene coated

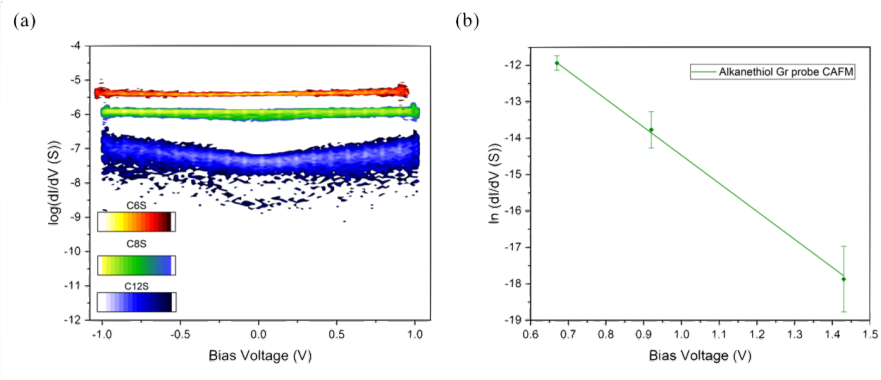

Figure 6.7: (a) Comparison of electrical conductance histograms acquired with CAFM (Gr coated probe) of C6S (red), C8S (greenish) and C12S (blue) SAMs; (b) Plot of natural logarithm of the conductance value $^{dI}/_{dV}$ at low bias vs thickness of the alkanethiol SAMs.

probe.

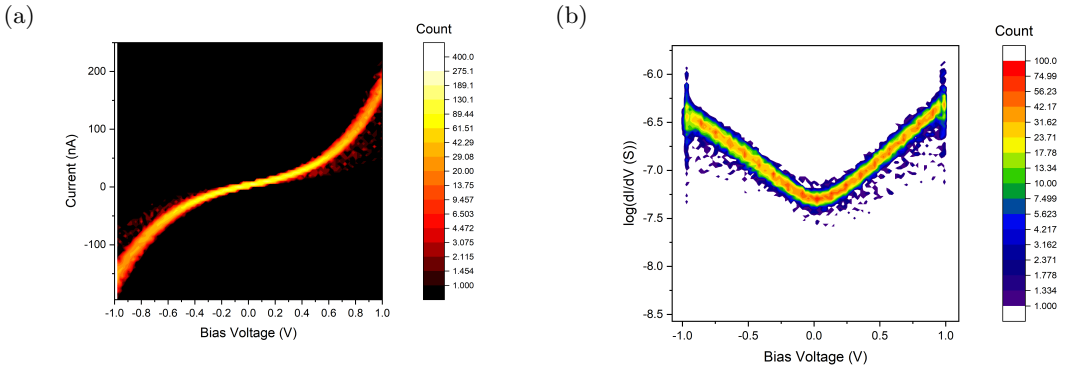

Figure 6.8: (a) I-V traces histogram of BPT SAM measured by CAFM using Graphene coated probe; (b) electrical conductance histogram.

Figure 6.8 shows the current as a function of applied bias voltage in single point measurement of BPT SAM using Graphene coated probes. Analysing the conductance values for bias values $-0.1V \leq V \leq 0.1V$, conductance was found to be $G = (5.01 \pm 0.49) \cdot 10^{-8}$S, very close to the value per single BPT molecule obtained with Pt probe $(3.1 \pm 0.6) \cdot 10^{-8}$S.

For the calculation of the contact area, the Reduced Young's Modulus of Gr coated probe was taken into account in the equations 5.3 and 5.4. The modulus of the Gr coated probe was measured in a dedicated channel by PF-AFM. The Z values of the reduced Young's modulus map channel of the Gr coated probe on Au substrate were then averaged and plotted as distribution. In fig.6.9, the Reduced Young's Modulus of Gr probes is shown together with the distribution obtained for Pt coated CAFM probe, where it is clear that the graphene coated probes result "softer" compared to the Pt counterpart. This properties, as seen in Section 5.4.7, make the Gr probe a very suitable tool for this

kind of "soft" material properties analysis giving more stability in the measurements as well as reducing the damaging of the probe itself.

The better coupling of graphene with some molecule head groups and its affinity with π systems will results fundamental for the enhancement of the electric and thermoelectric properties of the junctions in which one or both the metal electrodes are substituted with graphene electrodes.

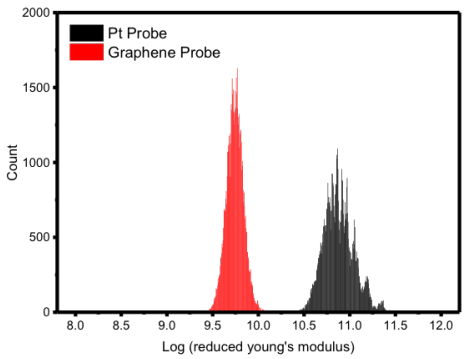

Figure 6.9: Comparison of the Reduced Young's Modulus of Pt and graphene CAFM coated probes measured with PF-AFM.

6.1.3 Peak force CAFM for SAMs electric transport characterisation

To test the working principle of the developed Peak Force-CAFM described in Section 5.4.5 topography, current map and electric transport studies were performed on the same set of SAMs studied by conventional contact CAFM with Pt and Graphene AFM probes.

The electric maps were acquired by applying 500mV DC voltage between the Au substrate and the CAFM Pt tip. In this work, the PF frequency was set to 1 kHz and used as a reference signal for the lock-in amplifier, as shown in fig.5.24. Electric maps and the topography map of the surface of C8S, C12S and BPT SAMs in a scan area of 350 x 350 nm are shown in fig.6.10.

In this case, the maps were acquired by switching the sign of the bias voltage in order to stimulate negative current, as seen by the switch of colour in d, e, f of fig.6.10 during the scan process.

The electric transport of the 4 SAMs was characterised using the point measurement methodology, applying a triangular bias voltage with the same frequency as the PF tapping frequency (1 kHz). In this way, using the PF frequency as ref for the lock-in, the

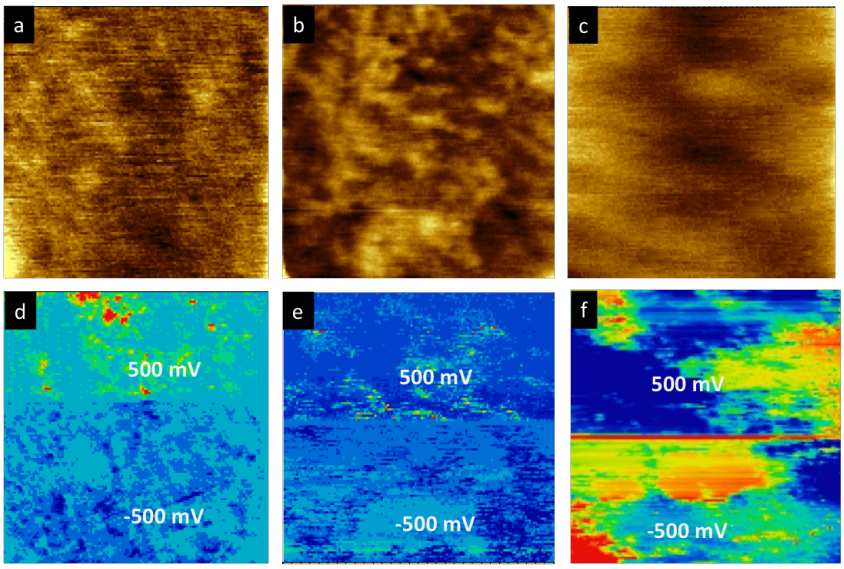

Figure 6.10: Topography of C8S (a), C12S (b) and BPT (c) SAMs, scan area = 350 nm x 350 nm. (d-f) current map of (a-c) recorded at 500 mV and -500 mV DC voltage using PF-CAFM.

current from the junction will rises only when tip and sample are in contact. The PF set-point was maintained at 2 nN. The multiple I-V traces acquired per each alkyl thiol SAMs are shown in fig.6.11.

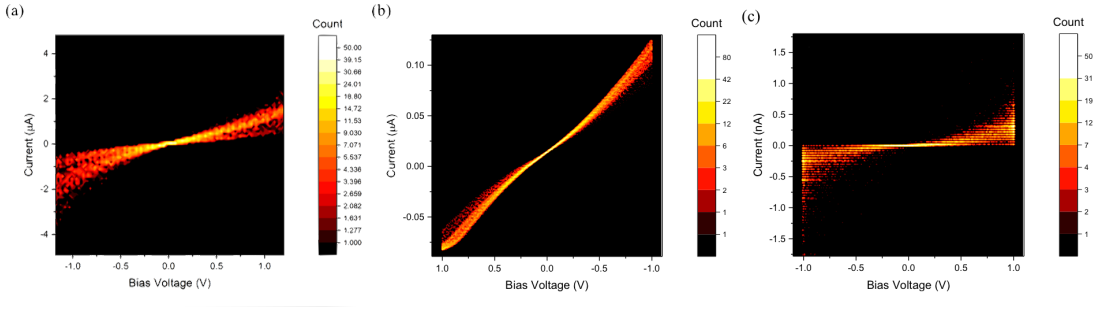

Figure 6.11: Histograms of current vs bias voltage traces (top) for (a) C6S, (b) C8S and (c) C12S SAMs acquired with PF-CAFM.

The average current values for all the studied SAMs are shown in fig.6.11 and were lower than the current values recorded with CAFM in contact mode (fig.6.2). One of the main reasons behind the drop in current flow in the molecular junctions is that the Peak Force AFM results in less time-interaction between probe and sample than CAFM used in contact mode. In addition, the separation of the electrodes (probe-substrate) is predicted to decrease by ≈ 0.5 nm between PF and contact modes (at applied normal forces of 0.2 and 2 nN, respectively); as such, the increased conductance is believed to arise from a change in the molecular tilt angle – relative to the electrode – due to the decreasing electrode separation at increasing normal force in contact mode AFM.

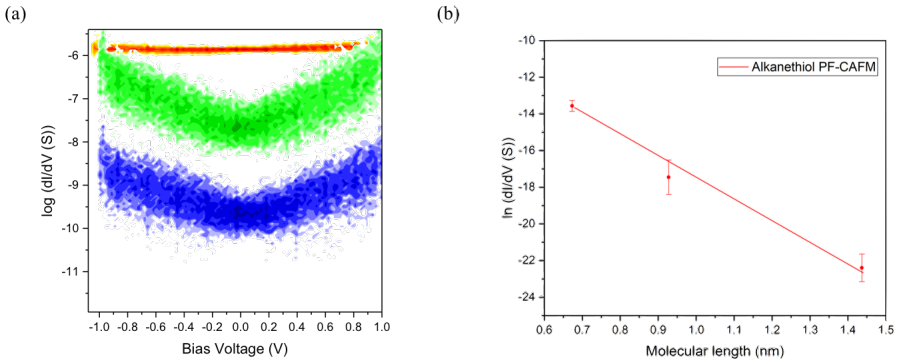

Figure 6.12: Comparison of PF-CAFM electrical conductance histograms of C6S (red), C8S (greenish) and C12S (blue) SAMs; (b) Plot of natural logarithm of the conductance values $^{dI}/_{dV}$ at low bias vs. thickness of the alkanethiol SAMs.

Specifically, the values of electrical conductance found were $(1.44 \cdot 10^{-6} \pm 0.36) \cdot 10^{-6}$S, $(3.75 \pm 3.06) \cdot 10^{-8}$S and $(4.47 \pm 2.13) \cdot 10^{-10}$S for C6S, C8S and C12S. The values of the electrical conductance G of the 3 set of alkythiol SAMs at zero bias voltage was plotted against the film thickness (or molecular length) and fitted following eq. 6.1, as shown in fig. 6.12.

From 6.12.b, we obtain $\beta = 11.9 \pm 1.8$ nm^{-1}, in good agreement with the β values obtained in the Sections 6.1.1 and 6.1.2, and inside literature values range for alkyl thiolate SAMs [165, 199].

The same analysis was performed on Biphenyl thiol SAM using PF-CAFM, and the I-V traces and conductance histograms are shown in fig. 6.13.

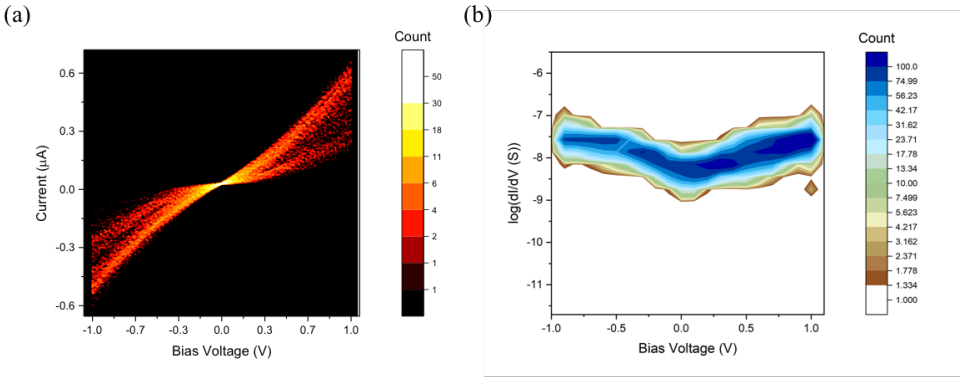

Figure 6.13: Histograms of I-V traces (a) and electrical conductance (b) measured for biphenyl thiol SAM with PF-CAFM.

The measured value of the electrical conductance G for the BPT SAM, using PF-CAFM, was $(4.32 \pm 2.52) \cdot 10^{-9}$S, which is 2 order magnitude lower than the value

obtained for the same SAM measured with contact mode CAFM ($(5.42 \pm 2.31) \cdot 10^{-7}$S). As mentioned above, the differences in the G values obtained is to attribute to the shorter interaction between probe and sample due to the intermittent contact.
As the PF-AFM feedback loop is based on the Peak force, namely the maximum interaction force between probe and sample, there is a dynamic force range during each tapping cycle. However, assuming the molecules do not change their conformation during the probe-sample interaction in PF-AFM, the Peak force set point can be considered, in first approximation, as the force applied on the molecules during the scan operation, making possible the extrapolation of the single molecular equivalent conductance G.

Comparing the 3 sets of measurements performed on alkyl thiolate SAMs with CAFM contact mode (Pt and Graphene coated probes) and PF-CAFM, it is possible to observe a slight deviation of the conductance data obtained with the latter method compared with contact mode CAFM, as displayed in fig.6.14.

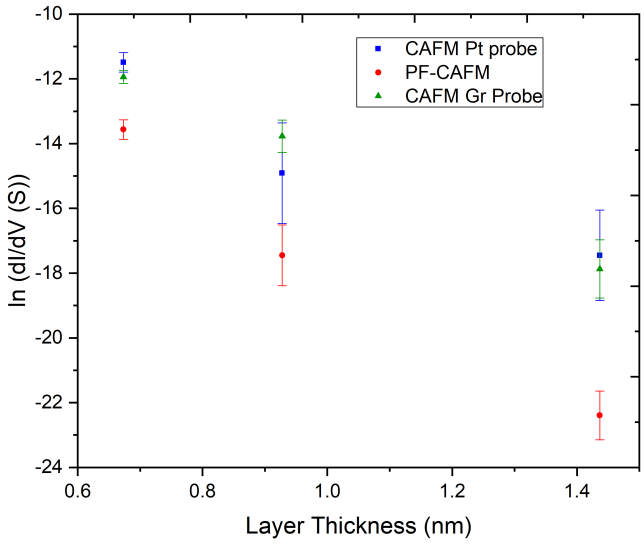

Figure 6.14: Comparison among the 3 current decay factor β measured with contact mode CAFM used with Pt (blue) and Graphene (green) coated AFM probes and PF-CAFM (red) for alkyl thiolate based SAMs.

The linear behaviour exhibited from the SAMs with the increase of the molecular length was found for all the three methodologies explored to probe the electric transport using AFM. In this case, the linearity found is clear evidence that the molecules between the two electrodes (Au and AFM probe) act as a tunnel barrier for the electrons in the two terminal of the junctions. The electrical conductance values for the 4 SAMs measured

with Pt and Graphene probe and with PF-CAFM are reported in table 6.2.

	G CAFM (Pt probe) (S)	G CAFM (Gr probe)(S)	G PF-CAFM(S)
C6S	1.02E-5	4.81E-5	1.44E-6
C8S	3.07E-6	7.55E-6	3.75E-8
C12S	2.63E-8	3.49E-8	4.47E-10
BPT	5.42E-7	3.61E-7	4.32E-9

Table 6.2: Comparison electrical conductance values measured for the 4 SAMs with contact mode CAFM (Pt and Graphene probe) and PF-CAFM.

The G values for the 4 molecular SAMs with different measurements methodology, PF-CAFM shows a drop of the electrical conductance of about 2 order of magnitude compared with the contact mode CAFM values obtained by Pt and Gr probe.

6.1.4 Thermoelectric characterisation

Among the 4 samples studied in this preliminary testing of the set-ups, 2 molecular SAMs with similar thickness C8S and BPT were chosen for thermoelectric characterisation through CAFM in contact and PF modes. In addition, the effect of the AFM probe coating material was studied to explore and better understand the different coupling between electrodes and SAMs. The main reason for choosing these two molecules was because they present comparable molecular length but significant differences in the transmission properties.

Thermoelectric properties were measured using the ThEFM set up described in Section 5.4.4 and 5.4.6.

Before any measurement on the SAMs, the Seebeck coefficient of the Au substrate was measured in contact mode ThEFM in order to be removed from the value of the Seebeck coefficient obtained every time for the different molecular SAMs.

From the thermal voltage analysis as a function of temperature, the Seebeck value of Au was found to be S=$\sim$ 3.4 $\mu V\,K^{-1}$, in good agreement with the typical values of the Seebeck coefficient for metal-metal junctions [189, 324]. However, the Seebeck coefficient for Au particularly, but metals in general, varies slightly from measurement to measurements, oscillating around zero Volt. In our experiment, the Seebeck value of Au was found to oscillate around $\sim$ 4 $\mu V\,K^{-1}$. This value was then subtracted to the thermal voltage recorded per each SAM in order to obtain the Seebeck coefficient of the junctions.

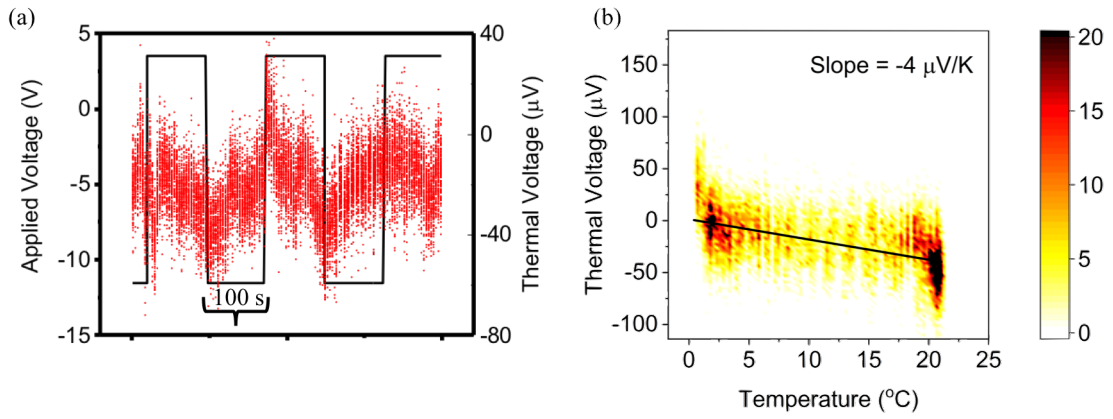

Figure 6.15: (a) Voltage applied on heater device and relative thermal voltage of TS Au substrate measured with ThEFM when a $\Delta T = 20$K is applied between probe and substrate; (b) 2D counter map of the thermal voltage values of Au vs. T obtained from (a), exhibiting a slope of of -3.4 $\mu V\,K^{-1}$.

The initial comparison of thermoelectric properties of C8S and BPT SAMs were made to studying the evolution of the thermal voltage by ThEFM and PF-ThEFM. For better stability of the thermal current measured, only two temperature were supplied by the heater device, providing a $\Delta T = 14$ K, to maximise the amount of thermal current added to the electric current flowing in the junction.

The data in fig.6.16 shows the thermal voltages collected from C8S and BPT SAMs grown on Au substrate, where (a, b, d, e) were obtained in contact mode using the in *"0 current"* mode and (c, f) were in obtained in PF mode using the *current mode*. For the values shown in fig.6.16.b and 6.16.e the Seebeck coefficient was calculated by :

$$S_{SAM} = S_{Au} - \frac{\Delta V}{\Delta T} \tag{6.2}$$

where S_{Au} is the Seebeck coefficient to Au, ΔV is the thermal voltage and ΔT the temperature difference between the sample and probe.

Using contact mode ThEFM, the calculated Seebeck coefficients for the two molecules were $S_{C8S} = 7.4 \pm 3.1$ $\mu V\,K^{-1}$, and $S_{BPT} = 23.3 \pm 7.3$ $\mu V\,K^{-1}$. The Seebeck of Au was also measured to have a Seebeck coefficient, $S_{Au} = 2.2$ $\mu V\,K^{-1}$. This result is comparable with other works present in literature on similar systems [41, 246, 325].

The positive Seebeck coefficient sign found for C8S and BPT indicates that the transport through the molecules is HOMO dominated, as detailed in 2.1.2. The measured Seebeck of C8S was about 2.5 times smaller than BPT, which is correlated with the

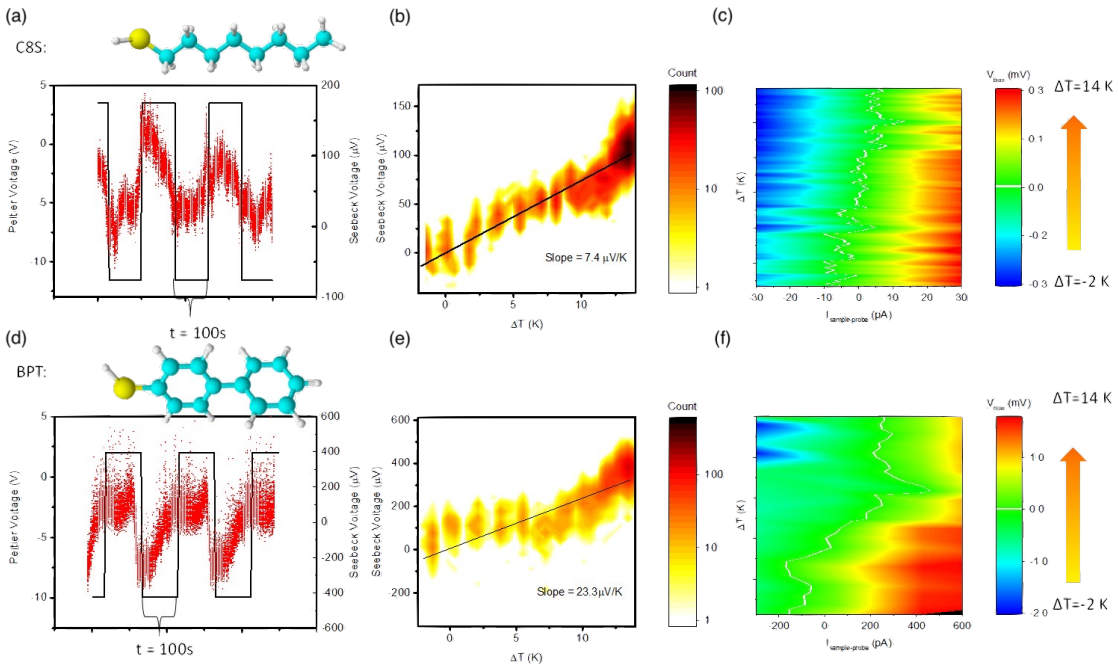

Figure 6.16: Thermoelectric characterisation of C8S (a-c) and BPT (d-f). (a) Heating Voltage vs Thermal voltage (b) ΔT vs thermal voltage (c) thermal current vs bias voltage and ΔT measured in peak force mode with PF-ThEFM. The white line in both the PF-ThEFM measurements represents the thermal current at 0 bias.

larger HOMO-LUMO gap of C8S and Fermi-energy E_f of the junction lies within in the gap tail of the HOMO resonance peak.

Using the non-0 current mode with PF-ThEFM, the thermal current rising due to the thermoelectric effect was added to the electric current generated in the junction applying a triangular wave ($V_{pp} = 1.2\ \mu\mathrm{V\,K^{-1}}$), as shown in fig 6.16.c and 6.16.f, which show the additional thermal current at zero bias voltage (white line) during increasing temperature. The shift of the current at V=0 due to the temperature difference is more evident for biphenyl thiol BPT SAM than the Octanethiol based SAM, indicating a higher Seebeck value. Using the relation 5.9, which correlate the thermal power to the thermal current, electric current, temperature and electrical conductance, the Seebeck coefficients were found to be $S_{C8S} = 9.3 \pm 3.1\ \mu\mathrm{V\,K^{-1}}$ and $S_{BPT} = 17.6 \pm 5.5\ \mu\mathrm{V\,K^{-1}}$, which are within measured uncertainties with the work in contact mode, as displayed in fig.6.17.

As expected, in contrast with the electric transport characterisation made with CAFM and PF-CAFM in the last Sections, this time no significantly difference in the Seebeck values were observed because the Seebeck coefficient was measured from the ratio between thermal current and the electrical current (Equation 5.9).

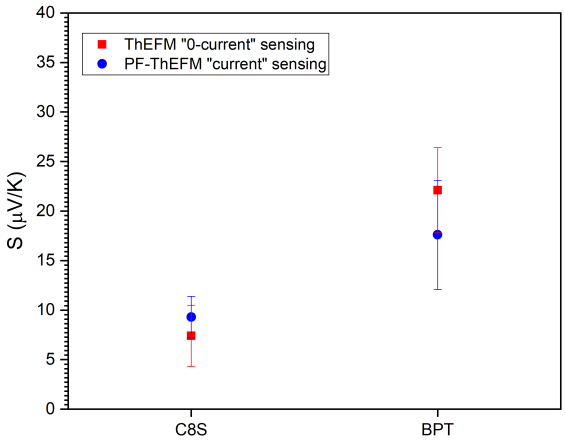

Figure 6.17: Comparison of Seebeck values measured with ThEFM and PF-ThEFM for C8S and BPT SAM.

The same SAMs thermoelectric properties were also investigated using Gr coated probes as a top electrode in ThEFM in order to see eventual enhancement of the Seebeck values due to the interaction between graphene and the molecules orbitals.
In order to compare the results obtained with Graphene coated probe with the ones for Pt probes, as first step, the Seebeck of the TS Au substrate was measured as shown in figure 6.18.

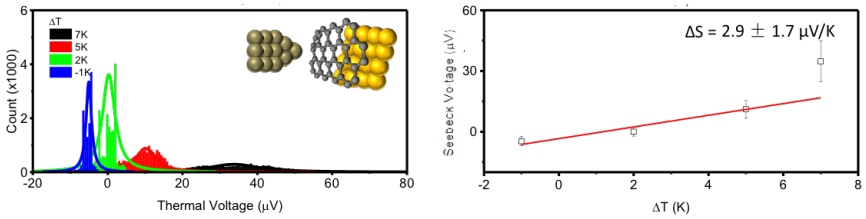

Figure 6.18: Template stripped Au thermal power distribution measured as a function of temperature difference ΔT between the substrate and ThEFM Graphene coated probe. On the right side, the average values of thermal voltage are plotted against ΔT.

From the linear fit of the thermal voltage for a set of 5 different ΔT, the Seebeck coefficient S of the Au substrate was calculated through the equation 6.2, resulting in 2.9 ± 1.7 $\mu V\,K^{-1}$, which is in great agreement with the S_{Au} found using Pt coated ThEFM probes.
Following the same procedure, the thermoelectric properties and the Seebeck coefficient measured with graphene coated AFM probe of C8S and BPT SAMs are shown in fig.6.19.

The Seebeck coefficients using *"0-current"* mode for the two molecular SAMs using

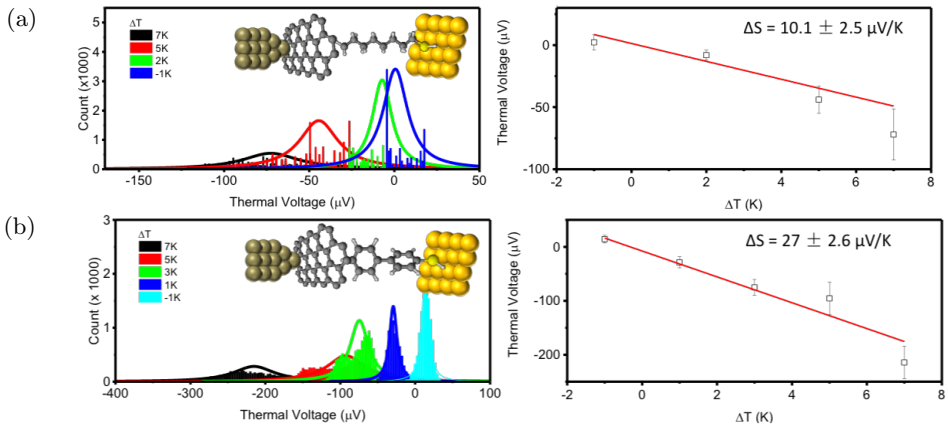

Figure 6.19: Measured thermal voltage distribution as function of temperature difference ΔT and plot of average thermal voltage vs ΔTT for C8S (a) and BPT (b) using graphene coated probe-as top electrode in ThEFM.

graphene coated probe were $S_{C8S} = 10.1 \pm 2.5$ μV K^{-1} and $S_{BPT} = 27.0 \pm 2.6$ μV K^{-1}. The measured values show a little increase of thermal power delivered by the molecules when one of the junction electrode is substituted by graphene. However, the slope of the thermal voltage trend is the same as measured by Pt probes and PF-ThEFM, confirming the reliability of the graphene coated probes.

The enhancement recorded can be attributed to the higher interaction of graphene with the molecules' head group, increasing the coupling between molecule and electrode and, to the higher interaction of graphene with conjugated π molecules. In addition, graphene exhibits superior electrical and thermal conductance, resulting in a consistent advantage for this kind of measurements. However, due to the probe's nature, the actual scheme of the junction can be considered as Pt-Gr-SAM-Au junction in where the graphene layer acts as a spacer between Pt electrode and SAMs.

The thermoelectric signature of the two SAMs for each different methodology (ThEFM Pt and Gr probes, PF-ThEFM) are reported in table 6.3.

	S ThEFM Pt probe (μV K^{-1})	S ThEFM (Gr probe) (μV K^{-1})	S PF-ThEFM (μV K^{-1})
C8S	7.4 ± 3.1	10.1 ± 2.5	9.3 ± 2.1
BPT	22.1 ± 4.3	27.0 ± 2.6	17.6 ± 5.5
Au	3.4 ± 1.9	2.9 ± 1.7	

Table 6.3: Thermoelectric signatures of C8S and BPT SAMs measured with ThEFM (Pt and Gr probes) and PF-ThEFM.

We observe that Gr probe ThEFM provided higher Seebeck values for both the SAMs and Au substrate. In contrast, the thermoelectric properties of SAMs measured in

current sensing mode gave the lower Seebeck values. Results are summarised in fig.6.20.

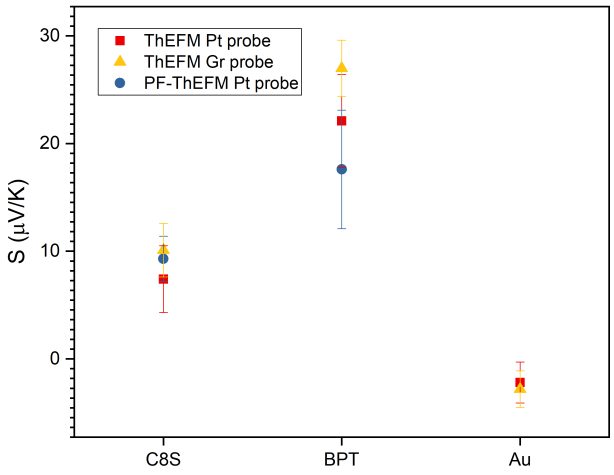

Figure 6.20: Seebeck coefficient of C8S and BPT SAMs measured with ThEFM (Pt and Gr probe) in *0-current sensing* and with PF-ThEFM. For comparison, the Seebeck value of the Au substrate is also shown together with the two SAMs.

6.2 Fullerene C_{60}

Fullerene C_{60} has been largely studied in literature for its electric properties due to the extended π system. In addition fullerene thin films has widely employed for hybrid solar cell [326, 327], transistor [328] and superconductive applications [329].
Recently, C_{60} single molecular junction have attracted interest due to its thermoelectric properties [37, 155]. Additionally, the possibility to stack molecular layers by π interaction using the Langmuir-Blodgett technique rather than covalently bonded molecules has been reported to enhance the thermal power S of molecular junctions via intermolecular interaction between molecular units [264]. In 2017, *Qian et Al.* reported the phononic contribution to thermal conductance in molecular junctions could be reduced up to the 95% via π stacking compared with that of covalently bonded systems [330]. Thus, compared with the covalently bonded systems, this type of π stacked configuration could maximise the S value and minimise the thermal conductance k, pushing ZT up. In this section, C_{60} layer formations by Langmuir-Blodgett technique and SAM and their electric and thermoelectric characterisation is presented. In particular, significant effort was made to optimise the preparation of the LB fullerene monolayer formation by varying solvents, concentrations, volumes, spreading condition and barrier speed.

6.2.1 Optimisation C_{60} LB layer formations

C_{60} has no amphiphilic character and is also non-polar, which make the formation of LB film formation particular tricky [331, 332]. Also, because of its particular spherical shape C_{60} has no characteristic. This makes it particularly difficult to theoretically explain the mechanisms by which monomolecular layers of fullerene form.
Due to its non-polar nature,C_{60} is very hydrophobic, exhibiting extremely low solubility in water of 1.3×10^{-11} mg mL^{-1} [304, 333, 334]. Despite the different properties to traditional "protocol" for LB film formation, C_{60} can still exhibit an isotherm (Π vs. MMA) analogous to those obtained for organic amphiphilic compounds.
Interestingly, the intermolecular potential of C_{60} molecules is not a Lennard-Jones type potential despite the molecule being fairly round [301]. A pair-potential type theoretical model (using the pairwise central force model) has been proposed to explain interactions between C_{60} molecules [335]. Since the theoretical sublimation line passes above the liquid-vapour critical point, Castillo et al. [301] postulated that C_{60} ML films should show no liquid phase. At the time, they stated that this would be the first example of a pure solid with no gas-liquid-solid triple point. However, they were unable to conclude

whether their experimental results were consistent with the theoretical model.
The hydrophobicity of C_{60} allows its spreading onto a smooth water subphase. However, the C_{60}-water interaction is relatively weak, making the fullerene molecules weakly bound to the water surface. Indeed, the van der Waals binding energy between two C_{60} molecules is of the same order as C_{60}-water binding energy, hence the lowest energy state for a C_{60} LB film is not an ML [336].
This is potentially the most significant hurdle that must be overcome in successfully creating stable monomolecular layers since systems tend to their minimum energy states. Furthermore, the probability to moves away from the water surface and binding to other C_{60} molecules to form multilayers or escaping the air-water interface entirely (i.e. on top of other molecules) need to be taken into account to optimise the C_{60} layer formation. The processes that lead to these disruptions in the ML were extensively analysed by Evans et al. [336] to explain how, despite the disruptive processes, a ML state can be formed at the air-water interface for specific circumstances.
Therefore, the formation mechanism of C_{60} ML LB formation can be seen as an initial cluster formation followed by a continuous gain of molecules from the edge molecules present in the cluster. This process, on average, results much faster than the promotion of another molecule on top of an existent cluster, ensuring the feasibility of C_{60} ML.
In this work, the LB formation of fullerene monolayer was studied by both micro-syringe spreading and ESI spreading in the manner explained in 3.1.2

Establishing the ideal conditions for ML deposition required a rigorous and systematic approach. The derived limits concerning the mean molecular area occupied per molecules (MMA $Å^2$) on the surface had to be adhered to each time. Additionally, repeatability of experiments within limits was essential.
The MMA of identical molecules spread onto the water surface is defined as the surface area occupied by each molecule. Calculating this value gives valuable information about the layer thickness, which is vital when trying to achieve ML deposition. MMA units are $Å^2\,mol^{-1}$ but are also often defined just as $Å^2$. The MMA can be calculated by considering the number of surface molecules and the available area onto which they are spread.
Each time an LB experiment is performed, a solution of known volume and concentration was used, so the total number of C_{60} molecules deposited, $N_{C_{60}}$, was calculated. The MMA was given by:

$$MMA = \frac{A_{LB}}{N_{C_{60}}} \tag{6.3}$$

As the barriers were compressed, the LB available area A_{LB} decreased; thus, the MMA of molecules decreased. The inner C_{60} diameter is about 7.1 Å, which gave a mean cross-section of 39.6 $Å^2$. Hence a lower limit on the MMA was fixed to be 39.6 $Å^2$, below which an ML was not achievable and usually causing multiple layers of molecules. Ultra-high vacuum scanning tunneling microscopy measurements have found the spacing of C_{60} clusters to be (11.0 ± 0.5) Å [337]. Since these measurements were taken in tightly packed C_{60} clusters, it can be presumed that a C_{60} ML would also exhibit similar spacing. So, considering 11 Å to be the average diameter of a C_{60} molecule, in an ML gave an MMA value of ~ 95 $Å^2$. Previous groups reported the formation of C_{60} monomolecular layers happening at limiting MMA values of (98.2 ± 2.3) $Å^2$ [338], 96 $Å^2$ [304], 94.1 $Å^2$ [303] and 95.6 $Å^2$ [339]. The limiting values were not expected to coincide exactly due the many influencing factors that affect the way in which monomolecular layers form.

A rough upper limit on the final MMA (after compression) of 100 $Å^2$ should increase the chances of reaching a stable solid phase of C_{60} ML. This "theoretic" limit of MMA was then considered in our experiment as an indicator of the goodness of the film formation.

As explained in Chapter 5, the electrospray ionisation was employed to the spreading of the solution of C_{60}. Toluene and Toluene-methanol (5:1) solutions were initially chosen due to the high solubility grade of fullerene in toluene. C_{60} powder (Aldrich, 98%) was weighed and mixed with toluene (or toluene/methanol) until the desired concentration was reached.

Initial steps focused on identifying the best compromise between concentration and volume. In order to optimise these two parameters, the average number of molecules was calculated starting from the available area of the LB trough, and considering the limits discussed before for the MMA.

The first approach explored the overall volume of solution being spread. A lower solution volume required a higher concentration of C_{60} to spread the required numbers of molecules $N_{C_{60}}$ giving the MMA range determined above. Initially 200 µL of solution 5.8×10^{-5} M, that would spread $N_{C_{60}} \simeq 7 \cdot 10^{15}$ mol was tested. Figure 6.21a shows two attempts of recording a two-cycle isotherm for the same solution of C_{60} in a distance of 30 minutes after the first two cycle.

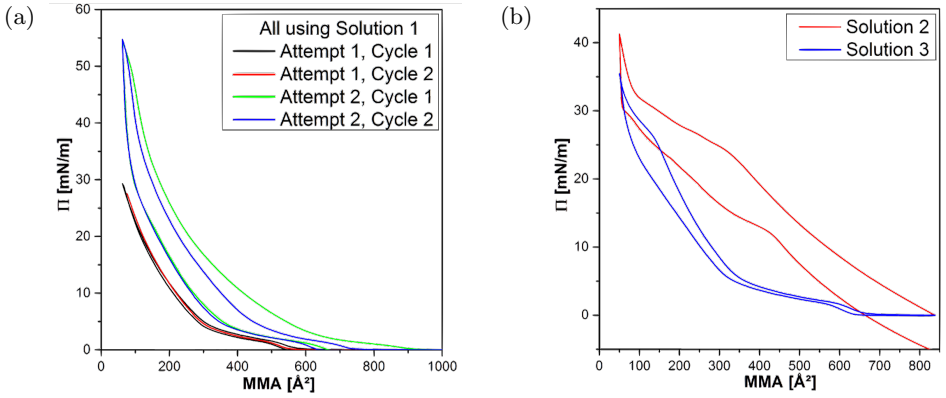

Figure 6.21: LB isotherm recorded using: (a) Solution 1: 200 µL of C_{60} solution ($5.8 \times 10{-}5$ M); (b) Solution 2 and 3 with equal $N_{C_{60}}$ but different volumes. Solution 2: 1 ml of C_{60} in (5:1) toluene and methanol ($1.5 \times 10{-}5$ M). Solution 3: 500 µL of C_{60} in (5:1) toluene and methanol with a concentration of ($2.9 \times 10{-}5$ M). Spreading 1 ml of solution failed to show the required distinct phase changes and low hysteresis between the expansion/compression of the barriers.

The isotherm obtained in fig.6.21a did not reach the desired final MMA and showed a lack of reproducibility. Neither maintaining the same numbers of molecules fixed, as displayed in fig.6.21b, ensured the same final results .

From Solution 2 in fig.6.21b isotherm, it is possible to state that spreading a higher volume results in a missing gas phase due to the high concentration of molecules at the initial stage of the compression, and undesired shape in the evolution of the isotherm during the compression of the film. In addition, the hysteresis recorded with Solution 2 in fig.6.21b underlying the failure in the selected parameter because of the considerable loss of molecules into the subphase. In contrast, Solution 3 showed distinct phase changes and a sharp rise at the correct expected MMA around 100 $Å^2$.

The parameter used for Solution 3 in fig. 6.21b (500 µL, $\sim 2 \times 10{-}5$ M) ensured a number of molecules within the upper and lower limit of MMA predicted before and thus was taken as a base parameter for the formation of LB C_{60} ML.

When depositing a layer using an LB system, it was important to know the pressure at which the solid ML phase will be observed. To determine this, successive compression and relaxation cycles of the surface needed to be repeatable. Similarly to other experiments, it was noted that successive isotherms of the same number of C_{60} spread onto the water were not always consistent, as shown in fig.6.22a. Furthermore, another variable relevant to isotherms was the barrier speed during compressions and relaxations, as displayed in fig.6.22b. For each experiment, a consistent barrier speed was always chosen, but changing the barrier speed for successive experiments may lead to different phase

change behaviour as shown in the inset of 6.22b.

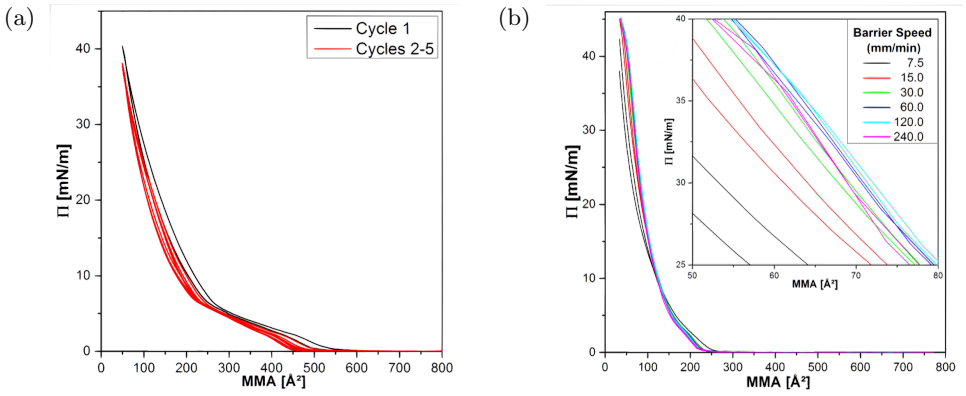

Figure 6.22: (a) Recorded LB isotherm Π vs MMA (7.5 mm min^{-1} barrier speed) in 5 cycles of compression-expansion of the LB barriers of ESI-spread C_{60} solution (500 µL, $\sim 2 \times 10{-}5$ M); (b) speed dependancy of LB isotherms for ESI-solution of C_{60} (500 µL, $\sim 3.5 \times 10{-}5$ M). The insert in (b) shows the enlarged isotherms of (b), displaying an increase in repeatability of isotherms at higher barriers speeds.

The isotherm shape of fig.6.22a changed slightly between the first and the second full cycle of compression-expansion of the barriers. However, the shape remained consistent for three successive full cycles, as it is possible to observe in the red curves relative to cycles 2-5. This result agrees with the results observed by *Obeng et al.* [304]. The vastly increased repeatability for each subsequent full cycle following the first compression and expansion was then demonstrated.

To investigate the dependency of the LB isotherm on the barrier speeds, a solution of C_{60} (500 µL, $\sim 3.5 \times 10{-}5$ M) was ESI-spread onto a water subphase and compressed then relaxed for six different steps of barrier speeds. The surface went through two full compression-relaxation cycles at each speed, and the resulting isotherms for different barrier speeds are combined in Figure 6.22b and in the inset zoomed region. The graphs showed little change between successive isotherms. The biggest difference noticed, in this case, was a slight increase in solid phase gradient with increased barrier speed.

From the isotherms shown in fig.6.22, both the solutions used for the repeatability test exhibited a limiting MMA at the end of the film's compression, which was comparable with the expected MMA for C_{60} molecules. The limit MMA values were calculated from the intercept at $\Pi = 0$ of the linear fit of the solid-like phase.

C_{60} isotherm (500 µL, $\sim 3.5 \times 10{-}5$ M) is shown in fig.6.23, comparing the isotherms obtained by micro-syringe spreading and ESI-spreading. In order to collect more information about the LB growth of the fullerene films during the barriers' compression, Brewster's angle microscopy BAM was employed to monitor the water surface during the compression at different Π.

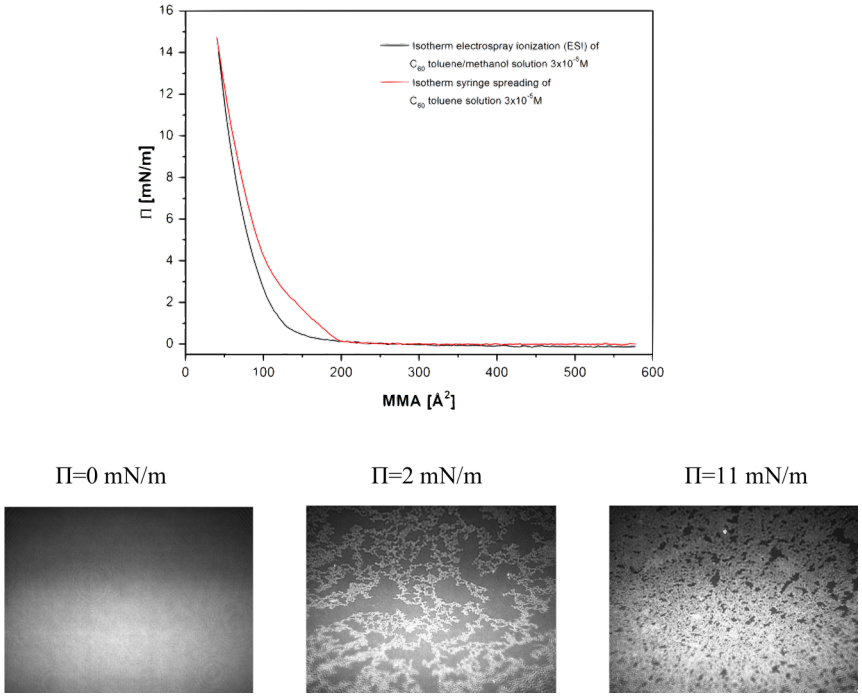

Figure 6.23: Π against MMA isotherms of 500 µL, $\sim 3.5 \times 10{-}5$ M C_{60} solution for ESI and micro-syringe spreading water subphase, exhibiting a solid-like phase with limiting MMA of 95 $Å^2$. The bottom line shows the BAM microscopies of the water surface during the compression of the film in three selected point, correspondent to gas phase $\Pi = 0$ mN m^{-1}, liquid-like phase $\Pi = 2$ mN m^{-1} and solid like phase $\Pi = 11$ mN m^{-1}.

Both the isotherms displayed a vertical solid phase which strongly agreed with groups who had claimed to observe ML LB C_{60} films. The isotherm seemed to move from the horizontal gas phase to the vertical, solid-like phase rapidly, without showing consistent liquid phase, when the solution was spread with ESI and in agreement with the theoretical prediction of *Castillo et Al* [301]. The two isotherms showed a long gas phase with no substantial changes until MMA of 200 $Å^2$ mol^{-1}, which can be interpreted as no reciprocal interaction of C_{60} molecules. The calculated limiting MMA at $\Pi = 0$ was $MMA_{(\Pi=0)} = 95.2 \pm 0.8 Å^2$ mol^{-1}, which is in agreement with past works made by *Obeng et Al.* [304], and thus suggesting the formation of a monomolecular layer of fullerene floating on the water subphase.

The solutions used in this work was chloroform-based solutions 2×10^{-5} M. This choice was made due to the better quality of transferred films and stability of the floating layer at high Π, as it is possible to observe in fig.6.24.

Once the optimal conditions for forming LB C_{60} ML were found, the floating ultra-thin

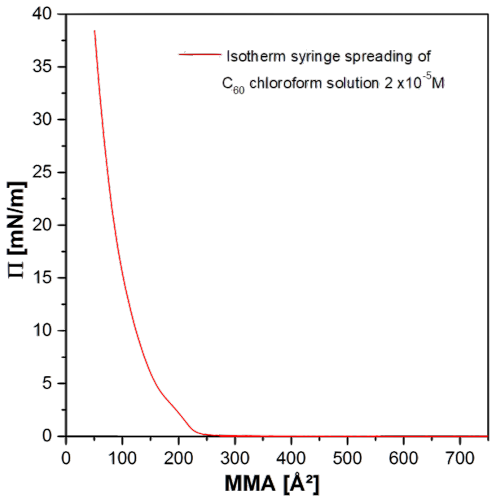

Figure 6.24: LB isotherm for C_{60} chloroform-based solution $\sim 2 \times 10^{-5}$ M.

film was transferred onto TS Au substrate using vertical transfer. In this procedure, the substrate was immersed inside the water surface before the spreading of the molecules. When the barriers were completely compressed, and thus the film formed, the substrate was withdrawn from the water at a fixed speed of 0.5 mm min^{-1}. The transferred film was then blown with nitrogen for a minute and incubated in a vacuum oven (10^{-2}mbar) overnight at 35 °C to let evaporate any solvent residual on the samples.
Transferred Fullerene LB films formed starting by toluene and chloroform solutions and transferred onto a gold substrate are shown in fig.6.25 and 6.26.

Despite the similar characteristics exhibited from the two isotherms relative to C_{60} toluene (fig.6.23) and chloroform solution (fig.6.24), is easy to observe that their morphology was quite different. As shown in fig.6.25, toluene solution-based C_{60} films exhibit small area islands of single layer of fullerene molecules (6.25.b) with thickness of $\sim 0.9 \pm 0.3$ nm, and with the simultaneous presence of chain-like structures with a thickness of 4-5 nm shown in fig.6.25.a and 6.25.c. The formation of chain-like structures was always observed in fullerene LB films formed strarting by toluene-based solutions.
In contrast, the chloroform-based solution displayed in figure 6.26 shows a larger film area, suggesting the formation of a continuous film over the TS Au surface. From the line profile shown in fig.6.26.c relative to the blue line, the thickness of the C_{60} LB film was measured to be 1.12 ± 0.28 nm, which is comparable to the films formed by toluene solutions. Comparing the two layers obtained from the two solutions, the ones formed in chloroform-based solution were chosen for further analysis. In addition, the

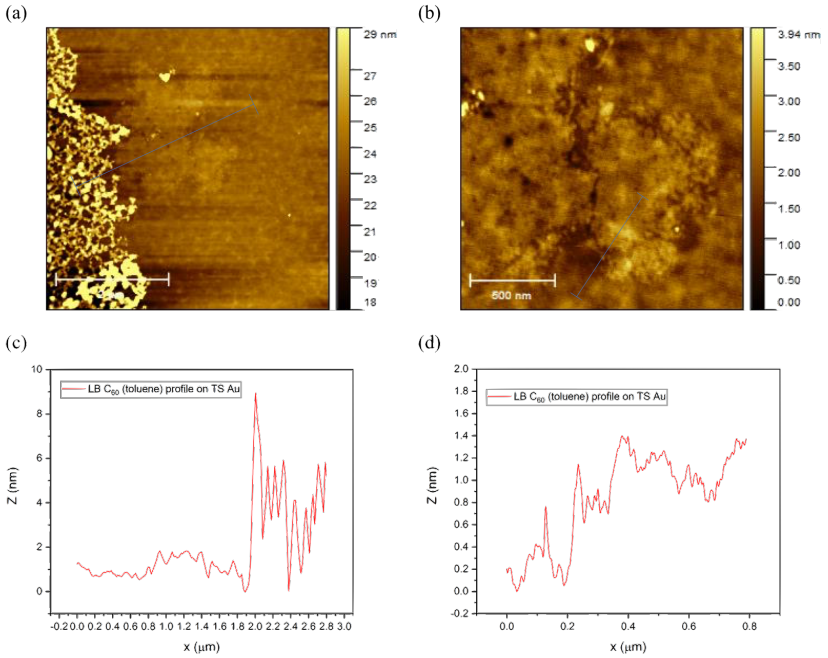

Figure 6.25: AFM topography of C_{60} layer on TS Au obtained from toluene-based fullerene solution in a scan area of 5×5 µm (a) and 1.5×1.5 µm (b) with the respective profiles lines (c,d) corresponded to the blue line and plotted on the bottom of each topography map.

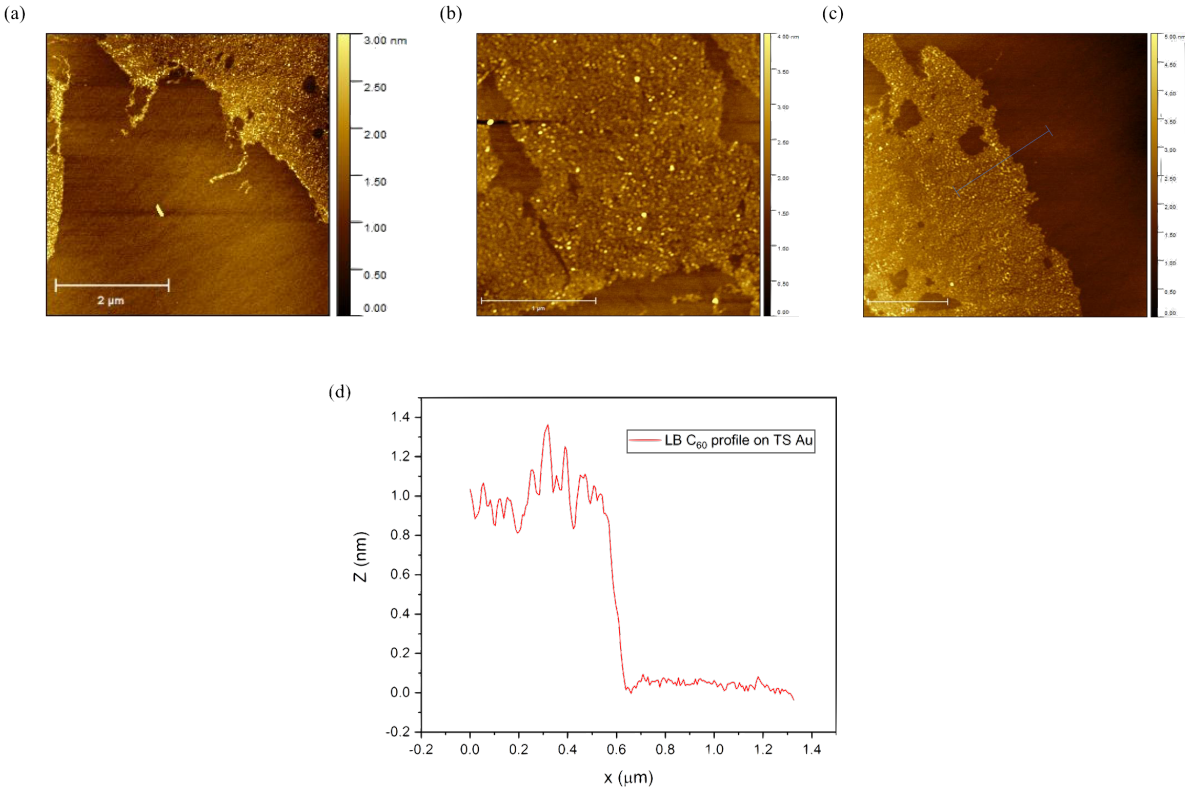

Figure 6.26: AFM mapping of C_{60} LB film on Au (chloroform solution) showing large area films of C_{60} single layer all over the surface (a, b, c). The profile of the LB film is shown in (d), correspondent to the blue line in figure (c).

uniformity of the fullerene layers formed by chloroform solutions allowed the possibility to performed successive dips of the Au substrate into the floating fullerene film, with the consequent controlled formation of multiple layers on top of the formed ML. An example of the second dip of the Au substrate, after the collection of the first C_{60} layer, is shown in figure 6.27.

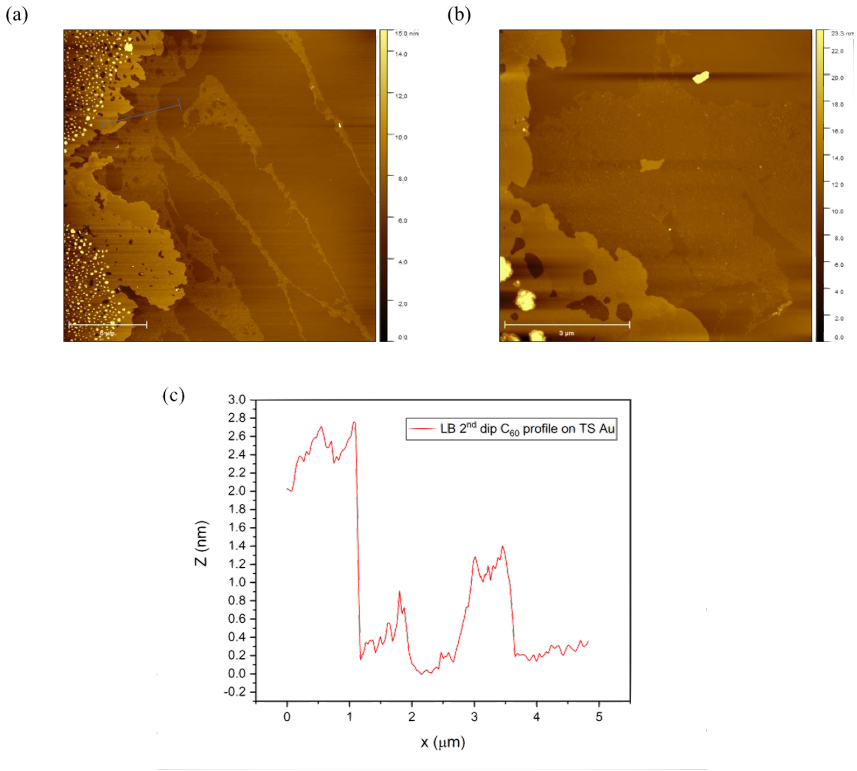

Figure 6.27: Large area AFM topography map 20×20 nm (a) and 7.5×7.5 nm (b) of C_{60} LB films after a second collection of the floating LB C_{60} layer. The profile relative to the blue line in (b) is reported in (c), showing the formation of multiple layers on top of the existent one.

The second dip of the Au substrate in the LB C_{60} film caused the formation of a successive fullerene film on top of the first transferred single layer and is clearly visible in fig.6.27. From the topography images of large area transferred films is still possible to appreciate the first C_{60} layer on the Au surface and underneath the second transferred layer. Interestingly, as can be observed from the profile line of figure 6.27.c, a second pass of the floating fullerene films caused the formation of a second layer with a total thickness of 2.81 ± 0.35 nm which correspond to 3 layers of fullerene stacked on top of each other. The formed layer had a very high degree of uniformity, with very low roughness. In addition, the second passage revealed the presence of thicker clusters of molecules on top of the uniform second layer. The presence of unexpected structures on the surface suggests that the floating fullerene LB film was irreversibly disrupted after

the first Au passage, causing the molecules' aggregation with consequent formation of thicker clusters.

6.2.2 C_{60} SAM

To compare the electric and thermoelectric properties for different C_{60} layer formations, SAMs of fullerene C_{60} were prepared using the same procedure used by *Yoshimoto et Al.* [340]. The C_{60} SAMs were prepared by dispersing the molecules in benzene (99.9%), forming a 10 µM solution. The solution was then deoxygenated for 10 min using nitrogen bubbling.
The TS-Au was immersed into the solutions straight after the deoxygenation. After SAMs growth, the sample was rinsed 5 times with fresh benzene and fresh ethanol to eliminate any physisorbed molecules or residual. The sample was then dried with nitrogen for a minute and incubated in a vacuum oven (10^{-2}mbar) overnight at 35 °C to let evaporate any solvent residual on the samples.

The SAM growth was monitored by QCM with a gold electrode (5 mm diameter, $\sim$ 5 kHz), measuring the electrode frequency before and after the SAM growth. Figure 6.28 shows the measured frequencies and their distributions for the QCM resonator system before and after the SAMs growth onto the QCM electrode.

QCM measurements shown in 6.28.a and 6.28.b display variation of frequency before and after the growth of $\Delta f = 9.62$ Hz which correspond to a deposited mass on the electrode of 135 ng. From equation 5.1, the area occupied per molecules was calculated to be around 140 Å^2. This is a bit higher than expected for C_{60} molecules measured by other groups ($\sim$ 100 Å^2), and giving a surface coverage of 81 %. The differences in coverage can be explained with the QCM electrode's roughness, as discussed for the alkyl thiols SAM counterparts. This assumption is also confirmed looking at fig.6.28.c and 6.28.d, where it is possible to observe a well uniform C_{60} SAM with a thickness comparable to a single fullerene molecule of $\sim$ 0.9 nm and without other physisorbed species on the surface.

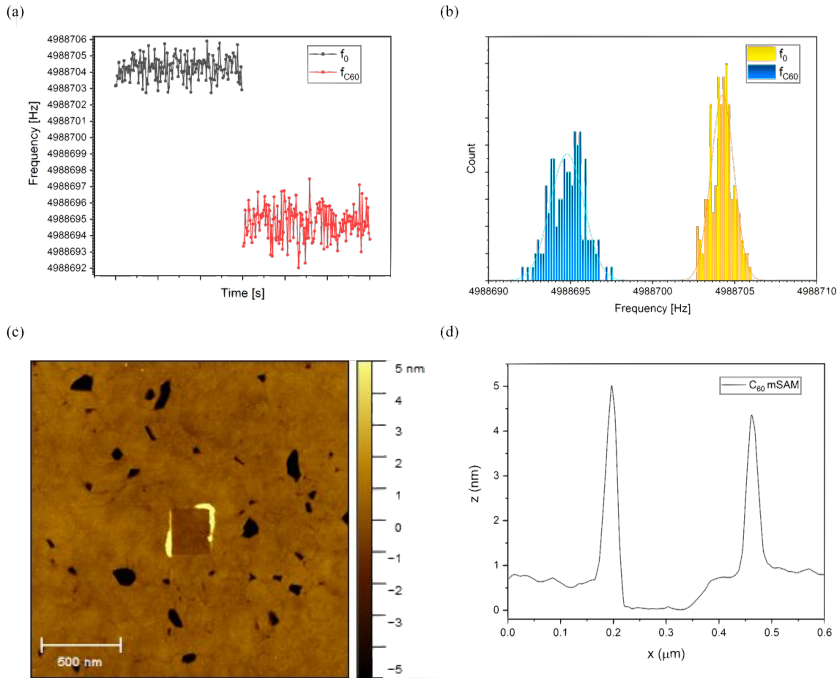

Figure 6.28: (a) QCM electrode frequencies measured for 150 seconds and their distributions (b) before and after the growth of C_{60} SAM. (c) AFM scan 2×2 µm of C_{60} SAM growth on TS Au after a window of 250nm was opened by nano-scratching of molecules. (d) vertical profile measured in correspondence of the scratched window, showing the formation of the SAM.

6.2.3 I-Vs characteristics and electric transport characterisation

The electric properties of fullerene ultra-thin films were characterised by conventional CAFM per each sample made by LB and self-assembled monolayer. In particular, the samples studied were a 1 nm and 2.8 nm C_{60} LB films, corresponding to 1 and 3 molecular units, formed by chloroform solution and transferred onto TS Au, and a 1 nm C_{60} SAM formed in benzene solutions.

The C_{60} LB samples' electrical conductance was studied by conventional electric maps using PF-CAFM and by single-point measurements in order to quantify the conductance of the different films. An example of electric map of fullerene island on Au is shown in Fig. 6.29.

During the mapping performed on the C_{60} clusters of fig.6.29, the bias voltage applied was kept at 2V since no signal from the junction was recorded under the 2V threshold, reflecting the large HOMO-LUMO band gap of fullerene.

The electric conductance of the LB layer shown in figure 6.26 and 6.27, was studied using the CAFM single point measurement. Figure 6.30 shows the I-Vs counter maps for the two C_{60} LB films contacted by the CAFM probe, together with the histograms of the electrical conductance.

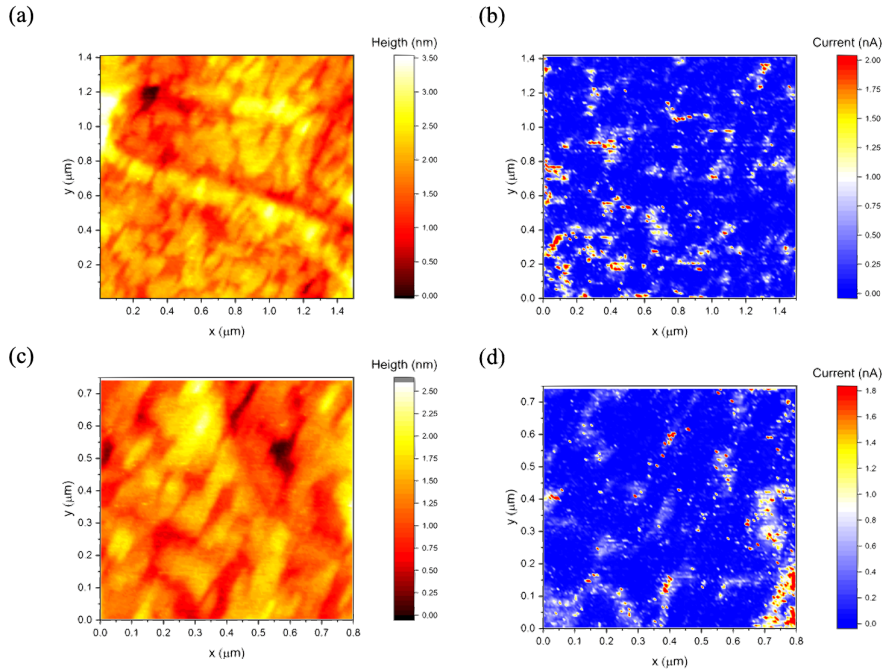

Figure 6.29: Topography (a,c) and current map (b,d) of fullerene clusters acquired with CAFM with 2V bias applied on the junction.

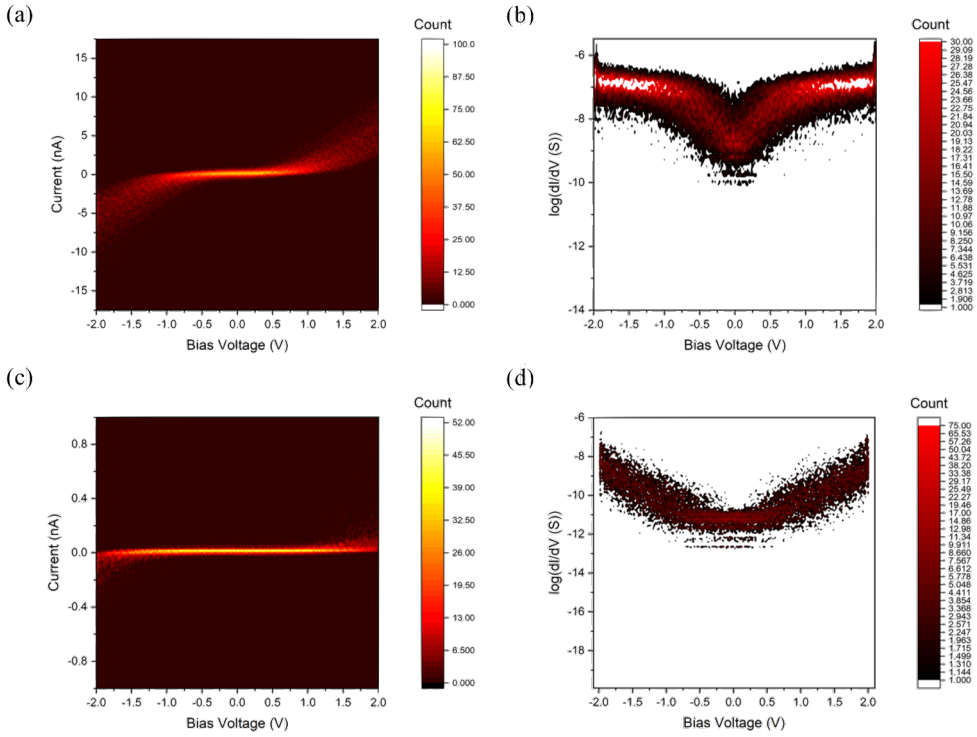

Figure 6.30: CAFM electricAL measurements on C_{60} LB films showing: (a) I-V traces acquired and conductance (log scale) counter map (b) for $\sim$ 1nm LB C_{60} film. The bottom line displays the electrical characterisation performed on 2.8 nm C_{60} film obtained with a second dip in the floating LB C_{60} film. (c) I-V histogram of the acquired values of current by CAFM with the relative conductance values histogram (d).

In the specific the values of G found for the two LB films were respectively $(2.39 \pm 0.19) \times 10^{-9}$ S for 1 nm LB C_{60} and $(3.89 \pm 0.38) \times 10^{-12}$ S for the ~ 3 nm layer.

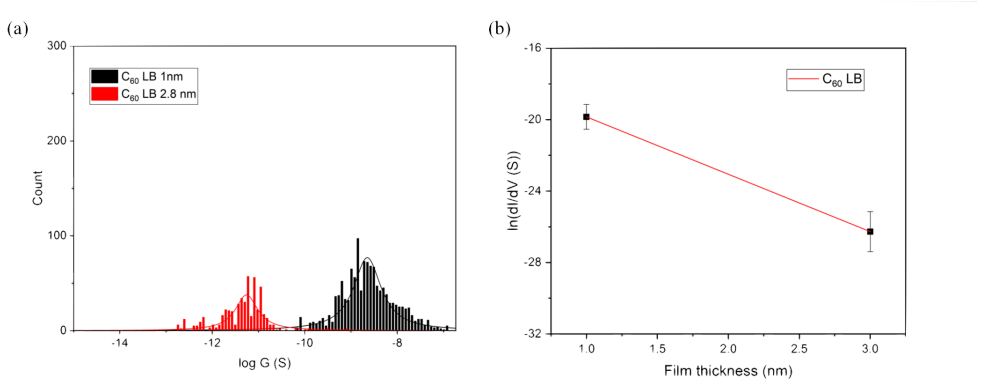

Figure 6.31: (a) Distributions of electrical conductance around $V = 0$ for C_{60} ultra-thin films with different thickness formed by LB; (b) Ln plot of molecular conductance measured for the two C_{60} LB films vs film thickness.

The current decay factor β calculated by interpolations of the two available points it is shown in fig. 6.31. Form equation 6.1, $\beta = 3.56\text{nm}^{-1}$ was calculated, which is in agreement to other reported values of β for conjugated molecular wires linked by covalent bond [291, 341]. However, the low number of points for the β fit is recognised here.

The electric properties of C_{60} SAM samples were studied in the same way used for the LB samples. Despite the multiple attempts in order to form successive physisorbed C_{60} layers on the top of the first SAM, this resulted in a systematic failure of uniform continuous thicker SAMs fullerene molecules, even after 24h of incubation of substrate in the molecular solution.

The C_{60} SAM shown in fig.6.28 presented a thickness of 0.84 ± 0.22 nm, without visible pins/holes structures on the sample surface. Also, no presence of physisorbed molecules on the surface was observed, highlighting the high uniformity of the obtained layer, and also confirmed from the presented QCM analysis of fig.6.28.

Figure 6.32 shows the electrical characterisation performed on the C_{60} SAM sample using CAFM point measurements applying a constant 2 nN normal force from the CAFM Pt Probe.

Interestingly, as it is possible to observe from fig.6.32, the C_{60} SAM sample exhibit a slightly higher electrical conductance at low bias voltage than the LB sample counterpart, but still inside the range of the uncertainties. The value of the film conductance was

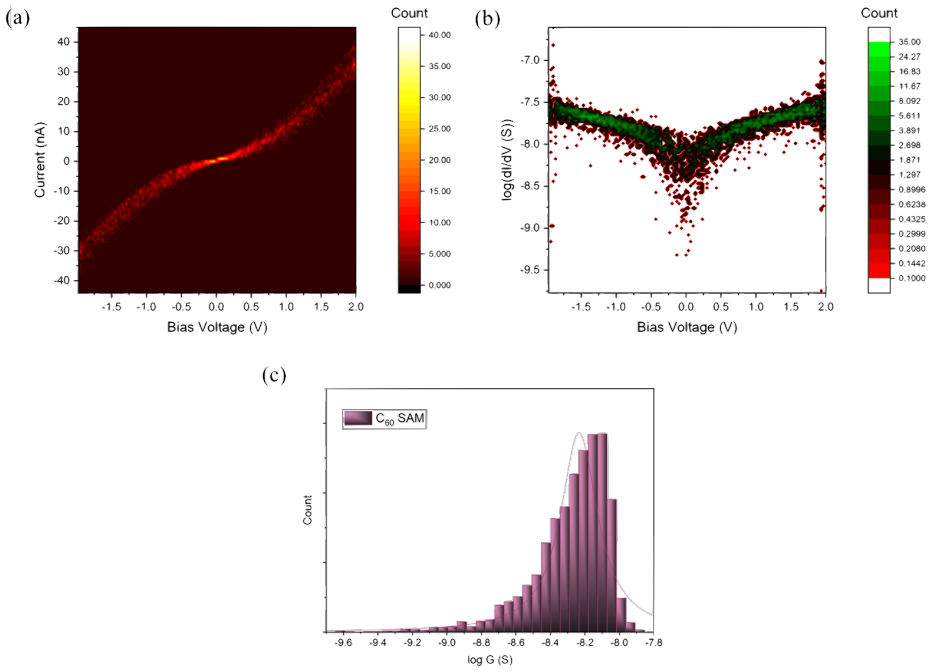

Figure 6.32: (a) C_{60} SAM I-Vs traces acquired with CAFM point measurements; (b) Calculated histogram of electrical conductance G (log scale) and distributions of G values at low bias (± 0.1 V).

measured to be $G = (1.44 \pm 0.41) \times 10^{-8}$ S, almost 5 times higher than the LB 1 nm C_{60} sample and, most likely, to attribute to the better quality of the C_{60} SAM sample. In fact, as is evident from the topography of the LB layer shown in figures 6.26 and 6.27, the films surface, especially in the single layer LB film, is quite rough ($\sim$ 300 pm) and not pretty uniform compared to the layer formed by SAM ($\sim$ 100 pm) and shown in fig.6.28. This peculiar characteristic was also observed in other electric comparisons of molecular film prepared by different methods (see Sec.6.3) but, it is clear here that a better surface uniformity and crystalline structure result in an enhancement of the charge transport even at room temperature, reducing the scattering rate between the electrons and the impurities or defects present in the structure [10, 16]. Also, rough surfaces increase the multiple scattering on the electrons at the interfaces. The higher amount of mismatched molecular structure observed for the LB sample weakens the orbital coupling and consequent suppression of the electrical conductance.

6.2.4 Thermoelectric characterisation

Thermoelectric properties of C_{60} ultra-thin films formed by LB and SAM were tested using ThEFM with the same approach used in the previous section. The temperature difference ΔT was supplied by the calibrated electric heater, and the Seebeck coefficient of the films was measured via equation 6.2. The measured thermal voltage for the two LB samples of 1 nm and 2.8 nm and the SAM C_{60} sample (0.87 nm) are shown in figure 6.33.

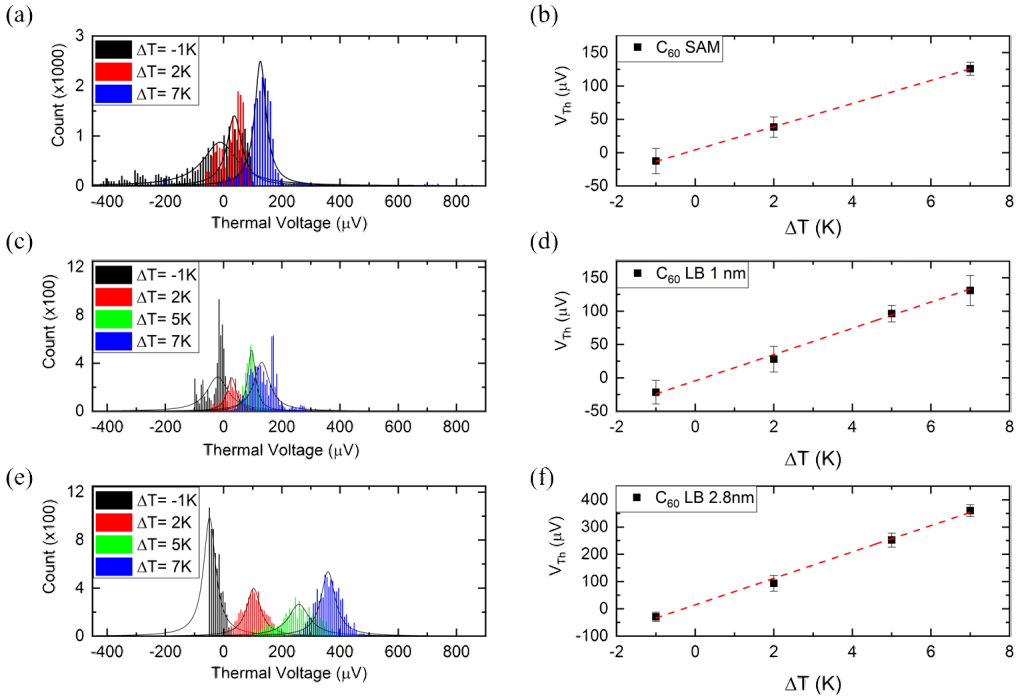

Figure 6.33: Thermoelectric characterisation of C_{60} ultra-thin films prepared by SAM and LB. (a,b) C_{60} SAM thermal voltage distributions and average thermal voltage vs ΔT, measured with ThEFM single point measurement. Red dashed line represents the linear fit of the measured data; (c,d) 1 nm C_{60} LB film thermal voltage distributions for four different $\Delta T = -1, 2, 5, 7$ K applied and plot of average value of Thermal voltage vs ΔT; (e,f) Measured thermal voltage values per each temperature difference applied and plot of thermal voltage vs ΔT for 2.8 nm C_{60} LB film.

The thermal voltage plots against the temperature difference ΔT presented in fig. 6.33 shows a positive slope of the thermal voltage per temperature difference for all the three C_{60} samples, which means negative Seebeck, sign based on the definition of Seebeck coefficient $S = -\Delta V/\Delta T$. In addition, the negative sign of S suggests the transport properties are LUMO dominated [41, 242, 325].

For the two C_{60} LB samples of 1 nm and 2.8 nm, corresponding to 1 and 3 C_{60} layer respectively, the measured Seebeck coefficient S from the plot (d), (f) of figure 6.33 were $S_{1nm} = -19.66 \pm 0.95$ μV K^{-1} and $S_{2.8nm} = -46.64 \pm 1.35$ μV K^{-1}.

The value of the Seebeck coefficient measured for the two LB samples is moving towards more negative values and, in particular, 2.8 nm of C_{60} film thickness gave the relative high value of $-46.64\ \mu V\,K^{-1}$, in good agreement with the trend observed form *Evangeli et Al.* [37] using an STM-BJ system to probe the thermoelectric properties of single C_{60} molecular junction. This effect was expected since increasing the numbers of C_{60} molecular units in-between the junction shrinks the HOMO-LUMO gap. This will sharpen the transmission resonance close the Fermi Energy E_f of the system, causing an enhancement of the thermoelectric properties of the C_{60} film.

The C_{60} SAM sample displayed a Seebeck coefficient $S_{SAM} = -17.21 \pm 0.84\ \mu V\,K^{-1}$ which is still in good agreement with the literature values for similar systems and very close to the S value found for 1nm C_{60} LB sample [270, 271]. The Seebeck value measured for the C_{60} SAM was slightly lower than the LB sample with comparable thickness. The difference in the measured Seebeck can be, one more time, explained by the big difference in the packing structure of the films obtained by SAM and LB. Indeed, defects in the structure, rough surfaces, and lattice mismatch present in the LB samples further sharpen the transmission function near E_F, with consequent enhancement of the thermoelectric properties.

The comparison of the Seebeck coefficient distributions measured for the three C_{60} ultra-thin films prepared by different techniques is presented in figure 6.34.

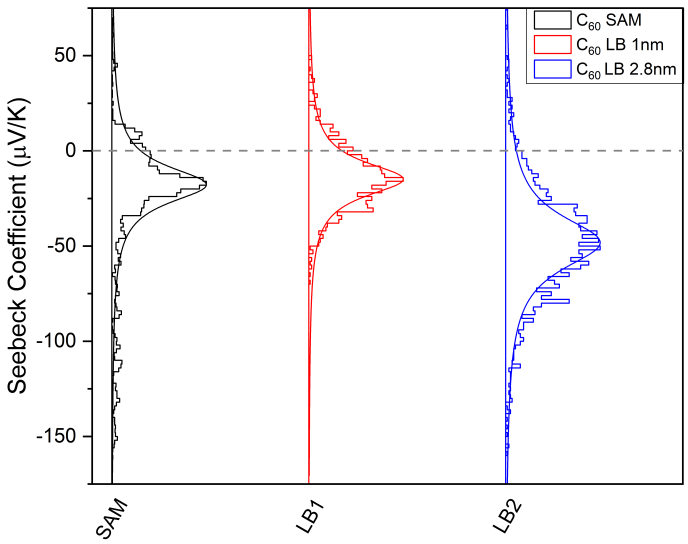

Figure 6.34: Comparison of Seebeck coefficient distribution of C_{60} ultra-thin films on TS Au formed by self assembly and Langmuir-Blodgett measured by ThEFM.

From these measurements, it appears that C_{60} ultra-thin film prepared by the LB technique are superior for TE application for several different reasons. Firstly, the main advantage of LB is the ability to deposit controlled numbers of molecular layers with a high grade of precision. Therefore, in principle, it would be possible to further increase the thermal power of these systems by increasing the numbers of the π stacked C_{60} layers. In addition, the non-perfect close-packed structure of LB films further enhances the thermal power of the C_{60} films, as discussed. Another factor that played a significant role in the samples' thermoelectric properties is the thermal conductance of the junction. This factor is indeed crucial for the complete characterisation of the thermoelectric properties of the C_{60} film.

The thermal conductance κ of the C_{60} LB films was studied using Scanning thermal microscopy (SThM). The thermal conductance of the molecular films was derived from the voltage drop of the SThM thermal probe, using the methodology recently published by *Spiece et Al.* for the thermal conductance modelling under ambient condition. An example of a thermal map performed on C_{60} LB layer presenting multiple thicker structures on the film surface is shown in fig. 6.35 together with its topography.

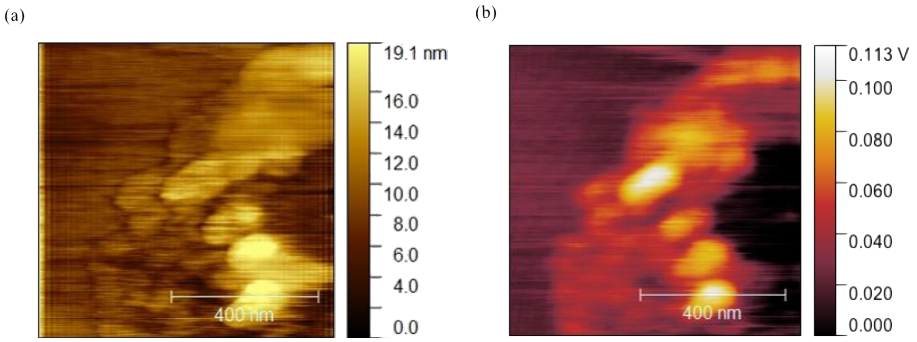

Figure 6.35: SThM mapping of C_{60} LB surface (750x750 nm scan area). (a) Topography of the film surface and (b) probe temperature map.

As already explained elsewhere, the contrast of the thermal map in fig.6.35.b represents the drop variation of the thermal resistance of the probe when in contact with the sample surface. In particular, brighter contrast of the thermal maps represents regions of the sample with lower thermal conductance than the regions with darker contrast. The SThM thermal probe was placed in the different region exhibited different contrast. The point measurements spectroscopy were performed with a continuous approach and retract of the thermal probe on the C_{60} film surface and measured its voltage drop. An

example of voltage drop recorded for 1 nm and 10 nm LB C_{60} films is reported in figure 6.36, showing the difference in the thermal resistance variation with the increase of the numbers of molecular layer in LB films.

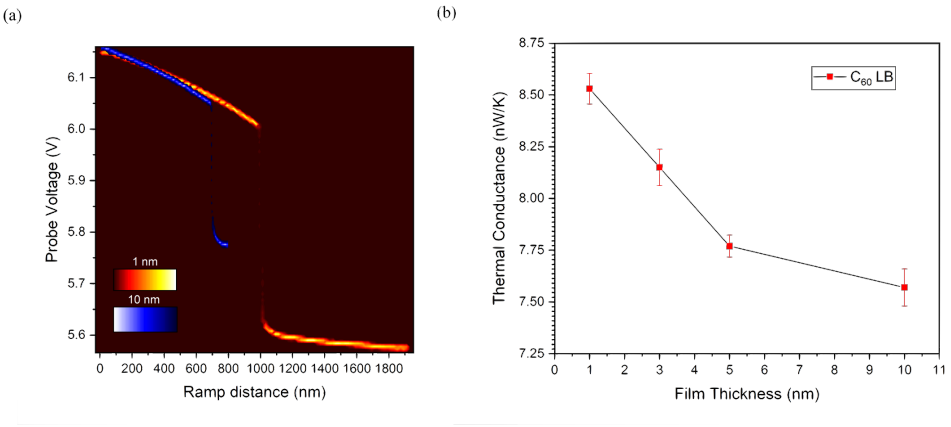

Figure 6.36: Example of thermal transport study on C_{60} LB film of 1 nm (red) and 10 nm (blue). (a) Thermal probe voltage drop vs ramp distance. The drop of the voltage represents the point in which the contact probe/sample was established; (b) Plot of thermal conductance of C_{60} film prepared by LB and calculated following the model developed by *Spiece et Al.* starting from the analysis of the point measurement shown in (a).

The dependence of the thermal conductance of the C_{60} LB film on the film thickness is shown in fig.6.36.b. From the plot, it is possible to observe a drop of the thermal conductance as the C_{60} film thickness increases due to weak π intermolecular coupling between C_{60} molecules layers in the z direction, weakening the phonon transport across the junction [330]. The drop of the thermal resistance of the SThM probe (see fig.6.36.a), was higher for 1 nm C_{60} than for the 10 nm C_{60} film. This characteristic could be attributed to the suppression of phonon transport. In fact, in the thicker molecular films, other heat transport process, like radiative heating, are dominating.

LB C_{60} thin films appear quite promising for TE applications, exhibiting high S already at 2.8 nm. However, the low electric conductance recorded for $\sim$ 3 nm, make these materials quite far from the thermoelectric goal of $ZT = 3$. The values of electrical conductance G, Seebeck Coefficient S and thermal conductance κ are reported, together with the calculated figure of merit Z, in table 6.4.

Film	Thickness (nm)	G (nS)	$S(\mu V\,K^{-1})$	k (nW/K)	Z
SAM	0.84 ± 0.21	14.4 ± 4.16	-17.2 ± 0.74		
LB1	1.12 ± 0.28	2.39 ± 0.19	-19.66 ± 0.65	8.53	1.08×10^{-10}
LB2	2.81 ± 0.35	$(3.89 \pm 0.38) \times 10^{-3}$	-46.64 ± 1.25	8.10	1.04×10^{-12}

Table 6.4: Resuming table for the values of conductance G, Seebeck coefficient and thermal conductance for the three C_{60} samples studied.

6.3 Tetraphenyl Zinc Porphyrin (Zn-TPP) thin films

In analogy to the work performed on the C_{60} ultra-thin films prepared with different techniques and π stacked by LB technique, here the electric and thermoelectric characterisation on Zinc Tetraphenyl porphyrin (Zn-TPP) realised by self-assembly technique, and LB are presented.

The interest in studying metallo-TPP ultra-thin films mostly lies in the stronger π interaction with each other [342–344] compare to fullerene C_{60} molecules and the possibility to easily alter the charge state of the metal core by chemical doping. The latter feature of this particular family of molecules makes metallo-TPP a promising molecule to explore quantum interference at room temperature to tailor and enhance the thermal power of molecular vertical junction.

The Zn-TPP ultra-thin films were formed on TS Au by self-assembly monolayers (SAMs) and Langmuir-Blogget (LB) deposition. Atomically flat template stripped (TS) gold (roughness $<$ 100 pm) was used as a bottom electrode for SAMs growth. The SAMs growth condition of Zn-TPP on Au followed the same parameter published by *Yoshimoto et al.* in 2004 [340]. The relationship between the number of molecules adsorbed on the substrate surface and the growing time was monitored via by quartz crystal microbalance (QCM) as shown in figure 6.37.

The thickness of the self-assembled film measured by AFM nano-scratching after 60 second growth was 0.45 nm which corresponds to a monomolecular layer of Zn-TPP. The QCM results displayed in fig.6.37 show the molecular density of the monolayer film is 0.98 $\mu mol\,m^{-2}$, corresponding to 169 $Å^2$ per molecule. Both QCM and AFM nano-scratch indicated the molecules continuously adsorbed on the sample surface even after monolayer formation. In contrast with the fullerene SAM growth, where no molecules were grown after the first layer of C_{60} molecules, this effect was quite expected as it has been reported that metallo-porphyrins are favoured to form multi-layered structures due to π stacking.

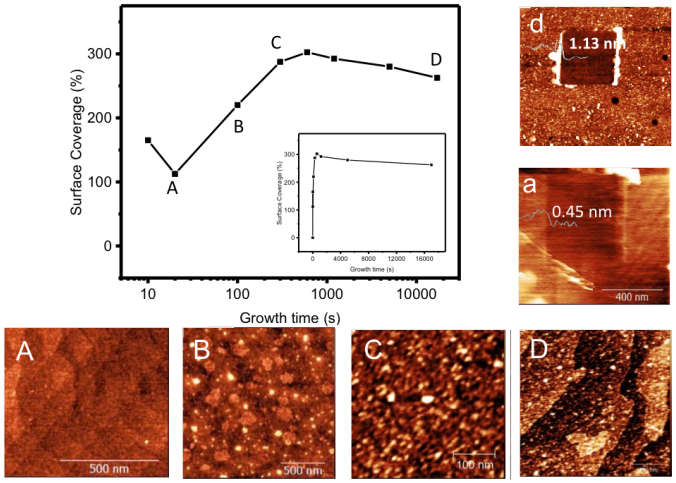

Figure 6.37: QCM analysis of Zn-TPP SAMs grown on Au substrate showing the surface coverage percentage as function of growing time in logarithmic and linear scale (insert). A,B,C,D represent the AFM topography images correspondent to the relative point shown in the QCM analysis of Zn-TPP. The AFM scan a and d show the film thickness of Zn-TPP at the point A and D of the surface coverage plot.

After 3 hours of growth, the averaged film thickness is 1.1 ± 0.3 nm (corresponding to 3-4 layers of molecules), and the film's molecular density is 2.7 µmol m^{-2}. This growing trend was observed to be "gentle" for long growing as the film thickness and molecular density on the substrate after 12 hours of growth resulted similar to the one with 3 hours growth.

The LB film formation was performed after the optimisation of volume, concentration and final MMA limiting area in the same way as the analysis conducted for the formation of C_{60} LB films. For the film formation 150 µL (3×10^{-4} M) Zn-TPP solution in toluene was evenly distributed on the water sub-phase using a glass micro-syringe dispensing 5 µL each droplet. A chromatography paper over-saturated with water was used for surface pressure monitoring, and the motion of the barriers was set to 5 mm/min. The LB isotherm of Zn-TPP was studied before the film deposition onto Au substrate, and the thickness and the topography of the film were characterised by AFM. As is possible to see in figure 6.38, clear phases transitions were observed when the molecular occupation area reaches 206 $Å^2$, where the molecules of Zn-TPP started to interact with each other.

Further compressing the LB barriers, the molecules will go through the liquid phase and, at the end, when the intermolecular distance is approaching the cross-sectional

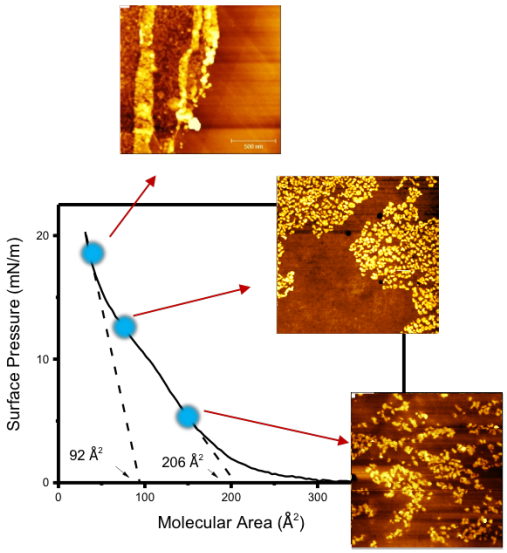

Figure 6.38: LB isotherm of Zn-TPP in toluene solutions and AFM images of the transferred film in the different highlighted on the isotherm plot.

area of the molecules, the molecules will form a close-packed structure, highlighted by the change of phase visible in fig.6.38. The TS gold substrate was dipped into the water surface in order to collect the floating Zn-TPP on the water surface at different surface pressures corresponded to the changes of phase of the molecules shown by the blue circles in figure 6.38 in order to study the evolution of the LB film during the compression of the molecules. The AFM topographies relative to the blue circles correspondent to different phases of the Zn-TPP are also shown in figure 6.38. In particular, it is worth noting that the film transferred onto the Au substrate at 92 $Å^2$, and corresponding to a solid-like phase of the Zn-TPP molecules, exhibited multiple molecular layers and wrinkles-like structures on the top of the LB films, indicating the formation of a thicker layer before the molecules reach the solid phase.

From the AFM topography images of the LB Zn-TPP films, it is clear that the deposited film's thickness and density can be easily controlled by solution concentration and the dipping point of surface pressure. Since the thicker structure was observed at 92 $Å^2$, the dipping point was kept in between the latter point and 206 $Å^2$. In fact, this particular point showed the presence of a thinner continuous film of Zn-TPP and thicker structures on top of the thinner layer.

However, despite the different attempt in forming a monomolecular layer of Zn-TPP, we failed to obtain single-layered molecular film by LB method due to the strong inter-molecular interactions of the molecules, which tend to form thicker clusters and island of molecules and thus, the thinnest film transferred onto the TS Au was about 1.3 nm as displayed in figure 6.39.

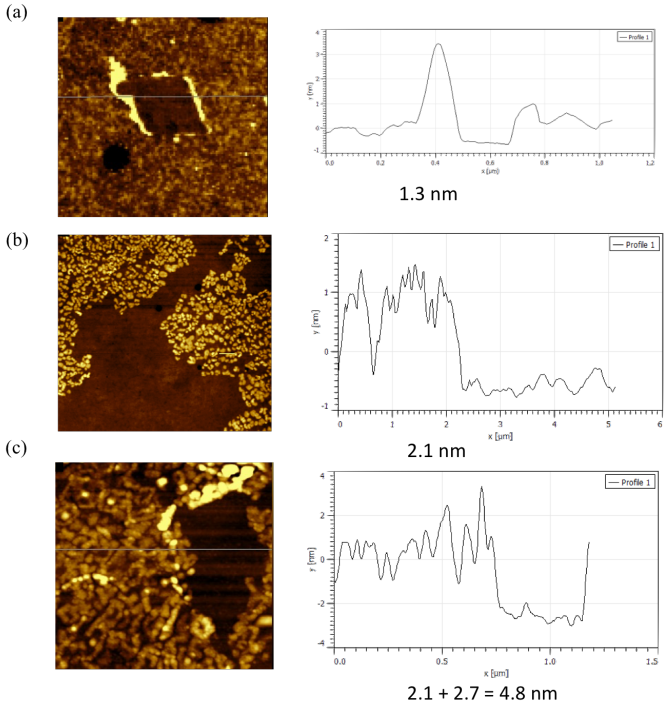

Figure 6.39: AFM topography of Zn-TPP ultra-thin films obtained by LB technique with height profiles analysis for (a) single LB dipping (thin area), (b) single LB dipping (thick area) and (c) double LB dipping.

The thicker film of Zn-TPP of figure 6.39.b corresponds respectively to the thicker area of the LB film obtained in the midpoint between 92 $Å^2$ and 206 $Å^2$. This film exhibits a thickness of 2.1 nm, while the Zn-TPP film shown in 6.39.c was obtained by a second immersion of the sample into the floating Zn-TPP film and led to the formation of a 4.8 nm thin film on the Au substrate.

The electric and thermoelectric properties and characteristics of LB and SAMs Zn-TPP ultra-thin films were studied using CAFM and ThEFM, comparing the different thickness, preparation methods and quality of the film.

6.3.1 I-Vs characteristics and electric transport characterisation

The electric transport of Zn-TPP multilayers π stacked created with LB and SAM was compared starting from the analysis of the I-V traces collected per each sample, using single point CAFM measurements. The I-V histograms of the 3 LB Zn-TPP films with thicknesses of 1.3 nm, 2.1 nm and 4.8 nm respectively, are presented in figure 6.40.

As is observed from the I-V traces in (a),(c) and (e) of fig.6.40, the current drops dramat-

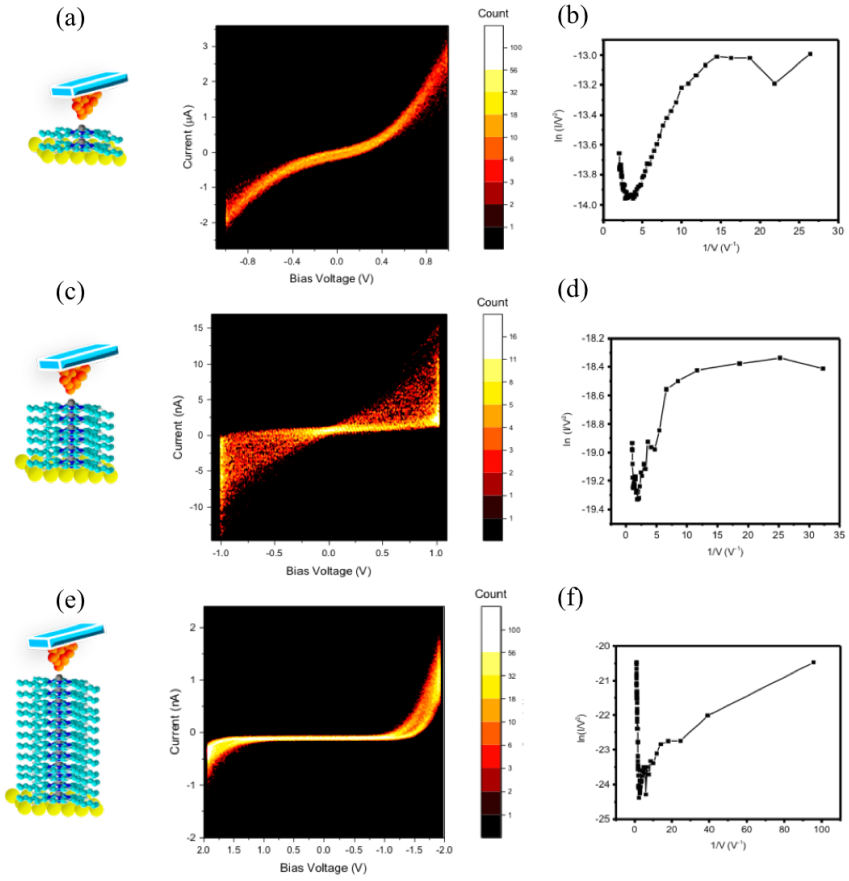

Figure 6.40: I-Vs traces acquired by CAFM of (a) 1.3 nm, (c) 2.1 nm and (e) 4.8 nm LB Zn-TPP. Images (b), (d) and (f) represent respectively the Fowler-Nordheim plot of the averaged I-V curves of LB Zn-TPP layers with different thickness.

ically once the numbers of molecular units, and therefore the film thickness, increases. In addition, as shown in (b), (d) and (f), from the average I-V plot obtained directly from the I-V traces acquired per each Zn-TPP sample, Fowler-Nordheim plots $\ln(I/V^2)$ vs $1/V$ were produced in order to better understand the transport mechanism, and have a qualitative idea of the evolution of the HOMO-LUMO gap of the films while the number of layers increases.

As described in Chapter 4, the minimum point in the F-N plots, known as transition voltage V_{trans}, is correlated with a transition of the charge transport regime, passing from a coherent tunnel to hopping or other field effect transport regimes, when the bias voltage increase as described by equations 4.1 and 4.2. Furthermore, it is possible to demonstrate that the transition point V_{trans} gives an indication of the bandgap size and, in this particular case, it is easy to observe how the transition voltage value V_{trans} moves towards lower V^{-1}, which indicates a shrinking of the HOMO-LUMO gap of Zn-TPP. There is nothing to be surprised about this characteristic since, theoretically, the addition of molecular units usually reduce the bandgap [208, 345, 346].

The electrical conductance values G at low bias voltage (0.1 V) for the three LB layer are compared in figure 6.41.

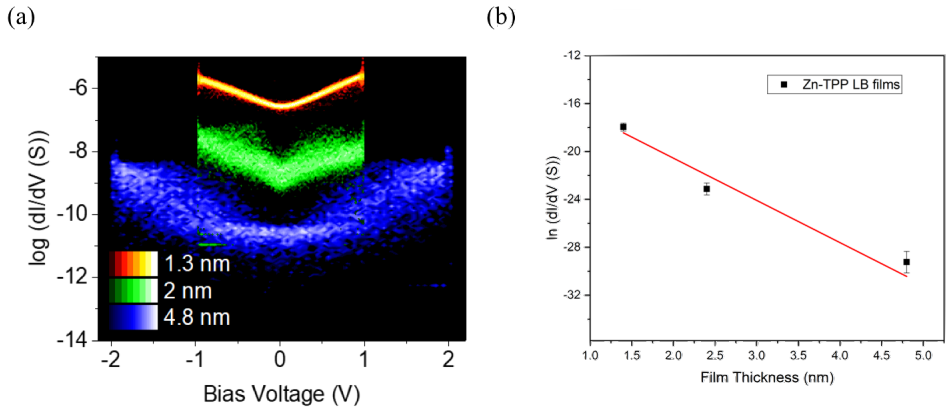

Figure 6.41: (a) Comparison of electrical conductance G histograms of LB Zn-TPP (log scale) and plot of natural logarithm of G against film thickness (b).

As already mentioned, from comparing the G values of the 3 LB films shown in figure 6.41.a, we can observe the drop of the electrical conductance of the films when the thickness increases, in agreement with the data obtained for C_{60} LB films and OPI systems [166].

A linear relationship between ln(G) vs film thickness was observed for the LB π stacked layers of Zn-TPP, which means the transport follows the tunnelling regime, even though the film thickness is already lying in the hopping region for reported covalently bonded systems found in literature [167, 217, 218].

The tunnelling decay coefficient β measured for Zn-TPP LB ultra-thin film was $\beta = 3.1 \pm 1.1$ nm^{-1}. The β value is similar to other reported values of conjugated molecular wires linked by covalent bond (for example, OPE wire ~ 2 nm^{-1} [291], OAE wire ~ 3.3 nm^{-1} [341], acene wires ~ 3.1 nm^{-1} [347], which means the height of the energy barrier do not increase too much with the absence of covalent linker. This, in particular, is quite promising because maintaining the electrical conductance and minimise the thermal conductance is vital for ZT optimisation in thermoelectric applications.

The electric transport regime was also studied for the Zn-TPP films prepared by self-assembly as described previously. The I-V traces recorded by CAFM for 0.45 nm Zn-TPP SAM is shown in figure 6.42.

The Zn-TPP SAM layers exhibit higher electrical conductance $\sim 10^{-6} S$ compared to the LB films studied, reflecting the thinner molecular barrier in-between the two metal electrodes (Au substrate and Pt CAFM probe) and the high order in the crystalline

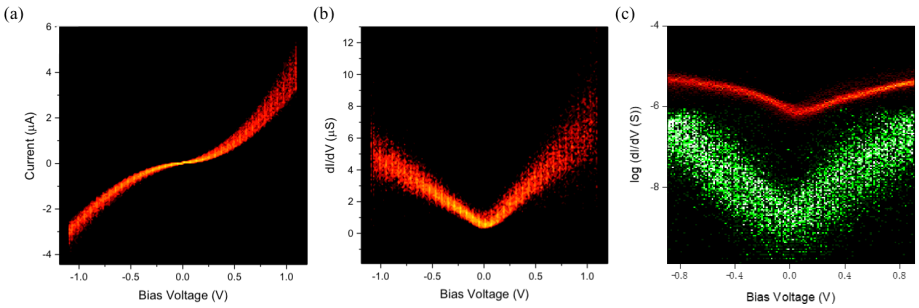

Figure 6.42: (a) Counter map of I-V traces of 0.45 nm Zn-TPP SAM on TS Au and histogram of the conductance values (b), derived from the I-V traces. (c) Comparison of electrical conductance in log scale of 0.45 nm (red) and 1.1 nm (green) Zn-TPP SAM.

structure of the Zn-TPP film. The values of the conductance of the two studied SAM Zn-TPP films shown in fig.6.42.c, and corresponding 1 and 3-4 Zn-TPP layers, were plotted in natural log scale in figure 6.43 for the comparison with the values obtained for the LB Zn-TPP π stacked films.

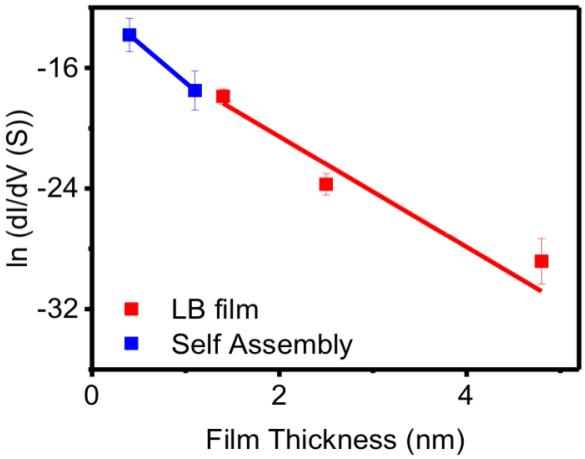

Figure 6.43: Plot of molecular conductance of Zn-TPP film prepared with different method vs thickness of films.

From the plot of ln(G) vs film thickness, a linear dependence of the electrical conductance as the thickness of molecular film increases was observed in all types of films. Fitting the data presented in figure 6.43 with equation 6.1, a current decay factor $\beta = 3.7 \pm 1.3$ nm^{-1} was found for the layers of Zn-TPP formed by self-assembly monolayer. The β found for the SAM was in good agreement with the β factor found for the LB films of $\beta = 3.1 \pm 1.1$ nm^{-1}, which confirm that the main transport regime at low bias is governed by resonant tunnelling of the electrons through the molecular barrier, no matter the preparation method used for the π stacking film formation.

6.3.2 Thermoelectric Characterisation

The Seebeck of the Zn-TPP ultra-thin film was measured by Thermoelectric Force Microscopy (ThEFM), following the same procedure and set-up employed in the previous Sections. The temperature difference, ΔT, was generated from the electric heater under the sample substrate, and the Seebeck Coefficient S, was calculated through equation 6.2.

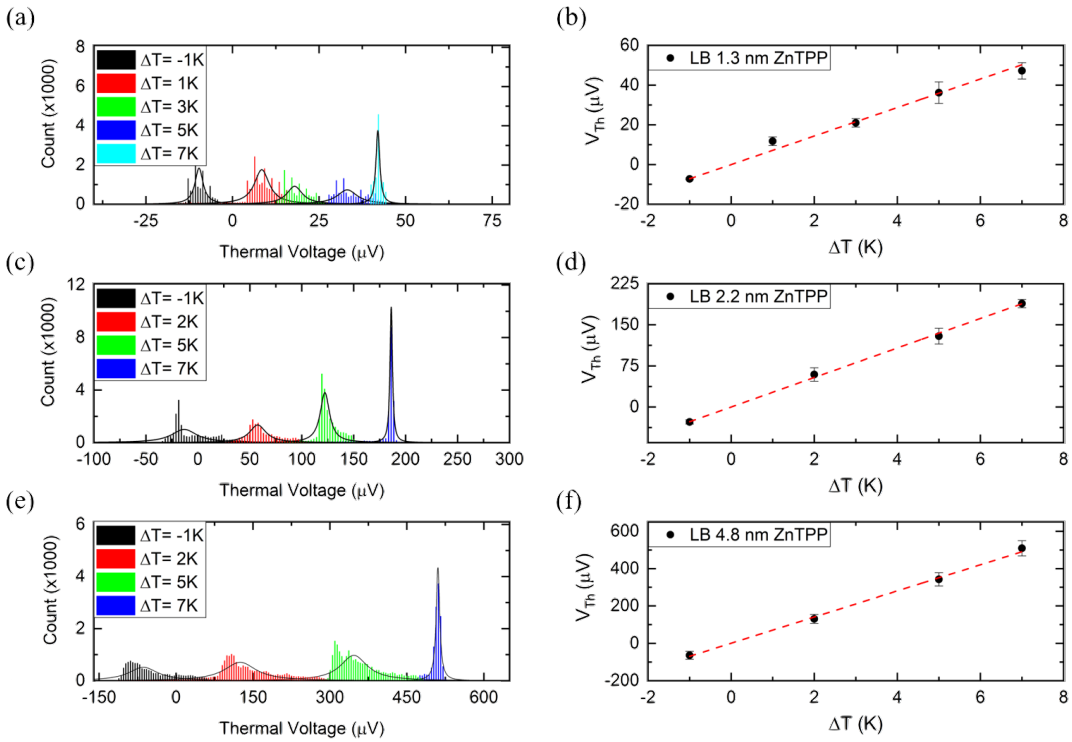

Figure 6.44: Thermal voltages distributions per each temperature difference applied between the Zn-TPP LB films and the ThEFM Pt probe for 1.3 nm (a), 2.2 nm (c) and 4.8 nm (e) LB Zn-TPP films; (b), (d), (f) average thermal voltages derived form the distributions of each molecular film plotted against ΔT.

The thermoelectric measurements performed on the Zn-TPP films of different thickness formed by LB technique are reported in figure 6.44, showing the distributions of the different thermal voltages acquired per each temperature difference ΔT and the plot of the thermal voltage vs ΔT used for the calculation of the Seebeck coefficient of the films formed by LB.

All measured LB films exhibited a positive slope of the thermal voltage, which meant negative Seebeck values for the Zn-TPP sample formed by LB π stacking. As for the measured C_{60} thermoelectric properties, the negative sign of the Seebeck coefficient for the Zn-TPP films emphasises the LUMO dominated transport. The values obtained for the three LB films were $S_{1.3} = -7.1 \pm 4.3\ \mu V\,K^{-1}$, $S_{2.2} = -26.93 \pm 9.61\ \mu V\,K^{-1}$ and

$S_{4.8} = -68.47 \pm 5.72\ \mu V\,K^{-1}$, respectively for 1.3, 2.2 and 4.8 nm Zn-TPP LB films. Using the same protocol, the thermal power of Zn-TPP films formed by self-assembly in solution was studied. The thermal voltage distribution values for the two Zn-TPP SAM films per each temperature, and the relative plot of the thermal voltage against the temperature difference applied in the junction by the electric heater, are reported in figure 6.45.

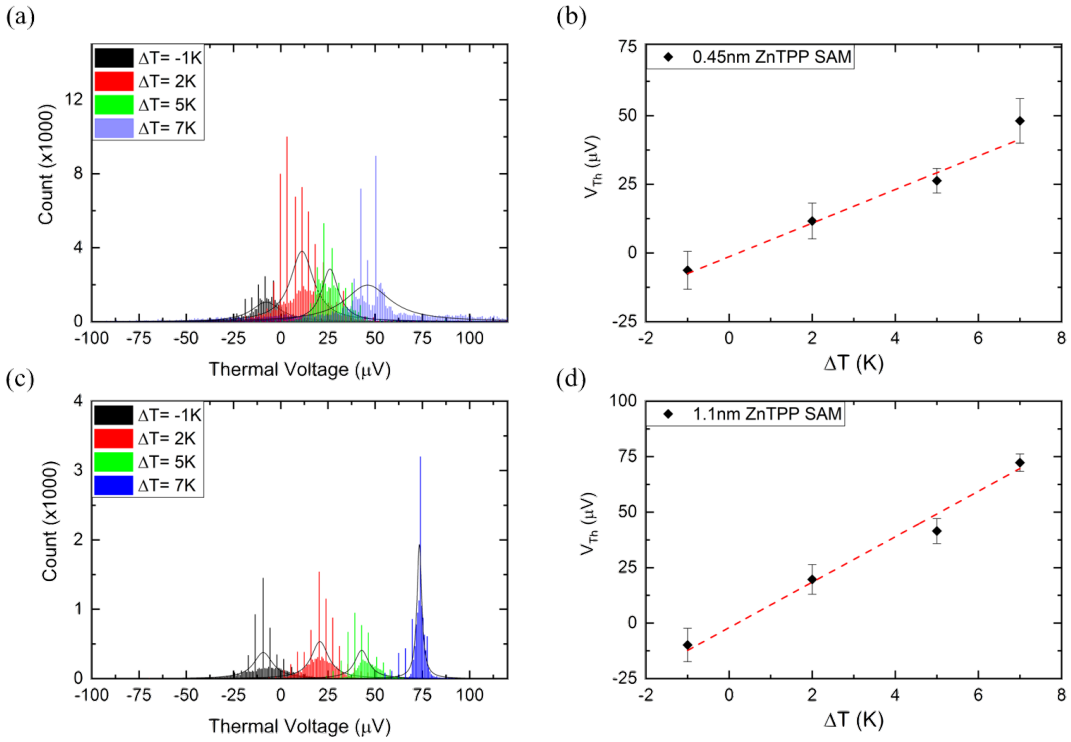

Figure 6.45: Distribution of the measured thermal voltages per each temperature difference in Zn-TPP SAM films with thickness of 0.45 nm (a) and 1.1 nm (c). (b, d) plots of average thermal voltages derived from the correspondent thermal voltage distributions against temperature difference for single layer Zn-TPP SAM (b) and 3-4 layer Zn-TPP SAM (d).

Again, from the plot (b) and (d) of fig.6.45, the films show negative Seebeck coefficient of $S_{0.45} = -6.4 \pm 1.72\ \mu V\,K^{-1}$ and $S_{1.1} = -9.1 \pm 2.9\ \mu V\,K^{-1}$ for the 0.45 nm and 1.1 nm Zn-TPP SAMs correspondingly. In analogy with the results obtained for the C_{60} SAM, the Zn-TPP layer formed by self-assembly shows a slight discrepancy with the Seebeck to their LB equivalent, as a direct consequence of the different film structural quality rising from the two preparation techniques.

The values of the Seebeck coefficient, obtained for each preparation methods, are plotted all together as a function of film thickness, as reported in figure 6.46.

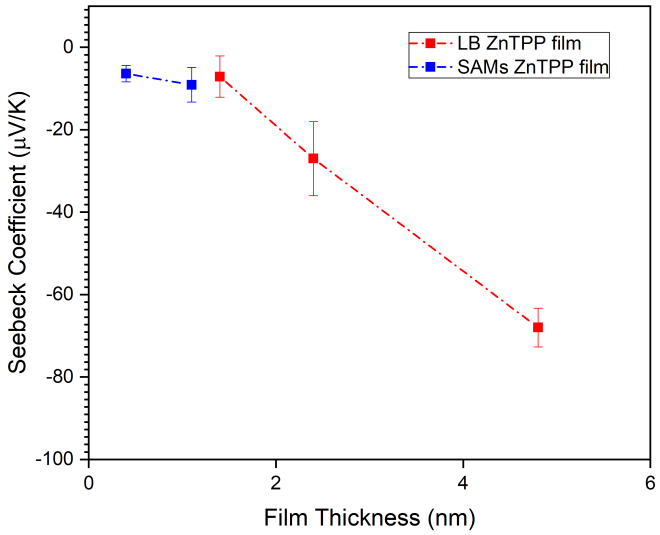

Figure 6.46: Comparison between Seebeck coefficients and film thickness for Zn-TPP films prepared by different methods.

It is clear from the plot of fig.6.46 how the Seebeck coefficient increases linearly with increasing film thickness due to the shrinking of the HOMO-LUMO gap, sharpening the resonance of the transmission function, as explained already for the fullerenes films. Furthermore, it is worth noting that the Seebeck coefficient for 4.8 nm Zn-TPP LB film was measured to be $S_{4.8} \approx -70\ \mu\mathrm{V\,K^{-1}}$, higher than any previous Seebeck value reported molecular thin film.

The experimental results were then compared with DFT simulations performed in Lancaster University by the Theoretical Molecular Transport Group of Professor Colin Lambert. From the DFT calculations shown in figure 6.47 it is possible to observe a high degree of agreement between the measured electrical conductance of the Zn-TPP films with different thickness and the simulations.

The theoretical decay factor $\beta = 3.1\ \mathrm{nm^{-1}}$ was in agreement with the β values measured by CAFM for Zn-TPP prepared with LB and SAM. Within some limits, the theoretical Seebeck coefficient reflects some of the found values for the thinner Zn-TPP films' thermal power but did not match the measured thermal power of thicker Zn-TPP layers. The discrepancies between some S measurements and the simulations performed were attributed to the presence of the films' defective structure as well as the fact that in principle, from our measurements, it is not possible to establish, with 100% of certainty, where the Fermi energy E_f lies.

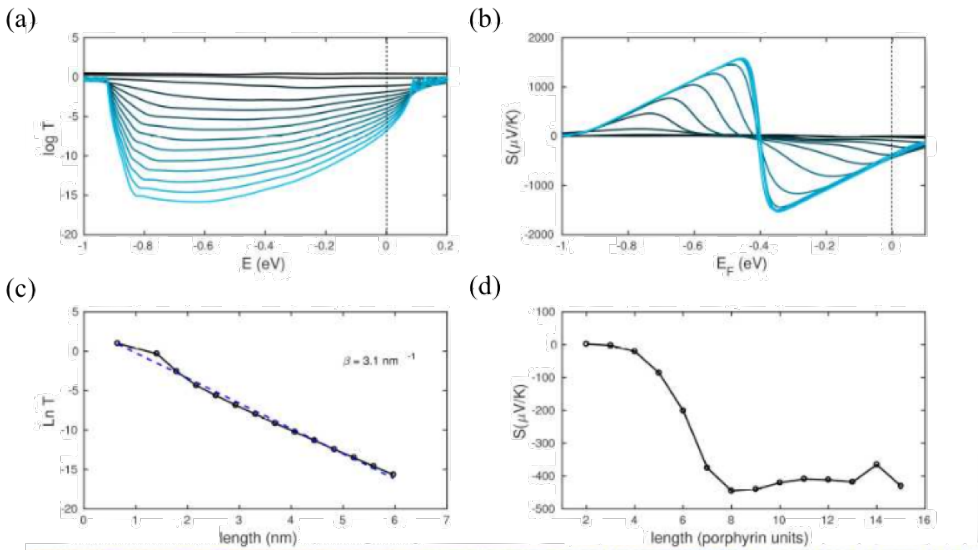

Figure 6.47: (a) Transmission function of Zn-TPP as a function of Fermi Energy position of the junction of increasing numbers of stacked Zn-TPP; (b) Calculated Seebeck coefficient for increasing numbers of Zn-TPP molecular units in the junction. (c,d) Values of transmission function and Seebeck coefficient calculated from (a) and (b) at $E_f = 0$.

To conclude the thermoelectric characterisation of the Zn-TPP samples, the thermal conductance of the samples was measured by scanning thermal microscopy. In analogy to the measurement done for the C_{60} sample, the films' thermal conductance was measured by quantifying the drop of voltage of a resistive probe when the tip-sample contact is established. The SThM map of LB Zn-TPP samples is displayed in figure 6.48, showing an example of thermal mapping and the plot of the measured thermal conductance κ as a function of the Zn-TPP film thickness.

The values of κ were obtained from the analysis of the SThM probe voltage drop, as shown in fig.6.48.c. For the same reason presented for the fullerene samples in Sec. 6.2.4, the thermal conductance shows an exponential drop for the LB samples when the number of molecular units is increased. The κ values obtained for the different Zn-TPP formed by different techniques are reported in table 6.5, together with a resume of the measured electrical conductances G, thermal power S, and the thermoelectric figure of merit Z.

Looking at the values of the figure of merit Z, calculated from the measured Seebeck, electrical and thermal conductance is clear that, despite all the efforts made to enhance the Seebeck coefficient S and suppress the phonon transport by stacking the molecular

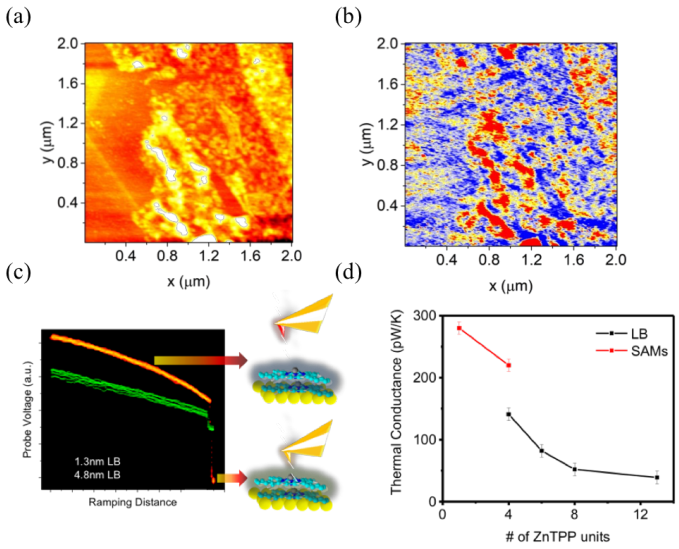

Figure 6.48: (a) Topography and (b) Thermal map of Zn-TPP LB film acquired by SThM. (c) SThM probe voltage drop during the engaging of the probe on the surface for different film thickness; (d) Thermal Conductance of Zn-TPP films formed by LB and SAM, as a function of film thickness.

Film	Thickness	G (nS)	$S(\mu V\,K^{-1})$	k (pW/K)	Z
SAM	0.45	1×10^3	-6.4 ± 1.7	289	1.4E-7
SAM2	1.1	25 ± 1.7	-9.1 ± 2.9	211	1.4E-08
LB1	1.3	17 ± 0.4	-7.1 ± 4.3	185	4.6E-9
LB2	2.4	$5 \times 10^{-2} \pm 4 \times 10^{-2}$	-26.9 ± 9.6	51	7.1E-10
LB3	4.8	$3 \times 10^{-4} \pm 1 \times 10^{-4}$	-68.4 ± 5.7	38	4.1E-11

Table 6.5: Values of electrical and thermal conductance G and κ, Seebeck coefficient S and the calculated thermoelectric figure of merit $Z = {}^{\sigma S^2}/_{\kappa}$ for the Zn-TPP films formed by self-assembly and LB.

layer by π interaction, the results were far from the goal of $ZT \approx 1$. The main reason behind this is the exponential drop of the electrical conductance with the increasing number of layers, resulting in a very small power factor σS^2. So, the main limitation in achieving higher Z in this particular case depends mainly on the poor electrical conductivity of the thicker molecular layers.

6.4 Strategies to tailor thermopower by reducing/oxidising the metal core in metallo-TPP

Among the possible strategies to further improve the figure of merit of molecular thin films, chemical doping is undoubtedly one of the most used and studied strategies in molecular electronics in order to enhance both the electrical conductance G and the thermal power S. The following Section will be dedicated to the study of the thermoelectric properties of metallo-porphyrins self-assembled monolayer exposed to Iodine molecules (I_2) vapour in order to study the effect of the eventual reducing/oxidising processes of the metal core of the porphyrin molecules on the thermoelectric properties of porphyrin SAMs.

As predicted and calculated by *Al-Galiby et Al.* in their study, the thermoelectric properties of metallo-porphyrins are pretty sensitive to the oxidation state of the metal core of the molecule [34]. The calculations performed in Fe+2 and Fe+3 and Mn+2, Mn+3 showed a clear dependence, along the plane of the molecule, of the thermal power and the electric transport on the oxidation state of the metal core, due to the shift of the Fermi energy of the junction. In fact, when the system acquires or donates an electron (reducing or oxidising respectively) from other molecules attached on the backbone of the molecules forming the film, the Fermi energy E_F will move towards, or away from, the transmission function resonance relative to the frontier orbitals HOMO-LUMO of the molecules, with a consequent enhancing (or quenching) of the thermoelectric properties of the junction.

In order to test this effect, a set of three porphyrin SAMs (Zn, Co, H_2) were grown following the same protocol described for the Zn-TPP film of the previous Section, submersing the TS Au in a toluene-based solution (1×10^{-4} M) for 1 hour and, after drying with nitrogen, the samples were incubated in a vacuum oven (10^{-2}mbar) overnight at 35 °C to let evaporate the solvent residuals.
The molecular films quality and thickness was studied by AFM nano-scratching, while the electrical conductance and thermoelectric properties of the three "as-grown" porphyrin-based SAMs were measured using CAFM and ThEFM using the same set-up employed for the other measurements of this work. Figure 6.49 shows the AFM topography of the three samples after the nano-scratching procedure with the corresponded height profiles measured in the scratched window.

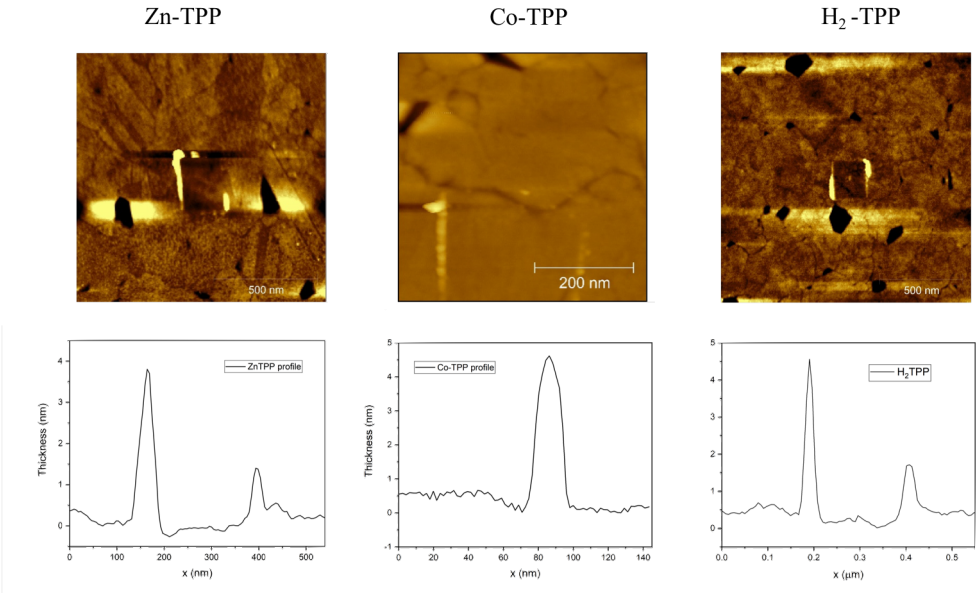

Figure 6.49: AFM topography and height analysis of the three porphyrin-based SAMs in correspondence of the window created by applying 20nN loading force to the AFM probe on a small area of the samples.

All three grown SAMs exhibited a layer thickness comparable to a single molecular layer of Zn-TPP, Co-TPP and H_2-TPP molecules, with an average thickness between 0.35 and 0.5 nm per sample. Once the formation of the layer was confirmed and the electric transport and the Seebeck value were measured for the set of "as-grown" porphyrins SAM, the samples were exposed to iodine molecules (I_2, Sigma Aldrich, $\geq 99.8\%$) in order to change the state of the metallic core of the molecules. In particular, iodine acts as an oxidising agent for the metallic atom of the molecules, withdrawing an electron from the metal and, as a consequence, shifting the Fermi energy E_f towards more negative values.

The "doping" process consisted of exposing the as-grown metallo-porphyrin SAMs to sublimated iodine molecules. Specifically, 0.5 mg of iodine molecules (I_2, Sigma Aldrich, $\geq 99.8\%$) were settled on a glass slide, covered with a borosilicate glass funnel and heated at 200 °C by a hot plate as shown in fig.6.50.a.

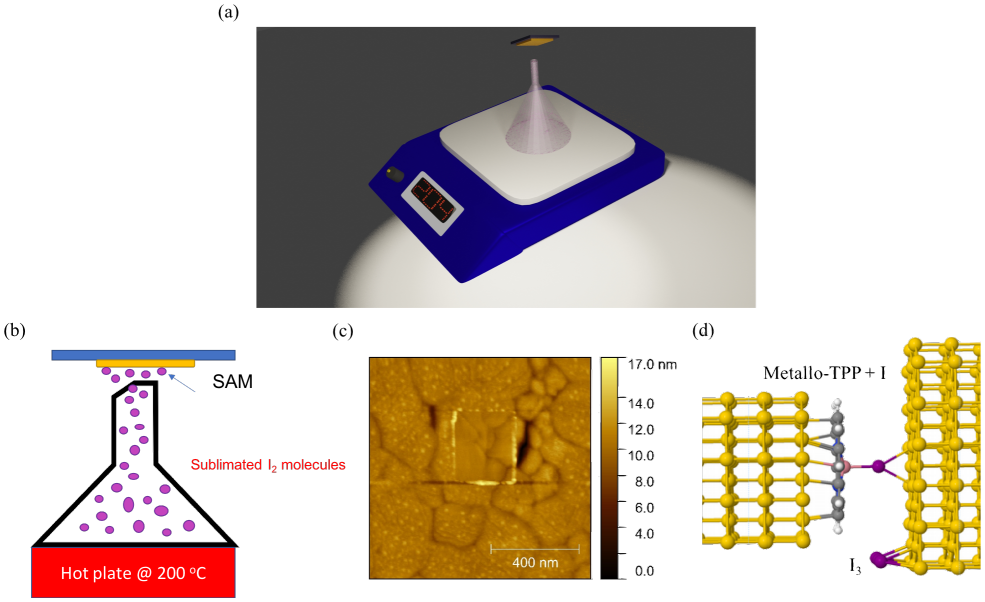

Figure 6.50: (a) Overview of the doping process of metallo-porphyrin SAMs; (b) Detailed scheme of the sublimation of the iodine molecules; (c) Topography of Co-TPP SAM on TS Au, after exposure of I_2 molecules for 1 min; (d) Ideal calculated configuration of the SAM's molecules after Iodine exposure.

During this procedure, the SAMs-funnel distance was fixed at 1 cm from the end of the funnel and exposed to the sublimated iodine molecules for 1 minute, as better illustrated in fig.6.50.b. The samples were then scanned by AFM immediately after the doping process. The presence of iodine molecules was confirmed by the presence of small clusters on the surface of the TPP SAMs after the exposure (fig.6.50.c). More likely, as shown from the ideal configuration predicted by the molecular dynamics group of Dr Hatef Saghedi in Warwick University in figure 6.50.d, the agglomerated material on the surface could represent I_3 clusters dislocated in all the surface, while the remaining I atoms are bonded with the metallic core of the metallo-porphyrin.

Therefore, assumed true the predicted configuration, the electric transport and thermoelectric properties of the I-doped SAMs were studied by CAFM and ThEFM and compared to the correspondent "as-grown" samples.

The following figure shows the electrical conductance distribution measured at low bias voltage for Zn-TPP, Co-TPP and H_2-TPP samples before and after being exposed to the iodine atoms.

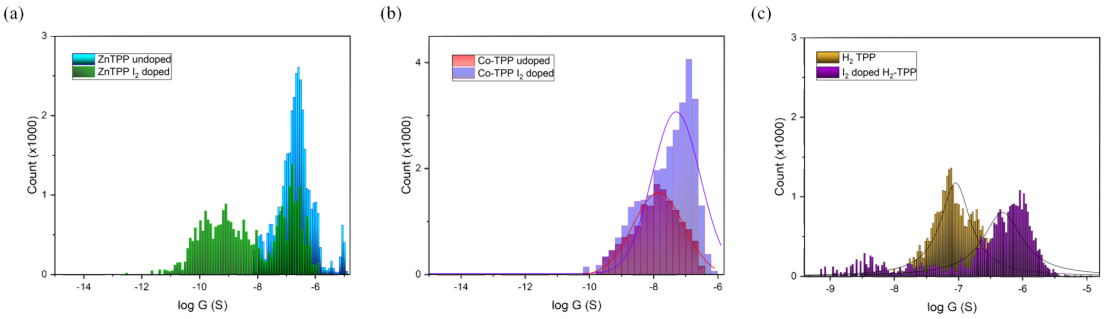

Figure 6.51: Distributions of electrical conductances (log scale) measured by CAFM in Zn-TPP (a), Co-TPP (b), and free-base H_2-TPP, before and after the doping process exposing the samples to iodine sublimated molecules.

As it is possible to observe from the distributions in figure 6.51 relative to the three porphyrin-based SAMs, the electrical conductance G does not seems affected by the presence of iodine, with minor exceptions in the free base porphyrin H_2-TPP and Zn-TPP. The measured electrical conductance values per SAM are reported in table 6.6 and scaled by the quantum of conductance G_0.

Film	G (S)	G/G_0
Zn-TPP	2.2E-7	2.8E-3
Zn-TPP+I	1.3E-7	1.2E-3
Co-TPP	1.4E-8	1E-4
Co-TPP+I	5.1E-8	6.6E-4
H_2-TPP	8.7E-8	1.1E-3
H_2-TPP+I	4.8E-7	6.3E-3

Table 6.6: Electrical conductance values measured by CAFM in the three films of metallo-porphyrin before and after the expose to iodine.

There were no appreciable differences between the electrical conductance G of Co-TPP before and after the doping process. Also, from fig.6.51.a is possible to observe a long tail in the conductance of Zn-TPP after the iodine exposure, exhibiting an additional peak at lower G. The additional peak was found to be caused by thicker region electrical conductance of the Zn-TPP SAM (fig.6.49). For this reason, it was excluded from the data during the analysis of the electrical conductance. So, neglecting the peak at low

G values, Zn-TPP showed similar electrical conductance before and after the iodine doping. Interestingly, the free-base H_2 porphyrin SAM revealed enhancement in its electrical conductance of about one order magnitude when the sample was exposed to the sublimated iodine molecules, as reported in figure 6.51.c.

The thermal power measurement of the three samples were performed by ThEFM. The thermal voltage distributions measured per each temperature difference for the Zn-TPP SAMs before and after the doping are presented in figure 6.52.

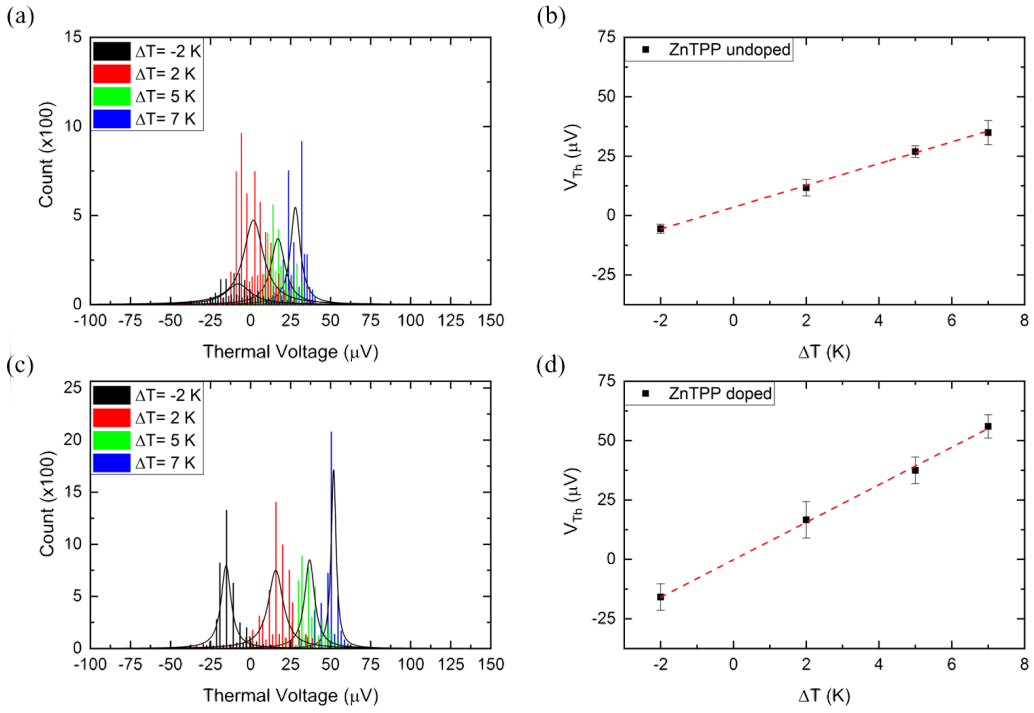

Figure 6.52: Thermal voltage distributions measured in Zn-TPP SAM together with the plots of the average values of the thermal power as a function of the temperature difference, before (a,b) and after (c,d) the exposure to iodine.

The Seebeck coefficient calculated from the fit of the measurements shown in figure 6.52.b and 6.52.d, was -5.30 ± 0.94 μV K^{-1} and -7.86 ± 1.17 μV K^{-1} for the as-grown and doped Zn-TPP SAM respectively. The measurements did not reveal any particular change in the thermal power S of the two samples, but just a slight increase of the Seebeck coefficient of the samples when exposed to iodine. However, the reasons behind this could be various since, for example, the presence of iodine on top of the molecules will increase the thickness of the SAM, creating a small rise in the Seebeck coefficient as discussed in Chapter 4. Another reason to justify the different thermal power measured could be attributed to the oxidation effect of the iodine molecule, even though this is

known to be almost ineffective for the Zinc metal core. Indeed, the depletion between the two resonance in the transmission function $T(E)$ relative to the HOMO-LUMO frontier orbitals has been calculated to be quite large in Zn-TPP, making the doping process for Zn-TPP employing Iodine molecules ineffective.

Figure 6.53 shows the thermoelectric measurements carried out for Co-TPP SAM before and after the doping through iodine exposure.

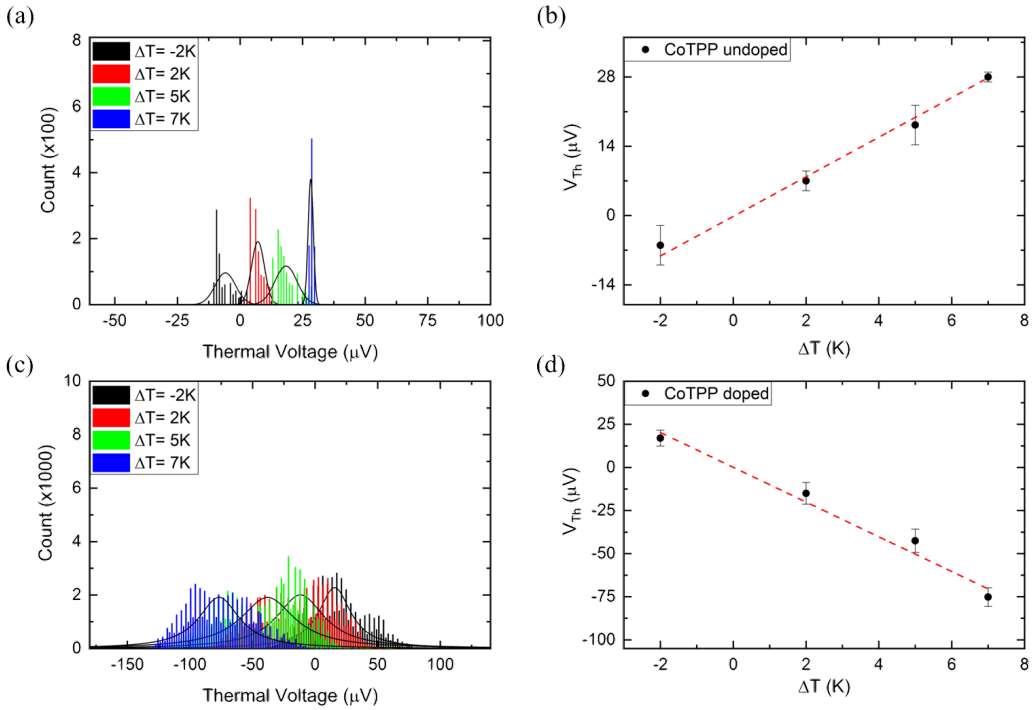

Figure 6.53: Distribution of thermal voltages measured by ThEFM per each temperature difference and relative plots of the average thermal voltages values as a function of ΔT for Co-TPP before (a,b) and after (c,d) the doping process.

This time we observe, from the plot presented in figure 6.53.b and 6.53.d, how the thermal voltage and thus, the Seebeck coefficient, switched sign, passing from negative to positive when Co-TPP SAMs were exposed to iodine. The Seebeck coefficients obtained from the linear fit of the plots shown in fig.6.53 for the as-grown and I doped Co-TPP SAMs were -4.00 ± 0.89 μV K^{-1} and $+10.07 \pm 5.69$ μV K^{-1}, respectively. This result is more evident in the plot of figure 6.54, showing the comparison of the Seebeck voltages obtained from the ThEFM measurements.

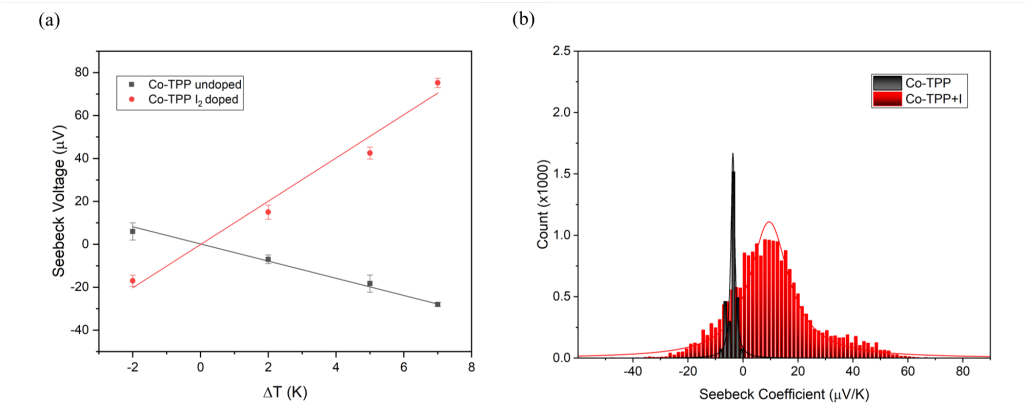

Figure 6.54: (a) Comparison of the average Seebeck voltages measured for Co-TPP SAM before and after the doping process, plotted against the temperature difference ΔT. Seebeck coefficient distributions for the two films (b).

The switching of the thermal power of the Co-TPP SAM after the presence of iodine has not been observed before, indirectly confirming the theoretical prediction made by *Al-Galiby et Al.* and opening a new route for the design of molecules-based TE devices, combining the doping effect with, for instance, the engineering of the thermal power by increasing the thickness of the films as proved in the previous section.
Physically, the switch of the sign of the Seebeck coefficient has to be attributed to the strong oxidising effect of the iodine atoms on the Co metal core of the porphyrin molecules. In fact, removing one electron from the Co-TPP molecule has the effect of shifting the Fermi Energy toward more negative values. But this time, in contrast with the Zn-TPP SAMs, the shift is enough to move the Fermi energy toward the HOMO resonance and, consequentially, giving a positive thermal power S.

To support our measurements, the same thermoelectric analysis was made on free-base H_2-TPP. This choice was made in order to confirm that what was measured in the two metallo-porphyrins was caused exclusively by the presence of iodine and not from other factors since H_2 porphyrins are, in principle, inert to the presence of iodine. The thermoelectric measurements of H_2-TPP SAMs are shown in figure 6.55, displaying the thermal voltages distributions acquired per each temperature and the plot of the average thermal voltage values obtained from the distributions as a function of ΔT.

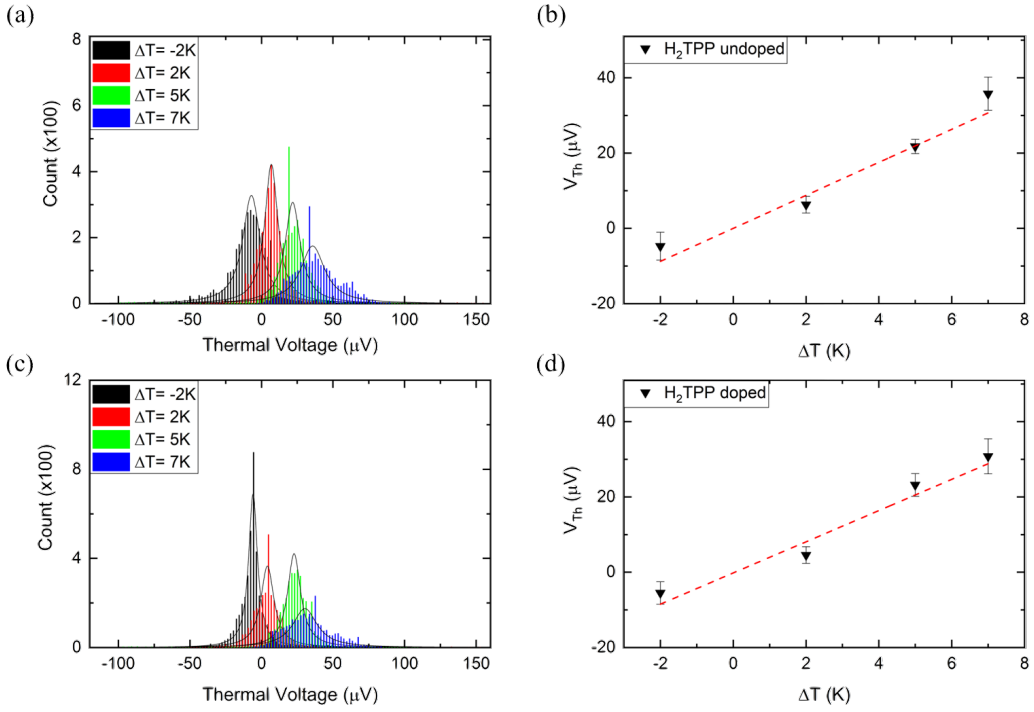

Figure 6.55: Thermal voltage distributions measured at four ΔT and plots of thermal voltage vs. temperature difference for H_2-TPP before (a,b) and after (c,d) the doping with iodine molecules.

As expected, and is evident form the thermoelectric analysis presented in figure 6.55.b and 6.55.d, the thermal power of the free-base porphyrin SAM as-grown and after the exposure to iodine are comparable. In particular, the Seebeck coefficient measured were -4.38 ± 1.39 μV K^{-1} and -4.17 ± 0.96 μV K^{-1} respectively for the undoped and doped samples, confirming the prediction that no changes in thermal power takes place due to the inefficacy of the doping procedure in free-base porphyrin SAMs.

For better comparison, the Seebeck coefficient of all the metallo-porphyrin before and after the iodine exposure are shown in figure 6.56 and the relative values are shown in table 6.7.

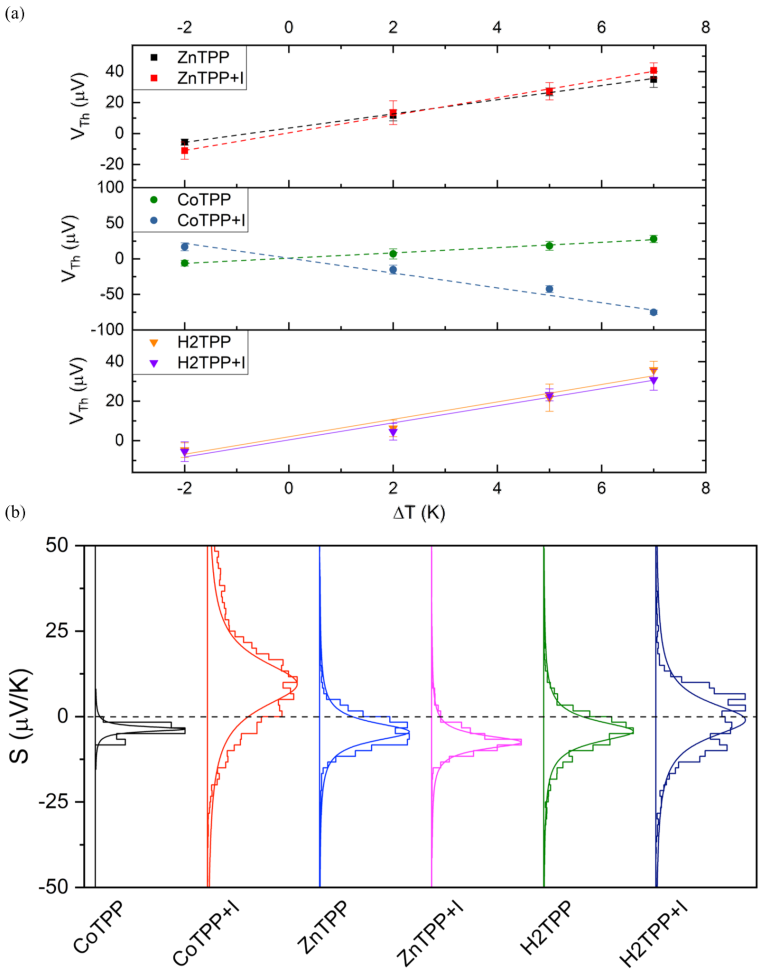

Figure 6.56: Comparison of the Seebeck coefficient distributions measured for the three different porphyrin-based SAMs before and after the exposure to Iodine.

Figure 6.56 gives a complete overview of the thermal power of metallo-porphyrins studied and, as is possible to observe from the graph, the negative Seebeck coefficient recorded for all samples but one, reflect the LUMO character of the molecules.

Film	G (S)	G/G_0	S μV K^{-1}
Zn-TPP	2.2E-7	2.8E-3	-5.30 ± 0.94
Zn-TPP+I	1.3E-7	1.2E-3	-7.86 ± 1.17
Co-TPP	1.4E-8	1E-4	-4.00 ± 0.89
Co-TPP+I	5.1E-8	6.6E-4	10.07 ± 5.69
H_2-TPP	8.7E-8	1.1E-3	-4.38 ± 1.39
H_2-TPP+I	4.8E-7	6.3E-3	-4.17 ± 0.96

Table 6.7: Electrical conductance and thermalpower measured by CAFM and ThEFM in porphyrin-based SAMs before and after the exposure to iodine.

Concluding, the overall effect of Iodine molecules can be considered as a negative gate for the energy levels of the TPP junctions, shifting the Fermi energy towards negative energy values. This effect is evident in the studies conducted in Co porphyrin SAMs, where the Co(II) metal core of the molecules shift to Co(III) when the samples were exposed to iodine. Since the oxidation of Co from 2+ to 3+ due to iodine has been largely studied in literature [348–350], we can certainly assume that the differences in the measured thermal power of Co-TPP SAMs have to be attributed to the change of the oxidation state of the metal core of the molecule in the presence of iodine.

In contrast, the small variation of the thermal power measured in the Zn-TPP samples before and after the iodine doping can not be attributed, this time to the iodine. In fact, since Zn has just one oxidation state (2+), it is impossible to further oxidise the metal core of the molecule, with consequently no changes in the transport properties and the thermal power. From theoretical calculations performed by the collaborator of this study, one hypothesis could be that the iodine molecules remain in their I_2 form when sublimated on the Zn-TPP SAM. In this way, there will not be single Iodine atoms bonded directly with the metal core of the Zn-TPP molecules, producing substantially no changes to the transport properties.

The latter configuration was also assumed to be valid for the free-base H_2-TPP, considering that the molecules should be inert to the I_2 molecules.

It is worth noting that the results obtained, as said, could help to better understand the electronic properties of oxide complex formation and the effect of charge transfer on self-assembled molecular-scale junctions thermoelectric properties. The presented strategy is a powerful alternative to the electrostatic gate used in nano-junction and three-terminal devices to tune the junctions' energy levels towards the frontier orbitals of the molecules, with no particular fabrication techniques required for the samples.

Chapter 7

Conclusions

The aim of this work was to demonstrate the feasibility of using molecular assembly and thin-film structures for thermoelectric energy generation. In this context, ThEFM has been proven to be a successful tool for probing the electrical conductance and the thermoelectric properties of molecular ultra-thin films.
In addition to the interest in the fundamental physical processes that occurs in these systems, one of the main reason for using molecular thin films and molecular self-assembled monolayers instead of single molecular junction for thermoelectric applications, lies in their integrability in device architectures, better stability to mechanical deformations and greater control of the conformation and morphology of the molecular films compared with the single molecules counterpart.
Indeed, as has been observed in sections 6.2 and 6.3, both the electrical conductance G and the thermoelectric properties of the molecular films are deeply influenced by the growth conditions and thus the quality of the molecular film.

Among the film formation techniques used in this thesis, the Langmuir-Blodgett technique has been proved to be a powerful technique to form molecular thin-films, with a precise and controlled thickness for non-amphiphilic molecules like fullerene C_{60} and planar molecules like Zinc Porphyrin Zn-TPP. In fact, thanks to the particular electronic structure of these molecules, and the more or less extended π systems, it was even possible to stack multiple layers of non-amphipillic molecules. This characteristic is particular to the LB technique since, as shown, once the mono-molecular floating film is formed, it is possible, in principle, to form as many layers as needed without limitation (Sec. 6.2.1).
However, the realisation of thicker structures is not always the desired characteristic

since, as has been seen in the calculation of the figure of merit for both C_{60} and Zn-TPP, thicker structures suppress the electric transport due to the increases of the tunnel barrier represented by the molecular film. Furthermore, as observed in the thermoelectric properties of Zn-TPP, molecular films formed by LB result, on average, in more defective and less uniform films. This characteristic creates a consequent enhancement of the thermal power due to the multiple scattering sites inside the semi-crystalline structure of the molecular films. However, if on the one hand, this characteristic could look attractive when the final goal is to enhance as much as possible the thermoelectric properties, on the other hand, this has a negative effect on the electrical conductance compared to molecular films realised by self-assembling (Sec. 6.3.1), which are, on average, more conductive than their LB counterparts.

Conductive probe AFM (CAFM) allowed the direct measurement of the electric properties and the thermal voltage traces of the samples when a difference of temperature ΔT was applied between the Au substrate and the AFM conductive probe, with high statistic (Section 5.4.2).

The combination of conventional CAFM with the intermittent contact mode, known as Peak Force AFM, allowed the simultaneous collection of the electric and nanomechanical properties of the molecular films. This point resulted in a crucial step of this work since, in addition to the possibility to obtain multi-physical properties of the material under investigation, the combination of these two techniques drastically reduces the friction between probe and sample, with consequent less damage to the molecular thin film during the measurements.

As explained in Section 5.4.5, due to the nature of the intermittent contact, the thermoelectric properties of the samples could not be studied by conventional methods. Since the difference in the time scale of the thermoelectric effect and the intermittent contact, a "thermal current Sensing" was developed for the study of the thermal power of different alkyl thiolate SAMs with different length.

The thermal power measured by current sensing PF-ThEFM and the conventional zero-current ThEFM results comparable and, in any case, inside the relative uncertainties values, demonstrating the feasibility of the developed methodology.

Moreover, in the framework of SPM development, the additional study on the effect of graphene as a top electrode material (CAFM probe) gave interestingly superior mechanical and electrical stability over longer time scan, ensuring a "softer contact" with the

sample surface and preserving the life-time of the probe itself (6.1.2).
The methodology developed for the Graphene coating of the AFM probes was possible thanks to the use of LB technique that, in contrast with other techniques and methodology reported in the literature, preserved the probe shape without the risk of the probe breaking.

Alkyl-thiolate based SAMs and conjugated molecular wires were employed to test the measurements techniques and demonstrating the validity of the measurements made by CAFM and ThEFM by comparison with theoretical DFT calculations and previous literature results on similar systems and single molecules counterparts. The measurements revealed increasing thermopower when the molecular length increases in very good agreement with the values in the literature.

Since the main aim of this work was the enhancement of the thermoelectric properties of molecular thin films or SAMs and the reduction of the phonon transport across the junction, it was decided to study the electric and thermoelectric properties of the molecular films varying the film thickness by stacking molecular layers by π interaction. In fact, it has been largely reported how the non-covalent bonded molecules suppress the phonon transport in the molecule and, as a consequence, enhance the thermal power and the thermoelectric figure of merit ZT.

This was verified in C_{60} and Zn-TPP molecular films. The measurements showed an increasing Seebeck coefficient with increasing the number of molecular layers by π stacking in both the molecules, showing a relatively high Seebeck coefficient of ~ -70 $\mu V\,K^{-1}$ in 4.8 nm Zn-TPP film formed by LB technique and almost -40 $\mu V\,K^{-1}$ in 2.8 nm C_{60} layer corresponding respectively to ~ 15 and ~ 3 layers of molecules.
In both samples, the measured thermopower enhanced when the molecular layers were formed by LB rather than SAM, displaying a linear dependency on the film thickness in good agreement with the literature values for C_{60} and Zn-TPP. The enhanced Seebeck in the LB samples is attributed to the more defective structure of the LB films, rich in vacancies and imperfections, which further suppress the phonon diffusion across the molecular junction. In addition, from the study of the thermal conductance of the sample by Scanning thermal microscopy (SThM), it was possible to calculate the figure of merit ZT, which defines the efficiency of a thermoelectric material. As is possible to

observe in table 6.4 and 6.5, the calculated values in the range of 10^{-7} and 10^{-12}, which are far from the desired $ZT = 1$ threshold useful for practice applications.
Despite all the effort and the strategies employed to enhance the thermoelectric properties of the molecular thin films, the exponential decay of the electrical conductance with the number of molecular layers makes these systems still poorly efficient. Recent studies, however, proved that some porphyrin-based molecular structures present a positive current decay factor β, with the consequent increases of the electrical conductance with the length of the molecules [259] This particular characteristic would surely help for the enhancement of the thermoelectric figure of merit of the junction, due the simultaneous increases of the Seebeck coefficient S and the electrical conductance G of the molecules.

Finally, the control and tailor of the intrinsic thermoelectric properties of metalloporphyrin based SAMs were largely tested in this thesis. Inspired by the theoretical work of *Al-Galiby et Al.* on the tuning the Seebeck coefficient of metallo-porhpyrins single molecular junctions [34], the experiments were focused on the tailoring of the thermal power of self-assembled monolayer of three metallo-porphyrins by using iodine molecules as chemical dopant . As shown in Section 6.4, the electric and thermoelectric properties of three porphyrin-based SAMs with different metal core atom (Zn, Co, free-base) were tested by ThEFM, before and after the exposure to sublimated iodine molecules (I_2), and the experimental results were compared with the theoretical calculations and molecular dynamics simulations performed by the group of theoretical transport in molecular system lead by Prof. Colin Lambert and Dr. Hatef Sadeghi.
Indeed, combining a chemical doping with thermopower capability may yield novel applications involving the Seebeck and the Peltier effect. The Seebeck coefficient, and therefore the temperature gradient in a material, depends on the slope of the transmission at the Fermi energy. Using chemical doping (or chemical gate), one could shift a resonance through the Fermi energy. While doing so, the slope of the transmission changes sign, as does the Seebeck coefficient.

The ability to reverse the sign of the Seebeck coefficient is a property that no material to date had been showing.

From the results, it was possible to observe no appreciable changes in the thermoelectric properties of Zn-TPP and H_2-TPP before and after the iodine doping while,

interestingly, the Co-TPP film exhibited a net change of sign of the measured Seebeck coefficient S ,from -4 to$+10$ $\mu V\,K^{-1}$ when the sample was exposed to the I_2 molecules. The change in the thermal power just in the Co-TPP and not elsewhere has been attributed to the change in the oxidation state of the Co metallic core of the porphyrin molecules, which results quite sensitive to iodine, as reported largely in literature [348–350]. In fact, the presence of iodine leads to the withdrawing of one electron from the Co atom and, consequently, shifting the Fermi energy E_f of the molecules towards negative energies. In contrast, and as expected, iodine did not show any effect on both Zn-TPP and free-base H_2-TPP. Indeed, since Zn presents only one oxidation state (2+), it is almost impossible for iodine to remove electrons from the zinc metal core of the porphyrin. Thus, the net effect produced on the thermoelectric properties of the molecules after the doping is overall null. In analogy, the fact that no changes were recorded in the Seebeck coefficient of the H_2-TPP after the iodine exposure reflects the inert condition of the free-base porphyrin that, without any metal core, do no interact with iodine, whose remain in its I_2 form forming just "contamination" on the surface.
Even though other confirmations are surely needed, especially about the configuration of the iodine molecules in the doped samples, this work put the basis of further outcomes on the possibility to tune *"ex-situ"* the thermoelectric properties of metallo-porphyrins based SAMs or other molecular species which form charge-transfer complex, giving the possibility to tune the Fermi energy of the junction towards positive or negative values, based on the particular dopant used. Thus, this process could be considered as a chemical gate of the energetic level of the molecular system under study and could be, in principle, a good alternative to the electrostatic gate of three terminal nano-junctions and devices, when the particular measurement or preparation techniques do not contemplate the presence of a third terminal.

Despite the tremendous opportunities molecules offer, the thermoelectricity in molecular electronics is still in its infancy, and many challenges still remain to be solved. One of them, for instance, is how to make reliable electric contact to single molecules. In fact, contacting molecules has attracted much attention, both from the electrode side and in terms of molecular design. In particular, questions related to the formation of strong connections between the molecule and the electrodes was partially solved in this work thanks to the employment of SPM techniques in order to test the thermoelectric and electric transport of molecular thin films, creating optimal and, especially, controlled

contact between the probe of the AFM (top electrode) and the surface of the molecules. In fact, as shown in Section 6.1, based on the loading force of the AFM probe, it was easy to control the number of molecules contacted during the measurements.

Bibliography

[1] GE Moore. Electronics 1965, 38.

[2] Richard P Feynman. There's plenty of room at the bottom. *Feynman and Computation: Exploring the Limits of Computers*, 1959.

[3] Arieh Aviram and Mark A Ratner. Molecular rectifiers. *Chemical physics letters*, 29(2):277–283, 1974.

[4] Frank Schwierz. Graphene transistors. *Nature nanotechnology*, 5(7):487, 2010.

[5] Forrest L Carter. The molecular device computer: point of departure for large scale cellular automata. *Physica D: Nonlinear Phenomena*, 10(1-2):175–194, 1984.

[6] Thomas S Arrhenius, Mireille Blanchard-Desce, Maya Dvolaitzky, Jean-Marie Lehn, and Jacques Malthete. Molecular devices: caroviologens as an approach to molecular wires—synthesis and incorporation into vesicle membranes. *Proceedings of the National Academy of Sciences*, 83(15):5355–5359, 1986.

[7] KL Kompa and RD Levine. A molecular logic gate. *Proceedings of the National Academy of Sciences*, 98(2):410–414, 2001.

[8] Bruce H Robinson and Nadrian C Seeman. The design of a biochip: a self-assembling molecular-scale memory device. *Protein Engineering, Design and Selection*, 1(4):295–300, 1987.

[9] JJ Hopfield, José Nelson Onuchic, and David N Beratan. A molecular shift register based on electron transfer. *Science*, 241(4867):817–820, 1988.

[10] Charles Kittel. Solid state physics. *Wiley, New York*, 19, 1976.

[11] Scheer Elke and Cuevas Juan Carlos. *Molecular electronics: an introduction to theory and experiment*, volume 15. World Scientific, 2017.

[12] LA Bumm, Jamie Jon Arnold, MT Cygan, TD Dunbar, TP Burgin, L Jones, David L Allara, James M Tour, and PS Weiss. Are single molecular wires conducting? *Science*, 271(5256):1705–1707, 1996.

[13] J Chen, MA Reed, AM Rawlett, and JM Tour. Large on-off ratios and negative differential resistance in a molecular electronic device. *science*, 286(5444):1550–1552, 1999.

[14] James M Tour, Mark A Reed, Jorge M Seminario, David L Allara, and Paul S Weiss. Molecular computer, August 6 2002. US Patent 6,430,511.

[15] MS Dresselhaus. Transport properties of solids. *Lecture Notes. In:-Solid State Physics-Part*, 1, 2001.

[16] Neil W Ashcroft, N David Mermin, et al. Solid state physics [by] neil w. ashcroft [and] n. david mermin., 1976.

[17] Safa O Kasap. *Principles of electronic materials and devices*, volume 2. McGraw-Hill New York, 2006.

[18] N. E. Cusack and Peter C. Kendall. The absolute scale of thermoelectric power at high temperature. 1958.

[19] H Julian Goldsmid. *Introduction to thermoelectricity*, volume 121. Springer, 2010.

[20] David Michael Rowe. *CRC handbook of thermoelectrics*. CRC press, 2018.

[21] Justin P. Bergfield and Mark A Ratner. Forty years of molecular electronics: Non-equilibrium heat and charge transport at the nanoscale. *Physica Status Solidi (B): Basic Research*, 250(11):2249–2266, 11 2013.

[22] Rama Venkatasubramanian, Edward Siivola, Thomas Colpitts, and Brooks O'quinn. Thin-film thermoelectric devices with high room-temperature figures of merit. *Nature*, 413(6856):597–602, 2001.

[23] TC Harman, MP Walsh, GW Turner, et al. Nanostructured thermoelectric materials. *Journal of electronic materials*, 34(5):L19–L22, 2005.

[24] TC Harman, PJ Taylor, MP Walsh, and BE LaForge. Quantum dot superlattice thermoelectric materials and devices. *science*, 297(5590):2229–2232, 2002.

[25] E. B. Ramayya, L. N. Maurer, A. H. Davoody, and I. Knezevic. Thermoelectric properties of ultrathin silicon nanowires. *Phys. Rev. B*, 86:115328, Sep 2012.

[26] A. J. Minnich, M. S. Dresselhaus, Z. F. Ren, and G. Chen. Bulk nanostructured thermoelectric materials: current research and future prospects. *Energy Environ. Sci.*, 2:466–479, 2009.

[27] XW Wang, H Lee, YC Lan, GH Zhu, G Joshi, DZ Wang, J Yang, AJ Muto, MY Tang, J Klatsky, et al. Enhanced thermoelectric figure of merit in nanostructured n-type silicon germanium bulk alloy. *Applied Physics Letters*, 93(19):193121, 2008.

[28] Giri Joshi, Hohyun Lee, Yucheng Lan, Xiaowei Wang, Gaohua Zhu, Dezhi Wang, Ryan W Gould, Diana C Cuff, Ming Y Tang, Mildred S Dresselhaus, et al. Enhanced thermoelectric figure-of-merit in nanostructured p-type silicon germanium bulk alloys. *Nano letters*, 8(12):4670–4674, 2008.

[29] Asegun S Henry and Gang Chen. Spectral phonon transport properties of silicon based on molecular dynamics simulations and lattice dynamics. *Journal of Computational and Theoretical Nanoscience*, 5(2):141–152, 2008.

[30] M S. Dresselhaus, G. Chen, M Y. Tang, R G. Yang, H. Lee, D Z. Wang, Z F. Ren, J.P. Fleurial, and P. Gogna. New directions for low-dimensional thermoelectric materials. *Advanced Materials*, 19(8):1043–1053, 2007.

[31] Yonatan Dubi and Massimiliano Di Ventra. Colloquium: Heat flow and thermoelectricity in atomic and molecular junctions. *Reviews of Modern Physics*, 83(1):131, 2011.

[32] Víctor M García-Suárez, Colin J Lambert, David Zs Manrique, and Thomas Wandlowski. Redox control of thermopower and figure of merit in phase-coherent molecular wires. *Nanotechnology*, 25(20):205402, apr 2014.

[33] Volodymyr V. Maslyuk, Steven Achilles, and Ingrid Mertig. Spin-polarized transport and thermopower of organometallic nanocontacts. *Solid State Communications*, 150(11):505 – 509, 2010.

[34] Qusiy H. Al-Galiby, Hatef Sadeghi, Laith A. Algharagholy, Iain Grace, and Colin Lambert. Tuning the thermoelectric properties of metallo-porphyrins. *Nanoscale*, 8:2428–2433, 2016.

[35] NR Claughton and CJ Lambert. Thermoelectric properties of mesoscopic superconductors. *Physical review b*, 53(10):6605, 1996.

[36] Justin P. Bergfield, Michelle A. Solis, and Charles A. Stafford. Giant thermoelectric effect from transmission supernodes. *ACS Nano*, 4(9):5314–5320, 2010.

[37] Charalambos Evangeli, Katalin Gillemot, Edmund Leary, M Teresa Gonzalez, Gabino Rubio-Bollinger, Colin Lambert, and Agrait Nicolás. Engineering the thermopower of c60 molecular junctions. *Nano letters*, 13(5):2141–2145, 2013.

[38] Magnus Paulsson and Supriyo Datta. Thermoelectric effect in molecular electronics. *Phys. Rev. B*, 67:241403, Jun 2003.

[39] R. F. Pierret. *Semiconductor Fundamentals*. Addison-Wesley, Reading, MA, 1996. Chap 3.2.2.

[40] Shannon K. Yee, Jonathan A. Malen, Arun Majumdar, and Rachel A. Segalman. Thermoelectricity in fullerene-metal heterojunctions. *Nano Letters*, 11(10):4089–4094, 2011. PMID: 21882860.

[41] Pramod Reddy, Sung-Yeon Jang, Rachel A Segalman, and Arun Majumdar. Thermoelectricity in molecular junctions. *Science*, 315(5818):1568–1571, 2007.

[42] A.W. Adamson and A.P. Gast. *Physical chemistry of surfaces*. Wiley, 1997.

[43] G. Barnes and I. Gentle. *Interfacial Science: An Introduction*. OUP Oxford, 2011.

[44] G.L. Gaines. *Insoluble monolayers at liquid-gas interfaces*. Interscience monographs on physical chemistry. Interscience Publishers, 1966.

[45] Francisco J Ibañez and Francis P Zamborini. Chemiresistive sensing with chemically modified metal and alloy nanoparticles. *Small*, 8(2):174–202, 2012.

[46] GE Poirier and ED Pylant. The self-assembly mechanism of alkanethiols on au (111). *Science*, 272(5265):1145–1148, 1996.

[47] Hans A Biebuyck, Colin D Bain, and George M Whitesides. Comparison of organic monolayers on polycrystalline gold spontaneously assembled from solutions containing dialkyl disulfides or alkanethiols. *Langmuir*, 10(6):1825–1831, 1994.

[48] Paul E Laibinis, George M Whitesides, David L Allara, Yu Tai Tao, Atul N Parikh, and Ralph G Nuzzo. Comparison of the structures and wetting properties of self-assembled monolayers of n-alkanethiols on the coinage metal surfaces, copper, silver, and gold. *Journal of the American Chemical Society*, 113(19):7152–7167, 1991.

[49] Colin D Bain, Joe Evall, and George M Whitesides. Formation of monolayers by the coadsorption of thiols on gold: variation in the head group, tail group, and solvent. *Journal of the American Chemical Society*, 111(18):7155–7164, 1989.

[50] Soichiro Yoshimoto and Kingo Itaya. Advances in supramolecularly assembled nanostructures of fullerenes and porphyrins at surfaces. *Journal of Porphyrins and Phthalocyanines*, 11(05):313–333, 2007.

[51] Koji Suto, Soichiro Yoshimoto, and Kingo Itaya. Two-dimensional self-organization of phthalocyanine and porphyrin: Dependence on the crystallographic orientation of au. *Journal of the American Chemical Society*, 125(49):14976–14977, 2003.

[52] Jinxuan Liu, Björn Schüpbach, Asif Bashir, Osama Shekhah, Alexei Nefedov, Martin Kind, Andreas Terfort, and Christof Wöll. Structural characterization of self-assembled monolayers of pyridine-terminated thiolates on gold. *Physical Chemistry Chemical Physics*, 12(17):4459–4472, 2010.

[53] Hennie Valkenier, Everardus H Huisman, Paul A van Hal, Dago M de Leeuw, Ryan C Chiechi, and Jan C Hummelen. Formation of high-quality self-assembled monolayers of conjugated dithiols on gold: base matters. *Journal of the American Chemical Society*, 133(13):4930–4939, 2011.

[54] Steven K Hau, Hin-Lap Yip, Hong Ma, and Alex K-Y Jen. High performance ambient processed inverted polymer solar cells through interfacial modification with a fullerene self-assembled monolayer. *Applied Physics Letters*, 93(23):441, 2008.

[55] Colin D Bain and George M Whitesides. Molecular-level control over surface order in self-assembled monolayer films of thiols on gold. *Science*, 240(4848):62–63, 1988.

[56] J Christopher Love, Lara A Estroff, Jennah K Kriebel, Ralph G Nuzzo, and George M Whitesides. Self-assembled monolayers of thiolates on metals as a form of nanotechnology. *Chemical reviews*, 105(4):1103–1170, 2005.

[57] Pascal Gehring, Achim Harzheim, Jean Spiece, Yuewen Sheng, Gregory Rogers, Charalambos Evangeli, Aadarsh Mishra, Benjamin J Robinson, Kyriakos Porfyrakis, Jamie H Warner, et al. Field-effect control of graphene–fullerene thermoelectric nanodevices. *Nano letters*, 17(11):7055–7061, 2017.

[58] Benjamin R Martin, Daniel J Dermody, Brian D Reiss, Mingming Fang, L Andrew Lyon, Michael J Natan, and Thomas E Mallouk. Orthogonal self-assembly on colloidal gold-platinum nanorods. *Advanced Materials*, 11(12):1021–1025, 1999.

[59] David L Allara and Ralph G Nuzzo. Spontaneously organized molecular assemblies. 1. formation, dynamics, and physical properties of n-alkanoic acids adsorbed from solution on an oxidized aluminum surface. *Langmuir*, 1(1):45–52, 1985.

[60] Ipsita A Banerjee, Lingtao Yu, Robert I MacCuspie, and Hiroshi Matsui. Thiolated peptide nanotube assembly as arrays on patterned au substrates. *Nano letters*, 4(12):2437–2440, 2004.

[61] Nurxat Nuraje, Ipsita A Banerjee, Robert I MacCuspie, Lingtao Yu, and Hiroshi Matsui. Biological bottom-up assembly of antibody nanotubes on patterned antigen arrays. *Journal of the American Chemical Society*, 126(26):8088–8089, 2004.

[62] Wenyong Wang, Takhee Lee, and Mark A Reed. Electron tunnelling in self-assembled monolayers. *Reports on Progress in Physics*, 68(3):523, 2005.

[63] P Legare, L Hilaire, M Sotto, and G Maire. Interaction of oxygen with au surfaces: A leed, aes and els study. *Surface Science*, 91(1):175–186, 1980.

[64] Amihood Doron, Ernesto Joselevich, Anat Schlittner, and Itamar Willner. Afm characterization of the structure of au-colloid monolayers and their chemical etching. *Thin Solid Films*, 340(1-2):183–188, 1999.

[65] T Gregory Schaaff and Robert L Whetten. Controlled etching of au: Sr cluster compounds. *The Journal of Physical Chemistry B*, 103(44):9394–9396, 1999.

[66] Gangaiah Mettela and Giridhar U Kulkarni. Facet selective etching of au microcrystallites. *Nano Research*, 8(9):2925–2934, 2015.

[67] Ralph G Nuzzo and David L Allara. Adsorption of bifunctional organic disulfides on gold surfaces. *Journal of the American Chemical Society*, 105(13):4481–4483, 1983.

[68] Mitsunori Hieda, Rafael Garcia, Matt Dixon, Tad Daniel, David Allara, and Moses Hung-Wai Chan. Ultrasensitive quartz crystal microbalance with porous gold electrodes. *Applied physics letters*, 84(4):628–630, 2004.

[69] Kenneth A Marx. Quartz crystal microbalance: a useful tool for studying thin polymer films and complex biomolecular systems at the solution- surface interface. *Biomacromolecules*, 4(5):1099–1120, 2003.

[70] Débora Gonçalves and Eugene A Irene. Fundamentals and applications of spectroscopic ellipsometry. *Quimica Nova*, 25(5):794–800, 2002.

[71] Dana M Rosu, Jason C Jones, Julia WP Hsu, Karen L Kavanagh, Dimiter Tsankov, Ulrich Schade, Norbert Esser, and Karsten Hinrichs. Molecular orientation in octanedithiol and hexadecanethiol monolayers on gaas and au measured by infrared spectroscopic ellipsometry. *Langmuir*, 25(2):919–923, 2009.

[72] Nongjian J Tao. Electron transport in molecular junctions. In *Nanoscience And Technology: A Collection of Reviews from Nature Journals*, pages 185–193. World Scientific, 2010.

[73] P Fenter, P Eisenberger, Jun Li, N Camillone III, S Bernasek, G Scoles, Trikur A Ramanarayanan, and KS Liang. Structure of octadecyl thiol self-assembled on the silver (111) surface: an incommensurate monolayer. *Langmuir*, 7(10):2013–2016, 1991.

[74] J Christopher Love, Daniel B Wolfe, Michael L Chabinyc, Kateri E Paul, and George M Whitesides. Self-assembled monolayers of alkanethiolates on palladium are good etch resists. *Journal of the American Chemical Society*, 124(8):1576–1577, 2002.

[75] J Christopher Love, Daniel B Wolfe, Richard Haasch, Michael L Chabinyc, Kateri E Paul, George M Whitesides, and Ralph G Nuzzo. Formation and structure of self-assembled monolayers of alkanethiolates on palladium. *Journal of the American Chemical Society*, 125(9):2597–2609, 2003.

[76] Alain Carvalho, Matthias Geissler, Heinz Schmid, Bruno Michel, and Emmanuel Delamarche. Self-assembled monolayers of eicosanethiol on palladium and their use in microcontact printing. *Langmuir*, 18(6):2406–2412, 2002.

[77] S. Wolf and R.N. Tauber. *Silicon Processing for the VLSI Era: Process technology*. Silicon Processing for the VLSI Era. Lattice Press, 2000.

[78] Xingyu Jiang, Derek A Bruzewicz, Mamie M Thant, and George M Whitesides.

Palladium as a substrate for self-assembled monolayers used in biotechnology. *Analytical chemistry*, 76(20):6116–6121, 2004.

[79] Daniel Käfer, Gregor Witte, Piotr Cyganik, Andreas Terfort, and Christof Wöll. A comprehensive study of self-assembled monolayers of anthracenethiol on gold: Solvent effects, structure, and stability. *Journal of the American Chemical Society*, 128(5):1723–1732, 2006.

[80] Zineb Mekhalif, Fabrice Laffineur, Nathalie Couturier, and Joseph Delhalle. Elaboration of self-assembled monolayers of n-alkanethiols on nickel polycrystalline substrates: Time, concentration, and solvent effects. *Langmuir*, 19(3):637–645, 2003.

[81] Efrosini Kokkoli and Charles F Zukoski. Effect of solvents on interactions between hydrophobic self-assembled monolayers. *Journal of colloid and interface science*, 209(1):60–65, 1999.

[82] Kevin A Peterlinz and R Georgiadis. In situ kinetics of self-assembly by surface plasmon resonance spectroscopy. *Langmuir*, 12(20):4731–4740, 1996.

[83] Oliver Dannenberger, J Jens Wolff, and Manfred Buck. Solvent dependence of the self-assembly process of an endgroup-modified alkanethiol. *Langmuir*, 14(17):4679–4682, 1998.

[84] Ryo Yamada, Hidetada Sakai, and Kohei Uosaki. Solvent effect on the structure of the self-assembled monolayer of alkanethiol. *Chemistry letters*, 28(7):667–668, 1999.

[85] Ryo Yamada, Hiromi Wano, and Kohei Uosaki. Effect of temperature on structure of the self-assembled monolayer of decanethiol on au (111) surface. *Langmuir*, 16(13):5523–5525, 2000.

[86] Mitsuo Kawasaki, Tomoo Sato, Takumi Tanaka, and Kazunori Takao. Rapid self-assembly of alkanethiol monolayers on sputter-grown au (111). *Langmuir*, 16(4):1719–1728, 2000.

[87] Farid Bensebaa, Raluca Voicu, Laurent Huron, Thomas H Ellis, and Erik Kruus. Kinetics of formation of long-chain n-alkanethiolate monolayers on polycrystalline gold. *Langmuir*, 13(20):5335–5340, 1997.

[88] Colin D Bain, Joe Evall, and George M Whitesides. Formation of monolayers by the coadsorption of thiols on gold: variation in the head group, tail group, and solvent. *Journal of the American Chemical Society*, 111(18):7155–7164, 1989.

[89] Christopher ED Chidsey. Free energy and temperature dependence of electron transfer at the metal-electrolyte interface. *Science*, 251(4996):919–922, 1991.

[90] Li Sun and Richard M Crooks. Imaging of defects contained within n-alkylthiol monolayers by combination of underpotential deposition and scanning tunneling microscopy: Kinetics of self-assembly. *Journal of the Electrochemical Society*, 138(8):L23, 1991.

[91] Randolph Shipley Klein. Book reviews: The papers of benjamin franklin, volume 20: January i through december 31, 1773, edited by william b. willcox. *Pennsylvania History*, 45(4):366–367, 1978.

[92] John William Strutt Baron Rayleigh. *Scientific papers*, volume 1. University Press, 1899.

[93] H Devaux. Smithsonian inst. *Ann. Rep*, 261, 1913.

[94] W. B. Hardy. The general theory of colloidal solutions. *Proceedings of the Royal Society of London. Series A, Containing Papers of a Mathematical and Physical Character*, 86(591):601–610, 1912.

[95] Irving Langmuir. The constitution and fundamental properties of solids and liquids. ii. liquids. *Journal of the American chemical society*, 39(9):1848–1906, 1917.

[96] Katharine B Blodgett. Films built by depositing successive monomolecular layers on a solid surface. *Journal of the American Chemical Society*, 57(6):1007–1022, 1935.

[97] Katharine B Blodgett and Irving Langmuir. Built-up films of barium stearate and their optical properties. *Physical Review*, 51(11):964, 1937.

[98] Lucy Netzer, Radu Iscovici, and Jacob Sagiv. Adsorbed monolayers versus langmuir–blodgett monolayers—why and how? i: From monolayer to multilayer, by adsorption. In *Langmuir–Blodgett Films, 1982*, pages 235–241. Elsevier, 1983.

[99] Masa-aki Kakimoto, Masa-aki Suzuki, Toru Konishi, Yoshio Imai, Mitsumasa Iwamoto, and Taro Hino. Preparation of mono-and multilayer films of aromatic

polyimides using langmuir–blodgett technique. *Chemistry Letters*, 15(5):823–826, 1986.

[100] Martin R Bryce and Michael C Petty. Electrically conductive langmuir–blodgett films of charge-transfer materials. *Nature*, 374(6525):771–776, 1995.

[101] Michael C Petty. *Langmuir-Blodgett films: an introduction*. Cambridge University Press, 1996.

[102] James W Whalen. Physical chemistry of surfaces, (adamson, arthur w.), 1983.

[103] George L Gaines Jr. Thermodynamic relationships for mixed insoluble monolayers. *Journal of colloid and interface science*, 21(3):315–319, 1966.

[104] Alan J Walton. *Three phases of matter*. Clarendon Press Oxford, 1983.

[105] Biolin Scientific.

[106] William Draper Harkins. *The physical chemistry of surface films*. Reinhold, 1952.

[107] Richard H Tredgold and RH Tredgold. *Order in thin organic films*. Cambridge University Press, 1994.

[108] Abraham Ulman. Ultrathin organic films: From langmuir-blodgett to self assembly. 1991.

[109] B Lin, Mc C Shih, TM Bohanon, GE Ice, and Pulak Dutta. Phase diagram of a lipid monolayer on the surface of water. *Physical review letters*, 65(2):191, 1990.

[110] RM Kenn, C Böhm, AM Bibo, IR Peterson, Helmuth Moehwald, J Als-Nielsen, and K Kjaer. Mesophases and crystalline phases in fatty acid monolayers. *The Journal of Physical Chemistry*, 95(5):2092–2097, 1991.

[111] SC Biswas, L Dubreil, and D Marion. Interfacial behavior of wheat puroindolines: study of adsorption at the air–water interface from surface tension measurement using wilhelmy plate method. *Journal of colloid and interface science*, 244(2):245–253, 2001.

[112] JF Baret, H Hasmonay, JL Firpo, JJ Dupin, and M Dupeyrat. The different types of isotherm exhibited by insoluble fatty acid monolayers. a theoretical interpretation of phase transitions in the condensed state. *Chemistry and Physics of Lipids*, 30(2-3):177–187, 1982.

[113] MC Petty. Characterization and properties. In *Langmuir-Blodgett Films*, pages 133–221. Springer, 1990.

[114] IR Peterson. Langmuir-blodgett films. *Journal of Physics D: Applied Physics*, 23(4):379, 1990.

[115] "Abraham Ulman". Part two - langmuir-blodgett films. In Abraham Ulman, editor, *An Introduction to Ultrathin Organic Films*, pages 101 – 236. Academic Press, San Diego, 1991.

[116] Gerd Binnig and Heinrich Rohrer. Scanning tunneling microscopy. *Surface science*, 126(1-3):236–244, 1983.

[117] Gerd Binnig, Calvin F Quate, and Ch Gerber. Atomic force microscope. *Physical review letters*, 56(9):930, 1986.

[118] Roland Wiesendanger and Wiesendanger Roland. *Scanning probe microscopy and spectroscopy: methods and applications*. Cambridge university press, 1994.

[119] Franz J. Giessibl. Advances in atomic force microscopy. *Rev. Mod. Phys.*, 75:949–983, Jul 2003.

[120] Gerhard Meyer and Nabil M. Amer. Novel optical approach to atomic force microscopy. *Applied Physics Letters*, 53(12):1045–1047, 1988.

[121] Brunero Cappella and Giovanni Dietler. Force-distance curves by atomic force microscopy. *Surface science reports*, 34(1-3):1–104, 1999.

[122] Franz J Giessibl. Advances in atomic force microscopy. *Reviews of modern physics*, 75(3):949, 2003.

[123] F.Dinelli. Ultrasonic force microscopy: surface properties mapping and stiffness evaluation at a nanoscale level. 1998.

[124] Ricardo Garcıa and Ruben Perez. Dynamic atomic force microscopy methods. *Surface science reports*, 47(6-8):197–301, 2002.

[125] Ichiro Tanaka, I Kamiya, H Sakaki, N Qureshi, SJ Allen Jr, and PM Petroff. Imaging and probing electronic properties of self-assembled inas quantum dots by atomic force microscopy with conductive tip. *Applied physics letters*, 74(6):844–846, 1999.

[126] Mario Lanza. *Conductive Atomic Force Microscopy: Applications in Nanomaterials*. John Wiley & Sons, 2017.

[127] Masakazu Nakamura, Hirotomo Yanagisawa, Seishi Kuratani, Masaaki Iizuka, and Kazuhiro Kudo. Characterization of organic nano-transistors using a conductive afm probe. *Thin Solid Films*, 438:360–364, 2003.

[128] David J Wold and C Daniel Frisbie. Fabrication and characterization of metal-molecule- metal junctions by conducting probe atomic force microscopy. *Journal of the American Chemical Society*, 123(23):5549–5556, 2001.

[129] Takao Ishida, Wataru Mizutani, Yoichiro Aya, Hisato Ogiso, Shinya Sasaki, and Hiroshi Tokumoto. Electrical conduction of conjugated molecular sams studied by conductive atomic force microscopy. *The Journal of Physical Chemistry B*, 106(23):5886–5892, 2002.

[130] Aleksandr Noy, Charles H Sanders, Dmitri V Vezenov, Stanislaus S Wong, and Charles M Lieber. Chemically-sensitive imaging in tapping mode by chemical force microscopy: relationship between phase lag and adhesion. *Langmuir*, 14(7):1508–1511, 1998.

[131] AJ Howard, RR Rye, and JE Houston. Nanomechanical basis for imaging soft materials with tapping mode atomic force microscopy. *Journal of applied physics*, 79(4):1885–1890, 1996.

[132] Q Zhong, D Inniss, K Kjoller, and VB Elings. Fractured polymer/silica fiber surface studied by tapping mode atomic force microscopy. *Surface Science Letters*, 290(1-2):L688–L692, 1993.

[133] Jan H Hoh and Paul K Hansma. Atomic force microscopy for high-resolution imaging in cell biology. *Trends in Cell Biology*, 2(7):208–213, 1992.

[134] B Tompkins. Multimode™ spm instruction manual, 1999.

[135] Maxim E Dokukin and Igor Sokolov. Quantitative mapping of the elastic modulus of soft materials with harmonix and peakforce qnm afm modes. *Langmuir*, 28(46):16060–16071, 2012.

[136] TJ Young, MA Monclus, TL Burnett, WR Broughton, SL Ogin, and PA Smith. The use of the peakforcetm quantitative nanomechanical mapping afm-based

method for high-resolution young's modulus measurement of polymers. *Measurement Science and Technology*, 22(12):125703, 2011.

[137] Peter Schon, Kristof Bagdi, Kinga Molnar, Patrick Markus, Bela Pukanszky, and G Julius Vancso. Quantitative mapping of elastic moduli at the nanoscale in phase separated polyurethanes by afm. *European Polymer Journal*, 47(4):692–698, 2011.

[138] Wiktoria Walczyk, Peter M Schön, and Holger Schönherr. The effect of peakforce tapping mode afm imaging on the apparent shape of surface nanobubbles. *Journal of physics: Condensed matter*, 25(18):184005, 2013.

[139] Hermann Schillers, Izhar Medalsy, Shuiqing Hu, Andrea L Slade, and James E Shaw. Peakforce tapping resolves individual microvilli on living cells. *Journal of Molecular Recognition*, 29(2):95–101, 2016.

[140] Kim Sweers, Kees Van Der Werf, Martin Bennink, and Vinod Subramaniam. Nanomechanical properties of α-synuclein amyloid fibrils: a comparative study by nanoindentation, harmonic force microscopy, and peakforce qnm. *Nanoscale research letters*, 6(1):270, 2011.

[141] Chanmin Su. Mapping quantitative mechanical properties at molecular scale using peak force tapping afm. *Microscopy and Microanalysis*, 16(S2):364–365, 2010.

[142] Jaroslav Ďurkovič, Monika Kardošová, and Rastislav Lagaňa. Imaging and measurement of nanomechanical properties within primary xylem cell walls of broadleaves. 2014.

[143] Boris V Derjaguin, Vladimir M Muller, and Yu P Toporov. Effect of contact deformations on the adhesion of particles. *Journal of Colloid and interface science*, 53(2):314–326, 1975.

[144] Yue Ding, Guang-Kui Xu, and Gang-Feng Wang. On the determination of elastic moduli of cells by afm based indentation. *Scientific reports*, 7:45575, 2017.

[145] Malgorzata Kopycinska-Müller, Roy H Geiss, and Donna C Hurley. Contact mechanics and tip shape in afm-based nanomechanical measurements. *Ultramicroscopy*, 106(6):466–474, 2006.

[146] HM Pollock and A Hammiche. Micro-thermal analysis: techniques and applications. *Journal of Physics D: Applied Physics*, 34(9):R23, 2001.

[147] Ali Assy and Séverine Gomès. Heat transfer at nanoscale contacts investigated with scanning thermal microscopy. *Applied Physics Letters*, 107(4):043105, 2015.

[148] Séverine Gomès, Ali Assy, and Pierre-Olivier Chapuis. Scanning thermal microscopy: A review. *physica status solidi (a)*, 212(3):477–494, 2015.

[149] Russell J Pylkki, Patrick J Moyer, and Paul E West. Scanning near-field optical microscopy and scanning thermal microscopy. *Japanese journal of applied physics*, 33(6S):3785, 1994.

[150] Phillip S Dobson, John MR Weaver, and Gordon Mills. New methods for calibrated scanning thermal microscopy (sthm). In *SENSORS, 2007 IEEE*, pages 708–711. IEEE, 2007.

[151] Yuan Zhang, PS Dobson, and JMR Weaver. High temperature imaging using a thermally compensated cantilever resistive probe for scanning thermal microscopy. *Journal of Vacuum Science & Technology B, Nanotechnology and Microelectronics: Materials, Processing, Measurement, and Phenomena*, 30(1):010601, 2012.

[152] Philippe Grossel, Olivier Raphaël, Françoise Depasse, Thierry Duvaut, and Nathalie Trannoy. Multifrequential ac modeling of the sthm probe behavior. *International journal of thermal sciences*, 46(10):980–988, 2007.

[153] KW Park, EM Krivoy, HP Nair, Seth Robert Bank, and ET Yu. Cross-sectional scanning thermal microscopy of eras/gaas superlattices grown by molecular beam epitaxy. *Nanotechnology*, 26(26):265701, 2015.

[154] T. Meier, F. Menges, P. Nirmalraj, H. Hölscher, H. Riel, and B. Gotsmann. Length-dependent thermal transport along molecular chains. *Phys. Rev. Lett.*, 113:060801, Aug 2014.

[155] Youngsang Kim, Wonho Jeong, Kyeongtae Kim, Woochul Lee, and Pramod Reddy. Electrostatic control of thermoelectricity in molecular junctions. *Nature nanotechnology*, 9(11):881–885, 2014.

[156] Manuel E Pumarol, Mark C Rosamond, Peter Tovee, Michael C Petty, Dagou A Zeze, Vladimir Falko, and Oleg V Kolosov. Direct nanoscale imaging of ballistic and diffusive thermal transport in graphene nanostructures. *Nano Letters*, 12(6):2906–2911, 2012.

[157] Fabian Menges, Heike Riel, Andreas Stemmer, Christos Dimitrakopoulos, and Bernd Gotsmann. Thermal transport into graphene through nanoscopic contacts. *Physical review letters*, 111(20):205901, 2013.

[158] Gwangseok Hwang and Ohmyoung Kwon. Measuring the size dependence of thermal conductivity of suspended graphene disks using null-point scanning thermal microscopy. *Nanoscale*, 8(9):5280–5290, 2016.

[159] RE Sparks, Víctor Manuel García-Suárez, D Zs Manrique, and Colin J Lambert. Quantum interference in single molecule electronic systems. *Physical Review B*, 83(7):075437, 2011.

[160] Adi Salomon, David Cahen, Stuart Lindsay, John Tomfohr, Vincent B Engelkes, and C Daniel Frisbie. Comparison of electronic transport measurements on organic molecules. *Advanced Materials*, 15(22):1881–1890, 2003.

[161] Tao Li, Jonas Rahlf Hauptmann, Zhongming Wei, Søren Petersen, Nicolas Bovet, Tom Vosch, Jesper Nygård, Wenping Hu, Yunqi Liu, Thomas Bjørnholm, et al. Solution-processed ultrathin chemically derived graphene films as soft top contacts for solid-state molecular electronic junctions. *Advanced Materials*, 24(10):1333–1339, 2012.

[162] Jan Hendrik Schön, Hong Meng, and Zhenan Bao. Self-assembled monolayer organic field-effect transistors. *Nature*, 413(6857):713–716, 2001.

[163] Maria El Abbassi, Sara Sangtarash, Xunshan Liu, Mickael Lucien Perrin, Oliver Braun, Colin Lambert, Herre Sjoerd Jan van der Zant, Shlomo Yitzchaik, Silvio Decurtins, Shi-Xia Liu, et al. Robust graphene-based molecular devices. *Nature nanotechnology*, 14(10):957–961, 2019.

[164] XD Cui, A Primak, X Zarate, J Tomfohr, OF Sankey, Ana L Moore, Thomas A Moore, D Gust, Gari Harris, and SM Lindsay. Reproducible measurement of single-molecule conductivity. *science*, 294(5542):571–574, 2001.

[165] Vincent B Engelkes, Jeremy M Beebe, and C Daniel Frisbie. Length-dependent transport in molecular junctions based on sams of alkanethiols and alkanedithiols: effect of metal work function and applied bias on tunneling efficiency and contact resistance. *Journal of the American Chemical Society*, 126(43):14287–14296, 2004.

[166] Seong Ho Choi, BongSoo Kim, and C Daniel Frisbie. Electrical resistance of long conjugated molecular wires. *Science*, 320(5882):1482–1486, 2008.

[167] Thomas Hines, Ismael Diez-Perez, Joshua Hihath, Hongmei Liu, Zhong-Sheng Wang, Jianwei Zhao, Gang Zhou, Klaus Müllen, and Nongjian Tao. Transition from tunneling to hopping in single molecular junctions by measuring length and temperature dependence. *Journal of the American Chemical Society*, 132(33):11658–11664, 2010.

[168] Ryan C Chiechi, Emily A Weiss, Michael D Dickey, and George M Whitesides. Eutectic gallium–indium (egain): a moldable liquid metal for electrical characterization of self-assembled monolayers. *Angewandte Chemie International Edition*, 47(1):142–144, 2008.

[169] Richard L McCreery. Molecular electronic junctions. *Chemistry of Materials*, 16(23):4477–4496, 2004.

[170] Fang Chen, Xiulan Li, Joshua Hihath, Zhifeng Huang, and Nongjian Tao. Effect of anchoring groups on single-molecule conductance: comparative study of thiol-, amine-, and carboxylic-acid-terminated molecules. *Journal of the American Chemical Society*, 128(49):15874–15881, 2006.

[171] JM Krans, JM Van Ruitenbeek, VV Fisun, IK Yanson, L De Jongh, and J. The signature of conductance quantization in metallic point contacts. *Nature*, 375(6534):767–769, 1995.

[172] Nathan P Guisinger, Mark E Greene, Rajiv Basu, Andrew S Baluch, and Mark C Hersam. Room temperature negative differential resistance through individual organic molecules on silicon surfaces. *Nano Letters*, 4(1):55–59, 2004.

[173] Robert M Metzger. Unimolecular electrical rectifiers. *Chemical reviews*, 103(9):3803–3834, 2003.

[174] Xiaoyin Xiao, Bingqian Xu, and Nongjian J Tao. Measurement of single molecule conductance: Benzenedithiol and benzenedimethanethiol. *Nano Letters*, 4(2):267–271, 2004.

[175] ZJ Donhauser, BA Mantooth, KF Kelly, LA Bumm, JD Monnell, Joshua James Stapleton, DW Price, AM Rawlett, DL Allara, JM Tour, et al. Conduc-

tance switching in single molecules through conformational changes. *Science*, 292(5525):2303–2307, 2001.

[176] Ganesh K Ramachandran, Theresa J Hopson, Adam M Rawlett, Larry A Nagahara, Alex Primak, and Stuart M Lindsay. A bond-fluctuation mechanism for stochastic switching in wired molecules. *Science*, 300(5624):1413–1416, 2003.

[177] Chun Ning Lau, Duncan R Stewart, R Stanley Williams, and Marc Bockrath. Direct observation of nanoscale switching centers in metal/molecule/metal structures. *Nano Letters*, 4(4):569–572, 2004.

[178] Christian Joachim, James K Gimzewski, Reto R Schlittler, and Corinne Chavy. Electronic transparence of a single c 60 molecule. *Physical review letters*, 74(11):2102, 1995.

[179] Bingqian Xu and Nongjian J Tao. Measurement of single-molecule resistance by repeated formation of molecular junctions. *science*, 301(5637):1221–1223, 2003.

[180] Jin He, Otto Sankey, Myeong Lee, Nongjian Tao, Xiulan Li, and Stuart Lindsay. Measuring single molecule conductance with break junctions. *Faraday discussions*, 131:145–154, 2006.

[181] Hongkun Park, Jiwoong Park, Andrew KL Lim, Erik H Anderson, A Paul Alivisatos, and Paul L McEuen. Nanomechanical oscillations in a single-c 60 transistor. *Nature*, 407(6800):57–60, 2000.

[182] Brijesh Kumar, Brajesh Kumar Kaushik, and Yuvraj Singh Negi. Organic thin film transistors: structures, models, materials, fabrication, and applications: a review. *Polymer Reviews*, 54(1):33–111, 2014.

[183] Li-Juan Zhang, Yi Zhang, Ren-Jie Zhang, and Xu-Sheng Feng. In situ afm investigations on degradation of self-assembled monolayers on mica: Effect of humidity. *Colloids and Surfaces A: Physicochemical and Engineering Aspects*, 293(1-3):195–200, 2007.

[184] JV Davidovits, V Pho, P Silberzan, and M Goldmann. Temperature influence on the formation of silanized monolayers on silica: an atomic force microscopy study. *Surface science*, 352:369–373, 1996.

[185] Sungsoo Kim, Hugo K Christenson, and Joan E Curry. The effect of humidity on the stability of an octadecyltriethoxysilane monolayer self-assembled on untreated and plasma-treated mica. *Langmuir*, 18(6):2125–2129, 2002.

[186] Christian A Martin, Dapeng Ding, Jakob Kryger Sørensen, Thomas Bjørnholm, Jan M Van Ruitenbeek, and Herre SJ Van Der Zant. Fullerene-based anchoring groups for molecular electronics. *Journal of the American Chemical Society*, 130(40):13198–13199, 2008.

[187] Hylke B Akkerman, Paul WM Blom, Dago M De Leeuw, and Bert De Boer. Towards molecular electronics with large-area molecular junctions. *Nature*, 441(7089):69–72, 2006.

[188] Amy Szuchmacher Blum, James G Kushmerick, David P Long, Charles H Patterson, John C Yang, Jay C Henderson, Yuxing Yao, James M Tour, Ranganathan Shashidhar, and Banahalli R Ratna. Molecularly inherent voltage-controlled conductance switching. *Nature Materials*, 4(2):167–172, 2005.

[189] Jonathan R Widawsky, Pierre Darancet, Jeffrey B Neaton, and Latha Venkataraman. Simultaneous determination of conductance and thermopower of single molecule junctions. *Nano letters*, 12(1):354–358, 2012.

[190] Marco Carlotti, Maarten Degen, Yanxi Zhang, and Ryan C. Chiechi. Pronounced environmental effects on injection currents in egain tunneling junctions comprising self-assembled monolayers. *The Journal of Physical Chemistry C*, 120(36):20437–20445, 2016.

[191] Maria A Rampi, Olivier JA Schueller, and George M Whitesides. Alkanethiol self-assembled monolayers as the dielectric of capacitors with nanoscale thickness. *Applied Physics Letters*, 72(14):1781–1783, 1998.

[192] Mark H Schoenfisch and Jeanne E Pemberton. Air stability of alkanethiol self-assembled monolayers on silver and gold surfaces. *Journal of the American Chemical Society*, 120(18):4502–4513, 1998.

[193] C Vericat, ME Vela, GA Benitez, JA Martin Gago, X Torrelles, and RC Salvarezza. Surface characterization of sulfur and alkanethiol self-assembled monolayers on au (111). *Journal of Physics: Condensed Matter*, 18(48):R867, 2006.

[194] Michel Godin, PJ Williams, Vincent Tabard-Cossa, Olivier Laroche, LY Beaulieu, RB Lennox, and Peter Grütter. Surface stress, kinetics, and structure of alkanethiol self-assembled monolayers. *Langmuir*, 20(17):7090–7096, 2004.

[195] Wenyong Wang, Takhee Lee, and Mark A Reed. Mechanism of electron conduction in self-assembled alkanethiol monolayer devices. *Physical Review B*, 68(3):035416, 2003.

[196] Takhee Lee, Wenyong Wang, James F Klemic, Jingshen J Zhang, Jie Su, and Mark A Reed. Comparison of electronic transport characterization methods for alkanethiol self-assembled monolayers. *The Journal of Physical Chemistry B*, 108(25):8742–8750, 2004.

[197] Bin Li, Changgan Zeng, Qunxiang Li, Bing Wang, Lanfeng Yuan, Haiqian Wang, Jinlong Yang, JG Hou, and Qingshi Zhu. First-principles simulation of scanning tunneling microscopy images of individual molecules in alkanethiol self-assembled monolayers on au (111). *The Journal of Physical Chemistry B*, 107(4):972–984, 2003.

[198] Keith M Beardmore, Joel D Kress, Niels Grønbech-Jensen, and AR Bishop. Determination of the headgroup-gold (111) potential surface for alkanethiol self-assembled monolayers by ab initio calculation. *Chemical physics letters*, 286(1-2):40–45, 1998.

[199] Jeremy M Beebe, Vincent B Engelkes, Larry L Miller, and C Daniel Frisbie. Contact resistance in metal- molecule- metal junctions based on aliphatic sams: Effects of surface linker and metal work function. *Journal of the American Chemical Society*, 124(38):11268–11269, 2002.

[200] LA Bumm, JJ Arnold, TD Dunbar, DL Allara, and PS Weiss. Electron transfer through organic molecules. *The Journal of Physical Chemistry B*, 103(38):8122–8127, 1999.

[201] Krzysztof Slowinski, Richard V Chamberlain, Cary J Miller, and Marcin Majda. Through-bond and chain-to-chain coupling. two pathways in electron tunneling through liquid alkanethiol monolayers on mercury electrodes. *Journal of the American Chemical Society*, 119(49):11910–11919, 1997.

[202] David J Wold and C Daniel Frisbie. Formation of metal- molecule- metal tunnel

junctions: microcontacts to alkanethiol monolayers with a conducting afm tip. *Journal of the American Chemical Society*, 122(12):2970–2971, 2000.

[203] A Lio, C Morant, DF Ogletree, and M Salmeron. Atomic force microscopy study of the pressure-dependent structural and frictional properties of n-alkanethiols on gold. *The Journal of Physical Chemistry B*, 101(24):4767–4773, 1997.

[204] Lindsay R Ditzler, Chandana Karunatilaka, Venkat R Donuru, Haiying Y Liu, and Alexei V Tivanski. Electromechanical properties of self-assembled monolayers of tetrathiafulvalene derivatives studied by conducting probe atomic force microscopy. *The Journal of Physical Chemistry C*, 114(10):4429–4435, 2010.

[205] Igor Touzov and Christopher B Gorman. Tip-induced structural rearrangements of alkanethiolate self-assembled monolayers on gold. *The Journal of Physical Chemistry B*, 101(27):5263–5276, 1997.

[206] James M. Tour. Molecular electronics. synthesis and testing of components. *Accounts of Chemical Research*, 33(11):791–804, 2000.

[207] J Reichert, R Ochs, D Beckmann, HB Weber, Mv Mayor, and H v Löhneysen. Driving current through single organic molecules. *Physical Review Letters*, 88(17):176804, 2002.

[208] Michael C Petty. *Organic and Molecular Electronics: From Principles to Practice*. John Wiley & Sons, 2019.

[209] Dirk M Guldi, Chuping Luo, Angela Swartz, Rafael Gómez, José L Segura, Nazario Martín, Christoph Brabec, and N Serdar Sariciftci. Molecular engineering of c60-based conjugated oligomer ensembles: Modulating the competition between photoinduced energy and electron transfer processes. *The Journal of organic chemistry*, 67(4):1141–1152, 2002.

[210] José L Segura, Nazario Martín, and Dirk M Guldi. Materials for organic solar cells: the c 60/π-conjugated oligomer approach. *Chemical Society Reviews*, 34(1):31–47, 2005.

[211] Ferdinand C Grozema, Yuri A Berlin, and Laurens DA Siebbeles. Mechanism of charge migration through dna: molecular wire behavior, single-step tunneling or hopping? *Journal of the American Chemical Society*, 122(44):10903–10909, 2000.

[212] Zhongming Wei, Tao Li, Karsten Jennum, Marco Santella, Nicolas Bovet, Wenping Hu, Mogens Brøndsted Nielsen, Thomas Bjørnholm, Gemma C Solomon, Bo W Laursen, et al. Molecular junctions based on sams of cruciform oligo (phenylene ethynylene) s. *Langmuir*, 28(8):4016–4023, 2012.

[213] T Meier, F Menges, P Nirmalraj, H Holscher, H Riel, and B Gotsmann. Length-dependent thermal transport along molecular chains. *Physical review letters*, 113(6):060801, 2014.

[214] Marshall D Newton. Quantum chemical probes of electron-transfer kinetics: the nature of donor-acceptor interactions. *Chemical Reviews*, 91(5):767–792, 1991.

[215] William B Davis, Walter A Svec, Mark A Ratner, and Michael R Wasielewski. Molecular-wire behaviour in p-phenylenevinylene oligomers. *Nature*, 396(6706):60–63, 1998.

[216] Ayelet Vilan. Analyzing molecular current-voltage characteristics with the simmons tunneling model: scaling and linearization. *The Journal of Physical Chemistry C*, 111(11):4431–4444, 2007.

[217] Jeremy M Beebe, BongSoo Kim, John William Gadzuk, C Daniel Frisbie, and James G Kushmerick. Transition from direct tunneling to field emission in metal-molecule-metal junctions. *Physical review letters*, 97(2):026801, 2006.

[218] Qi Lu, Ke Liu, Hongming Zhang, Zhibo Du, Xianhong Wang, and Fosong Wang. From tunneling to hopping: A comprehensive investigation of charge transport mechanism in molecular junctions based on oligo(p-phenylene ethynylene)s. *ACS Nano*, 3(12):3861–3868, 2009.

[219] Abraham Ulman. Formation and structure of self-assembled monolayers. *Chemical reviews*, 96(4):1533–1554, 1996.

[220] E Delamarche and B Michel. Structure and stability of self-assembled monolayers. *Thin Solid Films*, 273(1-2):54–60, 1996.

[221] J Nathan Hohman, Pengpeng Zhang, Elizabeth I Morin, Patrick Han, Moonhee Kim, Adam R Kurland, Patrick D McClanahan, Viktor P Balema, and Paul S Weiss. Self-assembly of carboranethiol isomers on au {111}: intermolecular interactions determined by molecular dipole orientations. *ACS nano*, 3(3):527–536, 2009.

[222] Chuancheng Jia and Xuefeng Guo. Molecule–electrode interfaces in molecular electronic devices. *Chemical Society Reviews*, 42(13):5642–5660, 2013.

[223] Sabina Caneva, Matthijs D Hermans, Martin Lee, Amador Garcia-Fuente, Kenji Watanabe, Takashi Taniguchi, Cees Dekker, Jaime Ferrer, Herre SJ van der Zant, and Pascal Gehring. A mechanically tunable quantum dot in a graphene break junction. *arXiv preprint arXiv:2002.03992*, 2020.

[224] Christian R Hansen, Thomas J Sørensen, Magni Glyvradal, Jacob Larsen, Sara H Eisenhardt, Thomas Bjørnholm, Martin M Nielsen, Robert Feidenhans'l, and Bo W Laursen. Structure of the buried metal- molecule interface in organic thin film devices. *Nano letters*, 9(3):1052–1057, 2009.

[225] Hossam Haick and David Cahen. Contacting organic molecules by soft methods: towards molecule-based electronic devices. *Accounts of chemical research*, 41(3):359–366, 2008.

[226] Yueh-Lin Loo, David V Lang, John A Rogers, and Julia WP Hsu. Electrical contacts to molecular layers by nanotransfer printing. *Nano Letters*, 3(7):913–917, 2003.

[227] Michael L Chabinyc, Xiaoxi Chen, R Erik Holmlin, Heiko Jacobs, Hjalti Skulason, C Daniel Frisbie, Vladimiro Mujica, Mark A Ratner, Maria Anita Rampi, and George M Whitesides. Molecular rectification in a metal-insulator-metal junction based on self-assembled monolayers. *Journal of the American Chemical Society*, 124(39):11730–11736, 2002.

[228] Martin M Thuo, William F Reus, Christian A Nijhuis, Jabulani R Barber, Choongik Kim, Michael D Schulz, and George M Whitesides. Odd-even effects in charge transport across self-assembled monolayers. *Journal of the American Chemical Society*, 133(9):2962–2975, 2011.

[229] Sungjun Park, Gunuk Wang, Byungjin Cho, Yonghun Kim, Sunghoon Song, Yongsung Ji, Myung-Han Yoon, and Takhee Lee. Flexible molecular-scale electronic devices. *Nature nanotechnology*, 7(7):438, 2012.

[230] Kostya S Novoselov, Andre K Geim, Sergei V Morozov, D Jiang, Y_ Zhang, Sergey V Dubonos, Irina V Grigorieva, and Alexandr A Firsov. Electric field effect in atomically thin carbon films. *science*, 306(5696):666–669, 2004.

[231] Gunuk Wang, Yonghun Kim, Minhyeok Choe, Tae-Wook Kim, and Takhee Lee. A new approach for molecular electronic junctions with a multilayer graphene electrode. *Advanced Materials*, 23(6):755–760, 2011.

[232] Tao Li, Martyn Jevric, Jonas R Hauptmann, Rune Hviid, Zhongming Wei, Rui Wang, Nini EA Reeler, Erling Thyrhaug, Søren Petersen, Jakob AS Meyer, et al. Ultrathin reduced graphene oxide films as transparent top-contacts for light switchable solid-state molecular junctions. *Advanced Materials*, 25(30):4164–4170, 2013.

[233] Martin Kűhnel, Marc H Overgaard, Morten C Hels, Ajuan Cui, Tom Vosch, Jesper Nygård, Tao Li, Bo W Laursen, and Kasper Nørgaard. High-quality reduced graphene oxide electrodes for sub-kelvin studies of molecular monolayer junctions. *The Journal of Physical Chemistry C*, 122(43):25102–25109, 2018.

[234] Sohyeon Seo, Misook Min, Junghyun Lee, Takhee Lee, Sung-Yool Choi, and Hyoyoung Lee. Solution-processed reduced graphene oxide films as electronic contacts for molecular monolayer junctions. *Angewandte Chemie International Edition*, 51(1):108–112, 2012.

[235] Mario Lanza, Teng Gao, Zixuan Yin, Yanfeng Zhang, Zhongfan Liu, Yuzhen Tong, Ziyong Shen, and Huiling Duan. Nanogap based graphene coated afm tips with high spatial resolution, conductivity and durability. *Nanoscale*, 5(22):10816–10823, 2013.

[236] Yugeng Wen, Jianyi Chen, Yunlong Guo, Bin Wu, Gui Yu, and Yunqi Liu. Multilayer graphene-coated atomic force microscopy tips for molecular junctions. *Advanced Materials*, 24(26):3482–3485, 2012.

[237] Aaron Tan, Seid Sadat, and Pramod Reddy. Measurement of thermopower and current-voltage characteristics of molecular junctions to identify orbital alignment. *Applied Physics Letters*, 96(1):013110, 2010.

[238] Hyunwook Song, Youngsang Kim, Yun Hee Jang, Heejun Jeong, Mark A Reed, and Takhee Lee. Observation of molecular orbital gating. *Nature*, 462(7276):1039–1043, 2009.

[239] Pascal Gehring, Martijn Van Der Star, Charalambos Evangeli, Jennifer J Le Roy, Lapo Bogani, Oleg V Kolosov, and Herre SJ Van Der Zant. Efficient heating of single-molecule junctions for thermoelectric studies at cryogenic temperatures. *Applied Physics Letters*, 115(7):073103, 2019.

[240] Youngsang Kim, Andrej Lenert, Edgar Meyhofer, and Pramod Reddy. Temperature dependence of thermopower in molecular junctions. *Applied Physics Letters*, 109(3):033102, 2016.

[241] Shaoyin Guo, Gang Zhou, and Nongjian Tao. Single molecule conductance, thermopower, and transition voltage. *Nano letters*, 13(9):4326–4332, 2013.

[242] Kanhayalal Baheti, Jonathan A Malen, Peter Doak, Pramod Reddy, Sung-Yeon Jang, T Don Tilley, Arun Majumdar, and Rachel A Segalman. Probing the chemistry of molecular heterojunctions using thermoelectricity. *Nano letters*, 8(2):715–719, 2008.

[243] Jonathan A Malen, Peter Doak, Kanhayalal Baheti, T Don Tilley, Arun Majumdar, and Rachel A Segalman. The nature of transport variations in molecular heterojunction electronics. *Nano letters*, 9(10):3406–3412, 2009.

[244] CM Finch, VM Garcia-Suarez, and CJ Lambert. Giant thermopower and figure of merit in single-molecule devices. *Physical review b*, 79(3):033405, 2009.

[245] Fabian Pauly, Janne K Viljas, and Juan Carlos Cuevas. Length-dependent conductance and thermopower in single-molecule junctions of dithiolated oligophenylene derivatives: A density functional study. *Physical Review B*, 78(3):035315, 2008.

[246] Jonathan A Malen, Peter Doak, Kanhayalal Baheti, T Don Tilley, Rachel A Segalman, and Arun Majumdar. Identifying the length dependence of orbital alignment and contact coupling in molecular heterojunctions. *Nano letters*, 9(3):1164–1169, 2009.

[247] Changgan Zeng, Bin Li, Bing Wang, Haiqian Wang, Kedong Wang, Jinlong Yang, JG Hou, and Qingshi Zhu. What can a scanning tunneling microscope image do for the insulating alkanethiol molecules on au (111) substrates? *The Journal of chemical physics*, 117(2):851–856, 2002.

[248] Chao-Cheng Kaun and Hong Guo. Resistance of alkanethiol molecular wires. *Nano letters*, 3(11):1521–1525, 2003.

[249] YX Zhou, F Jiang, H Chen, R Note, H Mizuseki, and Y Kawazoe. First-principles study of length dependence of conductance in alkanedithiols. *The Journal of chemical physics*, 128(4):044704, 2008.

[250] Jonathan R Widawsky, Wenbo Chen, Hector Vazquez, Taekyeong Kim, Ronald Breslow, Mark S Hybertsen, and Latha Venkataraman. Length-dependent thermopower of highly conducting au–c bonded single molecule junctions. *Nano letters*, 13(6):2889–2894, 2013.

[251] Yu-Shen Liu, Yi-Ren Chen, and Yu-Chang Chen. Thermoelectric efficiency in nanojunctions: a comparison between atomic junctions and molecular junctions. *ACS nano*, 3(11):3497–3504, 2009.

[252] Aaron Tan, Janakiraman Balachandran, Seid Sadat, Vikram Gavini, Barry D Dunietz, Sung-Yeon Jang, and Pramod Reddy. Effect of length and contact chemistry on the electronic structure and thermoelectric properties of molecular junctions. *Journal of the American Chemical Society*, 133(23):8838–8841, 2011.

[253] Janakiraman Balachandran, Pramod Reddy, Barry D. Dunietz, and Vikram Gavini. End-group-induced charge transfer in molecular junctions: Effect on electronic-structure and thermopower. *The Journal of Physical Chemistry Letters*, 3(15):1962–1967, 2012.

[254] Yongqiang Xue and Mark A Ratner. End group effect on electrical transport through individual molecules: A microscopic study. *Physical Review B*, 69(8):085403, 2004.

[255] Makusu Tsutsui, Kazumichi Yokota, Takanori Morikawa, and Masateru Taniguchi. Roles of vacuum tunnelling and contact mechanics in single-molecule thermopower. *Scientific reports*, 7:44276, 2017.

[256] Janakiraman Balachandran, Pramod Reddy, Barry D. Dunietz, and Vikram Gavini. End-group influence on frontier molecular orbital reorganization and thermoelectric properties of molecular junctions. *The Journal of Physical Chemistry Letters*, 4(22):3825–3833, 2013.

[257] Stefan Bilan, Linda A Zotti, Fabian Pauly, and Juan Carlos Cuevas. Theoretical study of the charge transport through c 60-based single-molecule junctions. *Physical Review B*, 85(20):205403, 2012.

[258] Weilong Xing, Jie Chen, Yingying Liang, Ye Zou, Yimeng Sun, Wei Xu, and Daoben Zhu. Optimization of the thermoelectric performance of layer-by-layer structured copper-phthalocyanine (cupc) thin films doped with hexacyanotrimethylene-cyclopropane (cn6-cp). *RSC Advances*, 9(55):31840–31845, 2019.

[259] Edmund Leary, Bart Limburg, Asma Alanazy, Sara Sangtarash, Iain Grace, Katsutoshi Swada, Louisa J Esdaile, Mohammed Noori, M Teresa González, Gabino Rubio-Bollinger, et al. Bias-driven conductance increase with length in porphyrin tapes. *Journal of the American Chemical Society*, 140(40):12877–12883, 2018.

[260] Artem Mishchenko, David Vonlanthen, Velimir Meded, Marius Burkle, Chen Li, Ilya V Pobelov, Alexei Bagrets, Janne K Viljas, Fabian Pauly, Ferdinand Evers, et al. Influence of conformation on conductance of biphenyl-dithiol single-molecule contacts. *Nano letters*, 10(1):156–163, 2010.

[261] Latha Venkataraman, Jennifer E Klare, Colin Nuckolls, Mark S Hybertsen, and Michael L Steigerwald. Dependence of single-molecule junction conductance on molecular conformation. *Nature*, 442(7105):904–907, 2006.

[262] Luke J O'Driscoll, Xintai Wang, Michael Jay, Andrei S Batsanov, Hatef Sadeghi, Colin J Lambert, Benjamin J Robinson, and Martin R Bryce. Carbazole-based tetrapodal anchor groups for gold surfaces: Synthesis and conductance properties. *Angewandte Chemie*, 132(2):892–899, 2020.

[263] See Kei Lee, Marius Buerkle, Ryo Yamada, Yoshihiro Asai, and Hirokazu Tada. Thermoelectricity at the molecular scale: a large seebeck effect in endohedral metallofullerenes. *Nanoscale*, 7(48):20497–20502, 2015.

[264] Laura Rincón-García, Ali K Ismael, Charalambos Evangeli, Iain Grace, Gabino Rubio-Bollinger, Kyriakos Porfyrakis, Nicolás Agraït, and Colin J Lambert. Molecular design and control of fullerene-based bi-thermoelectric materials. *Nature materials*, 15(3):289–293, 2016.

[265] Charalambos Evangeli, Manuel Matt, Laura Rincón-García, Fabian Pauly, Peter Nielaba, Gabino Rubio-Bollinger, Juan Carlos Cuevas, and Nicolás Agraït. Quantum thermopower of metallic atomic-size contacts at room temperature. *Nano letters*, 15(2):1006–1011, 2015.

[266] Achim Harzheim, Jakub K Sowa, Jacob L Swett, G Andrew D Briggs, Jan A Mol, and Pascal Gehring. Role of metallic leads and electronic degeneracies in thermoelectric power generation in quantum dots. *Physical Review Research*, 2(1):013140, 2020.

[267] Elinor Zerah-Harush and Yonatan Dubi. Enhanced thermoelectric performance of hybrid nanoparticle–single-molecule junctions. *Physical Review Applied*, 3(6):064017, 2015.

[268] SN Yaliraki, M Kemp, and Mark A Ratner. Conductance of molecular wires: Influence of molecule- electrode binding. *Journal of the American Chemical Society*, 121(14):3428–3434, 1999.

[269] Jeremy M Beebe, Vincent B Engelkes, Larry L Miller, and C Daniel Frisbie. Contact resistance in metal- molecule- metal junctions based on aliphatic sams: Effects of surface linker and metal work function. *Journal of the American Chemical Society*, 124(38):11268–11269, 2002.

[270] Shannon K Yee, Jonathan A Malen, Arun Majumdar, and Rachel A Segalman. Thermoelectricity in fullerene–metal heterojunctions. *Nano letters*, 11(10):4089–4094, 2011.

[271] See Kei Lee, Tatsuhiko Ohto, Ryo Yamada, and Hirokazu Tada. Thermopower of benzenedithiol and c60 molecular junctions with ni and au electrodes. *Nano letters*, 14(9):5276–5280, 2014.

[272] SS Kushvaha, W Hofbauer, YC Loke, Samarendra P Singh, and SJ O'Shea. Thermoelectric measurements using different tips in atomic force microscopy. *Journal of Applied Physics*, 109(8):084341, 2011.

[273] Alexandre R Champagne, Abhay N Pasupathy, and Daniel C Ralph. Mechanically adjustable and electrically gated single-molecule transistors. *Nano letters*, 5(2):305–308, 2005.

[274] Edgar A Osorio, Kasper Moth-Poulsen, Herre SJ van der Zant, Jens Paaske, Per Hedegård, Karsten Flensberg, Jesper Bendix, and Thomas Bjørnholm. Electrical manipulation of spin states in a single electrostatically gated transition-metal complex. *Nano letters*, 10(1):105–110, 2010.

[275] Jiwoong Park, Abhay N Pasupathy, Jonas I Goldsmith, Connie Chang, Yuval Yaish, Jason R Petta, Marie Rinkoski, James P Sethna, Héctor D Abruña, Paul L McEuen, et al. Coulomb blockade and the kondo effect in single-atom transistors. *Nature*, 417(6890):722–725, 2002.

[276] Ali Javey, Hyoungsub Kim, Markus Brink, Qian Wang, Ant Ural, Jing Guo, Paul McIntyre, Paul McEuen, Mark Lundstrom, and Hongjie Dai. High-κ dielectrics for advanced carbon-nanotube transistors and logic gates. *Nature materials*, 1(4):241–246, 2002.

[277] Pablo Jarillo-Herrero, Jing Kong, Herre SJ Van Der Zant, Cees Dekker, Leo P Kouwenhoven, and Silvano De Franceschi. Orbital kondo effect in carbon nanotubes. *Nature*, 434(7032):484–488, 2005.

[278] Nathaniel M Gabor, Zhaohui Zhong, Ken Bosnick, Jiwoong Park, and Paul L McEuen. Extremely efficient multiple electron-hole pair generation in carbon nanotube photodiodes. *Science*, 325(5946):1367–1371, 2009.

[279] Wonho Jeong, Kyeongtae Kim, Youngsang Kim, Woochul Lee, and Pramod Reddy. Characterization of nanoscale temperature fields during electromigration of nanowires. *Scientific reports*, 4(1):1–6, 2014.

[280] Achim Harzheim, Jean Spiece, Charalambos Evangeli, Edward McCann, Vladimir Falko, Yuewen Sheng, Jamie H. Warner, G. Andrew D. Briggs, Jan A. Mol, Pascal Gehring, and Oleg V. Kolosov. Geometrically enhanced thermoelectric effects in graphene nanoconstrictions. *Nano Letters*, 18(12):7719–7725, 2018.

[281] JP Bergfield and Charles A Stafford. Thermoelectric signatures of coherent transport in single-molecule heterojunctions. *Nano letters*, 9(8):3072–3076, 2009.

[282] Yan Geng, Sara Sangtarash, Cancan Huang, Hatef Sadeghi, Yongchun Fu, Wenjing Hong, Thomas Wandlowski, Silvio Decurtins, Colin J Lambert, and Shi-Xia Liu. Magic ratios for connectivity-driven electrical conductance of graphene-like molecules. *Journal of the American Chemical Society*, 137(13):4469–4476, 2015.

[283] CJ Lambert. Basic concepts of quantum interference and electron transport in single-molecule electronics. *Chemical Society Reviews*, 44(4):875–888, 2015.

[284] Hatef Sadeghi, Jan A Mol, Chit Siong Lau, G Andrew D Briggs, Jamie Warner, and Colin J Lambert. Conductance enlargement in picoscale electroburnt graphene nanojunctions. *Proceedings of the National Academy of Sciences*, 112(9):2658–2663, 2015.

[285] H Vazquez, R Skouta, S Schneebeli, M Kamenetska, R Breslow, L Venkataraman,

and MS Hybertsen. Probing the conductance superposition law in single-molecule circuits with parallel paths. *Nature Nanotechnology*, 7(10):663–667, 2012.

[286] Stefan Ballmann, Rainer Härtle, Pedro B Coto, Mark Elbing, Marcel Mayor, Martin R Bryce, Michael Thoss, and Heiko B Weber. Experimental evidence for quantum interference and vibrationally induced decoherence in single-molecule junctions. *Physical review letters*, 109(5):056801, 2012.

[287] Sriharsha V Aradhya and Latha Venkataraman. Single-molecule junctions beyond electronic transport. *Nature nanotechnology*, 8(6):399, 2013.

[288] Ferry Prins, Amelia Barreiro, Justus W Ruitenberg, Johannes S Seldenthuis, Núria Aliaga-Alcalde, Lieven MK Vandersypen, and Herre SJ van der Zant. Room-temperature gating of molecular junctions using few-layer graphene nanogap electrodes. *Nano letters*, 11(11):4607–4611, 2011.

[289] Carlos R Arroyo, Simge Tarkuc, Riccardo Frisenda, Johannes S Seldenthuis, Charlotte HM Woerde, Rienk Eelkema, Ferdinand C Grozema, and Herre SJ Van Der Zant. Signatures of quantum interference effects on charge transport through a single benzene ring. *Angewandte Chemie International Edition*, 52(11):3152–3155, 2013.

[290] Constant M Guédon, Hennie Valkenier, Troels Markussen, Kristian S Thygesen, Jan C Hummelen, and Sense Jan Van Der Molen. Observation of quantum interference in molecular charge transport. *Nature nanotechnology*, 7(5):305–309, 2012.

[291] Veerabhadrarao Kaliginedi, Pavel Moreno-García, Hennie Valkenier, Wenjing Hong, Víctor M García-Suárez, Petra Buiter, Jelmer LH Otten, Jan C Hummelen, Colin J Lambert, and Thomas Wandlowski. Correlations between molecular structure and single-junction conductance: a case study with oligo (phenylene-ethynylene)-type wires. *Journal of the American Chemical Society*, 134(11):5262–5275, 2012.

[292] Sriharsha V Aradhya, Jeffrey S Meisner, Markrete Krikorian, Seokhoon Ahn, Radha Parameswaran, Michael L Steigerwald, Colin Nuckolls, and Latha Venkataraman. Dissecting contact mechanics from quantum interference in single-molecule junctions of stilbene derivatives. *Nano letters*, 12(3):1643–1647, 2012.

[293] Colin J Lambert, Hatef Sadeghi, and Qusiy H Al-Galiby. Quantum-interference-enhanced thermoelectricity in single molecules and molecular films. *Comptes Rendus Physique*, 17(10):1084–1095, 2016.

[294] Matthias Ernzerhof, Min Zhuang, and Philippe Rocheleau. Side-chain effects in molecular electronic devices. *The Journal of chemical physics*, 123(13):134704, 2005.

[295] Troels Markussen, Robert Stadler, and Kristian S Thygesen. The relation between structure and quantum interference in single molecule junctions. *Nano letters*, 10(10):4260–4265, 2010.

[296] Xintai Wang, Troy LR Bennett, Ali Ismael, Luke A Wilkinson, Joseph Hamill, Andrew JP White, Iain M Grace, Tim Albrecht, Benjamin J Robinson, Nicholas J Long, et al. Scale-up of room-temperature constructive quantum interference from single molecules to self-assembled molecular-electronic films. *arXiv preprint arXiv:1911.04324*, 2019.

[297] Ruijiao Miao, Hailiang Xu, Maxim Skripnik, Longji Cui, Kun Wang, Kim GL Pedersen, Martin Leijnse, Fabian Pauly, Kenneth Warnmark, Edgar Meyhofer, et al. Influence of quantum interference on the thermoelectric properties of molecular junctions. *Nano letters*, 18(9):5666–5672, 2018.

[298] Cary J Miller, Paul McCord, and Allen J Bard. Study of langmuir monolayers of ruthenium complexes and their aggregation by electrogenerated chemiluminescence. *Langmuir*, 7(11):2781–2787, 1991.

[299] S Hénon and J Meunier. Microscope at the brewster angle: Direct observation of first-order phase transitions in monolayers. *Review of Scientific Instruments*, 62(4):936–939, 1991.

[300] Dirk Hoenig and Dietmar Moebius. Direct visualization of monolayers at the air-water interface by brewster angle microscopy. *The Journal of Physical Chemistry*, 95(12):4590–4592, 1991.

[301] R Castillo, S Ramos, and J Ruiz-Garcia. Direct observation of langmuir films of c60 and c70 using brewster angle microscopy. *The Journal of Physical Chemistry*, 100(37):15235–15241, 1996.

[302] Hua-Li Nie, Xuan Dou, Zhihong Tang, Hee Dong Jang, and Jiaxing Huang. High-yield spreading of water-miscible solvents on water for langmuir–blodgett assembly. *Journal of the American Chemical Society*, 137(33):10683–10688, 2015.

[303] Nicholas C Maliszewskyj, Paul A Heiney, David R Jones, Robert M Strongin, Maria A Cichy, and Amos B Smith III. Langmuir films of fullerene c60, fullerene epoxide c60o, and dihydrofulleroid c61h2. *Langmuir*, 9(6):1439–1441, 1993.

[304] Yaw S Obeng and Allen J Bard. Langmuir films of c60 at the air-water interface. *Journal of the American Chemical Society*, 113(16):6279–6280, 1991.

[305] Da-Ren Chen and David YH Pui. Experimental investigation of scaling laws for electrospraying: dielectric constant effect. *Aerosol Science and Technology*, 27(3):367–380, 1997.

[306] Soubir Basak, Da-Ren Chen, and Pratim Biswas. Electrospray of ionic precursor solutions to synthesize iron oxide nanoparticles: modified scaling law. *Chemical engineering science*, 62(4):1263–1268, 2007.

[307] L Todd Banner, Andrew Richter, and Eugene Pinkhassik. Pinhole-free large-grained atomically smooth au (111) substrates prepared by flame-annealed template stripping. *Surface and Interface Analysis: An International Journal devoted to the development and application of techniques for the analysis of surfaces, interfaces and thin films*, 41(1):49–55, 2009.

[308] Emily A Weiss, George K Kaufman, Jennah K Kriebel, Zhefeng Li, Richard Schalek, and George M Whitesides. Si/sio2-templated formation of ultraflat metal surfaces on glass, polymer, and solder supports: their use as substrates for self-assembled monolayers. *Langmuir*, 23(19):9686–9694, 2007.

[309] Home: Quartz crystal microbalance: the first scientific qcm entirely open.

[310] Günter Sauerbrey. Verwendung von schwingquarzen zur wägung dünner schichten und zur mikrowägung. *Zeitschrift für physik*, 155(2):206–222, 1959.

[311] Jean Spièce. *Quantitative mapping of nanothermal transport via Scanning Thermal Microscopy*. Springer Nature, 2019.

[312] J Spiece, C Evangeli, K Lulla, A Robson, B Robinson, and O Kolosov. Improving accuracy of nanothermal measurements via spatially distributed scanning thermal microscope probes. *Journal of Applied Physics*, 124(1):015101, 2018.

[313] Shu-Wei Liu, Hua-Ping Wang, Qiang Xu, Tian-Bao Ma, Gui Yu, Chenhui Zhang, Dechao Geng, Zhiwei Yu, Shengguang Zhang, Wenzhong Wang, et al. Robust microscale superlubricity under high contact pressure enabled by graphene-coated microsphere. *Nature communications*, 8(1):1–8, 2017.

[314] M Lanza, A Bayerl, T Gao, M Porti, M Nafria, GY Jing, YF Zhang, ZF Liu, and HL Duan. Graphene-coated atomic force microscope tips for reliable nanoscale electrical characterization. *Advanced Materials*, 25(10):1440–1444, 2013.

[315] Cristina Martin-Olmos, Haider Imad Rasool, Bruce H Weiller, and James K Gimzewski. Graphene mems: Afm probe performance improvement. *ACS nano*, 7(5):4164–4170, 2013.

[316] Fei Hui, Pujashree Vajha, Yuanyuan Shi, Yanfeng Ji, Huiling Duan, Andrea Padovani, Luca Larcher, Xiao Rong Li, Jing Juan Xu, and Mario Lanza. Moving graphene devices from lab to market: advanced graphene-coated nanoprobes. *Nanoscale*, 8(16):8466–8473, 2016.

[317] Cindra A Widrig, Chinkap Chung, and Marc D Porter. The electrochemical desorption of n-alkanethiol monolayers from polycrystalline au and ag electrodes. *Journal of electroanalytical chemistry and interfacial electrochemistry*, 310(1-2):335–359, 1991.

[318] Takashi Kakiuchi, Hideyuki Usui, Daisuke Hobara, and Masahiro Yamamoto. Voltammetric properties of the reductive desorption of alkanethiol self-assembled monolayers from a metal surface. *Langmuir*, 18(13):5231–5238, 2002.

[319] Roberto Carlos Salvarezza and Pilar Carro. The electrochemical stability of thiols on gold surfaces. *Journal of Electroanalytical Chemistry*, 819:234–239, 2018.

[320] Yanxi Zhang, Xinkai Qiu, Pavlo Gordiichuk, Saurabh Soni, Theodorus L Krijger, Andreas Herrmann, and Ryan C Chiechi. Mechanically and electrically robust self-assembled monolayers for large-area tunneling junctions. *The Journal of Physical Chemistry C*, 121(27):14920–14928, 2017.

[321] Tae-Wook Kim, Gunuk Wang, Hyoyoung Lee, and Takhee Lee. Statistical analysis of electronic properties of alkanethiols in metal–molecule–metal junctions. *Nanotechnology*, 18(31):315204, 2007.

[322] NA Burnham, RJ Colton, and HM Pollock. Work-function anisotropies as an origin of long-range surface forces. *Physical review letters*, 69(1):144, 1992.

[323] Elba Gomar-Nadal, Ganesh K Ramachandran, Fan Chen, Timothy Burgin, Concepcio Rovira, David B Amabilino, and Stuart M Lindsay. Self-assembled monolayers of tetrathiafulvalene derivatives on au (111): Organization and electrical properties. *The Journal of Physical Chemistry B*, 108(22):7213–7218, 2004.

[324] J Blatt. *Thermoelectric power of metals*. Springer Science & Business Media, 2012.

[325] Magnus Paulsson and Supriyo Datta. Thermoelectric effect in molecular electronics. *Physical Review B*, 67(24):241403, 2003.

[326] Li-Yong Gan, Qingyun Zhang, Yingchun Cheng, and Udo Schwingenschgl. Photovoltaic heterojunctions of fullerenes with mos2 and ws2 monolayers. *The Journal of Physical Chemistry Letters*, 5(8):1445–1449, 2014. PMID: 26269992.

[327] Leonid A Chernozatonskii, Alexander G Kvashnin, and Pavel B Sorokin. Heterostructures based on graphene and mos2 layers decorated by c60 fullerenes. *Nanotechnology*, 27(36):365201, 2016.

[328] Runfeng Chen, Cheng Lin, Huan Yu, Yuting Tang, Chao Song, Lihui Yuwen, Hai Li, Xiaoji Xie, Lianhui Wang, and Wei Huang. Templating c60 on mos2 nanosheets for 2d hybrid van der waals p-n nanoheterojunctions. *Chemistry of Materials*, 28(12):4300–4306, 2016.

[329] CM Varma, J Zaanen, and K Raghavachari. Superconductivity in the fullerenes. *Science*, 254(5034):989–992, 1991.

[330] Qian Li, Mikkel Strange, Ivan Duchemin, Davide Donadio, and Gemma C Solomon. A strategy to suppress phonon transport in molecular junctions using π-stacked systems. *The Journal of Physical Chemistry C*, 121(13):7175–7182, 2017.

[331] Chad A Mirkin and W Brett Caldwell. Thin film, fullerene-based materials. *Tetrahedron*, 52(14):5113–5130, 1996.

[332] Cong Yan, Aneta Dybek, Claire Hanson, Karina Schulte, AA Cafolla, John Dennis, and Philip Moriarty. Langmuir–blodgett films of c60 and c60o on silicon: Islands, rings and grains. *Thin Solid Films*, 517(5):1650–1654, 2009.

[333] Valerii Nikolaevich Bezmel'nitsyn, Aleksandr V Eletskii, et al. Fullerenes in solutions. *Physics-uspekhi*, 41(11):1091, 1998.

[334] D Heymann. Solubility of fullerenes c60 and c70 in seven normal alcohols and their deduced solubility in water. *Fullerene Science & Technology*, 4(3):509–515, 1996.

[335] LA Girifalco. Molecular properties of fullerene in the gas and solid phases. *The Journal of Physical Chemistry*, 96(2):858–861, 1992.

[336] Allan K Evans. Kinetics of langmuir films of fullerene c60. *The Journal of Physical Chemistry B*, 102(36):7016–7022, 1998.

[337] RJ Wilson, G Meijer, Donald S Bethune, RD Johnson, DD Chambliss, MS De Vries, HE Hunziker, and HR Wendt. Imaging c60 clusters on a surface using a scanning tunnelling microscope. *Nature*, 348(6302):621–622, 1990.

[338] Luis Otavio S Bulhoes, Yaw S Obeng, and Allen J Bard. Langmuir-blodgett and electrochemical studies of fullerene films. *Chemistry of materials*, 5(1):110–114, 1993.

[339] YF Xiao, ZQ Yao, and DS Jin. High-resolution electron-microscopy and electron-diffraction study on the c-60 langmuir-blodgett-films. *Journal of Physical Chemistry*, 98(21):5557–5558, 1994.

[340] Soichiro Yoshimoto, Eishi Tsutsumi, Yosuke Honda, Osamu Ito, and Kingo Itaya. Supramolecular assembly of [60] fullerene and highly ordered zinc octaethylporphyrin adlayer formed on au (111) surface. *Chemistry letters*, 33(7):914–915, 2004.

[341] Xiaotao Zhao, Cancan Huang, Murat Gulcur, Andrei S Batsanov, Masoud Baghernejad, Wenjing Hong, Martin R Bryce, and Thomas Wandlowski. Oligo (aryleneethynylene) s with terminal pyridyl groups: synthesis and length dependence of the tunneling-to-hopping transition of single-molecule conductances. *Chemistry of materials*, 25(21):4340–4347, 2013.

[342] Sarah M Mickley Conron, Leah E Shoer, Amanda L Smeigh, Annie Butler Ricks, and Michael R Wasielewski. Photoinitiated electron transfer in zinc porphyrin–perylenediimide cruciforms and their self-assembled oligomers. *The Journal of Physical Chemistry B*, 117(7):2195–2204, 2013.

[343] Xiao-Lei Zhang, Jian-Wei Jiang, Yi-Ting Liu, Shi-Tao Lou, Chun-Lei Gao, and Qing-Yuan Jin. Identifying the assembly configuration and fluorescence spectra

of nanoscale zinc-tetraphenylporphyrin aggregates with scanning tunneling microscopy. *Scientific reports*, 6:22756, 2016.

[344] Jinhua Cai, Haihui Chen, Jiangen Huang, Jingxia Wang, Dongliang Tian, Huanli Dong, and Lei Jiang. Controlled self-assembly and photovoltaic characteristics of porphyrin derivatives on a silicon surface at solid–liquid interfaces. *Soft matter*, 10(15):2612–2618, 2014.

[345] Claude Cohen-Tannoudji, Bernard Diu, and Franck Laloe. Quantum mechanics, volume 1. hermann and john wiley & sons. *Inc., Paris*, 1977.

[346] Simon M Sze and Kwok K Ng. *Physics of semiconductor devices*. John wiley & sons, 2006.

[347] BongSoo Kim, Jeremy M Beebe, Yongseok Jun, X-Y Zhu, and C Daniel Frisbie. Correlation between homo alignment and contact resistance in molecular junctions: aromatic thiols versus aromatic isocyanides. *Journal of the American Chemical Society*, 128(15):4970–4971, 2006.

[348] Kunio Ishikawa, Shunichi Fukuzumi, and Toshio Tanaka. Electron-transfer processes in the electrophilic cleavage of cobalt-carbon bonds of alkylcobalt (iii) complexes with iodine. *Inorganic Chemistry*, 28(9):1661–1665, 1989.

[349] Roger A Heckman and James H Espenson. Kinetics and mechanism of oxidation of cobalt (ii) macrocycles by iodine, bromine, and hydrogen peroxide. *Inorganic Chemistry*, 18(1):38–43, 1979.

[350] HA Hashem and MS Refat. Synthesis, spectroscopic, ac conductivity and thermal studies on co (iii) acetylacetonate-iodine complex. *Surface Review and Letters*, 13(04):439–449, 2006.